The $Li^6(\alpha,2\alpha)d$ Reaction at 50 to 80 MeV

by

John W. Watson

Thesis submitted to the Faculty of the Graduate School
of the University of Maryland in partial fulfillment
of the requirements for the degree of
Doctor of Philosophy
1970

APPROVAL SHEET

Title of Thesis: The $Li^6(\alpha,2\alpha)d$ Reaction at 50 to 80 MeV

Name of Candidate: John W. Watson
Doctor of Philosophy, 1970

Thesis and Abstract Approved: H G Pugh

Howel G. Pugh
Associate Professor
Department of Physics and Astronomy

Date Approved: 26 September 1969

PLEASE NOTE:

Some pages have indistinct print. Filmed as received.

UNIVERSITY MICROFILMS.

ABSTRACT

Title of Thesis: The $Li^6(\alpha,2\alpha)d$ Reaction at 50-80 MeV.

John W. Watson, Doctor of Philosophy 1970

Thesis directed by: Dr. Howel G. Pugh, Associate Professor

The $Li^6(\alpha,2\alpha)d$ reaction was studied at 50.4, 59.0, 60.5, 70.3 and 79.6 MeV bombarding energy. For each bombarding energy, several coincident energy spectra of the two emitted α-particles were measured. Special emphasis was placed on measuring spectra at pairs of angles where zero momentum (in the laboratory frame of reference) was possible for the residual deuteron. Using the constraints on three body kinematics, events corresponding to an $\alpha + \alpha + d$ final state were selected from the coincident energy spectra. The cross section for these events was projected onto the E_1 energy axis of the coincident spectra.

The projected energy spectra were analyzed with the Plane Wave Impulse Approximation. From those points in the projected spectra which corresponded to zero deuteron recoil momentum, off-mass-shell α-α scattering cross sections were extracted. These were found to be in excellent agreement with free α-α scattering cross sections, if free cross sections for the final state center of mass energy of the two α's in the $Li^6(\alpha,2\alpha)d$ reaction were chosen for the comparison. Off-mass-shell α-α cross sections were also extracted for data where the residual deuteron had a momentum of 30 MeV/c. These cross sections were also found to agree with free α-α scattering, but it was necessary to introduce an ad hoc shift in the α-α scattering angle to produce this agreement. Predictions of off-mass-shell α-α cross sections were made using a potential model. These indicate that the off-mass-shell cross section should indeed be very similar to the on-mass-shell cross section at the final state energy.

Using the Plane Wave Impulse Approximation a momentum distribution for α's in Li^6 was extracted from the experimental data. A cluster model for Li^6 was devised to fit the binding energy and r.m.s. charge radius of Li^6, as well as the $^3S_1$ α-d scattering phase shift. For comparison with the experimental data, the momentum wave function of the α-particle in Li^6 was calculated by taking the Fourier transform of the α-d relative motion. The theoretical and experimental momentum distributions were found to be in serious disagreement, both in magnitude and width at half maximum. By introducing a cut-off radius into the theoretical wave function, the discrepancies between theory and experiment were accounted for. It was also found, that if the cut-off radius is used as an adjustable parameter, then this Li^6 wave function and reaction model explains the magnitudes and widths of the α-d relative momentum distributions determined from a wide variety of other reactions.

TO

P.M. AND GEORGE

WHO CAME THIS WAY

BEFORE

AND TO

PHYLLIS AND HOWEL

WHO HELPED ME COME

THIS FAR

ACKNOWLEDGEMENTS

I wish to express my warmest gratitude to Professor Howel G. Pugh, not only for suggesting the experiment described in this work, but for the patient guidance and encouragement he has given me during my graduate studies at the University of Maryland.

I also wish to thank Drs. Harry Holmgren, Phil Roos, and Sandy Wall for their thoughtful discussions and assistance during my association with the University of Maryland cyclotron group.

I want to express my appreciation to Drs. David Goldberg and Jim Riddle for their excellent assistance in the execution and analysis of this experiment. I also want to thank Mr. Dan Bonbright, Dr. Mahavir Jain, Mr. Peter Frisbee, and Dr. Paul Perrin for their assistance and discussions. Thanks are also due to Mr. Jim Etter for his assistance with the electronics.

I want to thank Dr. Ian McCarthy for his invaluable assistance in planning the off-mass shell calculation presented here.

I would like to thank Mr. David Nelson and Dr. Neil Yoder for their excellent advice on computer programming. I am also indebted to the University of Maryland Computer Science Center for generous grants of computing time on Account (205/01/163).

I wish to thank Dr. Alex Zucker and all the staff of the ORIC cyclotron, especially Drs. Carl Ludemann and Charles Goodman for their support and cooperation. I am grateful for the support I have received from the United States Atomic Energy Commission under contract AT-(40-1)-3491.

I am indebted to Mr. John White and Mr. Lionel Watkins for their generous cooperation in preparing figures and duplicating this thesis, and Mrs. Betty Frisbee for proof reading, and to Mrs. Marilyn Grant and Mrs. Rosemary McAvoy for their help in typing.

I am eternally indebted to Dr. Fay Ajzenberg-Selove for introducing me to nuclear physics, to Howel Pugh and to the University of Maryland.

Lastly, none of this would have been possible without the love and support of my wife Phyllis.

TABLE OF CONTENTS

CHAPTER 1

INTRODUCTION

The experiment chosen for this research project is the $Li^6(\alpha,2\alpha)d$ nuclear reaction. The particular feature of interest in this reaction is the knockout process. In a knockout reaction, the incident projectile is presumed to interact strongly with only one constituent of the target nucleus, knocking it out of the target. In the absence of strong interactions of either the incident or the knocked out particle with the remainder of the target nucleus, the knockout reaction will resemble free scattering between the incident and knocked out particle. For this reason, the process is frequently described as "quasi-free scattering".

In the "impulse approximation" any interaction of the incident particle or the knocked out particle with the remainder of the nucleus is ignored. If the impulse approximation is valid a knockout reaction can yield information on the wave function in the target nucleus of the particle which was knocked out. This requires, however, that two of the three particles in the final state be detected in coincidence. Hence knockout reactions usually are technically difficult, and have low counting rates. The development during the last decade of high current medium energy accelerators with a small energy spread in the beam, solid state detectors, multiparameter-multichannel pulseheight analyzers and on-line computers has done much to overcome the experimental difficulties, and today knockout reactions are an important tool of nuclear structure physics.

The most thoroughly studied knockout experiment has been the (p,2p) reaction. A proton with an energy of 100 MeV or greater has a mean free path in a target nucleus that is comparable to nuclear dimensions, and

it would seem reasonable to make the impulse approximation for the (p,2p) reaction. Indeed (p,2p) experiments have shown that for energies in the 100 MeV range this is generally the case. Thorough reviews of (p,2p) reactions are given in (Be66) and (J66).

In recent years, there has been growing interest in knockout reactions where a bound cluster of nucleons such as a deuteron or an α-particle is knocked out of the target nucleus. These reactions are of considerable interest, because they can potentially yield information on clustering or correlations in nuclei. It is not clear, however, that neglecting any interaction of the incident and struck particles with the rest of the target is a good approximation for the case of cluster knockout. This is particularly true if complex projectiles such as α-particles are used. It is of considerable interest, therefore, to investigate in detail the reaction mechanism for cluster knockout, and in particular to test the validity of the impulse approximation for such reactions.

Recent experiments (J69) have shown that there is a relatively large cross section for knocking α-particles out of Li^6, and that the reaction seems to proceed by quasi-free scattering. The $Li^6(\alpha,2\alpha)d$ reaction was chosen for study because of this large cross section, and because the free α-α interaction has been rather thoroughly studied (D65). The purposes of the experiment were to study the α-α quasi-free scattering process in detail, and if possible to use the impulse approximation to extract information on the cluster structure of Li^6.

Section 1.1 Kinematics

One of the quantities that one wishes to determine for each event in the $Li^6(\alpha,2\alpha)d$ knockout reaction is the momentum of the knocked out α-particle before the reaction occurred. This is done by using what will be loosely described as the "impulse approximation", which relates this momentum to the momentum of the deuteron in the final state.

Figure 1.1 shows the initial and final states in the laboratory of the $Li^6 + \alpha \rightarrow \alpha + \alpha + d$ reaction. In the initial state the incident α has a

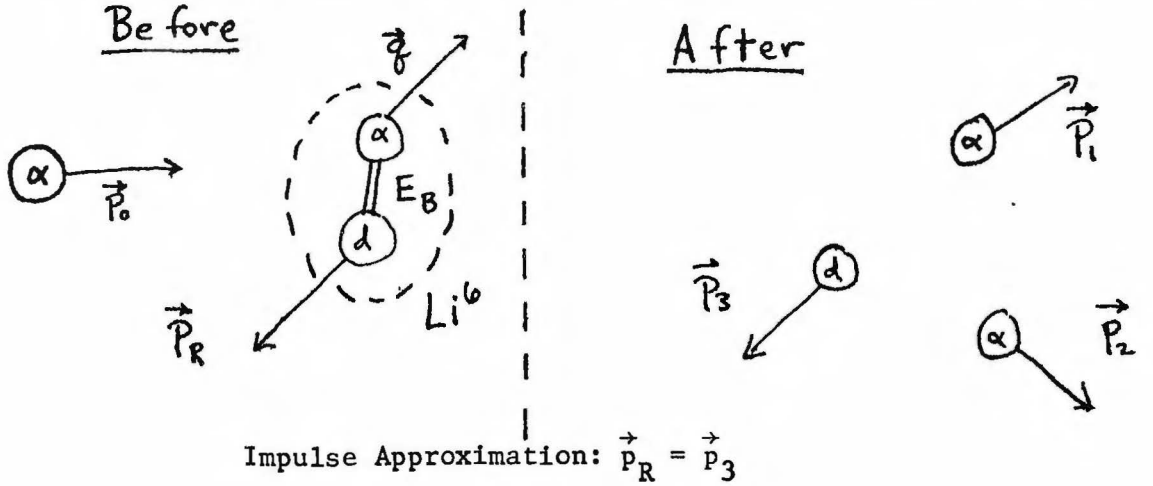

Figure 1.1 The $Li^6 + \alpha \rightarrow \alpha + \alpha + d$ Knockout Reaction

laboratory momentum $\vec{p}_0$, while the Li^6 nucleus is assumed to be a bound system of an α and a deuteron with a binding energy $E_B = 1.47$ MeV. The α in the Li^6 has a momentum $\vec{q}$, and the deuteron has a momentum $\vec{p}_R$. In the laboratory reference frame $\vec{q} = -\vec{p}_R$ because the target Li^6 is stationary. In the final state the two emitted α's have momenta $\vec{p}_1$ and $\vec{p}_2$, and the recoil deuteron has a momentum $\vec{p}_3$. In the impulse approximation the reaction is considered as a collision between the two α-particles, and the deuteron is assumed to be unaffected by the knockout process. Hence $\vec{p}_3 = \vec{p}_R$. Since $\vec{p}_R = -\vec{q}$, we obtain

$$\vec{q} = -\vec{p}_3 \qquad (1.1)$$

The distribution of α-particle momenta $\vec{q}$ in Li^6 is the square of the Fourier transform of the wave function for the α in Li^6. The product of the width of the momentum distribution and the nuclear size is approximately equal to $\hbar/2$ by the uncertainty principle: $\Delta x \Delta q \sim \hbar/2$ ~ 100 (MeV/c) fm. If the nuclear size is taken as 1.3 x $A^{1/3}$ fm., then Δx ~ 2.5 fm. and Δq ~ 40 MeV/c. Near $\vec{q} = 0$ the momentum distribution behaves like $|\vec{q}|^{2L}$ where L is the orbital angular momentum quantum number for the α-d relative motion wave function. Because this wave function is nearly all L = 0 (see chapter 5), the momentum distribution for the α-particle in Li^6 behaves like $|\vec{q}|^0$ near $\vec{q} = 0$, i.e., it is peaked at $\vec{q} = 0$ rather than having a minimum there. For the residual deuteron the corresponding momentum spread $\Delta\vec{p}_3$ ~ 40 MeV/c implies an energy distribution in the final state extending up to about 400 KeV. This makes direct detection of the deuteron unfeasible. However, the momentum $\vec{p}_3$ of the deuteron can be determined from measurements on the other particles.

In the final state there are 10 kinematic variables. The three momenta $\vec{p}_1$, $\vec{p}_2$, and $\vec{p}_3$ each have 3 components which in spherical coordinates will be called θ_i, ϕ_i and p_i for i = 1, 2, 3. In addition there is the energy loss in the reaction, which is equal to E_B (the binding energy of the αin Li^6) for transitions in which the residual deuteron is left in its ground state. Four-momentum conservation gives four equations of constraint on the ten variables, one for each component of four-momentum. Hence the determination of 6 kinematic quantities will completely specify the remainder. For this experiment, the six measured quantities were θ_1, ϕ_1, E_1, θ_2, ϕ_2, and E_2 the angles and kinetic energies of the two α-particles. Appendix 1 presents a derivation of $\vec{p}_3$ and E_2 given θ_1, ϕ_1, θ_2, ϕ_2, E_1, and E_B. Several other kinematic quantities are also derived.

The experiment was performed with "coplanar" geometry, i.e., with

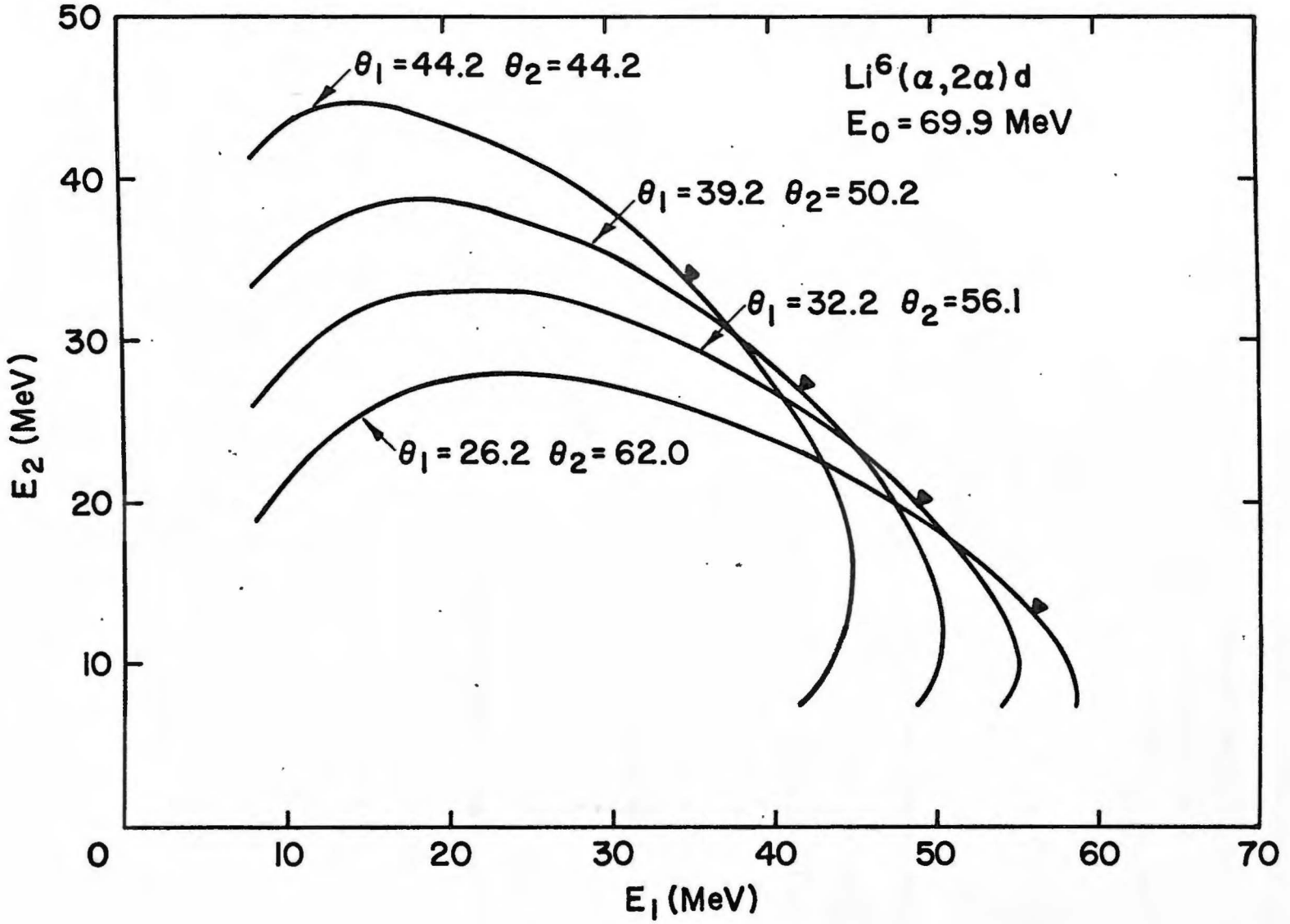

Figure 1.3: Four kinematic loci for the $Li^6(\alpha,2\alpha)d$ reaction at 69.9 MeV. The point where $\vec{q} = 0$ is indicated for each locus with an arrow.

$\phi_2 = \phi_1 + 180^o$. This means that the incident beam lies in the plane defined by the trajectories of the two detected α's. Figure 1.2 shows the geometry of the experiment. The angles θ_1 and θ_2 are measured relative to the incident

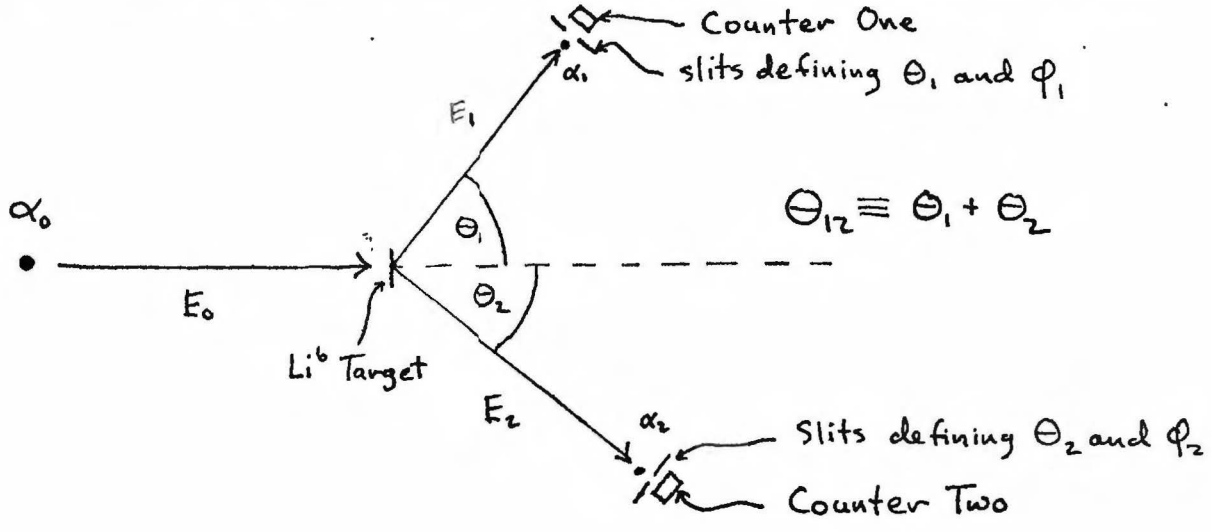

Figure 1.2: Experimental Geometry

beam direction. The separation angle between the two counters will be called θ_{12} and is equal to $\theta_1 + \theta_2$.

Data were taken for each pair of values of θ_1, θ_2 in the form of coincident two-dimensional energy spectra with E_1 and E_2, the energy signals from counters one and two, being the two energy axes. The kinematic constraints, for fixed values of θ_1, ϕ_1, θ_2, ϕ_2, and E_B determine a line or "kinematic locus" in the E_1 vs. E_2 plane. Every point on such a kinematic locus corresponds to a definite value of $\vec{p}_3$ or, using the impulse approximation, $\vec{q}$, the initial momentum of the knocked out α-particle. The values of $\vec{q}$ which occur on a given kinematic locus depend on θ_1, ϕ_1, θ_2, ϕ_2, and E_B. Since we will always be considering coplanar scattering, ϕ_1 and ϕ_2 will not be mentioned from now on. Figure 1.3 shows several typical kinematic loci for the $Li^6(\alpha,2\alpha)d$ reaction at 69.9 MeV. These values of θ_1 and θ_2 were selected so that one point with $\vec{q} = 0$ occurs on each locus. This point is where the

$(\alpha,2\alpha)$ knockout cross section is expected to be largest. The $\vec{q} = 0$ points are indicated with arrows. Along each locus, $|\vec{q}|$ increases monotonically as one moves away from the $\vec{q} = 0$ point.

In the process of data reduction, events falling on the kinematic locus corresponding to the desired value of E_B were projected onto the E_1 axis producing a "projected energy spectrum". For each value of E_1 in the spectrum, $\vec{p}_3$ hence $\vec{q}$ can be determined. The cross section of the projected spectrum is $d^3\sigma/d\Omega_1 d\Omega_2 dE_1$.

For the remainder of this thesis the following conventions will be used. Particle 0 is the incident α-particle. Particle T is the target Li^6 nucleus. Particles one and two are the two detected α's. Particle three is the "residual nucleus", the deuteron. These conventions will also be used for the subscripts on kinematic quantities. The following two terms will also be used: "Quasi-Free Peak" will refer to the peak near $\vec{p}_3 = 0$ in the projected energy spectra that is believed to be due to quasi-free α knockout from Li^6; "Quasi-Free Angle Pairs" will refer to a pair of angles θ_1 and θ_2 for which a $\vec{q} = 0$ point occurs on the kinematic locus.

Section 1.2 Theory (Plane Wave Impulse Approximation)

The theory that will be used for the analysis presented in this thesis is the Plane Wave Impulse Approximation (P.W.I.A.). In calculating the knockout cross section using P.W.I.A. one starts with the transition matrix (T matrix) element for the reaction

$$T_{fi} = \langle \phi_1(\vec{k}_1,\vec{r}_1)\,\phi_2(\vec{k}_2,\vec{r}_2)\,\phi_3(\vec{k}_3,\vec{r}_3)\,|T_{3B}|\,\phi_T(\vec{k}_T,\vec{r}_T)\,\psi_{rel}(\vec{R})\,\phi_o(\vec{k}_o,\vec{r}_o)\rangle \quad (1.3)$$

where ϕ_1, ϕ_2 and ϕ_3 are the wave functions of the two α's and the deuteron in the final state, ϕ_T is the wave function of the target nucleus, ψ_{rel} is the relative motion wave function of the α and the deuteron in the target, and ϕ_o is the wave function of the incident α . T_{3B} is the full 3 body transition operator. ϕ_1, ϕ_2, ϕ_3, ϕ_T, and ϕ_o are all plane waves.

$\psi_{rel}(\vec{R})$ can be expressed in terms of its Fourier Transform, the momentum space wave function $\Phi(\vec{q})$.

$$\begin{aligned}\psi_{rel}(\vec{R}) &= (2\pi)^{-3/2}\int e^{i\vec{q}\cdot\vec{R}/\hbar}\,\Phi(\vec{q})\,d\vec{q}\\ &= (2\pi)^{-3/2}\int e^{i\vec{q}\cdot\vec{r}_s/\hbar}\,\Phi(\vec{q})\,e^{i\vec{q}\cdot(\vec{R}-\vec{r}_s)/\hbar}\,d\vec{q}\\ &= \int \phi_s\left(\frac{\vec{q}}{\hbar},\vec{r}_s\right)\Phi(\vec{q})\,e^{i\vec{q}\cdot(\vec{R}-\vec{r}_s)/\hbar}\,d\vec{q} \quad (1.4)\end{aligned}$$

where $\vec{r}_s$ is the coordinate of the α in Li^6, in the same coordinate system in which $\vec{r}_1$, $\vec{r}_2$, $\vec{r}_3$, $\vec{r}_T$, and $\vec{r}_o$ are defined, and $\phi_s(\frac{\vec{q}}{\hbar},\vec{r}_s)$ is a δ-function normalized plane wave state. Then

$$T_{fi} = \int \langle \phi_1\phi_2\phi_3|T_{3B}|\phi_o\phi_s\phi_T\rangle\,\Phi(q)\,e^{i\vec{q}\cdot(\vec{R}-\vec{r}_s)/\hbar}\,d\vec{q} \quad (1.5)$$

Now one makes the approximation of replacing T_{3B}, the full 3-body transition operator by T_{2B}, the two body transition operator of the two α's. This, formally, is the impulse approximation. Then

$$T_{fi} = \iint d\vec{r}_3\,\phi_3\left[\langle\phi_1\phi_2|T_{2B}|\phi_o\phi_s\rangle\,\Phi(q)\right]\phi_T\,e^{i\vec{q}\cdot(\vec{R}-\vec{r}_s)/\hbar}\,d\vec{q} \quad (1.6)$$

The structure of the matrix element is now clear. The important factors are $\langle\phi_1\phi_2|T_{2B}|\phi_o\phi_s\rangle$, the α-α scattering matrix element and $\Phi(\vec{q})$, the momentum wave function of the α in Li^6. The remaining integrals in the matrix element

(1.6) can be reexpressed as delta functions in momentum. The relationship $\vec{q} = -\vec{p}_3$, which was called the impulse approximation in Section 1.1, is incorporated implicitly in the theory in these delta functions.

In calculating the cross section from T_{fi} the two "important" terms are squared, yielding $(\frac{d\sigma}{d\Omega})_{\alpha\alpha}$ (the α-α scattering cross section) and $|\Phi(q)|^2$. These are multiplied by a third factor involving phase space and other kinematic quantities. This third factor will be called "the kinematic factor". A full derivation of the P.W.I.A. cross section is given non-relativistically in (K68) and relativistically in (J69). The result is:

$$\frac{d^3\sigma}{d\Omega_1 d\Omega_2 dE_1} = (\text{Kinematic Factor}) \times \left(\frac{d\sigma}{d\Omega}\right)_{\alpha\text{-}\alpha} \times \left|\Phi(q)\right|^2 \qquad (1.7)$$

Non-relativistically, the kinematic factor is

$$(\text{Kinematic Factor}) = \frac{k_1 k_2}{k_0 \hbar^2} m_2 \left(\frac{m_0 + m_2}{m_2}\right)^2 \times \left[1 + \frac{m_2}{m_3} + \frac{m_2}{m_3}\frac{k_1}{k_2}\cos(\theta_1 + \theta_2) - \frac{m_2}{m_3}\frac{k_0}{k_2}\cos\theta_2\right]^{-1} \qquad (1.8)$$

For $Li^6(\alpha, 2\alpha)d$ this becomes

$$(\text{Kinematic Factor}) = \frac{4 m_\alpha k_1 k_2}{\hbar^2 k_0}\left(3 + \frac{2k_1}{k_2}\cos\theta_{12} - \frac{2k_0}{k_2}\cos\theta_2\right)^{-1} \qquad (1.9)$$

The kinematic factor includes in it terms which make $\left(\frac{d\sigma}{d\Omega}\right)_{\alpha\alpha}$ a center of mass cross section.

It is worth noting that $(d\sigma/d\Omega)_{\alpha\alpha}$ in (1.7) is an "off-mass-shell" cross section. This means that the center of mass energy in the initial state $|\phi_0\phi_s\rangle$ is not the same as the center of mass energy in the final state $\langle\phi_1\phi_2|$. This is because the α in Li^6 is not a free α, but is bound by 1.47 MeV. The term "off-mass-shell" refers specifically to the fact that for the bound α the normal relationship among the components of its four-momentum does not hold, namely

$$E^2 - \vec{q}^2 \neq m^2 \qquad (1.10)$$

The bound α in Li^6 might also be described as a "virtual particle" for this reason.

The approximation used in (1.6), namely replacing T_{3B} by T_{2B}, with the direct result that $\vec{q} = -\vec{p}_3$, is the impulse approximation. The overall treatment is called "Plane Wave Impulse Approximation" because ϕ_0, ϕ_1 and ϕ_2 are left as plane waves. In "Distorted Wave Impulse Approximation" (Be66) ϕ_0, ϕ_1 and ϕ_2 are replaced with distorted waves calculated in the optical potentials for the target nucleus (yielding χ_0) or the residual nucleus (yielding χ_1 and χ_2). Then $\langle \phi_1 \phi_2 | T_{2B} | \phi_0 \phi_3 \rangle \longrightarrow \langle \chi_1 \chi_2 | T_{2B} | \chi_0 \phi_3 \rangle$. It is not clear that such a calculation is reasonable for the $Li^6(\alpha,2\alpha)d$ reaction where the residual nucleus is a deuteron. If such a treatment were necessary, the relationship $\vec{q} = -\vec{p}_3$ would no longer be valid.

Knockout processes are often referred to as peripheral processes (F62), since the conditions for their occurrence are usually met in the surface or periphery of the nucleus. Peripheral processes are usually discussed in terms of Feynman diagrams. Figure 1.4 shows the Feynman diagram appropriate to the $Li^6 + \alpha \rightarrow \alpha + \alpha + d$ knockout process. The Li^6 emits a virtual α at the lower vertex. The real incident α interacts with this virtual α at the upper vertex. The amplitude for this diagram is the product of the amplitudes of the two

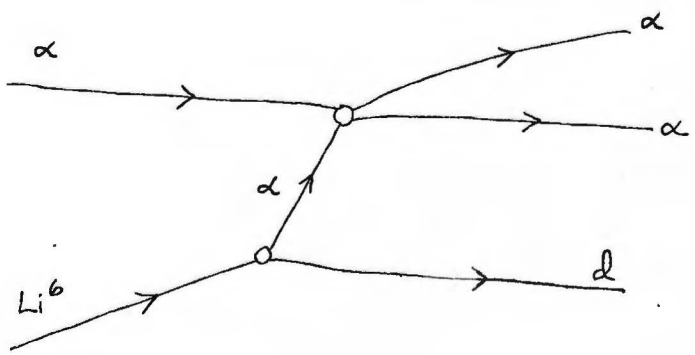

Figure 1.4: The Peripheral Diagram for the $Li^6(\alpha,2\alpha)d$ Knockout Reaction

vertices divided by the propagator for the virtual α . The amplitude for the lower vertex is the "form factor" characterizing the momentum distribution

for the virtual α . The amplitude for the upper vertex is the off-mass-shell α-α scattering amplitude. Thus the cross section will be the product of the squares of these two vertex amplitudes multiplied by phase space and other kinematic quantities. For a more complete discussion of the evaluation of peripheral diagrams for knockout and other reactions see (F62) or (S66).

The most important feature of the knockout cross section in P.W.I.A. (or the peripheral model) is that it factorizes into 3 terms. The kinematic factor is known (1.8), and is in general a rather slowly varying function. The two remaining factors, the square of the momentum wave function for an α in Li^6 and the α-α off-mass-shell cross section, are the interesting factors and P.W.I.A. will be used to study both.

Section 1.3 The Li^6 Ground State Wave Function

The ground state of the Li^6 nucleus has the following properties:

1) Spin and parity: $J^\pi = 1^+$

2) Magnetic moment: $\mu = +.822$ n.m. (W54)

3) Electric Quadrupole Moment: $Q = -(0.80 \pm 0.08)$ e mb (W64)

4) R.M.S. Charge Radius: $\langle r^2 \rangle^{1/2} = (2.61 \pm 0.\ )$ fm. (Y69)

5) R.M.S. Magnetic Moment Radius: (3.0 ± 0.45) fm. (R66).

Of interest in this experiment is the α+ d cluster structure for Li^6. Deuteron reduced widths for the Li^6 ground state have been extracted from a number of reactions at low energies. For α + d scattering, the low energy scattering phase shifts were analyzed by Galonsky and McEllistrem in terms of a dispersion formalism (G55). They found that the S-wave phase shift can be fit well with a hard sphere of radius 5.0 fm. However, their analysis of other low energy α-d scattering phase shifts leads them to prefer a hard sphere radius of 3.5 fm., which necessitates inclusion of a ground state tail in the S-wave phase shift and a deuteron reduced width for the Li^6 ground state of $\theta^2 = 0.51$. This number has a large uncertainty, however, and any value between zero and the Wigner limit is compatible with the data.

The $Li^6(p,He^3)He^4$ reaction has been studied at 15 and 18.5 MeV by Likely and Brady (L56). Using Plane Wave Born Approximation (P.W.B.A.) they find a deuteron reduced width θ^2 for this reaction of 0.30 at 15 MeV, and 0.45 at 18.5 MeV. The $Li^6(n,t)He^4$ reaction has been studied by Frye (F54) at 14 MeV. His data has also been analyzed by Likely and Brady (L56). Using P.W.B.A., they find a deuteron reduced width for this reaction of 0.5. Their conclusion, after considering the deficiencies in this method of analysis is that, "The true deuteron reduced width in Li^6 may then be of the order of 0.5, the greatest value of θ^2 above, or even greater."

Although there are considerable uncertainties in the values of the deuteron reduced width for the Li^6 ground state discussed in the preceeding two paragraphs, they all suggest a substantial probability of deuteron clustering. A variety of other reactions which provide information on the $\alpha + d$ cluster wave function of Li^6, as well as clustering probabilities are discussed in Chapter 4. These include the $Li^6(p,pd)He^4$, $Li^6(\alpha,\alpha d)He^4$, $Li^6(\pi^-,2n)He^4$, $Li^6(p,p\alpha)d$, $Li^6(\alpha,2\alpha)d$, $C^{12}(Li^6,d)O^{16}$, and $O^{16}(Li^6,d)Ne^{20}$ reactions.

Section 1.4 Experimental Objectives

As discussed in Section 1.2, the knockout cross section in P.W.I.A. factorizes into three terms:

$$\frac{d^3\sigma}{d\Omega_1 d\Omega_2 dE_1} = (\text{Kinematic Factor}) \times \left(\frac{d\sigma}{d\Omega}\right)_{\alpha-\alpha} \times \left|\Phi(\vec{q})\right|^2 \quad (1.11)$$

This factorizability was used to study both the reaction mechanism and Li^6 structure.

The objectives of this experiment were threefold. The first objective was to study off-mass-shell α-α scattering in the knockout process. By keeping $\vec{q}$ fixed, that is by kinematically selecting points with the same value of $\vec{q}$, the factor $|\Phi(\vec{q})|^2$ could be held constant, and the α-α off-mass-shell cross section could be extracted from the measured cross section $d^3\sigma/d\Omega_1 d\Omega_2 dE_1$. This was possible because the kinematic factor is explicitly known (Formula 1.8). Using this technique, the off-mass-shell cross section was determined as a function of both bombarding energy and scattering angle. The experimental off-mass-shell α-α cross sections were then compared with free α-α cross sections at nearby points on the mass shell, and with off-mass-shell cross sections calculated with a phenomenological α-α potential.

The second objective was to study the cluster structure of Li^6. Once the behavior of the off-mass-shell cross section was established, this was used to extract $|\Phi(q)|^2$ from $d^3\sigma/d\Omega_1 d\Omega_2 dE_1$. The measured $|\Phi(q)|^2$ was then compared with the momentum distribution derived from a cluster model wave function for Li^6.

The third objective was to study the validity of the Plane Wave Impulse Approximation which was used in the extraction of $(d\sigma/d\Omega)_{\alpha-\alpha}$ and $|\Phi(q)|^2$ from the data. This was studied through the overall consistency of the analysis outlined in the two previous paragraphs.

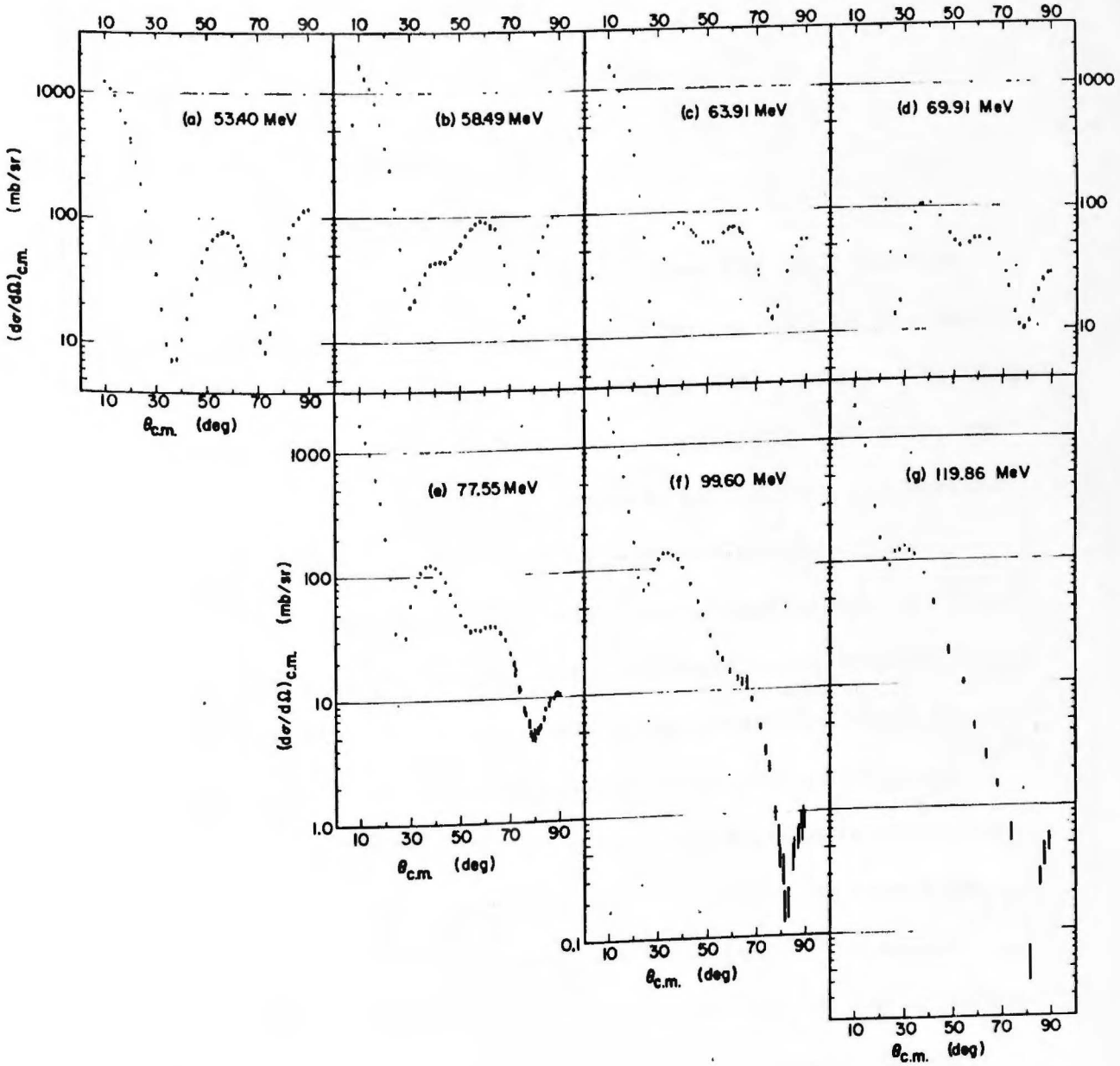

Figure 2.1: Differential cross sections for elastic α-α scattering, in the center of mass system. Data is from (D65). The laboratory bombarding energies are:

a) 53.40 MeV b) 58.49 MeV
c) 63.91 MeV d) 69.91 MeV
e) 77.55 MeV f) 99.60 MeV
g) 119.86 MeV

CHAPTER 2

THE EXPERIMENT: $Li^6(\alpha,2\alpha)d$

Section 2.1 Design of the Experiment

2.1.1 Choice of Energies and Angles

The P.W.I.A. was already known to be fairly good for this reaction (J69), hence it could be used to design the experiment. Because the binding energy for the breakup of Li^6 into an α-particle and a deuteron (1.47 MeV) is quite small when compared with the bombarding energy (50 - 80 MeV), the kinematics for α knockout are very nearly the same as for free α-α scattering. We therefore begin with a discussion of free α-α scattering.

For free α-α scattering, neglecting relativistic correction, the center-of-mass scattering angle θ_{cm} is twice the laboratory scattering angle θ_1. Since the two particles are of equal mass, the separation angle between them, $\theta_{12} = \theta_1 + \theta_2$, is 90^o in the laboratory (180^o in the c.m. system). Because these are identical particles, the c.m. cross section is symmetric about $\theta_{cm} = 90^o$ ($\theta_1 = 45^o$). For "quasi-free" knockout with no recoil momentum for the deuteron, very nearly the same conditions hold. The angles in the laboratory θ_1 and θ_2, will both be slightly smaller (on the order of 1^o in the energy range of interest) to compensate for the energy lost in breaking up Li^6.

The free α-α differential cross section has been measured as a function of angle at several energies in the region of interest (D65). The angular distributions for bombarding energies of 53.4, 58.5, 63.9, 69.9, 77.6, 99.6 and 120 MeV are shown in Fig. 2.1. In addition, $d\sigma/d\Omega$ has been measured as a function of energy from 24 MeV to 54 MeV at $\theta_{cm} = 20^o$, 31^o, 55^o, and 90^o (D65). For reasons to be discussed later, scattering angles of smaller than

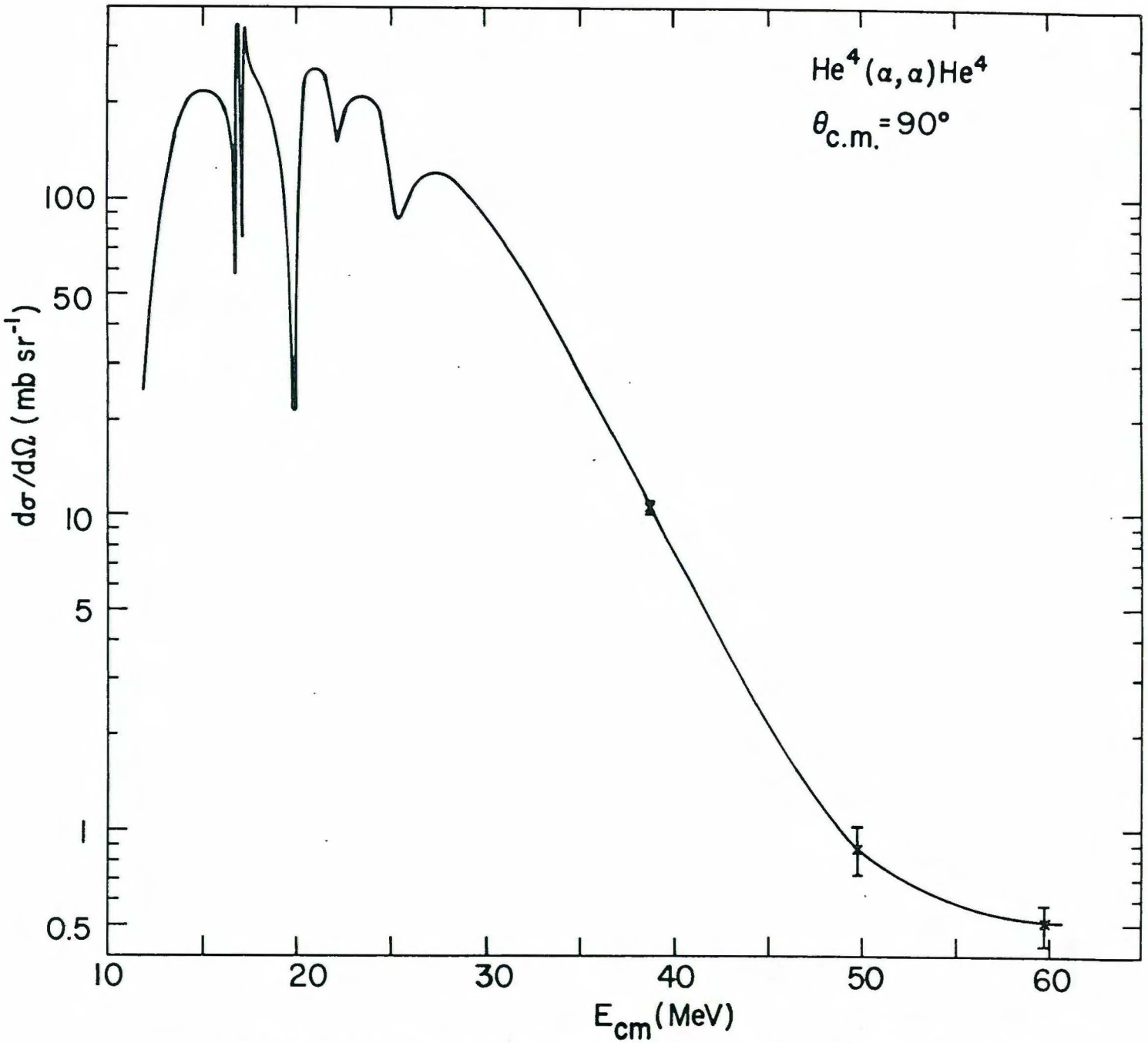

Figure 2.2: The differential cross section for elastic α-α scattering at 90° in the center of mass, as a function of center of mass energy. The data was taken from (D65).

50° in the center-of-mass (25° in the lab) are kinematically inaccessible in this $Li^6(\alpha,2\alpha)$ experiment. In the range of 50° to 90° in the center-of-mass, the notable features of the α-α cross section are the deep minimum in the vicinity of 73° - 83° which shifts gradually to larger angles at larger energies, the dramatic fall of the cross section for $\theta_{cm} = 90^{\circ}$, shown in Fig. 2.2, and the change in the relative heights of the maxima at 90° and about 60°.

One of the experimental objectives discussed in Section 1.4 was the determination of the off-mass-shell α-α differential cross section. The angles and bombarding energies used in the $Li^6(\alpha,2\alpha)d$ reaction were chosen to see if the above features of on-mass-shell α-α scattering were present in the off-mass-shell scattering. In particular, it was decided that $\vec{q} = 0$ would be the primary "fixed" value of $\vec{q}$ for the extraction of off-mass-shell cross sections. Therefore, a large number of "quasi-free" angle pairs were studied, so that data for $\vec{q} = 0$ could be extracted. In addition, each measurement at a quasi-free angle pair gave a complete measurement of $|\Phi(q)|^2$ for comparison with theory.

2.1.2 Particle Identification

It is necessary to identify the particles observed, as well as measure their energies. Because of the limited possibilities for competing processes, full identification was not necessary, but a system of single channel analyzers and discriminators could be used together with a knowledge of the kinematics of various possible processes to eliminate all but the desired events.

The detectors were Silicon surface barrier and Lithium drifted Silicon detectors. A two counter ΔE - E combination consisting of a totally depleted Silicon surface barrier ΔE detector and a 3 mm Li - drifted Silicon E

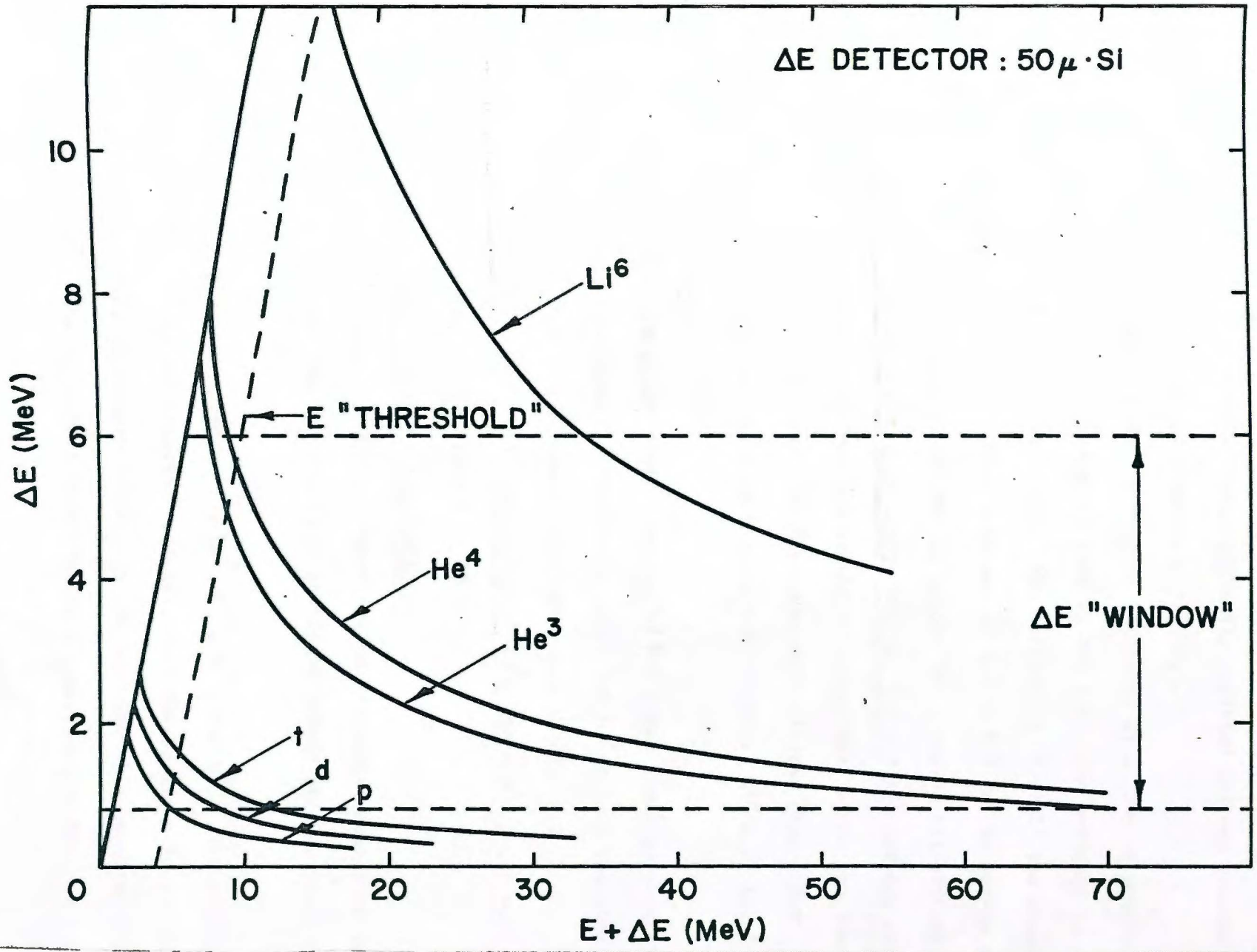

Figure 2.3: Response of a two detector ΔE-E array to various charged particles. The ΔE counter is a 50μ Si solid state detector. The ordinate ΔE is the energy loss in the ΔE detector. The abscissa ΔE+E is the energy loss in both counters. A "window" on the ΔE response and a "level"on the E response are indicated.

detector was used to detect α-particle one (E_1). A similar ΔE - E combination using a ΔE detector with a 1500 μ partially depleted Silicon surface barrier E detector was used for α-particle two (E_2).

Fig. 2.3 shows the response to various particles of a 50μ ΔE detector coupled with a counter thick enough to stop 70 MeV α's. The ordinant is "ΔE" the response of the ΔE detector. The abcissa is "E + ΔE" the summed response of the two counters. When a window of 0.8 to 6.0 MeV is set on the ΔE signal and a lower level of 4.0 MeV is set on the E signal all protons and all deuterons except those with energy between 5.0 and 8.0 MeV are eliminated. Note that these deuterons can easily be recognized, since the lowest energy α-particle which can reach the E counter with greater than 4 MeV energy, is 10 MeV. For reactions on heavier contaminants, Li^6's of less than 34 MeV are excluded also.

It should be pointed out here, that the 10 MeV lower limit on α-particle energies restricts the kinematic regions in which the $Li^6(\alpha,2\alpha)d$ reaction could be studied. From the kinematic loci presented in Fig. 1.3 it is clear that for values of θ_1 smaller than $\sim 25^\circ$, the $\vec{q} = 0$ point will be lost due to the restriction that $E_2 > 10$ MeV.

2.1.3 Elimination of Competing Reactions

There are two types of competing reactions to consider: reactions due to target contaminants, and Li^6 reactions involving 3 body breakup modes other than $Li^6(\alpha,2\alpha)d$.

The probable contaminants are H^1, Li^7, C^{12}, N^{14}, and O^{16}. Three body breakup involving H^1 cannot contribute at all, with the particle identification system described in Section 2.1.2. The Li used for this experiment is rated as 96% Li^6. The $Li^7(\alpha,2\alpha)t$ reaction has a cross section some 10 times

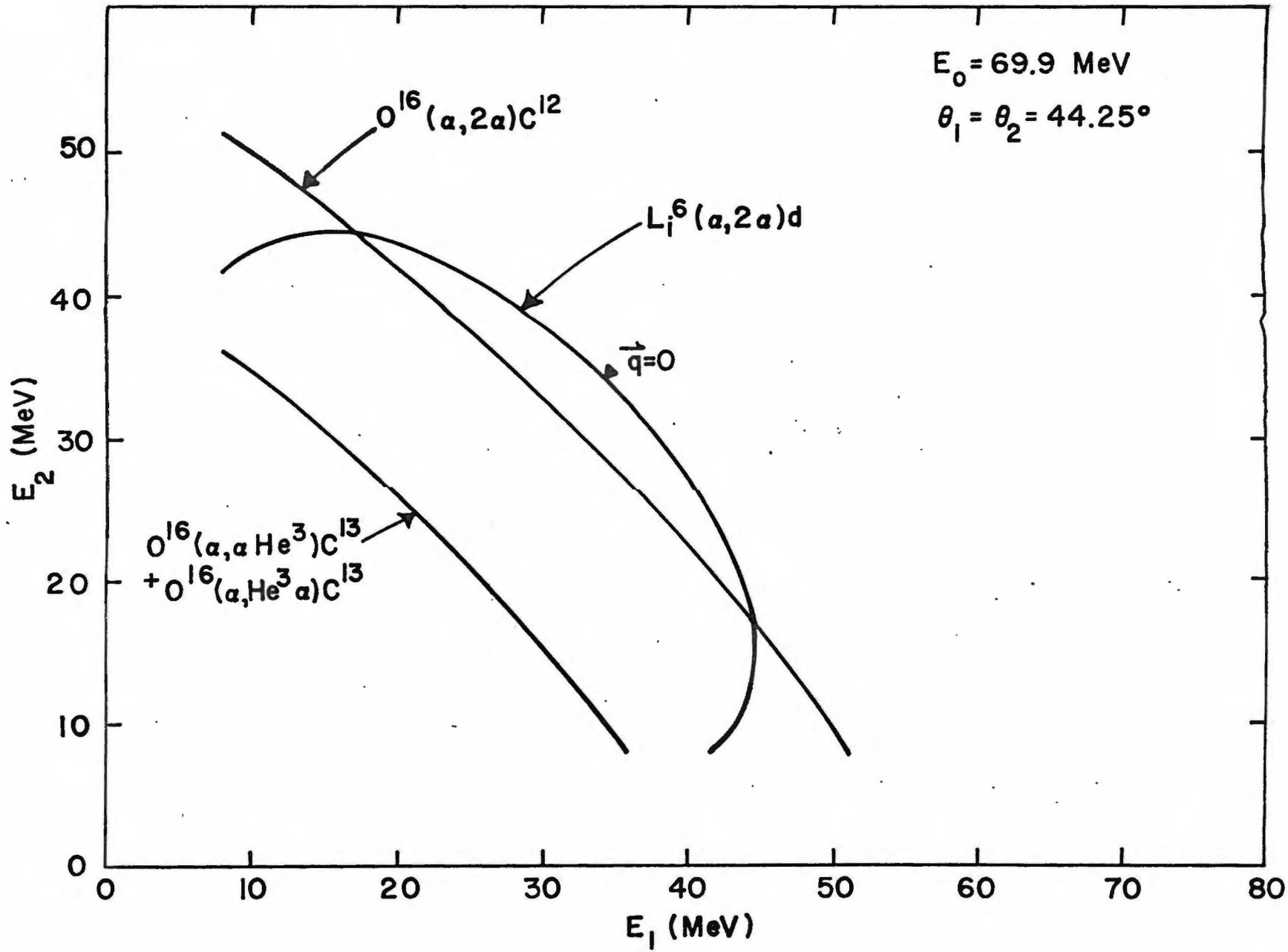

Figure 2.4: Kinematic loci for the $Li^6(\alpha,2\alpha)d$, $O^{16}(\alpha,2\alpha)C^{12}$, $O^{16}(\alpha,\alpha He^3)C^{13}$ and $O^{16}(\alpha,He^3\alpha)C^{13}$ reactions at 69.9 MeV bombarding energy. $\theta_1 = \theta_2 = 44.25°$.

smaller than $Li^6(\alpha,2\alpha)d$ (J69). Other reactions on Li^7, such as $Li^7(\alpha,\alpha He^3)H^4$, etc., have highly unfavorable Q values. Hence Li^7 caused no difficulty.

The kinematics for 3 body breakup with C^{12}, N^{14} and O^{16} are all very similar. O^{16} will be shown as a representative case. Figures 2.4 and 2.5 show the $Li^6(\alpha,2\alpha)d$, $O^{16}(\alpha,2\alpha)C^{12}$, $O^{16}(\alpha,\alpha He^3)C^{13}$, and $O^{16}(\alpha,He^3\alpha)C^{13}$ reactions at 69.9 MeV for $\theta_1 = 44.2^o$, $\theta_2 = 44.2^o$ and for $\theta_1 = 26.2^o$, $\theta_2 = 62^o$. It is clear that in the region of zero recoil momentum for the $Li^6(\alpha,2\alpha)d$ reaction, the other reactions can be distinguished kinematically. Furthermore the upper level on the ΔE signal in Fig. 2.3 eliminates most Li^6's from the possible three body reactions on C^{12}, N^{14} and O^{16}.

Three body breakup reaction on Li^6 with no α-particles in the final state have such a large Q value they need not be considered. The remaining possible reactions are $Li^6(\alpha,2\alpha)d$, $Li^6(\alpha,\alpha He^3)t$, $Li^6(\alpha,He^3\alpha)t$. Figures 2.6 and 2.7 show the kinematic loci for the above three reactions at 69.9 MeV for $\theta_1 = 44.2^o$, $\theta_2 = 44.2^o$ and for $\theta_1 = 26.2^o$, $\theta_2 = 62^o$. Also included is the threshold for the $Li^6(\alpha,2\alpha)np$ four body reaction. Again it is clear that the $Li^6(\alpha,2\alpha)d$ reaction is clearly distinguishable from the other on the basis of kinematics.

2.1.4 Reaction Mechanisms Contributing to the $Li^6(\alpha,2\alpha)d$ Reaction

Quasi-free knockout is not the only mechanism leading to the $Li^6(\alpha,2\alpha)d$ reaction. We must consider competition from other reaction mechanisms. Five diagrams for possible mechanisms are shown in Fig. 2.8. There is one diagram with one vertex and four diagrams with two vertices with this final state. Diagrams with more than two vertices will not be considered.

Diagram 2.8a represents the process usually known as instantaneous breakup. If the matrix element M for this process is assumed to be constant, then the cross section is proportional to phase space.

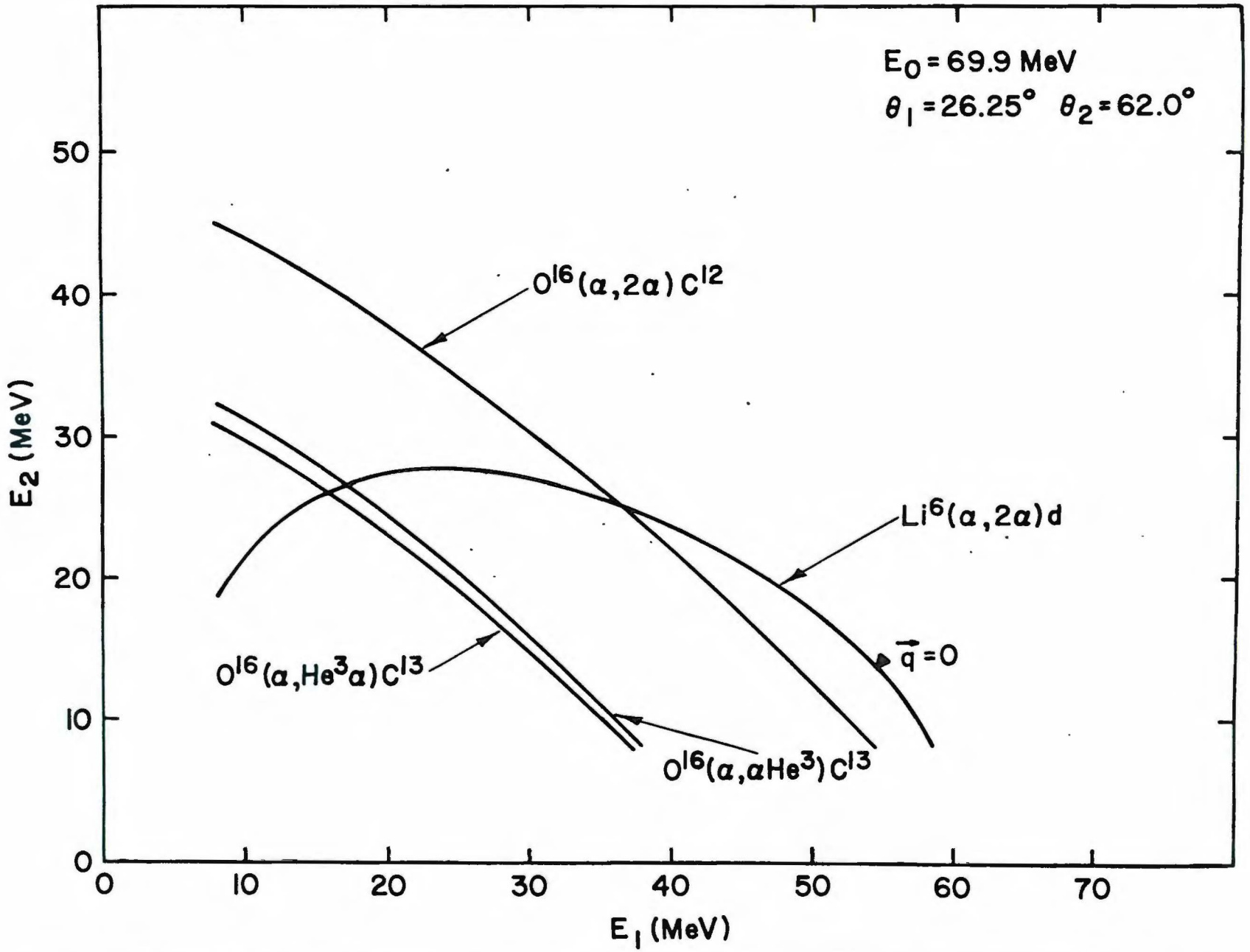

Figure 2.5: Kinematic loci for the $Li^6(\alpha,2\alpha)d$, $O^{16}(\alpha,2\alpha)C^{12}$, $O^{16}(\alpha,\alpha He^3)C^{13}$ and $O^{16}(\alpha,He^3\alpha)C^{13}$ reactions at 69.9 MeV bombarding energy. $\theta_1 = 26.25°$; $\theta_2 = 62.0°$.

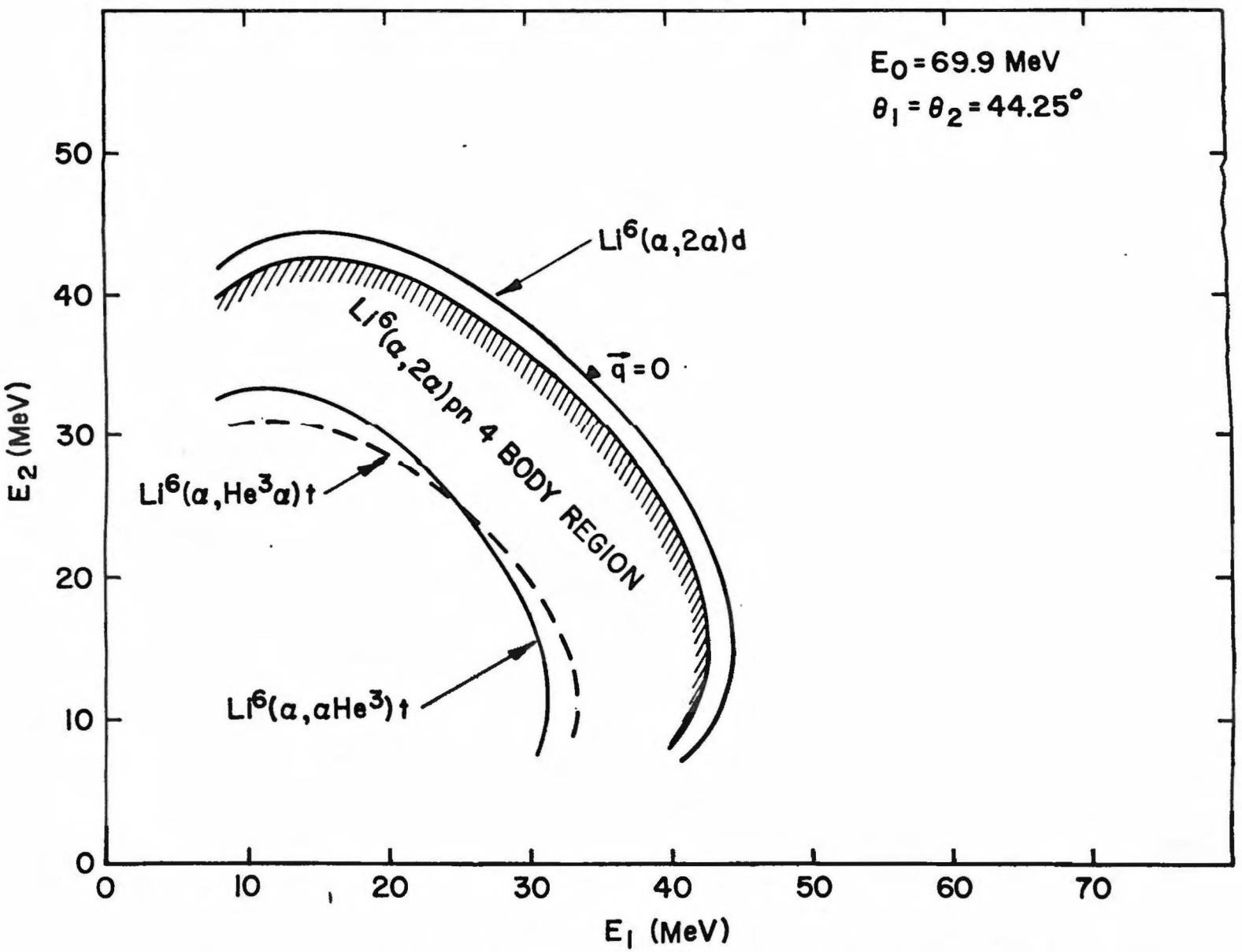

Figure 2.6: Kinematic loci for the $Li^6(\alpha,2\alpha)d$, $Li^6(\alpha,\alpha He^3)t$ and $Li^6(\alpha,He^3\alpha)t$ reactions at 69.9 MeV bombarding energy. The boundary of the $Li^6(\alpha,2\alpha)np$ four-body breakup region is also shown. $\theta_1 = \theta_2 = 44.25°$.

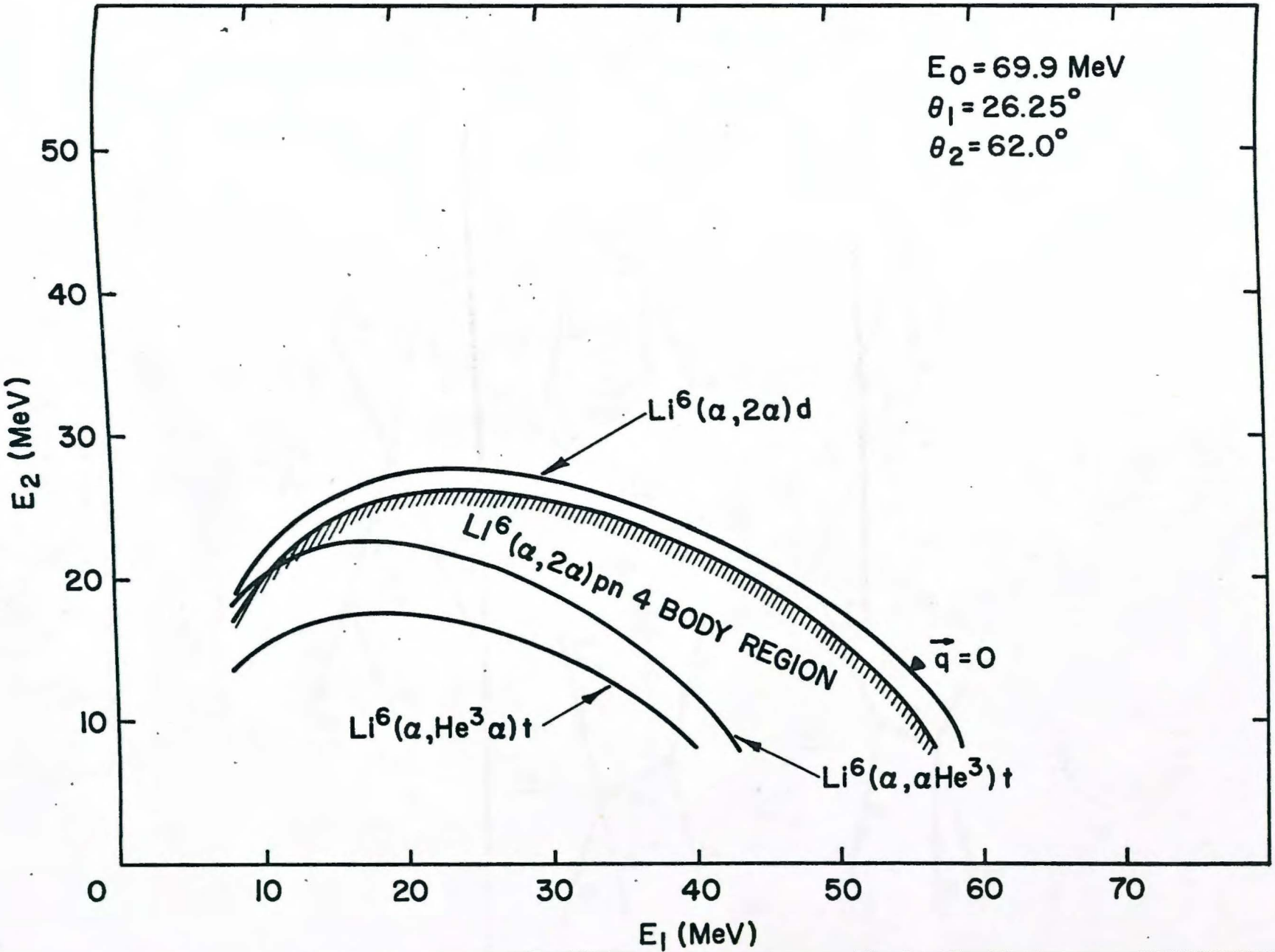

Figure 2.7: Kinematic loci for the $Li^6(\alpha,2\alpha)d$, $Li^6(\alpha,\alpha He^3)t$ and $Li^6(\alpha,He^3\alpha)t$ reactions at 69.9 MeV bombarding energy. The boundary of the $Li^6(\alpha,2\alpha)np$ four-body breakup region is also shown. $\theta_1 = 26.25°$; $\theta_2 = 62.0°$.

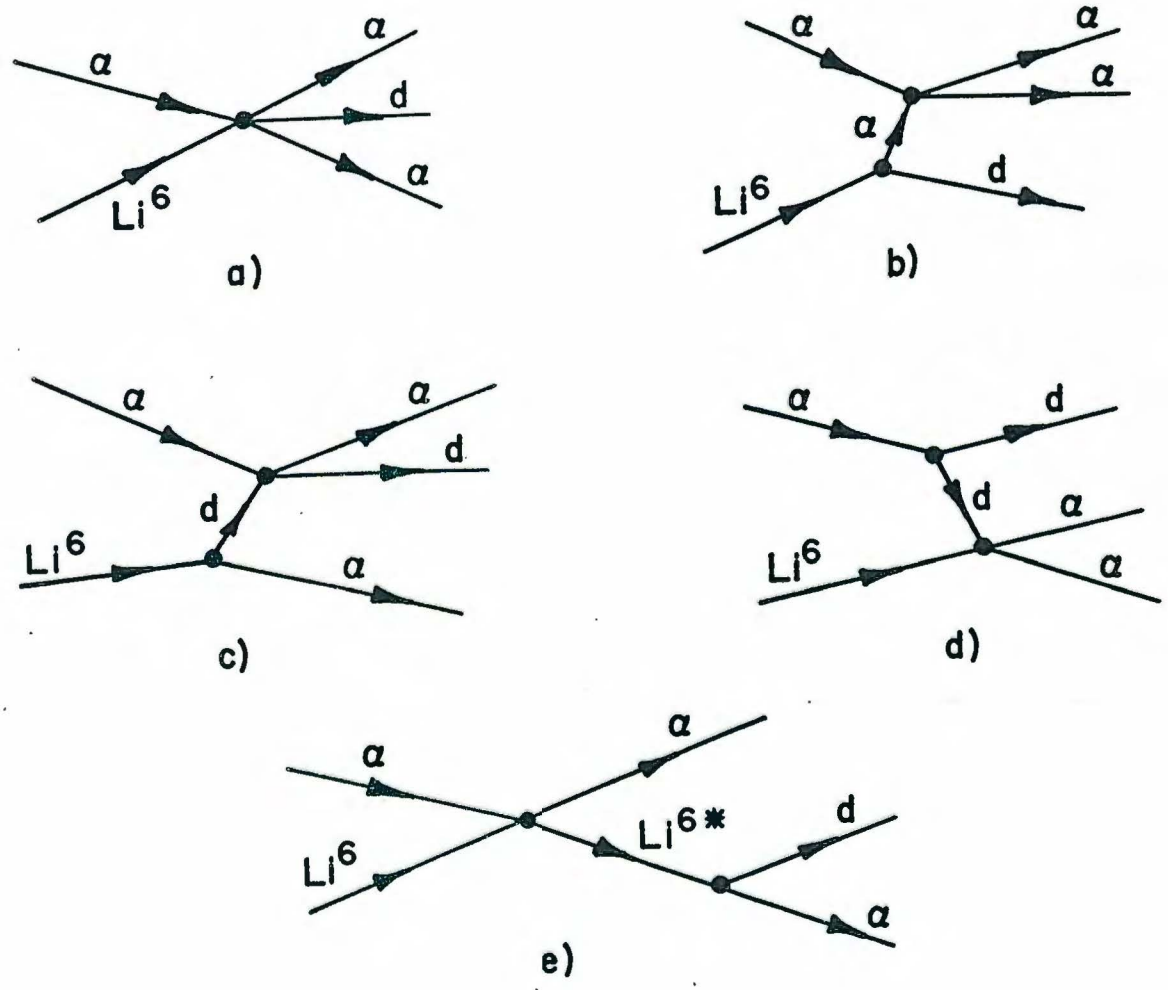

Figure 2.8: Five Feynman diagrams for the $Li^6 + \alpha \rightarrow \alpha + \alpha + d$ reaction.

$$\frac{d^3\sigma}{d\Omega_1 d\Omega_2 dE_1} = \frac{|M|^2}{(2\pi)^5} \frac{m_o m_1 m_2 p_1 p_2}{p_o} \left(1 + \frac{m_2}{m_3} + \frac{m_2}{m_3}\frac{p_1}{p_2}\cos\theta_{12} - \frac{m_2}{m_3}\frac{p_o}{p_2}\cos\theta_2\right)^{-1} \quad (2.1)$$

Near the quasi-free peak, this is a smoothly varying, almost constant function. It is, in fact, proportional to the kinematic factor (1.8). Previous studies of the $Li^6(\alpha,2\alpha)d$ reaction (J69) have shown that the contribution of this type of process is small.

Figure 2.8b is the quasi-free α-α scattering already discussed in Section 1.2, the reaction mechanism of interest. Figure 2.8c is quasi-free α-d scattering. If the same analysis is applied to this reaction as was applied to 2.8b, it is seen that the maximum contribution is expected when the internal momentum of the α in the Li^6 is zero. Experimentally, we can only detect this α if it has an energy of at least 10 MeV i.e. a momentum of at least 245 MeV/c. This is very far out in the tail of the momentum wave function for Li^6 as determined by previous measurements (see Section 5.6), so that the contributions from this reaction mechanism are likely to be negligible.

Figure 2.8d represents a reaction mechanism where the incident α emits a virtual deuteron which undergoes the $d + Li^6 \rightarrow \alpha + \alpha$ reaction. This reaction, like that in diagram 2.8c, can be excluded on kinematic grounds. The conditions of the knockout experiment are generally that the deuteron be stationary in the lab. For the deuteron in the final state of diagram 2.8d to be stationary in the lab, the virtual deuteron must be emitted with a momentum of 300 MeV/c or greater, a rather unlikely event. In addition, the threshold for breakup of He^4 into two deuterons lies some 20 MeV above the He^4 ground state, leading to a small d + d cluster component to the He^4 wave function. The necessity for a rearrangement collision at the lower vertex is expected to reduce the importance of this mechanism still further.

$$\frac{d^3\sigma}{d\Omega_1 d\Omega_2 dE_1} = \frac{|M|^2}{(2\pi)^5} \frac{m_o m_1 m_2 p_1 p_2}{p_o} \left(1 + \frac{m_2}{m_3} + \frac{m_2}{m_3}\frac{p_1}{p_2}\cos\theta_{12} - \frac{m_2}{m_3}\frac{p_o}{p_2}\cos\theta_2\right)^{-1} \qquad (2.1)$$

Near the quasi-free peak, this is a smoothly varying, almost constant function. It is, in fact, proportional to the kinematic factor (1.8). Previous studies of the $Li^6(\alpha,2\alpha)d$ reaction (J69) have shown that the contribution of this type of process is small.

Figure 2.8b is the quasi-free α-α scattering already discussed in Section 1.2, the reaction mechanism of interest. Figure 2.8c is quasi-free α-d scattering. If the same analysis is applied to this reaction as was applied to 2.8b, it is seen that the maximum contribution is expected when the internal momentum of the α in the Li^6 is zero. Experimentally, we can only detect this α if it has an energy of at least 10 MeV i.e. a momentum of at least 245 MeV/c. This is very far out in the tail of the momentum wave function for Li^6 as determined by previous measurements (see Section 5.6), so that the contributions from this reaction mechanism are likely to be negligible.

Figure 2.8d represents a reaction mechanism where the incident α emits a virtual deuteron which undergoes the $d + Li^6 \rightarrow \alpha + \alpha$ reaction. This reaction, like that in diagram 2.8c, can be excluded on kinematic grounds. The conditions of the knockout experiment are generally that the deuteron be stationary in the lab. For the deuteron in the final state of diagram 2.8d to be stationary in the lab, the virtual deuteron must be emitted with a momentum of 300 MeV/c or greater, a rather unlikely event. In addition, the threshold for breakup of He^4 into two deuterons lies some 20 MeV above the He^4 ground state, leading to a small d + d cluster component to the He^4 wave function. The necessity for a rearrangement collision at the lower vertex is expected to reduce the importance of this mechanism still further.

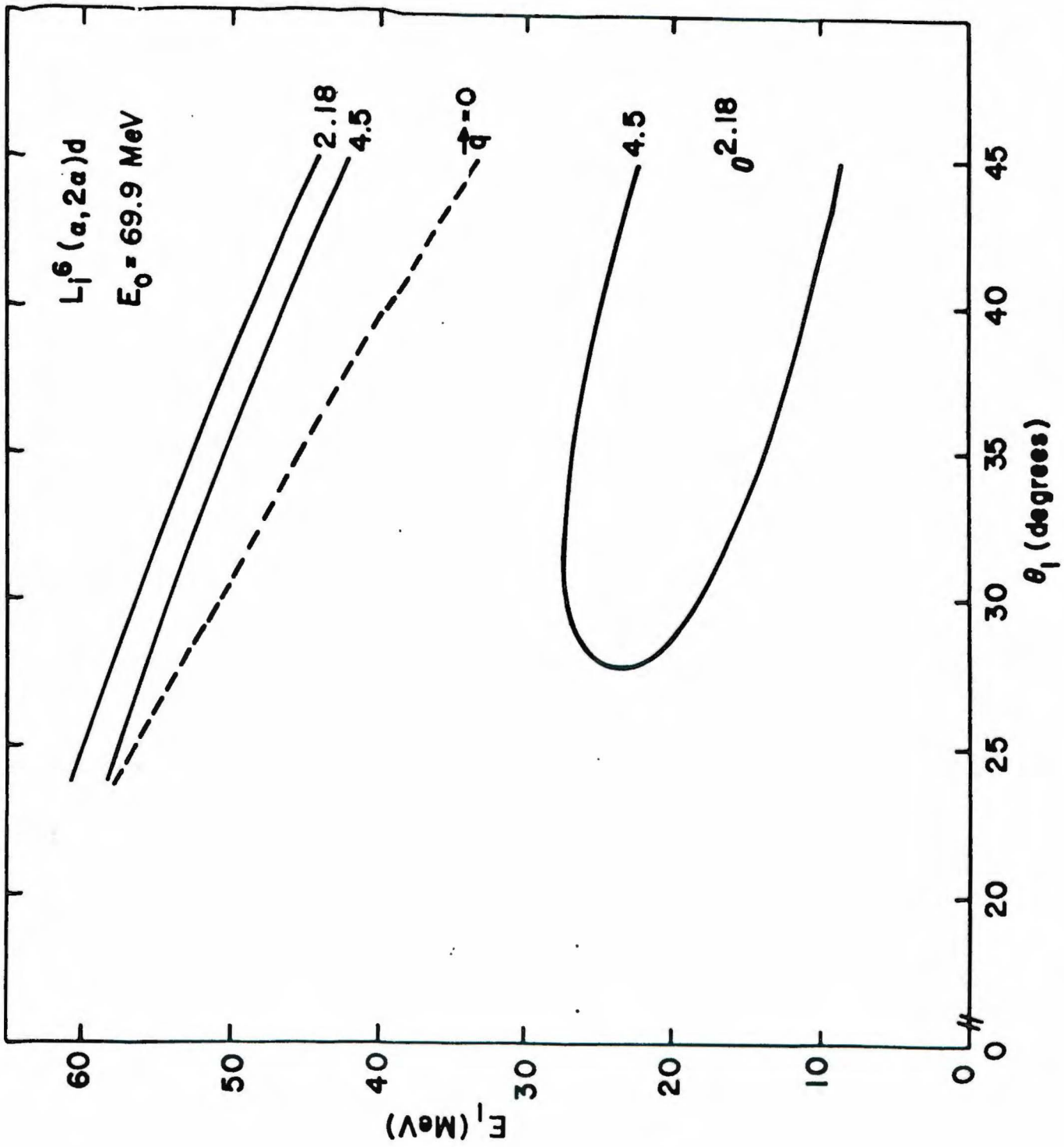

Figure 2.9: Energies at which sequential peaks will appear in the projected energy spectra for the $Li^6(\alpha,2\alpha)d$ reaction at 69.9 MeV bombarding energy, as a function of θ_1. The display is for quasi-free angle pairs, and θ_2 is unique for each value of θ_1. The excitation energies of the states of Li^6 through which the sequential reactions pass are indicated. The energy at which $\vec{q} = 0$ is also indicated.

The last diagram, Fig. 2.8e, is the most troublesome. This diagram represents a "sequential process" of the following type:

$$\alpha + Li^6 \rightarrow \alpha + Li^{6*} \quad \text{(2.2)}$$
$$\hookrightarrow \alpha + d$$

The only discrete states of Li^6 strongly excited by inelastic α scattering are the 2.18 MeV (3^+) state and the 4.5 MeV (2^+) state (W69). For sequential processes, E is uniquely determined by θ, from inelastic scattering kinematics. The two α's arising from the reaction (2.2) will be called the "inelastic" α and the "breakup" α to specify their roles in the process. The kinematics of a sequential process proceeding via a given state in Li^6 are determined by the kinematics of inelastic scattering. If the "inelastic" α is scattering into counter 1, its energy E_1 is uniquely determined by θ_1, from inelastic scattering kinematics. A peak will then occur on the kinematic locus at that value of E_1. Similarly, if the "inelastic" α is scattered into counter 2, a peak will occur on the kinematic locus at that value of E_2 determined by θ_2.

As the angles of the two detectors are changed, the energies at which these sequential peaks occur will also change. Figure 2.9 shows energies at which sequential peaks will appear for quasi-free angle pairs, when the bombarding energy is 69.9 MeV. The abscissa is θ_1 of the quasi-free angle pair (θ_2 is unique for each θ_1), the ordinant is E_1, the energy coordinate for the projected spectra. The high energy curves labeled 2.18 and 4.5 correspond to the "inelastic" α scattering into counter 1 via the 2.18 and 4.5 MeV states of Li^6. The low energy curves correspond to the "inelastic" α scattering into counter 2 and the "breakup" α being detected by counter 1. Also shown is the energy where $\vec{q}$, the momentum (in the initial state) of the knocked out α is

zero. It is clear that as the angle θ_1 gets smaller, sequential processes will be occurring closer and closer to the zero recoil point. At $\theta_1 = 25^o$ the $\vec{q} = 0$ point and a peak due to a sequential breakup via the 4.5 MeV state of Li^6 will virtually coincide. This is an additional reason for 25^o being the limit for meaningful study of quasi-free α-α scattering from Li^6.

2.1.5 Optimization of Experimental Resolution

The experimental resolution problem to be discussed in this section is that of the effects caused by the large solid angles which must be used in such a low counting rate coincidence experiment. The effects of averaging the data over a finite range of energy E_1 (to improve statistics) will also be considered.

In Section 1.1 it was demonstrated that there are six independent kinematic variables. One of these, E_2, will be used to specify the Q value of the reaction. The cross section to be extracted, therefore, is a five fold differential quantity, $d\sigma/d(\cos\theta_1)d\phi_1\, d(\cos\theta_2)d\phi_2$ more conveniently written as $d\sigma/d\Omega_1 d\Omega_2 dE_1$. The resolution problem is that the experimental set up has of necessity finite sizes for $\Delta\Omega_1$, $\Delta\Omega_2$ and ΔE_1, the solid angles of the two detectors and the E_1 energy bin. To analyze the effects of finite resolution, a large computer program, MOMRATH, was written. A description of this program is given in Appendix 2. The measured cross section is an average of the differential cross section over the allowed range of the five independent variables. If the measured cross section is called σ_M, then

$$\sigma_M = \frac{1}{\Delta\Omega_1 \Delta\Omega_2 \Delta E_1} \int_{\Delta\Omega_1} d\Omega_1 \int_{\Delta\Omega_2} d\Omega_2 \int_{\Delta E_1} dE_1 \, \frac{d\sigma}{d\Omega_1 d\Omega_2 dE_1} \qquad (2.3)$$

To the extent that one has a theory for $d\sigma/d\Omega_1 d\Omega_2 dE_1$, one can calculate the "smearing effects" that make σ_M different from the true cross section for the centers of the detectors and the E_1 energy bin.

MOMRATH produces two types of output. First of all for a given reaction it can calculate the "resolution function" or distribution over the five dimensional volume $\Delta\Omega_1$, $\Delta\Omega_2$, ΔE_1 of some kinematic quality such as q the recoil momentum, or E_2 the energy of the second detected particle. This resolution function is independent of any theory of the cross section, and relates strictly to the physical set up of the experiment. It gives, in effect, the resolving power of the system for a particular kinematic quantity. Secondly, the relative importance of each of the five independent variables is also accessed for a given geometry. Given a theory for $d\sigma/d\Omega_1 d\Omega_2 dE_1$ (usually that $d\sigma/d\Omega_1 d\Omega_2 dE_1$ depends on $|\bar{\Phi}(q)|^2$ only, assuming that $\left(\frac{d\sigma}{d\Omega}\right)_{free}$ and the kinematic factor are effectively constant), the quantity σ_m can be calculated, giving a direct measure of the amount of smearing.

Studies with MOMRATH have shown that finite resolution effects become important only near $\vec{q} = 0$, or when one of the quantities important in determining the shape of the cross section has its first derivative pass through zero. Thus, since the object of this experiment is to measure cross sections at $\vec{q} = 0$, it is important to determine to what extent these measurements will be in error.

The reason why resolution effects are important near $\vec{q} = 0$ can be seen as follows. Assume that $|\bar{\Phi}(q)|^2$ is the function that determines the shape of the cross section. This is a function of $|\vec{q}|$ only. When the nominal value of $|\vec{q}|$ (i.e. the value for the centers of the counters and the center of the E_1 energy bin) is well away from zero, the smearing of $|\vec{q}|$ caused by the finite sizes of the counters will tend to even out, with the average still near the nominal value. When the nominal value of $|\vec{q}|$ is zero, however, the deviation

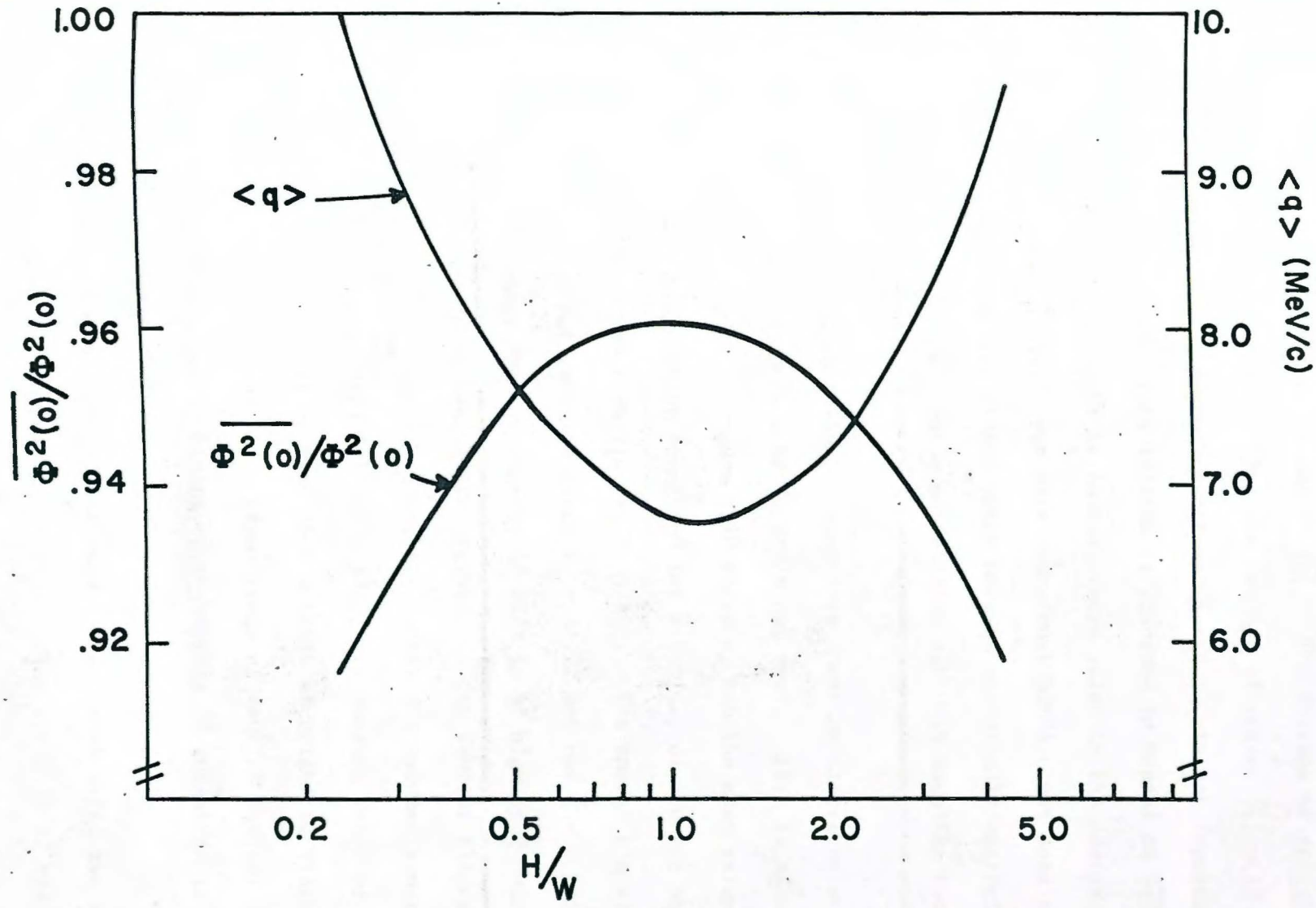

Figure 2.10: $\langle q \rangle$, the mean value of q, and $\overline{|\Phi(0)|^2}$, the smeared value of $|\Phi(0)|^2$ as a function of H/W, the height to width ratio of the counters in the $Li^6(\alpha,2\alpha)d$ reaction at 69.9 MeV. The area of the counters is kept constant at two square degrees each. $\theta_1 = \theta_2 = 44.25^\circ$.

will all be towards larger values of $|\vec{q}|$. The average of vector $\vec{q}$ will still be very close to $\vec{q} = 0$, but the average of scalar $|\vec{q}|$ will not be. Away from $\vec{q} = 0$ this distinction between $\vec{q}$ and $|\vec{q}|$ is not important. At $\vec{q} = 0$ it is, since the cross section is presumed to depend on $|\vec{q}|$ not $\vec{q}$.

MOMRATH has been found to have enormous value in the design of this and other experiments (J69). For this experiment MOMRATH was used to choose solid angles and counter shapes which have an essentially negligible effect on the resolution in $|\vec{q}|$, while maintaining adequate counting rates at most angles and energies.

For the studies to follow, a prototype momentum distribution of a Gaussian with a width at half maximum of 30 MeV/c was used. This is close to $|\phi(q)|^2$ as determined by (J69). Figure 2.10 shows σ_m and the mean value of $<q>$ of the above mentioned "resolution function" for a variety of counter shapes for $Li^6(\alpha,2\alpha)d$ at 69.9 MeV with $\theta_1 = \theta_2 = 44.25°$. The energy bin width E_1 has been fixed at 400 KeV centered about $E_1 = 34.22$ MeV the $\vec{q} = 0$ point. The counter shapes range from $\frac{1}{2}°$ high by 4° wide to 4° high by $\frac{1}{2}°$ wide, all with the same solid angle of two square degrees. Both counter shapes are the same. For σ_m, since $\left(\frac{d\sigma}{d\Omega}\right)_{free}$ and the kinematic factor are assumed constant, what is actually plotted is $\overline{\phi^2(0)}/\phi^2(0)$ where $\overline{\phi^2(0)}$ the smeared value of $\phi^2(q)$ for the nominal $\vec{q} = 0$ point. It is seen that a ratio of height to width of about unity is optimum, but that for a broad range of counter shapes, the smearing effect is relatively small, giving approximately 5% reduction in the "measured" $\overline{\phi^2(0)}$ from the "actual" $\phi^2(0)$.

The resolution in q is not the sole factor in choosing the slit shapes. Other factors must be considered, as well. The width $\Delta\theta$ of the slits will affect the width of the peaks seen in sequential processes. Above and beyond the intrinsic widths of such peaks, they will acquire a kinematic spread directly proportional to $\Delta\theta$. Typically, for the 2.18 MeV state of Li^6, at E_o=69.9 MeV,

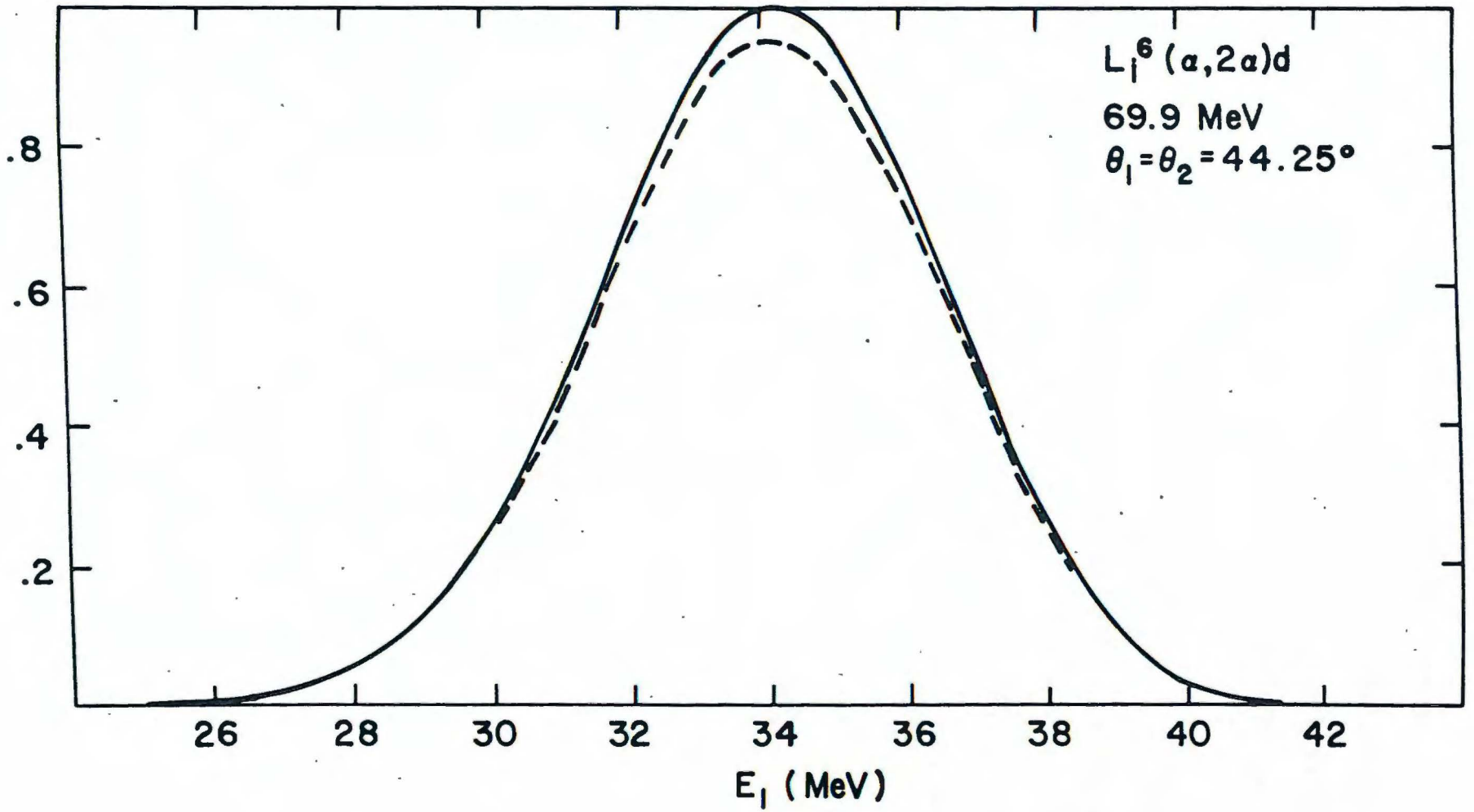

Figure 2.11: The effects of finite resolution for a sample "spectrum" for the $Li^6(\alpha,2\alpha)d$ reaction at 69.9 MeV bombarding energy. The solid curve is the spectrum for an unsmeared Gaussian momentum distribution with a half width at half maximum of 30 MeV/c. The dashed curve is the smeared measurement with $\Delta\theta = 1°$, $\Delta\varphi = 2°$ and $\Delta E = 400$ KeV.

with $\theta_1 = 44^\circ$, the kinematic spread for inelastic α scattering is 850 Kev/degree. It is important to limit the kinematic spread introduced into these peaks, first of all to localize them in the measured spectra and limit their encroachment into the quasi-free peaks, and secondly so that elastic and inelastic α scattering can be used for energy calibrations.

Another consideration is the efficient utilization of the active area of the detectors (which are always circular). To achieve a given solid angle with a tall narrow slit necessitates the use of a much smaller percentage of the active area of a detector than if the slit were square. This shortens the life of a detector since the radiation is concentrated in a small area, leading to rapid radiation damage.

Given these additional considerations, a slit shape of 2° high and 1° wide was decided upon, seeing that this does not seriously worsen the effects of finite resolution from their values for the optimum slit shape.

To gauge the effects of finite resolution for values of $\vec{q}$ other than zero, Figure 2.11 shows a "spectrum" for $\theta_1 = \theta_2 = 44.2^\circ$ with $E_o = 69.9$ MeV along with the unsmeared $\phi^2(q)$. It is clear that only near $\vec{q} = 0$ are there noticeable differences between the smeared and unsmeared curves.

TABLE 2.1

Target Number	Thickness (Chem. Analysis)	Relative Thickness	Relative Counting Rate	$\frac{\text{Rel. Thickness}}{\text{Rel. Counting Rate}}$
6	0.456 mg. cm^{-2}	.586	0.73	0.80
7	0.779 mg. cm^{-2}	1.00	1.00	1.00
8	0.846 mg. cm^{-2}	1.09	1.02	1.07

Table 2.1: Thickness determined by chemical analysis and relative counting rates for elastic alpha scattering for three Li^6 targets.

Section 2.2 Execution of the Experiment

2.2.1 Targets, Scattering Chamber, Detectors

Self-supporting Li targets were made using the procedure in Appendix 3. Three 96% isotopically pure Li^6 targets were placed in the scattering chamber. One of these was used for the $Li^6(\alpha,2\alpha)d$ reaction. The others were used to help in assessing the reliability of the target thickness measurement, performed as follows. With a beam energy of 60.5 MeV, elastic and inelastic α scattering (singles) spectra were measured with all three targets. After the experiment, known areas of all three targets were chemically analyzed for Li content, and the thicknesses determined by this method were compared with the relative counting rates for α scattering from the three targets.

Table 2.1 gives a comparison of the two methods. The discrepancy between the two methods for determining relative thickness is presumably due to non-uniformity in the thickness. Target number 7 was used for the $Li^6(\alpha,2\alpha)d$ reaction, and its thickness will be taken as 0.78 $mg.cm^{-2}$ $\pm$ 25%.

The scattering chamber used for this experiment was designed by Dr. Charles Goodman of Oak Ridge National Laboratories. It is 30 inches in diameter, and is equipped for two independent counters. The angle of one counter, (which will be called counter 1) and the separation angle between the counters are independently adjustable to an accuracy of better than 0.1°. The target angle was fixed for this experiment at 0° (target normal to the beam). A check of the zero reading for the counter angles was made at the beginning of the experiment by taking singles spectra on both sides of the beam with the same counter. The nominal angles were found to be correct to within $\pm$ 0.05°.

The two counters as dicussed in Section 2.1.2 each consisted of two Si solid state detectors. For counter 1 the ΔE detector was a 61μ Si surface barrier detector, the "E" or thick detector was a 3000 μ Si (Li) detector. For counter 2 the ΔE detector was a 55 μ Si surface barrier detector, the "E" detector was a 1500 μ Si surface barrier detector.

The defining slits in front of each counter were 0.025 in. Ta 1/8" wide by 1/4" high at a distance of 7" from the center of the chamber, for a nominal 1° x 2° size. The actual solid angles were: $\Delta\Omega_1 = 5.85 \times 10^{-4} \pm 1.5\%$, $\Delta\Omega_2 = 5.68 \times 10^{-4} \pm 2\%$.

2.2.2 The Beam

The α-particle beam from the Oak Ridge Isochronous cyclotron was analyzed by a 153°, 50 inch radius $n = \frac{1}{2}$ analyzing magnet. The exit slit of the magnet was 100 mils wide, giving an energy spread to the beam of 1 part in 500. The beam energy was calculated from the magnetic field in the analyzing magnet, as measured by a nuclear magnetic resonance probe and from the geometry of the slits.

The beam currents used in the experiment ranged from 10 to 100 nanoamps. The beam passing through the target was stopped in a Faraday cup and the total charge was measured with a current integrator and a scaler. The integrator was calibrated after the run with a 1 μ amp source. The calibration is believed to be accurate to better than 3%.

During the course of the run the beam spot on the target was checked from time to time with a phosphorescent screen. The location was observed to wander laterally, generally less than 1/32 of an inch, but sufficient to affect the angular accuracy of the measurement. With a detector at a distance of 7 inches and at an angle of 26°, this wander corresponds to a 0.2° uncertainty in the measured angle. This will be taken as the accuracy with which angles were known.

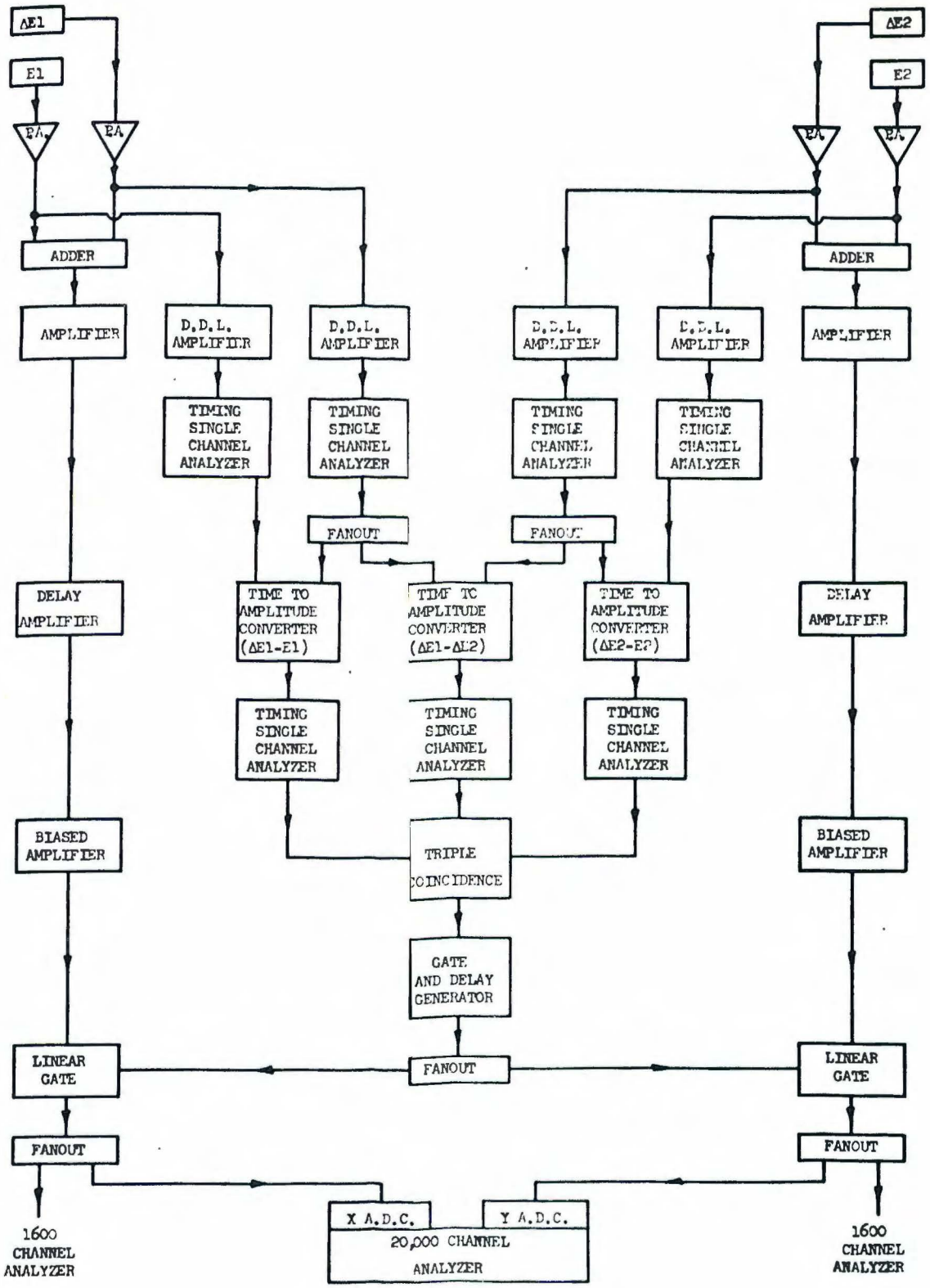

Figure 2.12: Block diagram of the electronics. See the text for further details.

2.2.3 Electronics

A block diagram of the electronics is given in Figure 2.12. The preamplifiers were Tennelec Model TC-150 charge sensitive preamplifiers. The output signals of the preamplifiers were split, and for each counter the ΔE and E signals were added by inverting one signal, balancing their relative amplitudes with variable impedances (in the "ADDER" unit) and feeding them into the differential inputs of a Tennelec TC-200 amplifier. The added signals were delayed and fed into a Tennelec TC-250 biased amplifier. The outputs of the biased amplifiers were gated and fed into the X and Y analog-to-digital converters (A.D.C.'s) of a Victoreen 20,000 channel two dimensional pulse height analyzer operating in a 100 channel (Y or E_2) by 200 channel (X or E_1) mode.

The gating signals were derived from the following coincidence circuitry. The second (split) output of each preamp was fed into a double delay line amplifier (Ortec Model 410 for the E_1 and E_2 signals, Canberra Model 1410 for the ΔE_1 and ΔE_2 signals). The outputs of these amplifiers were fed into single channel analyzers (S.C.A.'s) which were set to give the partial particle identification described in Section 2.1.2. The outputs of the S.C.A.'s were fed in pairs into time-to-amplitude converters (T.A.C.'s). The pairs were $\Delta E_1 - E_2$, $\Delta E_2 - E_2$, and $\Delta E_1 - \Delta E_2$. The outputs of the three T.A.C.'s were fed through three more S.C.A.'s set to allow only events from the same beam r.f. burst to pass. The outputs of these three S.C.A.'s were sent into an Ortec Model 409 triple coincidence unit. When a triple coincidence occurred the output signal triggered a gate generator which opened the gates for the linear signals to enter the X and Y A.D.C.'s of the 20,000 channel analyzer.

This somewhat redundant coincidence circuitry allowed switching between coincidence and singles counting without changing any cables or connections. Singles spectra were taken with each counter for each angle pair and stored in the lowest X and Y channels of the 20,000 channel analyzer. The switch from coincidence to singles could be achieved by throwing two switches on the triple coincidence unit, and moving one pin on the program board of the analyzer, with no need to interfere with the gating circuitry.

In addition to the above electronics, scalers were used to record the number of pulses out of the S.C.A.'s after the $E_1 - \Delta E_1$ T.A.C. and the $E_2 - \Delta E_2$ T.A.C., on the output of the triple coincidence unit, on the current integrator and on a kilocycle clock which ran only while the analyzer was in the accumulate mode. The scaler outputs on the two T.A.C.'s were checked after the experiment was completed and no irregularities were found.

A SCIPP 1600 channel pulse height analyzer was also available for this experiment. It was used to monitor the data as it was being taken by displaying either the gated $E_1 + \Delta E_1$ or the gated $E_2 + \Delta E_2$ signal.

To determine the extent to which dead time losses from the electronics effected the experimental measurements, the following procedure was carried out during part of the experiment. While data were being taken, signals from a four channel pulser were fed simultaneously into the preamplifiers for the four solid state detectors, at a rate of about 1/sec. These signals had the shape and pulse heights to simulate two α-particles with $E_1 \sim 80$ MeV and $E_2 \sim 70$ MeV. A peak from the pulser signals appeared in the two dimensional energy spectra in a region well away from the $Li^6(\alpha,2\alpha)d$ kinematic locus. From the number of counts in this peak, the rate of the pulser, and the time for which data were accumulated, dead times were estimated.

TABLE 2.2

E_o	θ_1	θ_2
70.3 MeV	44.25°	35.25°, 38.25°, 41.25°, 44.25°*, 47.25°, 50.25°
	41.25°	44.25°, 47.25°*, 50.25°
	38.25°	38.2°, 41.2°, 44.2°, 47.2°, 50.2°*
	36.75	51.7°*
	35.25°	50.2°, 53.2°*, 56.2°
	32.25°	47.15°, 50.15°, 53.15° 56.15°*, 59.15°, 62.15°
	29.25°	59.10°*
	26.25°	58.0°, 61.0°, 64.0°
79.6 MeV	44.3°	44.3°*
	41.3°	47.3°*
	39.8°	45.8°, 48.8°*, 51.8°
	38.3°	50.3°*
	36.8°	51.8°*
	35.3°	53.3°*
	32.3°	56.2°*
	29.3°	56.2°, 59.2°*, 62.2°
	26.3°	62.1°*
60.5 MeV	44.15°	44.15°*
59.0 MeV	44.15°	44.15°*
	41.15°	47.15°*
	38.15°	50.10°*
	35.15°	53.10°*
	32.15°	56.05°*
	29.15°	58.90°*
50.4 MeV	44.1°	44.1°*
	41.1°	47.1°*
	38.1°	50.1°*
	35.1°	53.1°*
	32.1°	56.1°*

Angles and Energies at which Data was taken

Asterisk (*) indicates "quasi-free" angle pair

In general, dead time was found to be in the range of 4% to 8%. This relative constancy is partly due to an attempt to keep the singles rates for the two counters constant by adjusting the cyclotron beam intensity. For the measurements where θ_1 was smallest, however, dead times may have been larger than the above figure.

2.2.4 "Semi On-Line" Data Processing

A S.E.L. 850A computer with a 16,000 word memory and disc storage was used for "semi on-line" data handling. When a two dimensional spectrum was completed, the memory of the 20,000 channel analyzer could be transferred to the disc storage of the S.E.L. 850A and was thus immediately available for preliminary processing.

A program was used which generated two hyperbolae across the two dimensional data array and summed the y channels between the hyperbolae for every X channel. This program was used to provide preliminary projected spectra within minutes, and was of great value in allowing the experimenters to keep track of the data as it was being taken.

2.2.5 Data Taken

Table 2.2 lists the angle pairs and energies at which data was taken. In addition, singles spectra were recorded for each angle of every pair, for use in energy calibrations.

CHAPTER 3

DATA REDUCTION

Section 3.1 Energy Calibrations

Energy calibrations were obtained from the singles data taken for both counters at each angle pair. The data was stored in the lowest channel in each direction, i.e. the E_1 singles along the E_1 axis (x axis) the E_2 singles along the E_2 axis (y axis). From these singles spectra the elastic α scattering peaks were used as calibration points.

The overall accuracy of the E_1 calibration established by this method is believed to be better than 100 KeV. There is some scatter in the points caused by the wander of the beam spot mentioned in Section 2.2.2 The E_1 channel width is 395 KeV.

Some difficulty was experienced because of the one degree width of the slits in front of the counters. In a region of the elastic scattering angular distribution where the cross section is varying rapidly as a function of angle the elastic scattering peak will have a maximum at an energy corresponding to some angle slightly different than the nominal angle (the angle for the center of the slits). Figure 3.1 shows the elastic α scattering angular distributions at 70.3, 79.6, 59.0 and 50.4 MeV, taken from the above mentioned singles spectra. It can be seen that the counting rate can vary by as much as 25% in one degree. A crude estimate of the effect on the calibration of counting rate variations across the face of the counters gives a maximum error of less than 60 KeV.

The overall accuracy of the E_2 calibration is believed to be better than 200 KeV. The E_2 calibration is not as critical as that for E_1, since the E_2 variable is integrated over to produce projected spectra, and it

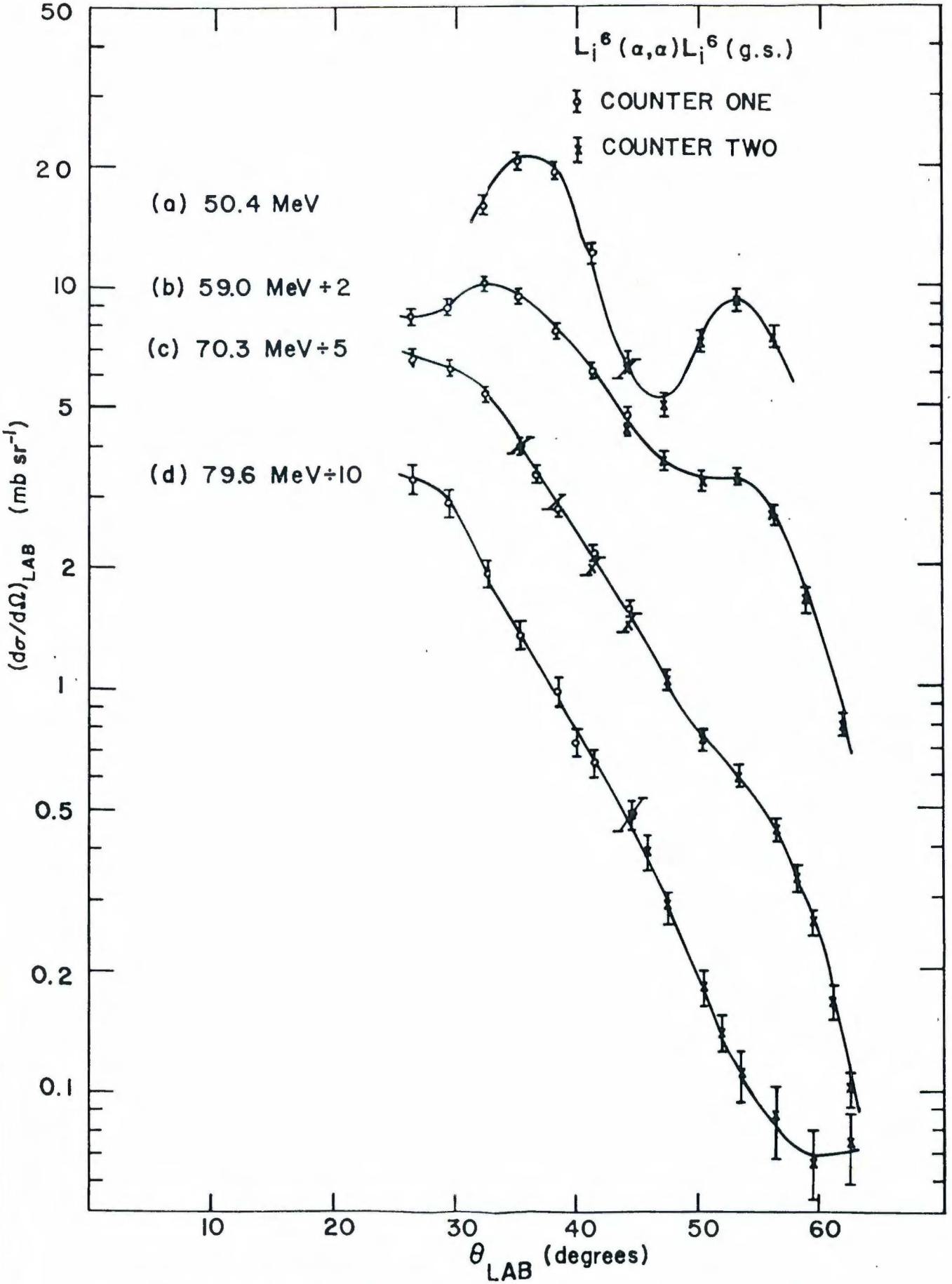

Figure 3.1: Differential cross sections in the laboratory for elastic scattering of α-particles from Li^6, at four bombarding energies. The curves serve only to connect points for the same bombarding energy.

is necessary only that it be good enough to include the proper channels in the integral.

A problem closely associated with the accuracy of the energy calibration, is the accuracy with which the $\vec{q} = 0$ point can be determined (see Section 4.1). The 0.2° uncertainty in the angles can cause an uncertainty of up to 200 KeV. in the energy for which $\vec{q} = 0$ actually occurs. Coupled with the 100 KeV uncertainty in the calibration there could be a total error of up to 300 KeV in determination of the $\vec{q} = 0$ point.

Section 3.2 Projection of the Data onto the E_1 Axis

The projection of the data onto the E_1 axis was done in the following manner. Using the energy calibrations discussed in the previous section, curves were generated across the 100 x 200 channel data array. These correspond to kinematic loci for the $Li^6(\alpha,2\alpha)d$ reaction with Q values of 0.0 and -3.0 MeV. The actual Q value is -1.47 MeV. For a given E_1 channel all the events in the E_2 channels lying between the two kinematic loci (including those channels through which the loci passed) were summed. This was done only for the solution to three body kinematic (see Appendix 1) corresponding to larger values of E_2. This is the solution containing the $\vec{q} = 0$ point.

The separation of the experimental kinematic locus from the region of 4 body events corresponding to an $\alpha + \alpha + n + p$ final state (Q value = -3.69 MeV) is quite clean, and it appears that almost none of these events is included in the sums.

TABLE 3.1

Source	Percent Error
Solid Angles	3.5%
Target Thickness	25%
E_1 Energy Bin Width	$\leq$.5%
Faraday Cup	$\leq$ 3%
Total	$\leq$ 32%

Contributions to the Error in the Absolute Cross Sections

Section 3.3 Absolute Magnitude of the Cross Sections.

Table 3.1 gives the contributions of various sources to the uncertainty in the absolute magnitude of the cross sections. The total uncertainty is ± 32%, with the largest contribution being due to uncertainty in the target thickness. For different spectra and within a given spectrum, relative errors are all taken to be statistical, i.e. the square root of the number of counts. However, the estimates of dead time losses, discussed in Section 2.2.3 should be borne in mind when comparing cross sections from different spectra. The relative uncertainty is less than ± 2% except possibly at the very smallest values of θ_1.

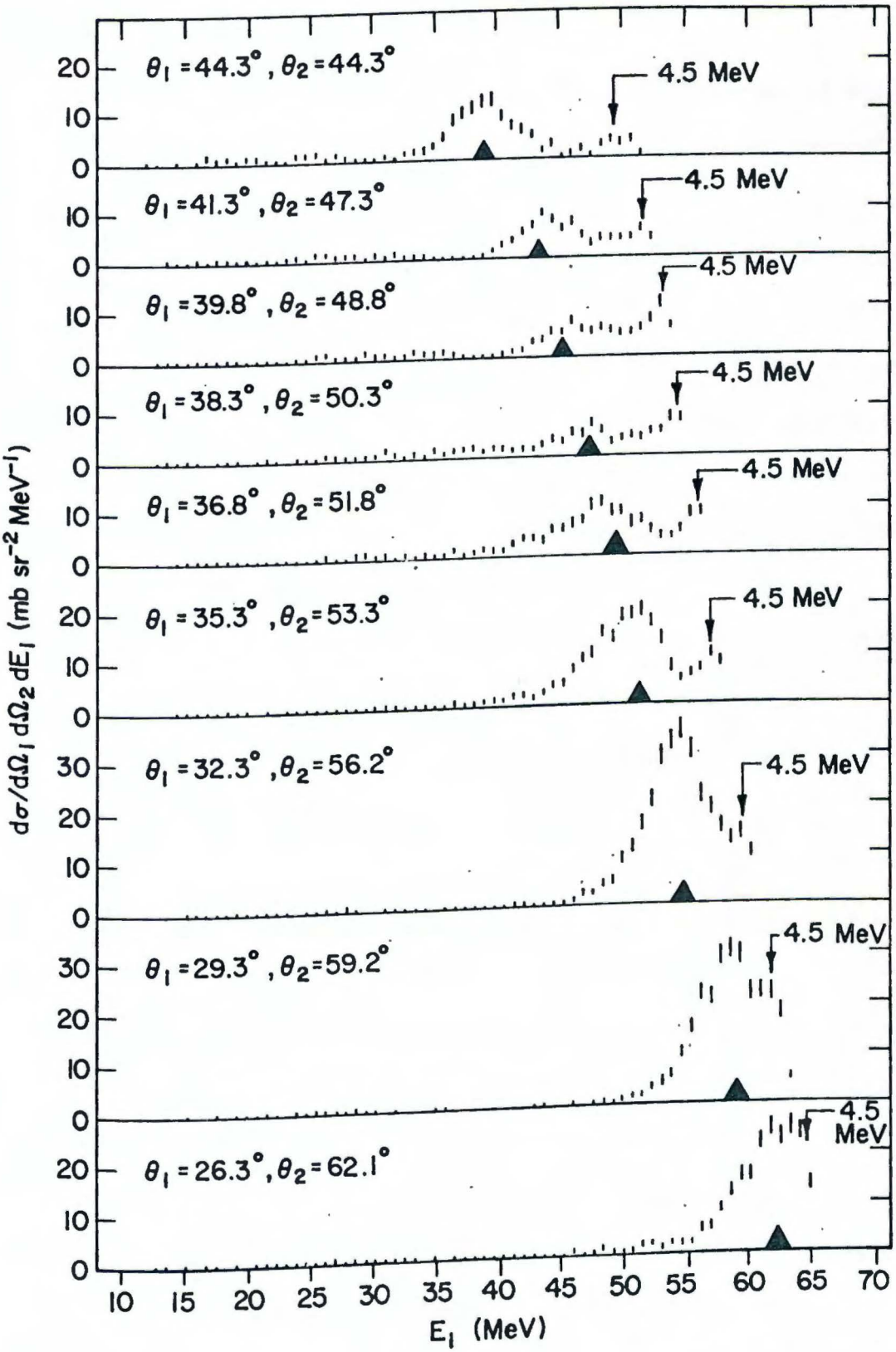

Figure 3.2: Projected energy spectra for nine quasi-free angle pairs for 79.6 MeV bombarding energy. The point with $\vec{q} = 0$ in each spectrum is indicated by an arrow on the E_1 axis. Sequential peaks are labeled according to the state of Li^6 through which the sequential reaction passes.

Section 3.4 Results

The experimental data will now be presented in a series of Figures (3.2 to 3.13). The data is in the form of projected energy spectra ($d\sigma/d\Omega_1 d\Omega_2 dE_1$ vs. E_1).

For the data at 79.6 MeV bombarding energy, the spectra are displayed with pairs of channels summed to improve the statistics of each point. The E_1 channel width for these spectra is therefore 790 KeV. Fig. 3.2 shows the energy spectra for 9 quasi-free angle pairs at a bombarding energy of 79.6 MeV. For all of these spectra, θ_{12}, the separation angle between the two counters, is roughly constant and equal to $\sim 88.5^\circ$. θ_1 varies between 44.3° and 26.3°. In each spectrum, the point where $\vec{q} = 0$ occurs is indicated by an arrow on the E_1 axis. The location of the sequential peak due to the 4.5 MeV state of Li^6 is also indicated on each spectrum.

It is of interest to note that the magnitude of the cross section at $\vec{q} = 0$ varies greatly as θ_1 changes. It has a minimum near 38.3° and maxima at 90° and 32.3°. This behavior is remarkably similar to the behavior of free α-α scattering in the vicinity of 80 MeV, as seen in Fig. 2.1 (Remember that for free α-α scattering $\theta = \frac{1}{2}\theta_{cm}$).

Figures 3.3, 3.4 and 3.5 show similar sets of spectra for bombarding energies of 70.3, 59.9, and 53.4 MeV. Remarks similar to those made about Fig. 3.2 apply here also. It is interesting to note in comparing the four spectra with $\theta_1 = \theta_2 \sim 44^\circ$ that the cross section for $\vec{q} = 0$ drops by a factor of about 15 between 50.4 MeV and 79.6 MeV. This is strikingly similar to the behavior with bombarding energy of the free α-α cross section at $\theta_{cm} = 90^\circ$ as shown in Fig. 2.2 .

Fig. 3.8 shows six energy spectra at a bombarding energy of 70.3 MeV, with $\theta_1 = 44.25^\circ$. θ_2 varies between 50.25° and 35.25°. The possibility

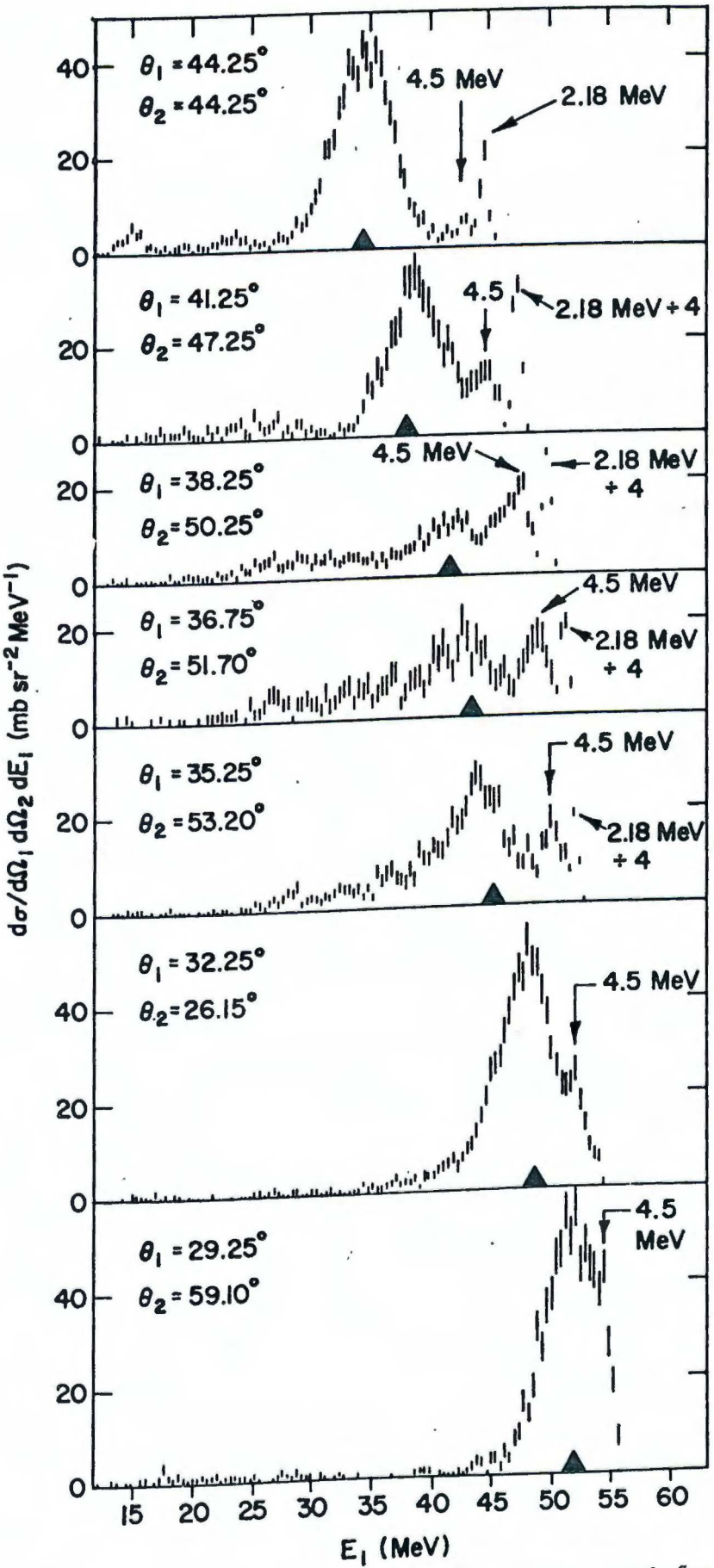

Figure 3.3: Projected energy spectra for seven quasi-free angle pairs for 70.3 MeV bombarding energy. The point with $\vec{q} = 0$ in each spectrum is indicated by an arrow on the E_1 axis. Sequential peaks are labeled according to the state of Li^6 through which the sequential reaction passes.

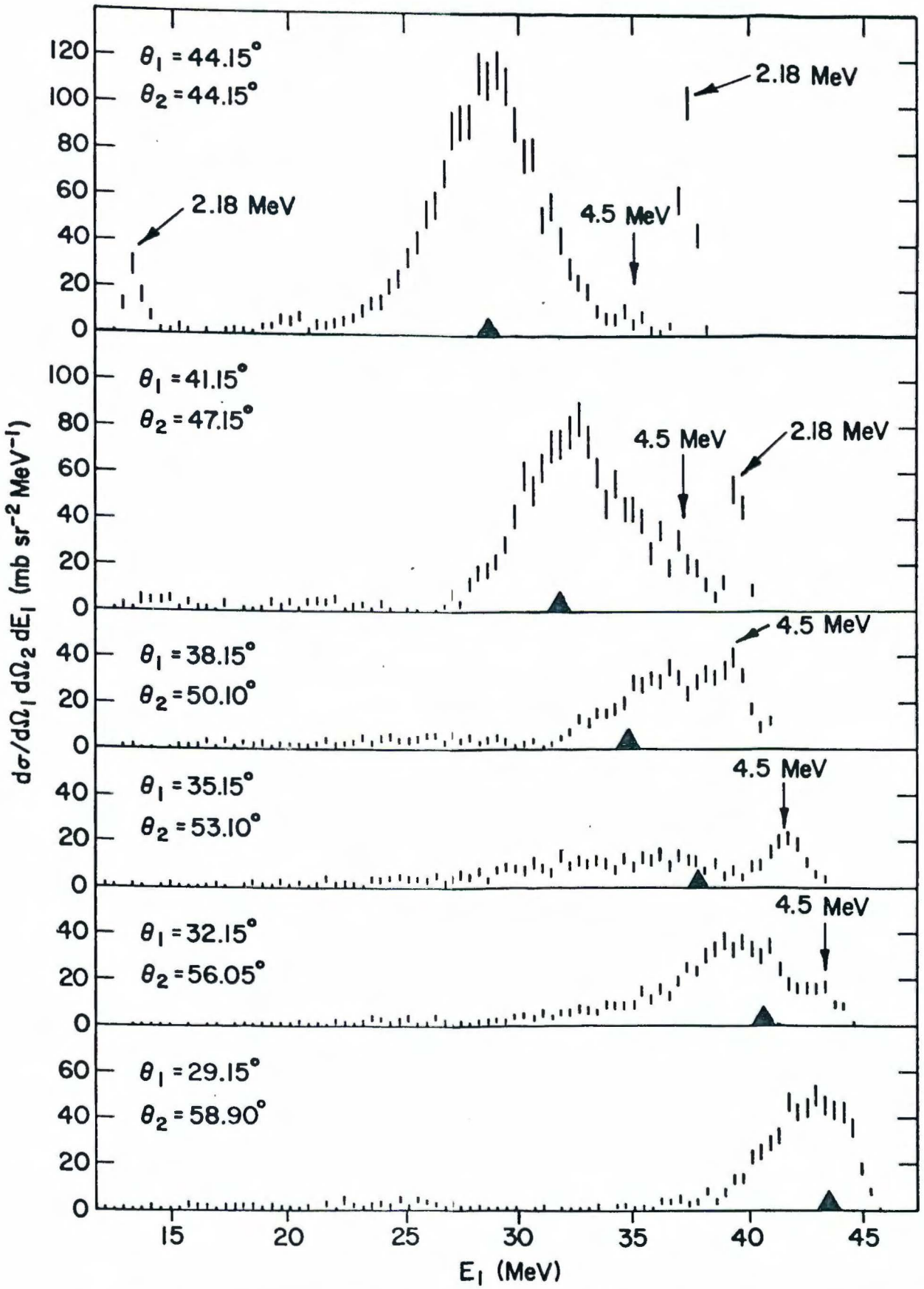

Figure 3.4: Projected energy spectra for six quasi-free angle pairs, for 59.0 MeV bombarding energy. The point with $\vec{q} = 0$ in each spectrum is indicated by an arrow on the E_1 axis. Sequential peaks are labeled according to the state of Li^6 through which the sequential reaction passes.

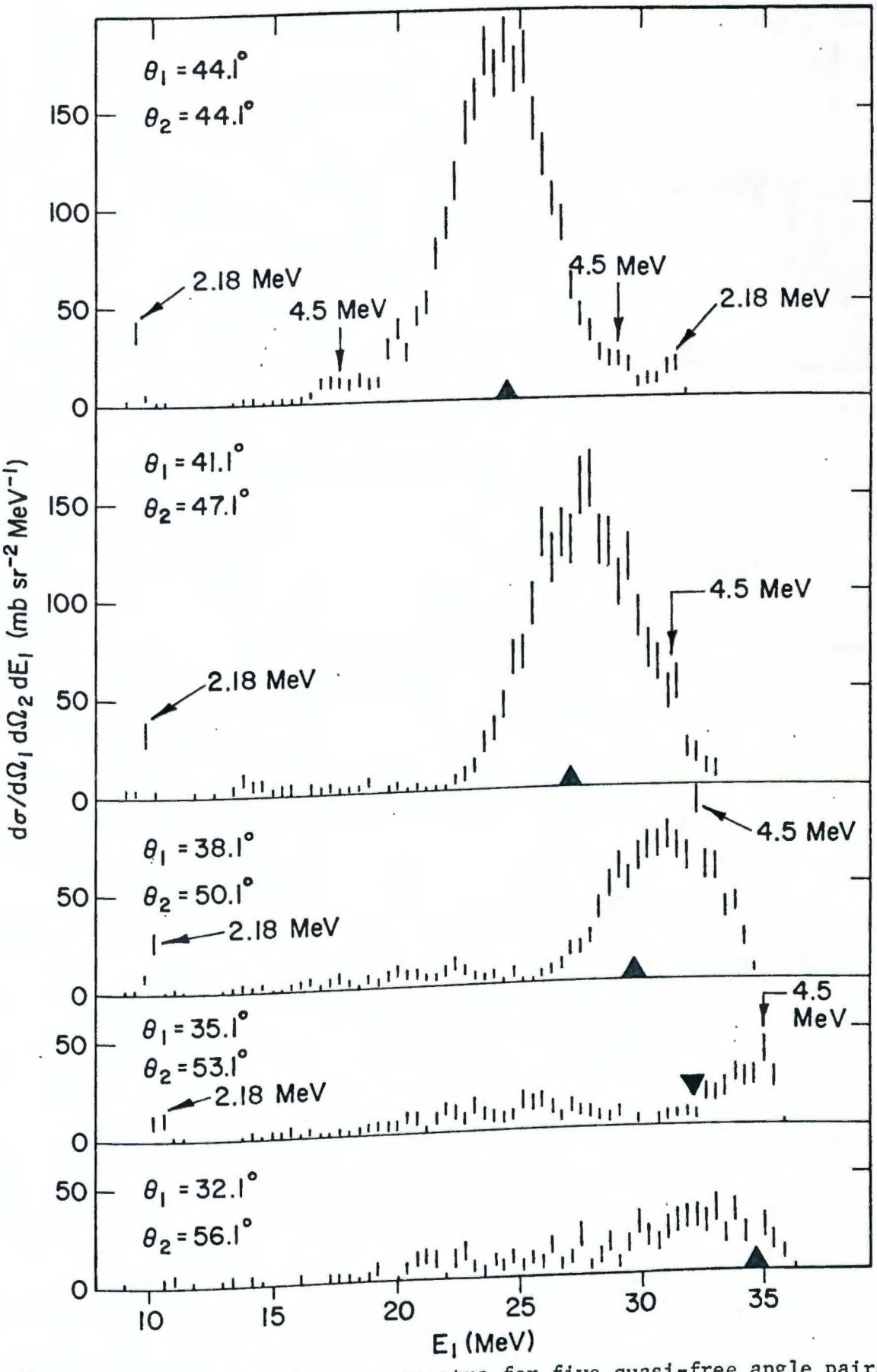

Figure 3.5: Projected energy spectra for five quasi-free angle pairs, for 50.4 MeV bombarding energy. The point with $\vec{q} = 0$ in each spectrum is indicated by an arrow on the E_1 axis. Sequential peaks are labeled according to the state of Li^6 through which the sequential reaction passes.

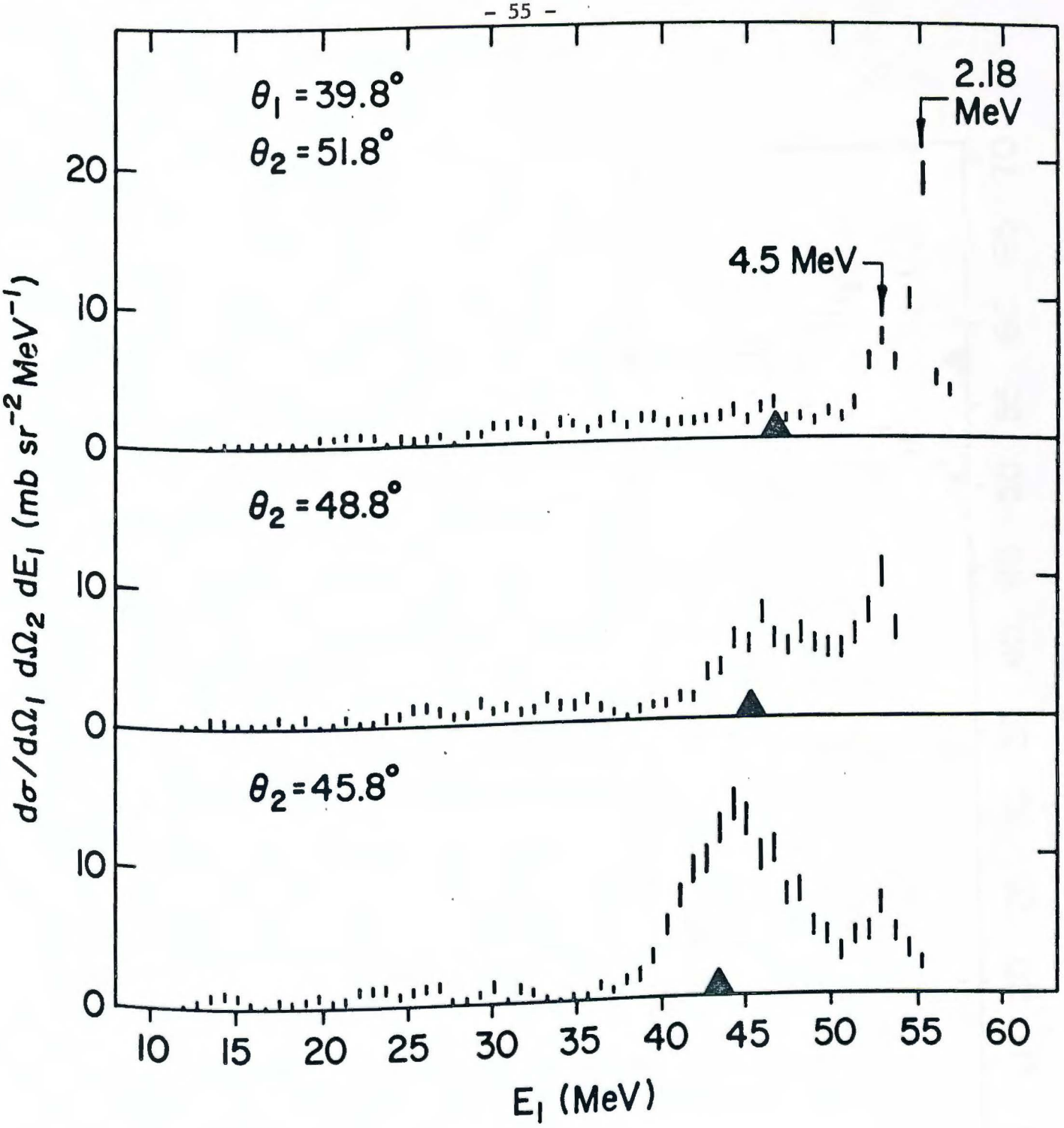

Figure 3.6: Projected energy spectra for three angle pairs with $\theta_1 = 39.8^\circ$ for 79.6 MeV bombarding energy. The point with the minimum value of q in each spectrum is indicated by an arrow on the E_1 axis. Sequential peaks are labeled according to the state of Li^6 through which the sequential reaction passes.

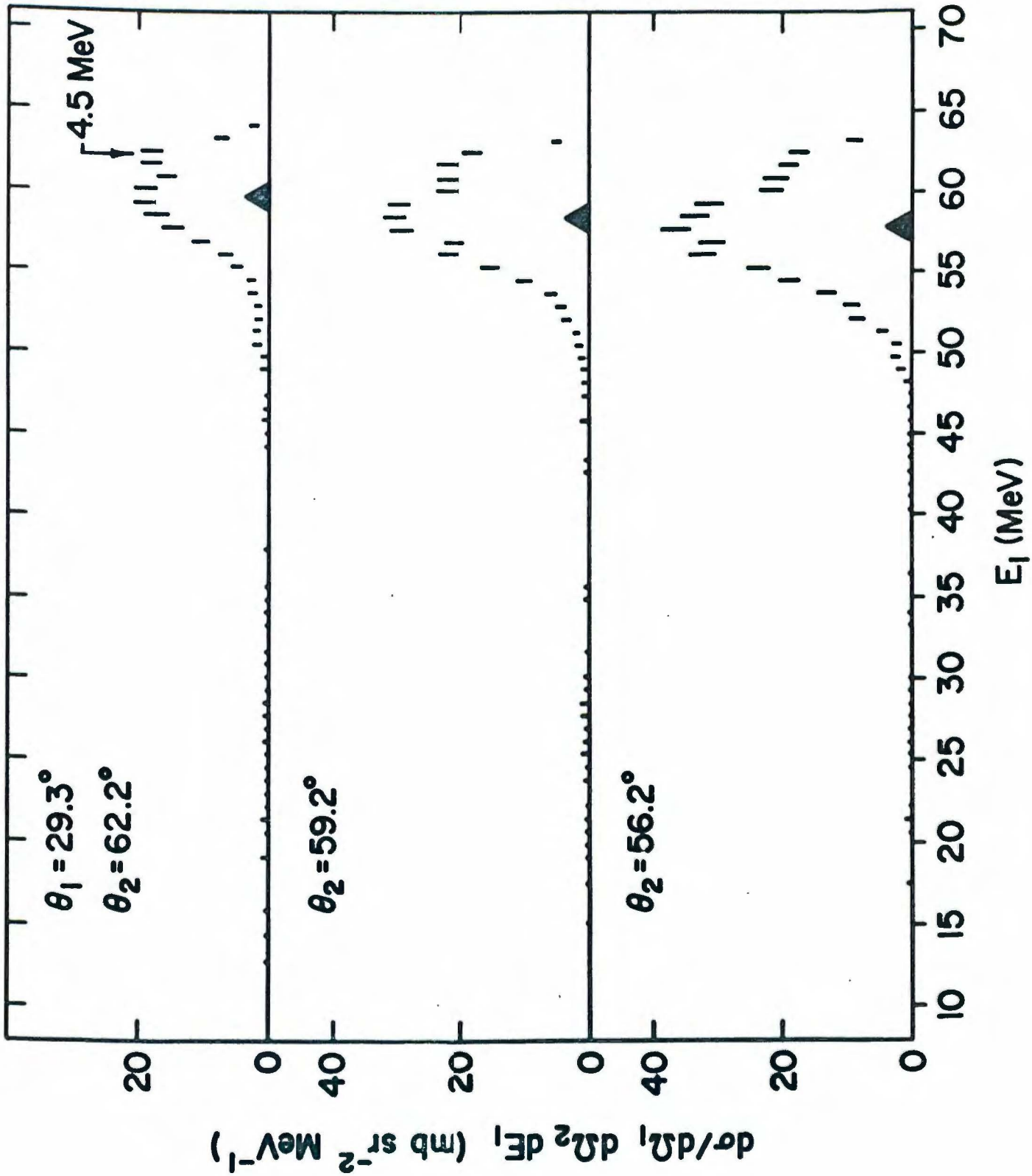

Figure 3.7: Projected energy spectra for three angle pairs with $\theta_1 = 29.3^\circ$ for 79.6 MeV bombarding energy. The point with the minimum value of q in each spectrum is indicated by an arrow on the E_1 axis. Sequential peaks are labeled according to the state of Li^6 through which the sequential reaction passes.

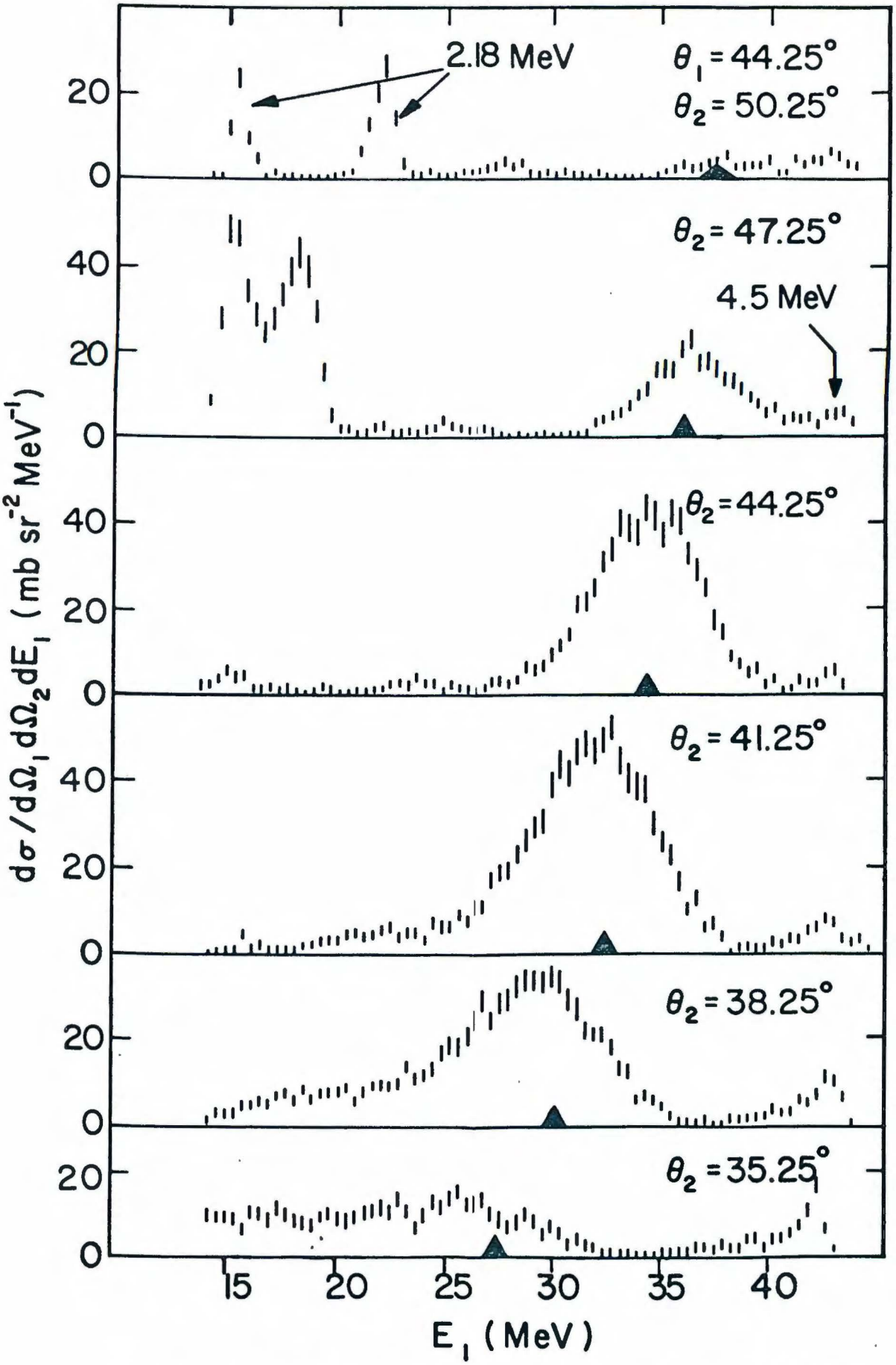

Figure 3.8: Projected energy spectra for six angle pairs with $\theta_1 = 44.25^{o}$ for 70.3 MeV bombarding energy. The point with the minimum value of q in each spectrum is indicated by an arrow on the E_1 axis. Sequential peaks are labeled according to the state of Li^6 through which the sequential reaction passes.

of $\vec{q} = 0$ occurs only in the spectrum for $\theta_2 = 44.25^\circ$, but an arrow indicates where the point of minimum $\vec{q}$ occurs in each spectrum. Sequential groups corresponding to the 4.5 MeV state of Li^6 occur on the high energy side of the quasi-free peak in all the spectra. Because the value of E_1 for these events is uniquely determined by the value of θ_1 (see discussion in Section 2.1.4) this group occurs at the same value of E_1 in all six spectra. For the spectra with $\theta_2 = 50.25^\circ$ and 47.25°, sequential groups corresponding to the 2.18 MeV state of Li^6 occur on the low energy side of the quasi-free peak. These groups of events are due to the inelastically scattered α being detected by counter two. For each θ_2 the value of E_2 for these groups is unique, but the value of E_1 is not, because the kinematic locus can be double valued. For the values of θ_2 smaller then 47.25° shown here, the energy of inelastically scattered α's from the 2.18 MeV state of Li^6 is larger than any value of E_2 on the kinematic locus and so no sequential groups occur from that process.

As mentioned previously, the only point with $\vec{q} = 0$ in Fig. 3.8 occurs in the spectrum with $\theta_2 = 44.25^\circ$. The minimum value of $\vec{q}$ in the other spectra gets larger, the further θ_2 is from 44.25°. In general, the cross sections at these "q min." points gets smaller as "q min." gets larger. This is what might be expected if $|\Phi(q)|^2$ was the only strongly varying factor in the cross section. In fact $|\Phi(q)|^2$ is not the only strongly varying factor determining the cross section. The spectra in Fig. 3.2 showed that $(d\sigma/d\Omega)_{\alpha-\alpha}$ also seems to play a strong role in determining the cross section.

Figures 3.6, 3.7, and 3.9 to 3.13 show other sets of spectra for bombarding energies of 79.6 and 70.3 MeV. For each figure, θ_1 is the same for all the spectra. The same general comments that were made about Fig. 3.8 apply to these figures as well. There are some individual differences, however. In Fig. 3.10, for instance, the only point with $\vec{q} = 0$ occurs in the top

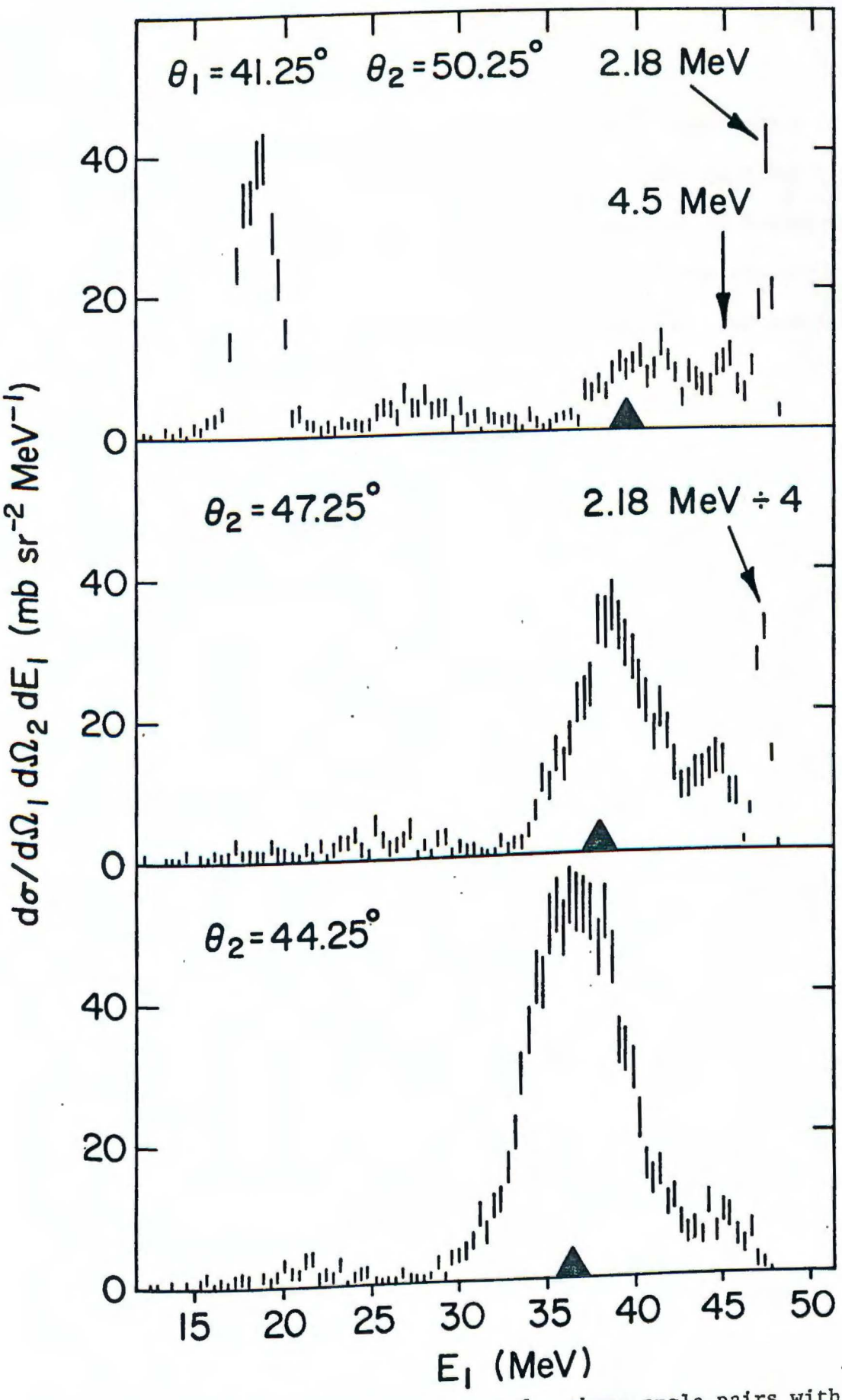

Figure 3.9: Projected energy spectra for three angle pairs with $\theta_1 = 41.25^\circ$ for 70.3 MeV bombarding energy. The point with the minimum value of q in each spectrum is indicated by an arrow on the E_1 axis. Sequential peaks are labeled according to the state of Li^6 through which the sequential reaction passes.

spectrum, with $\theta_1 = 38.25^\circ$ and $\theta_2 = 50.2^\circ$. Again the minimum value of $|\vec{q}|$ increases as θ_2 gets further away from 50.2°. But in this case the cross section seems to increase as "q min." gets larger, instead of decrease. This is the opposite of what one would expect if $|\Phi(\vec{q})|^2$ was the only strongly varying factor of the cross section. This feature and other anomalies will be discussed in more detail in Chapter 5.

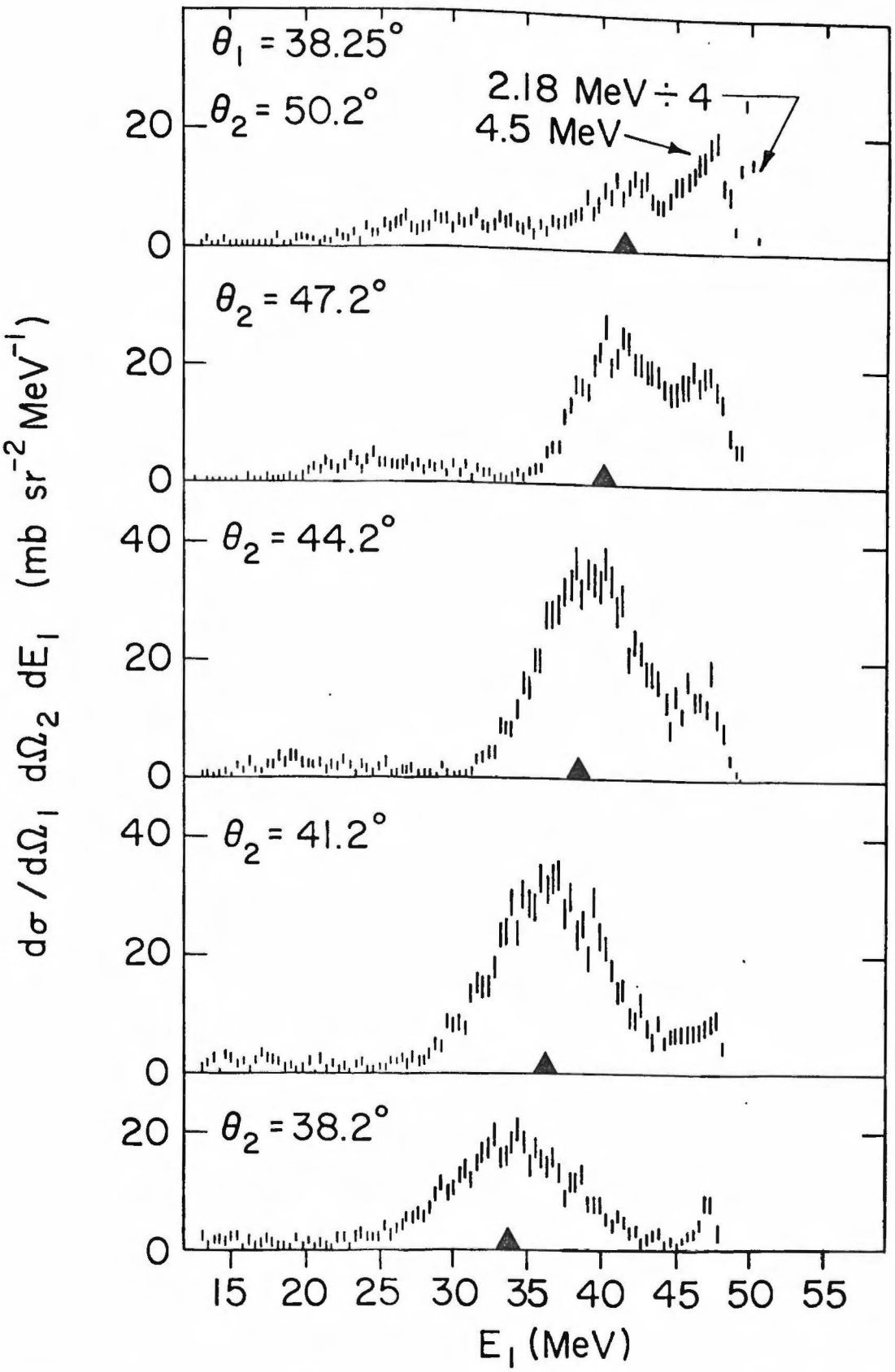

Figure 3.10: Projected energy spectra for five angle pairs with $\theta_1 = 38.25°$ for 70.3 MeV bombarding energy. The point with the minimum value of q in each spectrum is indicated by an arrow on the E_1 axis. Sequential peaks are labeled according to the state of Li^6 through which the sequential reaction passes.

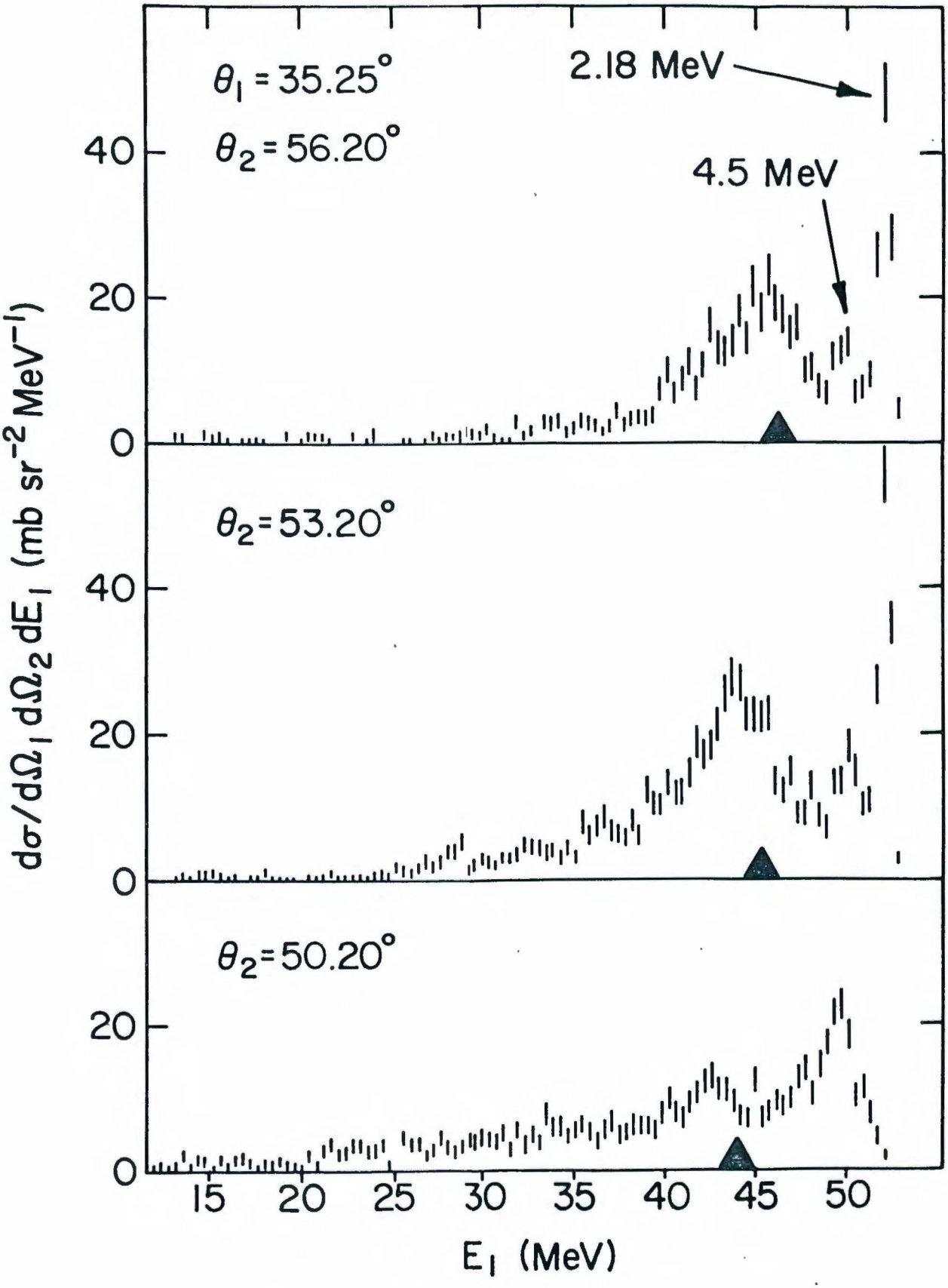

Figure 3.11: Projected energy spectra for three angle pairs with $\theta_1 = 35.25°$ for 70.3 MeV bombarding energy. The point with the minimum value of q in each spectrum is indicated by an arrow on the E_1 axis. Sequential peaks are labeled according to the state of Li^6 through which the sequential reaction passes.

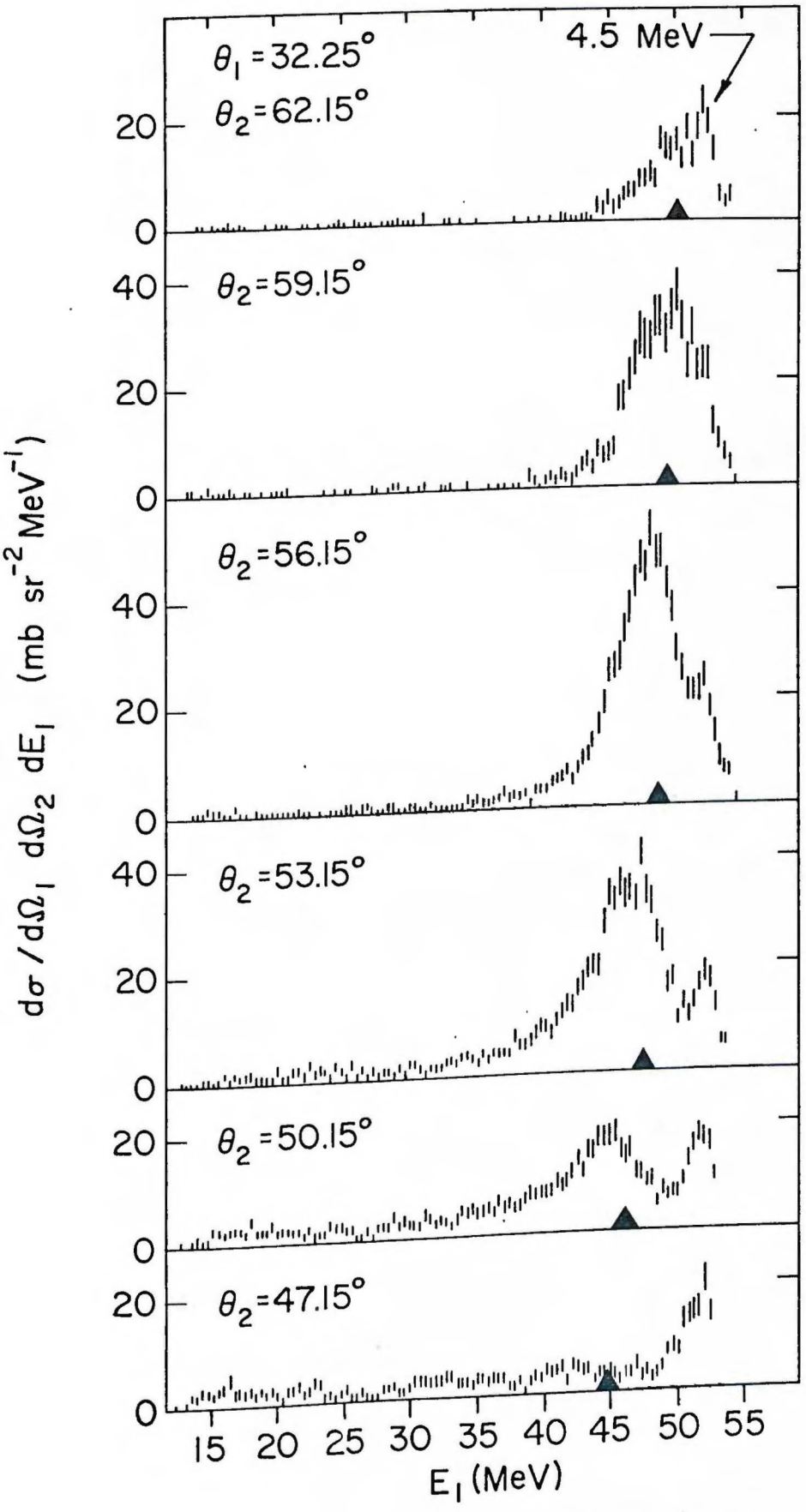

Figure 3.12: Projected energy spectra for six angle pairs with $\theta_1 = 32.25^\circ$ for 70.3 MeV bombarding energy. The point with the minimum value of q in each spectrum is indicated by an arrow on the E_1 axis. Sequential peaks are labeled according to the state of Li^6 through which the sequential reaction passes.

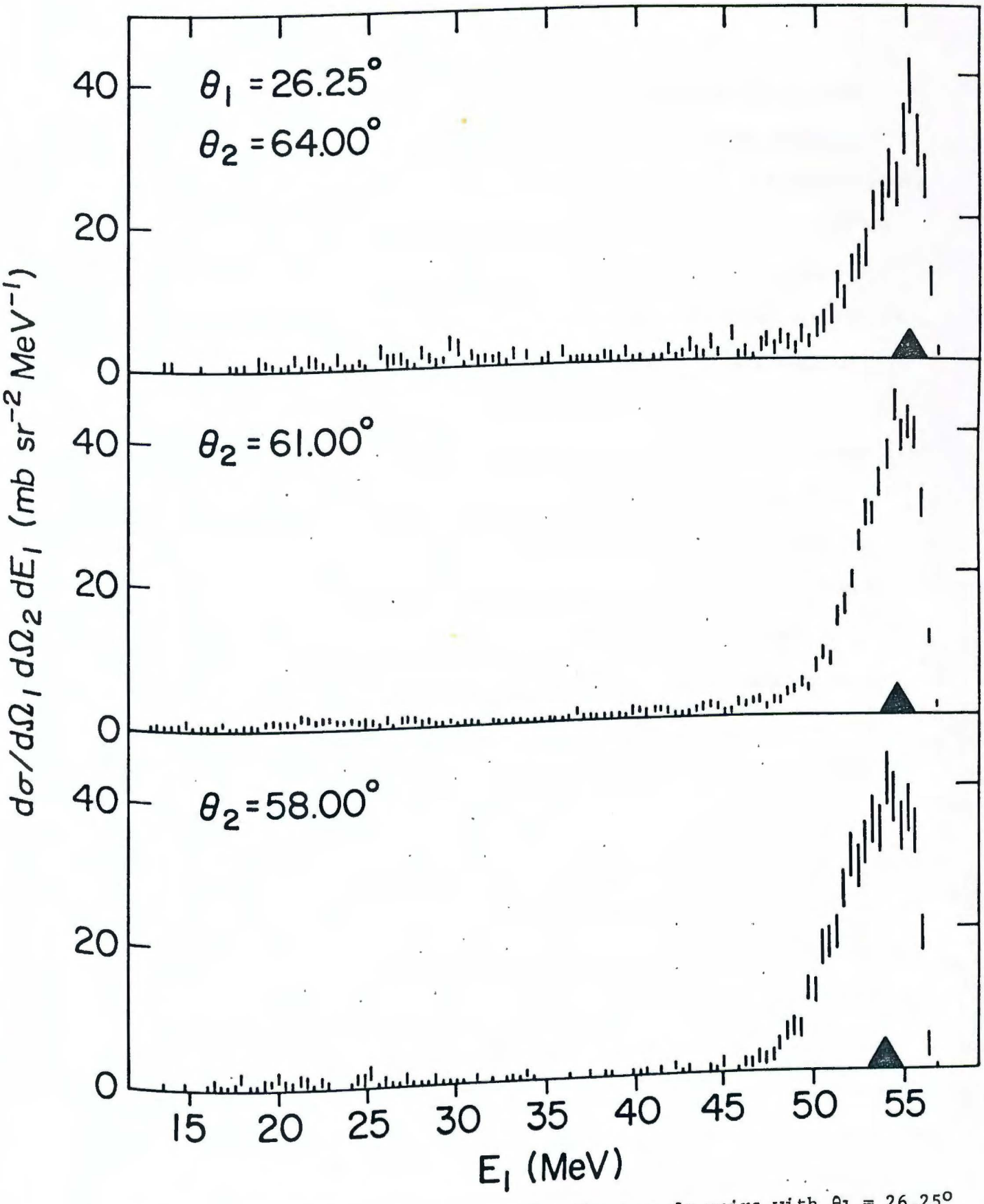

Figure 3.13: Projected energy spectra for three angle pairs with $\theta_1 = 26.25°$ for 70.3 MeV bombarding energy. The point with the minimum value of q in each spectrum is indicated by an arrow on the E_1 axis. In all three spectra the sequential peak due to the 4.5 MeV state of Li^6 coincides almost exactly in energy with the quasi-free peak, and so has not been indicated separately.

Section 3.5 Sequential Processes

The concern in this experiment with sequential processes has so far been largely how to select regions of phase space in which they are unimportant when compared with quasi-free scattering. As discussed in Section 2.1.4, the only states seen strongly in inelastic α scattering on Li^6 are the 2.18 MeV (3^+) and the 4.5 MeV (2^+) states. This is, in general, a criterion for a state to contribute to the three body $\alpha + \alpha + d$ final state via sequential decay. Indeed these two states do seem to be the only ones which appear strongly in the spectra presented in Figs. 3.2 - 3.13.

Angular correlation measurements of sequential breakup reactions can provide information on the angular momentum quantum numbers of the intermediate state. They are often used in this way for reactions followed by γ-decay to study the intermediate state. Given a knowledge of the quantum numbers of the intermediate state, angular correlations can be used to study matrix elements of the formation of that state in the reaction being studied. Examples of this type of study in the $Li^6(\alpha,2\alpha)d$ reaction are reported by Dolinov (Do69) at 25 MeV bombarding energy and Matsuki (Ma68) at 29.4 MeV bombarding energy.

The angular correlation data in this experiment does not cover a large enough angular range for an analysis of the sequential processes to be worthwhile. Of considerable interest, however, is the possibility of interference between the quasi-free and sequential components of the cross section for the $\alpha + \alpha + d$ final state. Presumably the matrix elements for the diagrams in Figs. 2.8b and 2.8c should be added and then squared yielding an interference term. One place to look for such interference, either constructive or destructive, would be in a region of phase space where the contributions of both diagrams are non-negligible.

As an example, consider Fig. 3.12. Here are six spectra with $\theta_1 = 32.25^\circ$ for $E_0 = 70.3$ MeV. In the bottom spectrum, with $\theta_2 = 47.15^\circ$ the quasi-free peak is quite small. The sequential peak due to the 4.5 MeV state of Li^6 shows clearly with its long tail. This tail is also seen in the inelastic scattering (singles) spectra which were used for the energy calibration (see Section 3.1). As θ_2 increases, the position of the sequential peak remains fixed, but the quasi-free peak shifts to higher energies, until in the top spectrum with $\theta_2 = 62.15^\circ$ they almost coincide. As the two peaks get closer together, there appears to be no discernible interference between them. The cross section in the region between the peaks can, within statistics, be explained by the simple addition of the shapes of the two peaks, as seen when they are clearly separated in the spectra near the bottom of the figure.

No positive evidence either for (or against) interference has been found in any of the spectra. This is not to say that interference doesn't occur, but it is not strong enough to be evident upon close examination of the spectra.

CHAPTER 4

THE α-α OFF-MASS-SHELL CROSS SECTION

A particle is said to be "virtual" if the square of its four-momentum is not equal to minus the square of its rest mass, i.e.

$$\mathcal{P}^2 = \vec{p}^2 - \epsilon^2 \neq -m^2$$

The particle is said to be a "distance" $\Delta E = m - (-\mathcal{P}^2)^{1/2}$ off-mass-shell.

The struck particle in the $Li^6(\alpha,2\alpha)d$ reaction is, in the model illustrated by the Feynman diagram below, a virtual α-particle in this sense

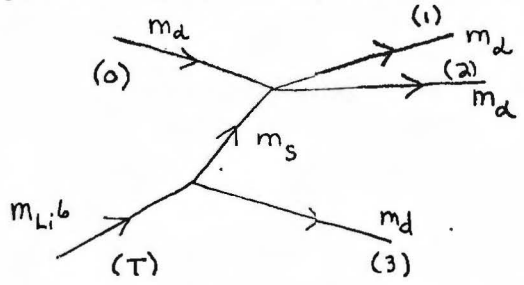

Conservation of four-momentum at the two vertices requires that the transferred particle has an invariant mass different from that of a free α-particle. The elastic scattering at the upper vertex is said to be off the mass-shell by the distance $m_\alpha - m_s$. This quantity is readily calculated as follows: four momentum conservation at the lower vertex implies

$$\mathcal{P}_s = \mathcal{P}_T - \mathcal{P}_3 \tag{4.2}$$

Hence

$$\mathcal{P}_s = [-\vec{P}_3 ; i(m_T - m_3 - T_3)]$$
$$= [\vec{q} ; i(m_2 - E_B - T_3)] \tag{4.3}$$

Hence

$$m_s = [(m_2 - E_B - T_3)^2 - q^2]^{1/2} \tag{4.4}$$

If one then makes a non-relativistic approximation

$$m_s \approx m_2 - E_B - q^2\left(\frac{m_2+m_3}{2m_2m_3}\right) \tag{4.5}$$

Then if the rest mass of the virtual α is called m_2 one finally finds that the transferred particle (and also the collision) is off the mass-shell by the distance

$$\Delta E = m_2 - m_s \approx E_B + q^2/2\mu \tag{4.6}$$

Three kinematic variables are needed to specify the off-mass-shell cross section. The ones chosen here are E_i, the initial c.m. energy of the two α-particles, E_f, the final c.m. energy of the two α-particles and θ_{cm}, the c.m. scattering angle. Derivations of these quantities are given in Appendix 1. Note that the notation is different in Appendix 1: $E_i \equiv T_i \equiv T_{0S\,cm}$; $E_f \equiv T_f \equiv T_{12cm}$. The difference between E_i and E_f is just $E_B + q^2/2\mu$, the distance of the collision from the mass-shell. The differential cross section may then be written as $d\sigma/d\Omega(E_i, E_f, \theta cm)$.

In this chapter α-α off-mass-shell cross sections will be presented which were extracted from the spectra presented in Chapter 3 by assuming the validity of the P.W.I.A. The primary off-mass-shell data will be taken from the points for which $\vec{q} = 0$. A second set of data will be taken from points where $|\vec{q}| = 30$ MeV/c.

Of particular interest are on-mass-shell approximations to the observed off-mass-shell cross section. In many previous quasi-free scattering experiments, such approximations have been used without careful investigation of their validity. There is no clear guide in the theory as to what on-mass-shell cross

section is the best approximation. In p-α scattering it has been observed (C59) that the on-energy-shell cross section is largely a function of momentum transfer only, hence a fairly plausible choice of the free cross section to use in (1.7) can be made (J63). For α-α scattering, however, this strong dependence on one variable does not exist, and there is no obvious prescription for the on-energy-shell cross section to use in (1.7). Two possible on-mass-shell approximations to $d\sigma/d\Omega(E_i, E_f, \theta_{cm})$ will be investigated. These are $d\sigma/d\Omega(E_i, \theta_{cm})$ and $d\sigma/d\Omega(E_f, \theta_{cm})$. These will be referred to as the E_i and E_f approximations. Other choices for on-mass-shell approximations could, of course, be made.

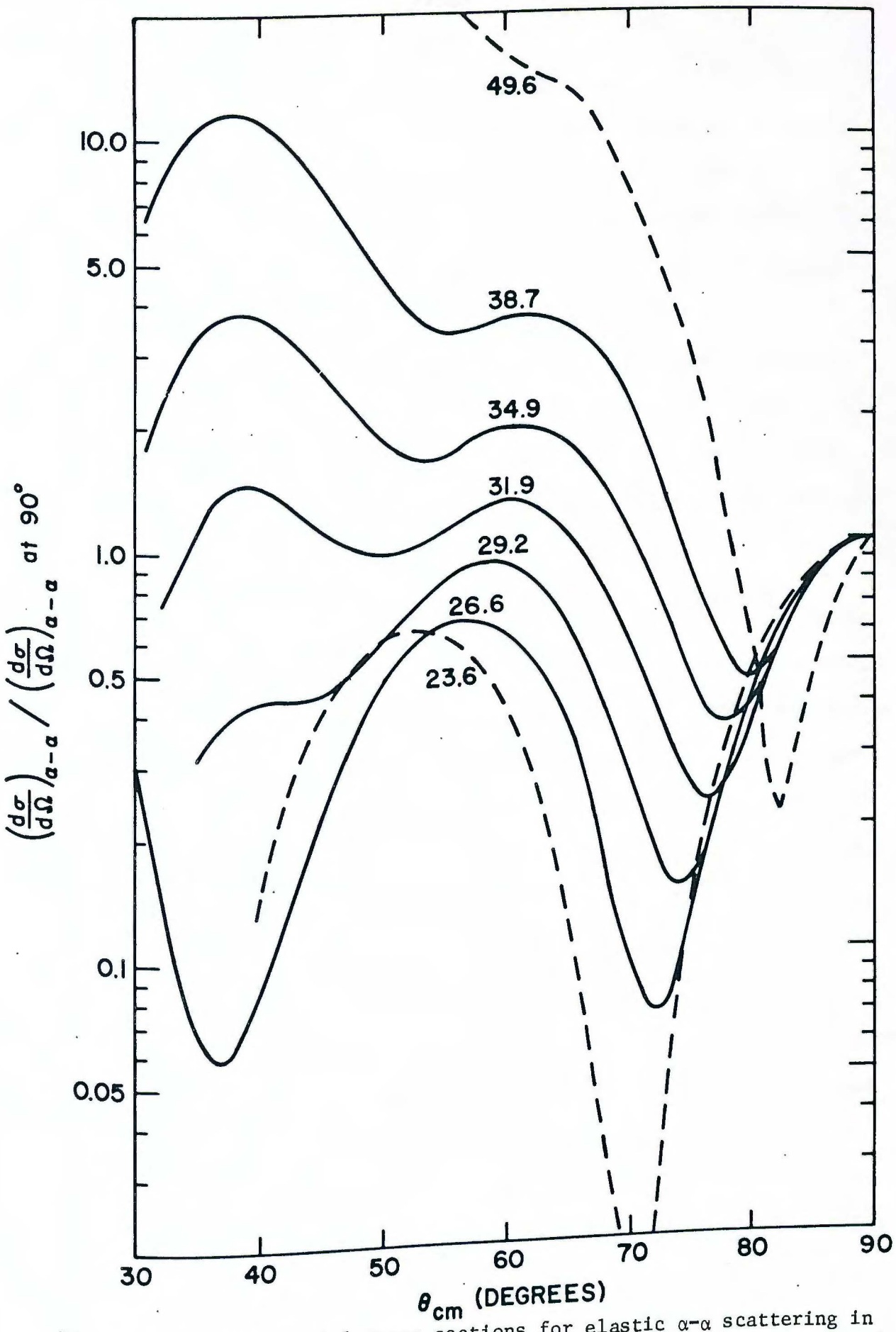

Figure 4.1: Differential cross sections for elastic α-α scattering in the center of mass system. The angular distributions are all normalized to unity at $\theta_{cm} = 90^{o}$. Center of mass energies are indicated for each curve. The data is taken from (D65) and (C60).

Section 4.1 Off-Mass-Shell Cross Sections at $\vec{q} = 0$

In the spectra presented in Figures 3.3 - 3.13, there are 26 points where $\vec{q} = 0$ occurs. In addition one spectrum was measured with $\theta_1 = \theta_2 = 44.15^o$ at $E_o = 60.5$ MeV which contains a $\vec{q} = 0$ point, and the three spectra with $\theta_1 = 26.25^o$ and $E_o = 70.3$ MeV can be interpolated to yield another $\vec{q} = 0$ point. Thus there are 28 data points in all with $\vec{q} = 0$.

For these 28 data points the cross section at $\vec{q} = 0$ was extracted, with allowance made in the error for the ± 300 KeV or ± 3/4 channel uncertainty in the energy of the $\vec{q} = 0$ point. These cross sections were then divided by the kinematic factor (1.8) yielding the product of the effective α-α cross section and $|\Phi(\vec{q} = 0)|^2$:

$$\left(d^3\sigma/d\Omega_1 d\Omega_2 dE_1\right) \times (K.F.)^{-1} = \left(d\sigma/d\Omega\right)_{eff.} \times \left|\Phi(\vec{q}=0)\right|^2 \qquad (4.7)$$

The free α-α cross sections have been measured at very nearly the energies needed to compare free and quasi-free angular distributions. It is necessary, however, in view of the accuracy of the present data to interpolate between the angular distributions of (D65) and (C60). Figure 4.1 shows the free α-α cross sections at center of mass energies of 23.6, 26.6, 29.2, 31.9, 34.9, 38.7 and 49.6 MeV, all normalized to unity at 90^o. Displayed in this form, the systematics of the free α-α data are clearer. It is then easier to make reasonable interpolations for the free cross sections at the desired energies, for the 59.0, 70.3 and 79.6 MeV quasi-free data. Recent unpublished data (B69) indicates that there are no new resonances in α-α scattering between 55 and 70 MeV bombarding energy. Thus a smooth interpolation of the data currently available seems reasonable. For the 50.4 MeV data, the cross section for $E_f = 25.1$ MeV is already available from (C60). For $E_i = 23.6$ MeV the cross section can be generated from the

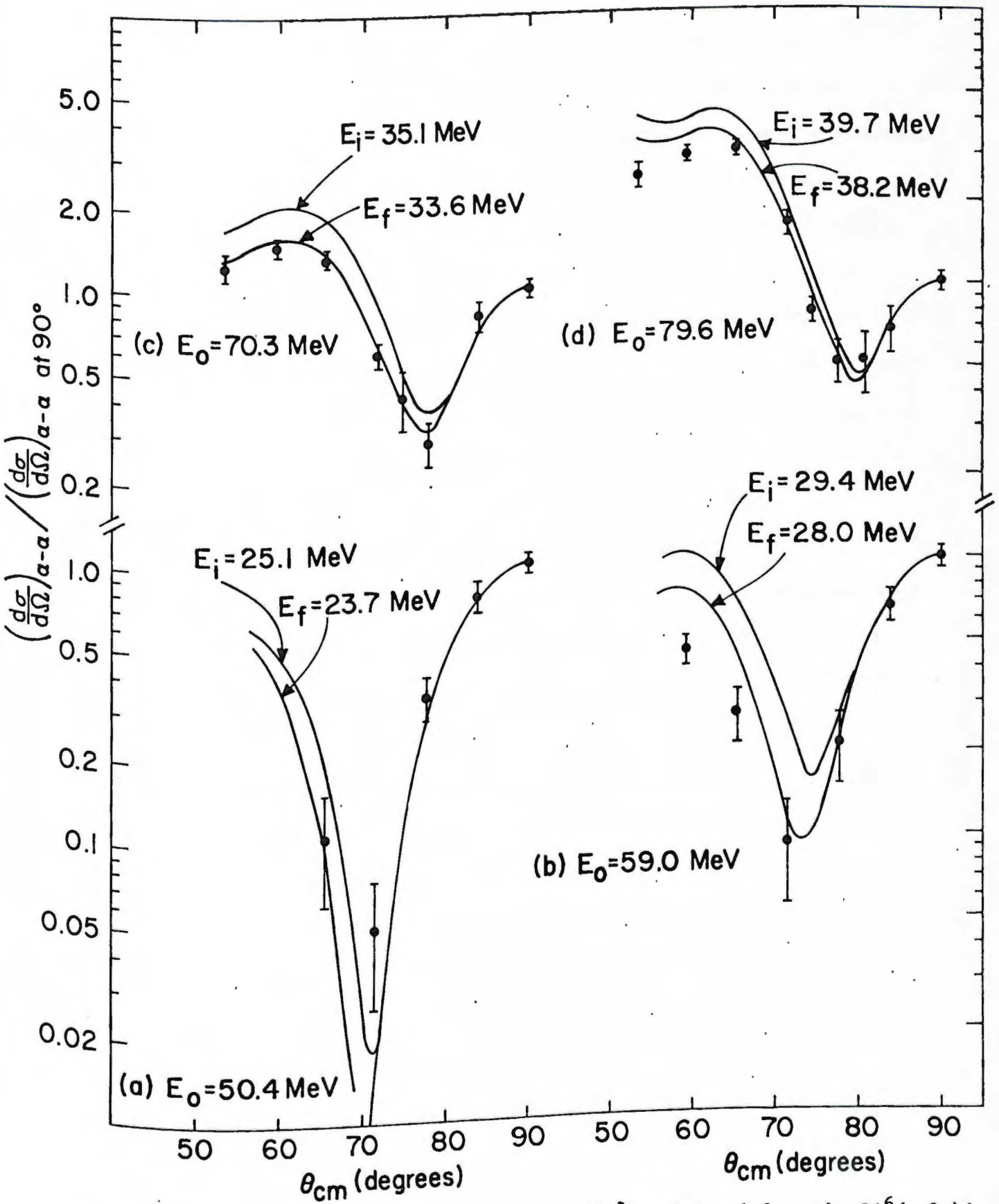

Figures 4.2 (a) - (d): The off-mass-shell $(d\sigma/d\Omega)_{\alpha\alpha}$ deduced from the $Li^6(\alpha,2\alpha)d$ reaction at 50.4, 59.0, 70.3, and 79.6 MeV, plotted against θ_{cm} for the α-α collision. The solid curves are interpolated values of $(d\sigma/d\Omega)_{\alpha\alpha}$ for free scattering, using the data of (D65) and (C60). The results are normalized to unity at $\theta_{cm} = 90^o$.

phase shifts reported in (D65).

The free cross sections for E_f and E_i together with the quasi-free angular distributions are shown in Figure 4.2. It is clear that for $\theta_{cm} > 65^o$ E_f is superior to E_i, and the agreement for E_f seems to be very good indeed. However, for smaller angles it would seem that deviations from E_f begin to occur, particularly in the 79.6 and 59 MeV data. An alternate way of displaying the data is to present excitation functions for $(d\sigma/d\Omega)$ at a fixed angle, as a function of energy. The five data points corresponding to $\theta_{cm} = 90^o$ are shown in Figure 4.3, plotted against both E_i and E_f. Also shown is the free (or on-mass-shell) α-α excitation function for $\theta_{cm} = 90^o$. The quasi-free data has been normalized in both cases to give a "best fit". The normalization factor for E_i is $|\Phi(0)|^2 = 2.67 \times 10^{-7} (\text{MeV/c})^{-3} \text{sr}^{-1} = 2.05 \text{ fm.}^3 \text{sr}^{-1}$. For E_f it is $|\Phi(0)|^2 = 1.97 \times 10^{-7} (\text{MeV/c})^{-3} \text{sr}^{-1} = 1.51 \text{ fm.}^3 \text{sr}^{-1}$. In either case, one can say that the agreement of the energy dependence of the free and the quasi-free cross sections is very good indeed. It is clear from Figure 4.3 that a somewhat better fit is obtained for E_f than for E_i, but the case cannot be made strongly.

Figures 4.4, 4.5 and 4.6 show excitation functions for $\theta_{cm} = 83.8^o$, 77.7^o, 71.5^o, 65.4^o, 59.3^o and 53.2^o. The quasi-free data is again plotted against both E_i and E_f. The free α-α excitation functions are also shown, with the data between 22 and 26 MeV being generated from the phase shifts given in (D65). The normalization of the quasi-free data to the free data is the same as for Figure 4.3. It again appears that E_f provides a better fit to the data, given the normalization to the 90^o excitation function.

It would appear from the overall comparison of the quasi-free and free α-α cross sections, that for $\vec{q} = 0$, the factorization of the P.W.I.A. cross section is remarkably good, if E_f is used for the free cross sections.

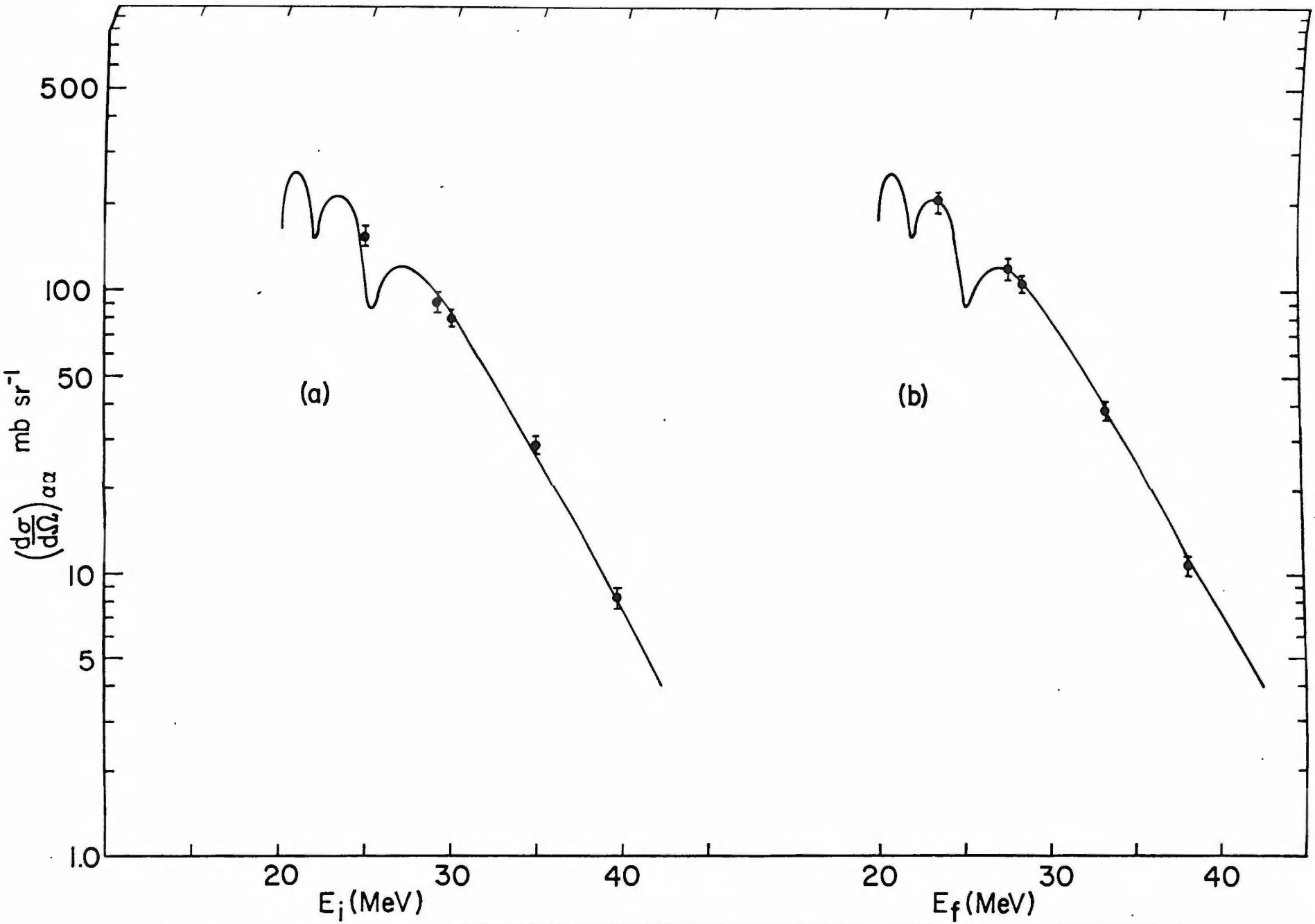

Figures 4.3 (a) and (b): The off-mass-shell $(d\sigma/d\Omega)_{\alpha\alpha}$ deduced from the $Li^6(\alpha,2\alpha)d$ reaction at $\theta_{cm} = 90^o$, plotted against E_i and E_f the initial state and final state α-α c.m. energies. The data points are normalized using $|\Phi(0)|^2 = 2.05$ fm^3 sr^{-1} for (a) and $|\Phi(0)|^2 = 1.51$ fm^3 sr^{-1} for (b). The solid curve is $(d\sigma/d\Omega)_{\alpha\alpha}$ for $\theta_{cm} = 90^o$ from (D65).

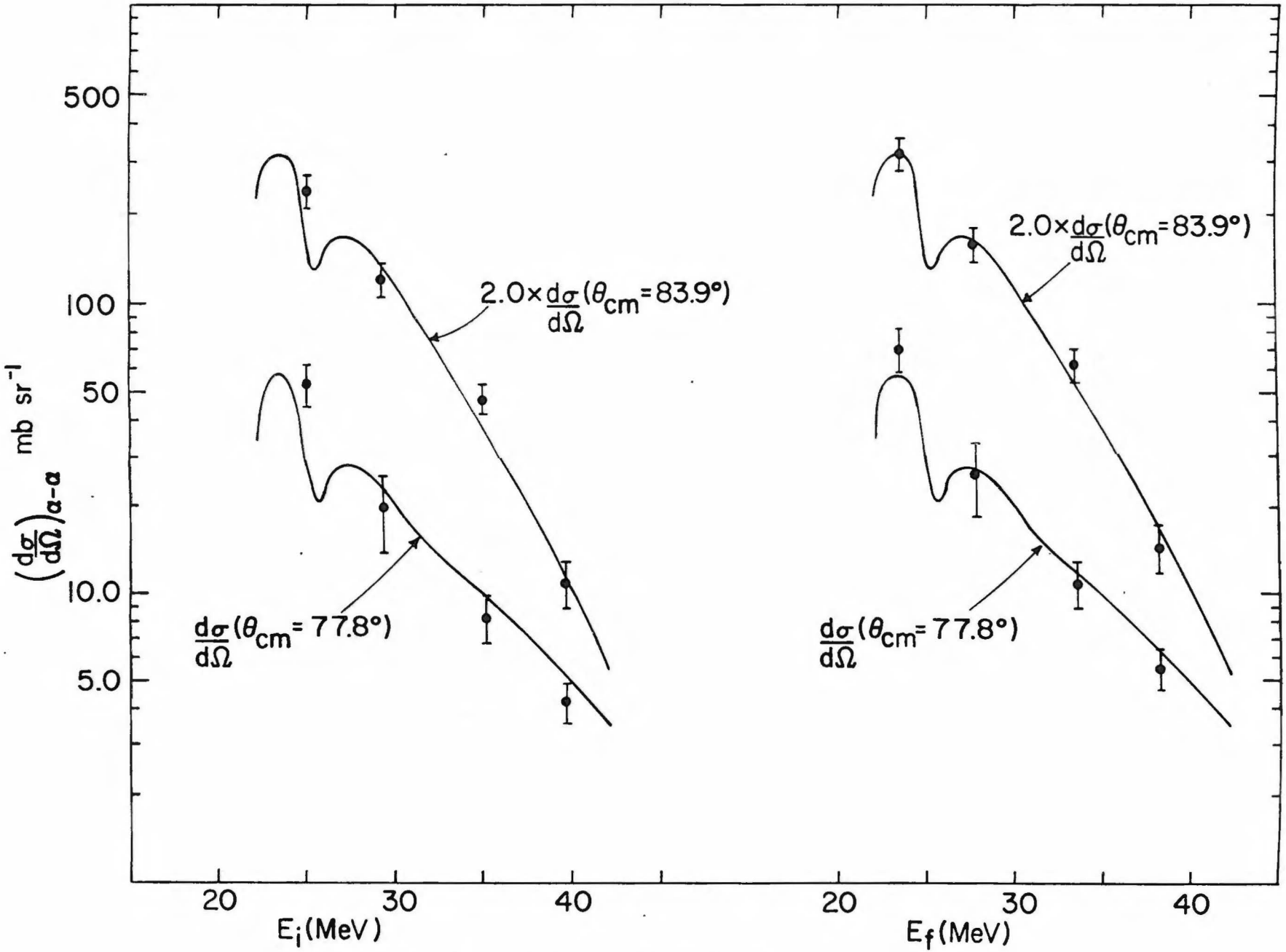

Figures 4.4 (a) and (b): Same as for Figure 4.3 except the data is for $\theta_{cm} = 83.9^{o}$ and 77.8^{o}.

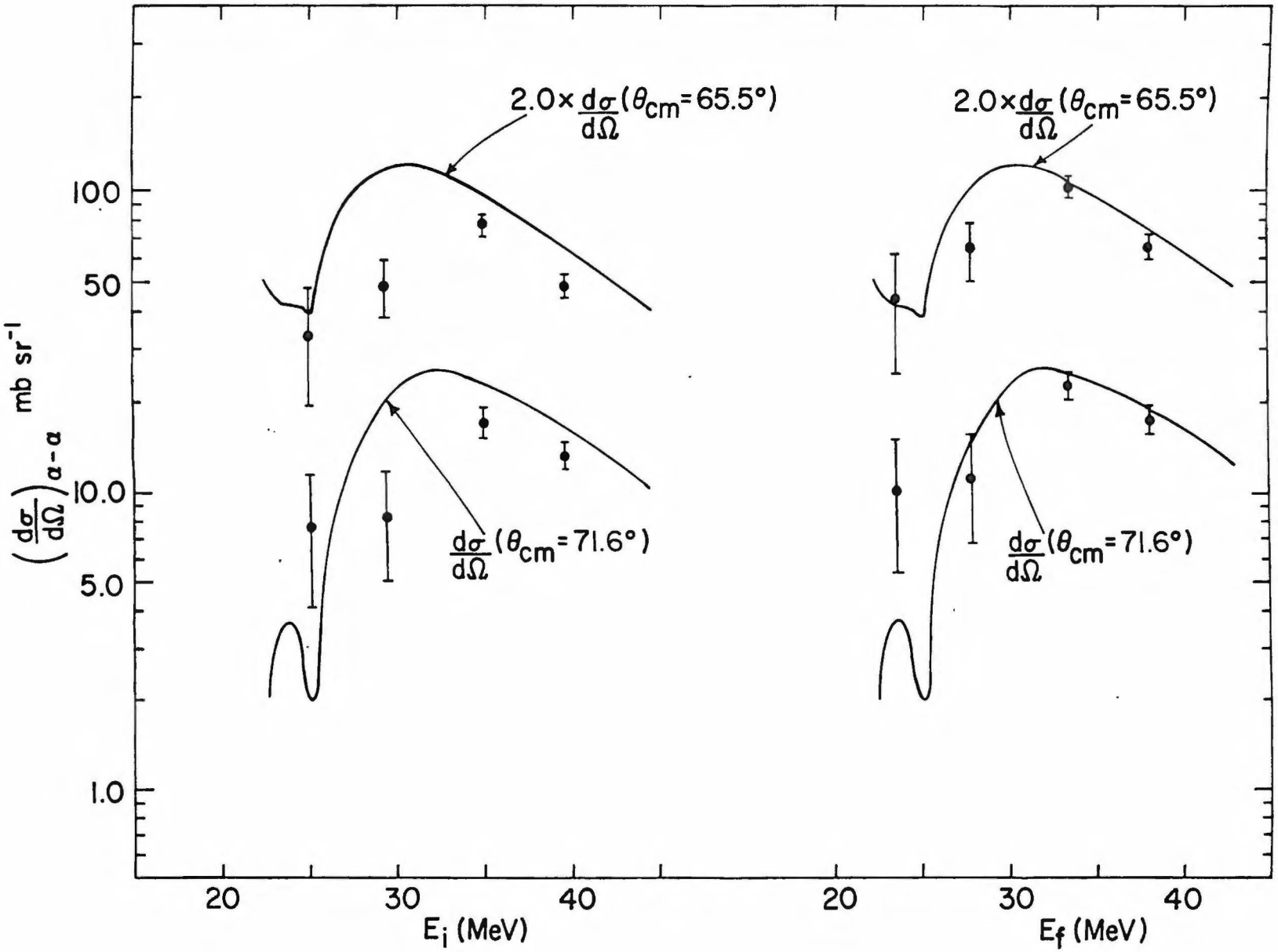

Figures4.5 (a) and (b): Same as for Figure 4.3 except the data is for θ_{cm} = 71.6° and 65.5°.

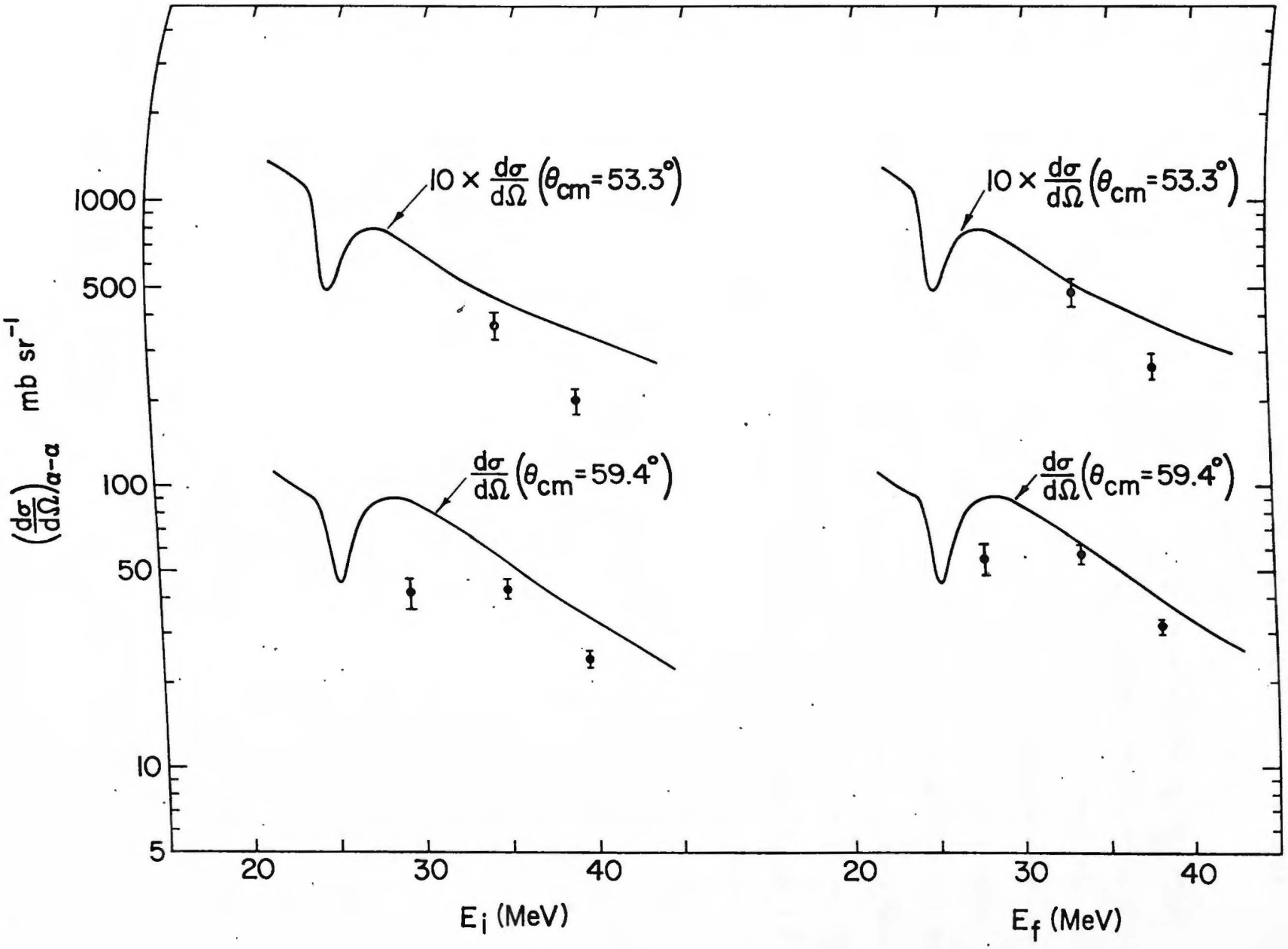

Figures 4.6 (a) and (b): Same as for Figure 4.3 except the data is for $\theta_{cm} = 59.4^{o}$ and 53.3^{o}.

Whether the normalization factor $|\Phi(0)|^2 \sim 2.0 \times 10^{-7}(\text{MeV/c})^{-3}\text{sr}^{-1}$ is reasonable or not will be considered in Chapter 5.

Some comments should be made on the choice of the E_f approximation. Firstly, it should be remembered that E_f is merely an on-energy-shell approximation to the desired off-energy-shell cross section. Some off-energy-shell calculations are discussed later in this chapter. Secondly, absorption effects may in fact be important, and there is no reason to expect these to be the same for all scattering angles. Thus the apparent preference for E_f from the angular distributions may be an accidental effect of increasing absorption with decreasing scattering angle. The overall impression of the data, however, is that P.W.I.A. appears to give excellent results for $\vec{q} = 0$.

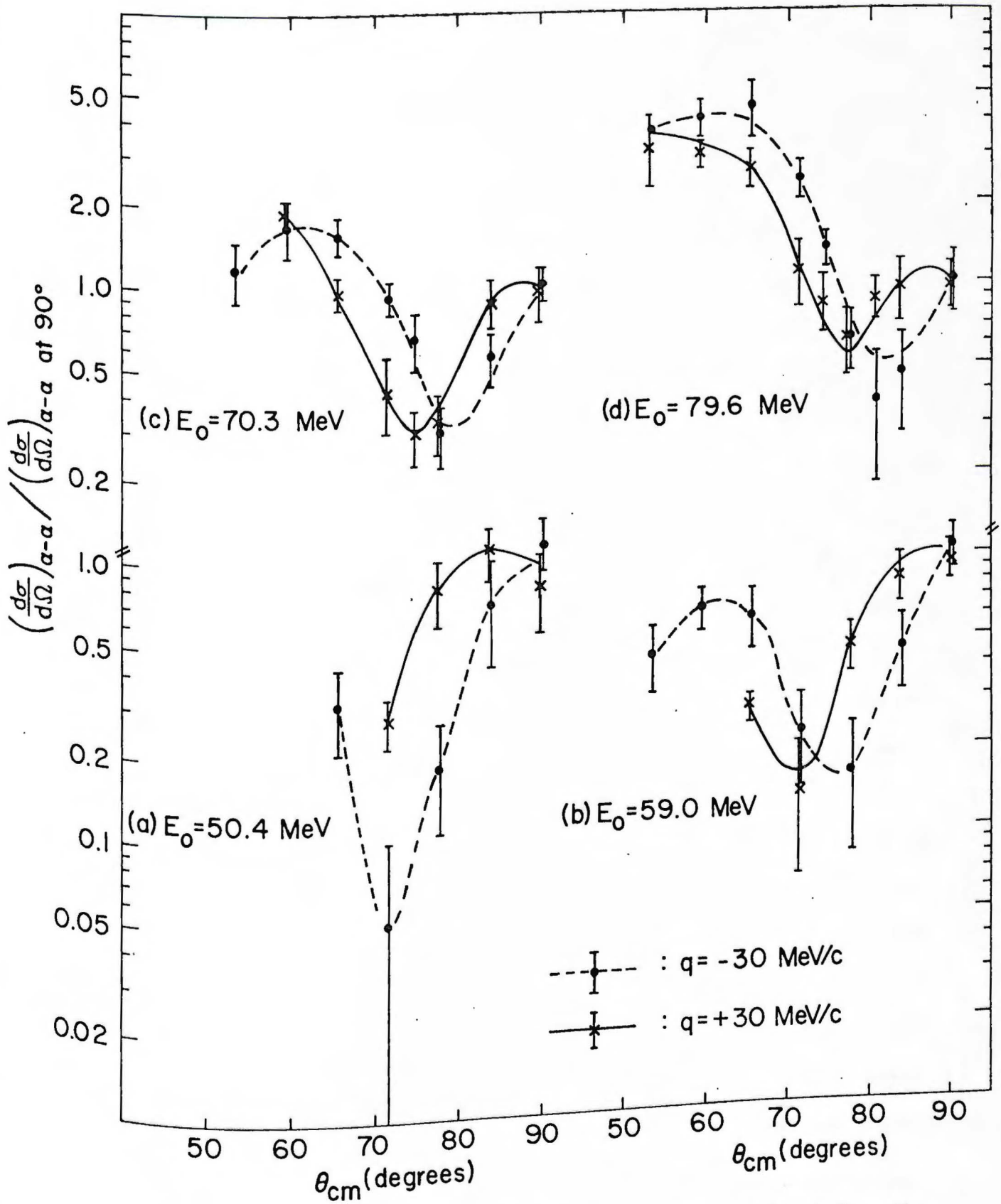

Figures 4.7 (a) - (d): The off-mass-shell $(d\sigma/d\Omega)_{\alpha\alpha}$ deduced from the $Li^6(\alpha,2\alpha)d$ reaction at 50.4, 59.0, 70.3 and 79.6 MeV, plotted against θ_{cm} for the α-α collision. The data is extracted from points with q = ± 30 MeV/c in spectra with θ_{12} ~88°. The curves serve merely to connect the points.

Section 4.2 Off-Mass-Shell Cross Sections for $q \neq 0$

Having extracted off-mass-shell cross sections for $\vec{q} = 0$ and having determined that the factorization of the quasi-free cross section for $\vec{q} = 0$ seems valid, the next logical step is to look at the data where $\vec{q} \neq 0$. For an exploratory investigation, the data for $|\vec{q}| = 30$ MeV/c have been chosen. In each spectrum containing a $\vec{q} = 0$ point, there are two points at which $|\vec{q}| = 30$ MeV/c. These points are roughly the half-maximum points on either side of the quasi-free peak. For convenience these will be called q = -30 MeV/c or the q = +30 MeV/c points, depending on whether the point falls on the low energy or the high energy side of the quasi-free peak, respectively.

These q = ± 30 MeV/c points have the property that all the points for one actual bombarding energy correspond very nearly to the same values of E_i and E_f. However, the q = + 30 MeV/c and the q = - 30 MeV/c points correspond to two different directions for the recoil deuteron. The q = -30 MeV/c points all have the deuteron recoiling at a laboratory angle of $85^\circ \pm 2^\circ$ relative to the beam on the side of counter one. The q = +30 MeV/c points all have the deuteron recoiling at an angle of $85^\circ \pm 2^\circ$ relative to the beam, but on the side of counter two.

Figure 4.7 shows the q = ± 30 MeV/c angular distributions. The errors on the data include the ± 300 KeV uncertainty in the determination of the q = ± 30 MeV/c points. The data has been normalized by taking the q = +30 MeV/c and the q = -30 MeV/c points for the spectra with $\theta_1 = \theta_2 \sim 44^\circ$ and setting their mean equal to unity. Smooth curves have been drawn through the various angular distributions to guide the reader's eye. It is immediately obvious that the two angular distributions are systematically different.

This difference between q = +30 MeV/c and q = -30 MeV/c constitutes a definite failure of P.W.I.A., since the two effective cross sections

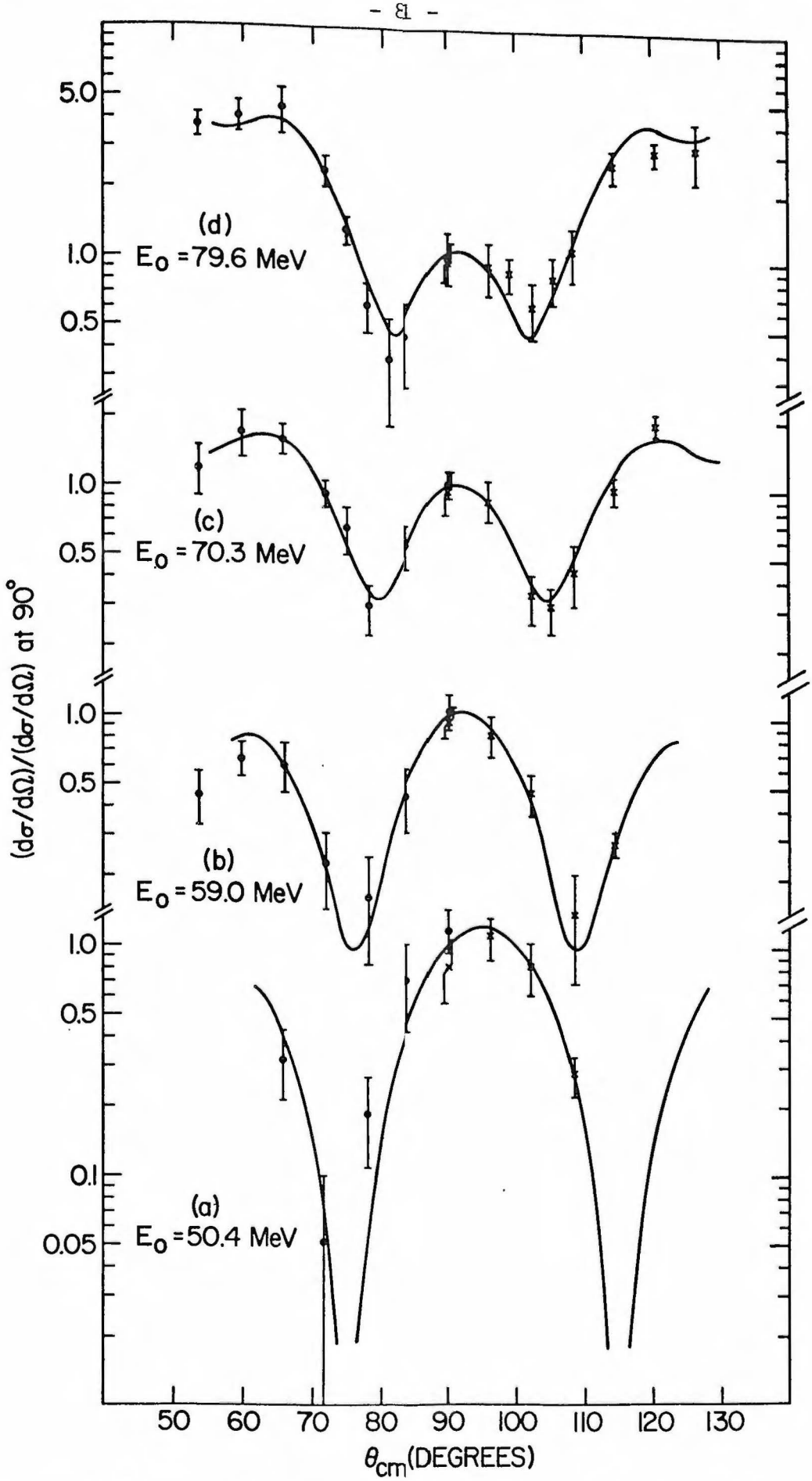

Figures 4.8 (a) - (d): The data from Figure 4.7 (a) - (d) but in this case with the q = +30 MeV/c data displayed for ($\pi - \theta_{cm}$). The curves are interpolated free α-α cross sections for E_f, the final state center of mass energy. The curve for each energy has been shifted in angle to match the behavior of the off-mass-shell data.

should be identical. It is interesting, however, to note how they differ. When the +30 MeV/c and the -30 MeV/c effective α-α cross sections are different, it means that the quasi-free peak is not centered at $\vec{q} = 0$, but is "shifted" in energy to a slightly different value of E_1. This shift is not always in the same direction, however, as is evident from the way the curves for the +30 MeV/c and -30 MeV/c data cross.

There is, however, a similarity between the q = + 30 MeV/c and the q = -30 MeV/c data if the one set is shifted a few degrees relative to the other. The smooth curves drawn through the q = +30 MeV/c and the q = -30 MeV/c data are quite similar in shape, but seem to be offset from each other by a few degrees. It is interesting to replot the data of Figure 4.7 with q = +30 MeV/c data plotted against (π-θ). This is equivalent to ignoring the symmetrization of the α-α cross section and assuming the presence of the deuteron somehow makes the two α's distinguishable.

In Figure 4.8 the smooth curves are the cross sections for E_f from Figure 4.3 displayed for ($\theta + \Delta$) and ($\pi - \theta - \Delta$) where Δ is a shift introduced to make the curves pass through the data as well as possible. Note that Δ is different for each energy. The normalization of all four curves was chosen to make them pass through unity at 90°. With this latitude in plotting the curves, it is possible to make them pass through most of the data points. It is interesting to note that Δ decreases with energy. At 50.4 MeV $\Delta \sim 5^{\circ}$; at 79.6 MeV $\Delta \sim 2^{\circ}$.

This shift Δ is similar to the shifts from symmetry about $\vec{q} = 0$ often observed in wave functions extracted from angular correlations in knockout reactions. In the latter case, $d^3\sigma/d\Omega_1 d\Omega_2 dE_1$ is divided by $(d\sigma/d\Omega)$ and $|\Phi(q)|^2$ is extracted; in the present case, $d^3\sigma/d\Omega_1 d\Omega_2 dE_1$ is divided by $|\Phi(q)|^2$ and $(d\sigma/d\Omega)$ is extracted. In both cases a shift in angle is observed.

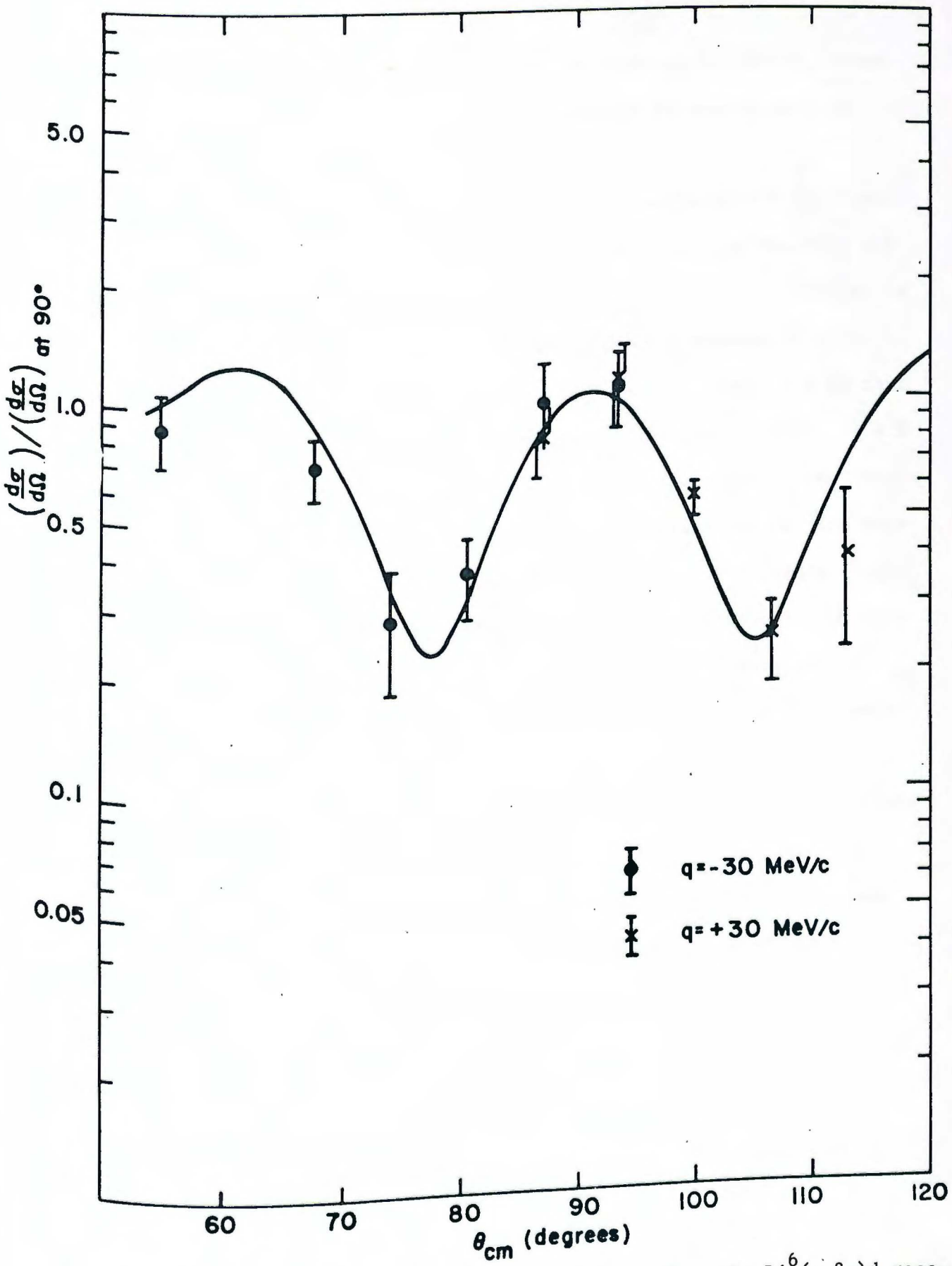

Figure 4.9: The off-mass-shell $(d\sigma/d\Omega)_{\alpha\alpha}$ deduced from the $Li^6(\alpha,2\alpha)d$ reaction at 70.3 MeV, plotted against θ_{cm}. The data is extracted from points with $q = \pm 30$ MeV/c in spectra with $\theta_{12} \sim 85^o$. The data for $q = +30$ MeV/c is displayed for ($\pi - \theta_{cm}$). The curve is an interpolated free α-α cross section for E_f, shifted slightly in angle to match the behavior of the off-mass-shell data.

This type of shift has often been attributed to distortion effects, though it is not clear that distortion is the only possible mechanism that can produce "shifts".

There is one more fairly complete set of data available for the type of test presented in Figure 4.8. There are six angle pairs in the 70.3 MeV data with $\theta_{12} \sim 85^{o}$. For these spectra effective cross sections can also be extracted for q = ± 30 MeV/c. None of these six spectra contains $\vec{q} = 0$ points. The one difference between this data and that in Figure 4.8 is that $E_f = 31.7$ MeV for all the data points. This data is displayed in Figure 4.9 with the q = +30 MeV/c data displayed for ($\pi - \theta$). The curve is the interpolated free cross section for 31.7 MeV shifted and normalized in the same manner as the curves in Figure 4.9. In this case, the curve actually misses many of the points, and the shift Δ used here is only about 1^{o}. The quality of the "fit" is too poor and the number and range of data points is too limited, however, to draw any strong conclusions about the size or significance of Δ .

The results in this section show that P.W.I.A. does not give a perfect descriptions of the reaction mechanism for quasi-free knockout when $q \neq 0$. It would seem, however, that distortion effects are fairly small and seem to decrease with bombarding energy. The qualitative features of the P.W.I.A. cross section are still strongly present in the data.

Section 4.3 Off-Mass-Shell Calculations

4.3.1 Theory

In this section, off-mass-shell cross sections for α-α scattering will be calculated with a phenomenological α-α potential. For other studies of this problem see Balashov and Meboniya(B68). The following conventions will be used: $\phi(k)$ is a plane wave of momentum $\hbar k$, $\chi(k)$ is a Coulomb distorted wave, and $\psi(k)$ is the full scattering wave function. The subscripts i and f will refer to the initial and final states.

The cross section for elastic scattering on the mass-shell is (R67)

$$\frac{d\sigma}{d\Omega} = \frac{2\pi}{\hbar v_i} \left| \langle \phi_f(k_f) | V | \psi_i^{(+)}(k_i) \rangle \right|^2_{E_f = E_i} \rho_f(E_i) \tag{4.8}$$

where ρ_f is the density of final states.

$$\rho_f(E_i) = \frac{1}{(2\pi)^3} k_f^2 \frac{dk_f}{dE_f}\bigg|_{E_i = E_f} = \frac{1}{(2\pi)^3} \frac{m k_f}{\hbar^2}\bigg|_{E_f = E_i} \tag{4.9}$$

Then

$$\frac{d\sigma}{d\Omega} = \frac{2\pi}{\hbar v_i} \left| \langle \phi_f(k_f) | V | \psi_i^{(+)}(k_i) \rangle \right|^2_{E_f = E_i} \times \left(\frac{m k_f}{(2\pi)^3 \hbar^2} \right)\bigg|_{E_f = E_i}$$

$$= \frac{m^2}{4\pi^2 \hbar^4} \left| \langle \phi_f(k_f) | V | \psi_i^{(+)}(k_i) \rangle \right|^2_{E_f = E_i} \times \frac{k_f}{k_i}\bigg|_{E_f = E_i} \tag{4.10}$$

On the mass-shell $k_f = k_i$. Off the mass-shell the $E_f = E_i$ restriction is dropped but the k_f/k_i term is retained. Thus the off-mass-shell cross section is

$$\frac{d\sigma}{d\Omega} = \frac{k_f}{k_i} \frac{m^2}{4\pi^2 \hbar^4} \left| \langle \phi_f(k_f) | V | \psi_i^{(+)}(k_i) \rangle \right|^2 \equiv \left(\frac{d\sigma}{d\Omega} \right)_I \tag{4.11}$$

It can also be expressed as

$$\frac{d\sigma}{d\Omega} = \frac{k_f}{k_i} \frac{m^2}{4\pi^2\hbar^4} \left| \langle \psi_f^{(-)}(k_f) | V | \phi_i(k_i) \rangle \right|^2 \equiv \left(\frac{d\sigma}{d\Omega}\right)_{II} \tag{4.12}$$

These two forms will not necessarily give the same cross section off the mass-shell though they must on the mass-shell. Whether $(d\sigma/d\Omega)_I$ (4.11) or $(d\sigma/d\Omega)_{II}$ (4.12) is the better expression off the mass-shell is related to whether $\frac{d\sigma}{d\Omega}(E_i)$ or $\frac{d\sigma}{d\Omega}(E_f)$ is a better on-mass-shell approximation and both forms will be investigated.

The "T matrix" element $\langle \phi_f(k_f) | V | \psi_i^{(+)}(k_i) \rangle$ will now be converted into the "two potential" form. It seems at first that the numerical calculation of $\langle \phi_f | V | \psi_i^{(+)} \rangle$ is a perfectly well defined operation. If V is an infinite range potential, however, it is not possible to calculate $\langle \phi_f | V | \psi_i^{(+)} \rangle$ numerically, hence the "two potential" approach. V is separated into two potentials, a long range and a short range one, which will be called $V_{coulomb}$ and $V_{nuclear}$ or V_o and V_1 respectively.

$$V = V_c + V_N = V_0 + V_1 \tag{4.13}$$

Coulomb or "distorted" waves are defined as

$$\begin{aligned} \chi_f^{(\pm)} &= \phi_f + \frac{1}{E_f - H_0 \pm i\epsilon} V_0 \chi_f^{(\pm)} \\ &= \phi_f + \frac{1}{E_f - H_0 - V_0 \pm i\epsilon} V_0 \phi_f \end{aligned} \tag{4.14}$$

The T matrix is

$$T_{fi} = \langle \phi_f | V | \psi_i^{(+)} \rangle = \langle \phi_f | V_0 | \psi_i^{(+)} \rangle + \langle \phi_f | V_1 | \psi_i^{(+)} \rangle \tag{4.15}$$

Replacing ϕ_f with (4.14) yields

$$T_{fi} = \langle \phi_f | V_0 | \psi_i^{(+)} \rangle + \langle \chi_f^{(-)} | V_1 | \psi_i^{(+)} \rangle$$

$$- \langle \phi_f | V_0 \frac{1}{E_f - H_0 - V_0 \pm i\epsilon} V_1 | \psi_i^{(+)} \rangle \qquad (4.16)$$

Now the first terms above can be reexpressed using the following identity

$$\frac{1}{E - H_0 + i\epsilon} = \frac{1}{E - H_0 - V_0 + i\epsilon} - \frac{1}{E - H_0 - V_0 + i\epsilon} V_0 \frac{1}{E - H_0 + i\epsilon} \qquad (4.17)$$

This is used to express $\psi_i^{(+)}$ in a more convenient form:

$$\begin{aligned}
\psi_i^{(+)} &= \phi_i + \frac{1}{E_i - H_0 + i\epsilon} (V_0 + V_1) \psi_i^{(+)} \\
&= \phi_i + \frac{1}{E_i - H_0 - V_0 + i\epsilon} (V_0 + V_1) \psi_i^{(+)} \\
&\quad - \frac{1}{E_i - H_0 - V_0 + i\epsilon} V_0 \frac{1}{E_i - H_0 + i\epsilon} (V_0 + V_1) \psi_i^{(+)} \\
&= \phi_i + \frac{1}{E_i - H_0 - V_0 + i\epsilon} (V_0 + V_1) \psi_i^{(+)} \\
&\quad - \frac{1}{E_i - H_0 - V_0 + i\epsilon} V_0 (\psi_i^{(+)} - \phi_i) \\
&= \chi_i^{(+)} + \frac{1}{E_i - H_0 - V_0 + i\epsilon} V_1 \psi_i^{(+)}
\end{aligned} \qquad (4.18)$$

Substituting this into the first term of (4.16) yields

$$T_{fi} = \langle \phi_f | V_0 | \chi_i^{(+)} \rangle + \langle \phi_f | V_0 \frac{1}{E_i - H_0 - V_0 + i\epsilon} V_1 | \psi_i^{(+)} \rangle$$

$$+ \langle \chi_f^{(-)} | V_1 | \psi_i^{(+)} \rangle - \langle \phi_f | V_0 \frac{1}{E_f - H_0 - V_0 + i\epsilon} V_1 | \psi_i^{(+)} \rangle \qquad (4.19)$$

On the energy -shell the second and fourth terms normally cancel since $E_f = E_i$. Off the energy-shell they do not. However, these two terms can be combined into a more useful form.

$$\begin{aligned}
&- \langle \phi_f | V_0 \frac{1}{E_f - H_0 - V_0 + i\epsilon} V_1 | \psi_i^{(+)} \rangle + \langle \phi_f | V_0 \frac{1}{E_i - H_0 - V_0 + i\epsilon} V_1 | \psi_i^{(+)} \rangle \\
&= - \langle \phi_f | V_0 \left[\frac{1}{E_f - H_0 - V_0 + i\epsilon} - \frac{1}{E_i - H_0 - V_0 + i\epsilon} \right] V_1 | \psi_i^{(+)} \rangle \\
&= - \langle \phi_f | V_0 \left[\frac{1}{E_f - H_0 - V_0 + i\epsilon} (E_f - E_i) \frac{1}{E_i - H_0 - V_0 + i\epsilon} \right] V_1 | \psi_i^{(+)} \rangle
\end{aligned} \qquad (4.20)$$

Now using (4.18) and (4.14) this becomes

$$+ (E_i - E_f) \langle \chi_f - \phi_f | \psi_i - \chi_i \rangle \tag{4.21}$$

Thus altogether

$$T_{fi} = \langle \phi_f | V_0 | \chi_i^{(+)} \rangle + \langle \chi_f^{(-)} | V_1 | \psi_i^{(+)} \rangle + (E_i - E_f) \langle \chi_f - \phi_f | \psi_i - \chi_i \rangle \tag{4.22}$$

Equation (4.22) is exact. The matrix element $\langle \phi_f | V_0 | \chi_i^{(+)} \rangle$ is the "Coulomb amplitude". On the mass-shell this term is known exactly:

$$\langle \phi_f | V_0 | \chi_i^{(+)} \rangle_{\text{on shell}} = \frac{-4\pi\hbar^2}{2m} f_c(\theta) \tag{4.23}$$

$$f_c(\theta) = \frac{-\eta}{2k \sin^2 \frac{\theta}{2}} \exp\left\{-i\eta \log\left(\sin^2 \frac{\theta}{2}\right) + 2i\sigma_0\right\} \tag{4.24}$$

Where

$$\eta = \frac{\mu z z' e^2}{\hbar k} \tag{4.25}$$

μ is the reduced mass for the scattering system and σ_0 is the "zeroth Coulomb phase shift".

The author is unaware of a closed form expression for $f_c(\theta)$ off the energy-shell. This term could be treated in 1st Born Approximation. Then

$$f_c(\theta) \sim \frac{-2\mu z z' e^2}{\hbar^2 (\vec{k}_1 - \vec{k}_2)^2} = -\frac{2\mu z z' e^2}{\hbar^2 (k_1^2 + k_2^2 - 2k_1 k_2 \cos\theta)} \tag{4.26}$$

The last term in (4.22) vanishes on the mass-shell. Off the mass-shell it is not clear how it behaves, but it probably remains small and can be neglected.

It remains now to put the second term in (4.22), $\langle \chi_f^{(-)} | V_1 | \psi_i^{(+)} \rangle$, the "nuclear" term into a calculable form by making a partial wave expansion. The potential used will be local but ℓ dependent. The nuclear part of the T matrix is

$$T_N = \langle \chi_f^{(-)} | V_N | \psi_i^{(+)} \rangle \tag{4.27}$$

Expanding χ_f and ψ_i in partial waves:

$$\psi_i^{(+)}(k_i) = 4\pi \sum_{\ell'} i^{\ell'} e^{i\sigma_{\ell'}(k_i)} u_{\ell'}(k_i, r) Y_{\ell'}^{0\,*}(\hat{k}_i) Y_{\ell'}^{0}(\hat{r}) \tag{4.28}$$

$$\chi_f^{(+)}(k_f) = 4\pi \sum_{\ell} i^{-\ell} e^{i\sigma_\ell(k_f)} F_\ell(k_f, r) Y_\ell^m(\hat{k}_f) Y_\ell^{m\,*}(\hat{r}) \tag{4.29}$$

where the k_i direction has been taken as the z axis of a spherical polar coordinant system. The σ_ℓ (k)'s are "Coulomb phase shifts" and the F_ℓ are the "Regular Coulomb Waves". U_ℓ is the solution to the Schrodinger equation for the full potential minus a <u>point</u> Coulomb potential.

Using (4.28) and (4.29),

$$T_N = 16\pi^2 \sum_{\ell\ell' m} \int i^{\ell' - \ell} e^{i(\sigma_{\ell'}(k_i) + \sigma_\ell(k_f))} u_{\ell'}(k_i, r) V_\ell(r) F_\ell(k_f, r) \times Y_{\ell'}^{0\,*}(\hat{k}_i) Y_\ell^m(\hat{k}_f) \int Y_\ell^{m\,*}(\hat{r}) Y_{\ell'}^0(\hat{r})\, d\hat{r} \tag{4.30}$$

The integral over r yields $\delta_{\ell\ell'} \cdot \delta_{m0}$ and

$$T_N = 16\pi^2 \sum_{\ell} \int e^{i[\sigma_\ell(k_i) + \sigma_\ell(k_f)]} u_\ell(k_i, r) V_\ell(r) F_\ell(k_f, r)\, r^2 dr \times Y_\ell^{0\,*}(\hat{k}_i) Y_\ell^0(\hat{k}_f) \tag{4.31}$$

Now

$$Y_\ell^{0\,*}(k_i) Y_\ell^0(k_f) = \frac{(2\ell+1)}{4\pi} P_\ell(\cos\theta) \tag{4.32}$$

where θ is the center-of-mass scattering angle. Then

$$T_N = 4\pi \sum_\ell (2\ell+1) P_\ell(\cos\theta)\, e^{i(\sigma_\ell(k_f)+\sigma_\ell(k_i))} \times \int u_\ell(k_i,r)\, V_\ell(r)\, F_\ell(k_f,r)\, r^2 dr \tag{4.33}$$

If (4.33) is compared with the usual partial wave expansion for $f(\theta)$, the scattering amplitude on the mass-shell (with $k_f = k_i$), then

$$\frac{-\mu}{2\pi\hbar^2} T_N = f_N(\theta) = \frac{1}{ik} \sum_\ell (2\ell+1) P_\ell(\cos\theta)\left(e^{2i\delta_\ell}-1\right) e^{2i\sigma_\ell} \tag{4.34}$$

It is then obvious that on the mass-shell

$$\left(e^{2i\delta_\ell}-1\right) = \frac{-i\,4\mu k}{\hbar^2} \int u_\ell(k,r)\, V(r)\, F_\ell(k,r)\, r^2 dr \tag{4.35}$$

Thus on the mass-shell the formalism developed in this section can be used to calculate phase shifts.

The final step in calculating the cross sections is to symmetrize the scattering amplitudes, because in the final state the two particles are identical Bosons.*

Thus

$$\frac{d\sigma}{d\Omega}(\theta)_{\alpha-\alpha} = \left(\frac{\mu}{2\pi\hbar^2}\right)^2 \frac{k_f}{k_i} \left| T_N(\theta) + T_N(\pi-\theta) + \frac{2\pi\hbar^2}{\mu}\left[f(\theta) + f_c(\pi-\theta)\right]\right|^2 \tag{4.36}$$

where $T_N(\theta)$ is given by (4.27) and $f_c(\theta)$ is given by (4.24) or by (4.26). The odd ℓ partial waves in T_N vanish under the symmetrization operation above and the even ℓ waves are doubled leaving

$$\frac{d\sigma}{d\Omega}(\theta)_{\alpha-\alpha} = \left(\frac{\mu}{2\pi\hbar^2}\right)^2 \frac{k_f}{k_i} \left| 2T_N(\theta)_{\ell\ \text{even}} + \frac{2\pi\hbar^2}{\mu}\left[f_c(\theta) + f_c(\pi-\theta)\right]\right|^2 \tag{4.37}$$

---

*Whether or not symmetrization is needed in the initial state is not clear, since the particles are not identical (one is off the mass-shell). However the final state is the one detected, and there the particles are identical.

To calculate T_N, a computer code was assembled largely out of subroutines from SCAT4, the U.C.L.A. optical model code (M61) as modified by Dr. Ian McCarthy. These generated $u_\ell(k)$, $F_\ell(k)$, and $\sigma_\ell(k)$. Further modifications were made by this author to generate $V_\ell(k)$ in the form described in Section 4.3.2. The integral in (4.33) was performed with the trapezoidal approximation.

4.3.2 The α-α Potential

To calculate the α-α cross section in the T-matrix formalism presented in Section 4.3.1, a potential is needed. Darriulat et al. (D65) give a phenomenological α-α potential devised to fit α-α scattering phase shifts up to 120 MeV. This was the potential selected for use. This potential has the following form:

$$V_{\alpha\alpha}(r) = U_1\left[1+\exp\left(\frac{r-r_1}{a_1}\right)\right]^{-1} - \left\{U_2+iW\right\}\left[1+\exp\left(\frac{r-r_2}{a_2}\right)\right]^{-1} + V_c(r) \tag{4.38}$$

This potential is basically a Woods-Saxon potential with an inverted Woods-Saxon repulsive core. The Coulomb potential was fixed as that for a uniformly charged sphere of 2 fm. radius. The imaginary well strength W was fixed at 5 MeV for energies greater than 40 MeV and zero for energies smaller than 40 MeV. The potential is ℓ dependent and includes partial waves up to $\ell = 8$.

To test the program described in Section 4.3.1 this potential was used to calculate on-mass-shell phase shifts δ_ℓ according to (4.35). In the process it was discovered that although the Darriulat potential did indeed provide good fits to the real parts of the δ_ℓ's, it was seriously in error in the imaginary parts. Not only were the imaginary phase shifts wrong, but their "balance" was wrong so that some of the partial waves were too weak or too strong and the cross sections had the wrong shape as well as the wrong magnitude.

TABLE 4.1

ℓ	U_1	r_1	a_1	U_2	W	r_2	a_2
0	150 MeV	1.65 fm	0.1 fm	9.2 MeV	3.5 MeV	3.72 fm	0.4
2	150	1.63	0.05	16	6.0	3.55	0.3
4	220	1.2	0.05	71	11.5	2.48	0.46
6				50	8.0	2.96	0.53
8				110	35.0	2.00	0.65

Parameters for the phenomenological α-α potential used for the calculation of off-mass-shell cross sections.

To attempt to correct for this deficiency, the imaginary well strength W was adjusted for each partial wave. It was found that this did not seriously affect the real phase shifts as remarked in (D65). It was not possible, however, to fit the imaginary phase shifts well at all energies with this procedure, indicating that the shape of the imaginary potential may be different from the one chosen in (D65). For the purposes of the present investigation, the imaginary well strengths were adjusted to give a reasonable fit to the imaginary phase shifts in the vicinity of 70 to 80 MeV. Table 4.1 lists the parameters actually used in (4.38) for the potential. Fig. 4.10 shows the experimental imaginary phase shifts from (D65) and those calculated for the potential in (4.38) with W = 5 MeV, 10 MeV, and the values listed in Table 4.1.

4.3.3 Results

In this section, some results will be presented from calculations using the formalism of Section 4.3.1 and the potential of Section 4.3.2. To give an overall view of the quality of the potential, Figure 4.11 shows the data from (D65) for bombarding energies of 53.4, 58.5, 63.9, 69.9, 77.6 and 99.6 MeV. Also shown are the cross sections generated by the potential (4.38) using the parameters in Table 4.1. The general behaviour of the data is reproduced in the cross sections from the potential, but the agreement is only qualitative. At 53.4 and 99.6 MeV the fit is rather poor, but at 69.9 and 77.6 MeV it is not too bad.

In view of the high accuracy of the off-mass-shell cross sections extracted in the earlier sections of this chapter, the fits with the potential to the free scattering data are not good enough to make a direct comparison with the $(\alpha,2\alpha)$ data. The calculations presented here will be exploratory,

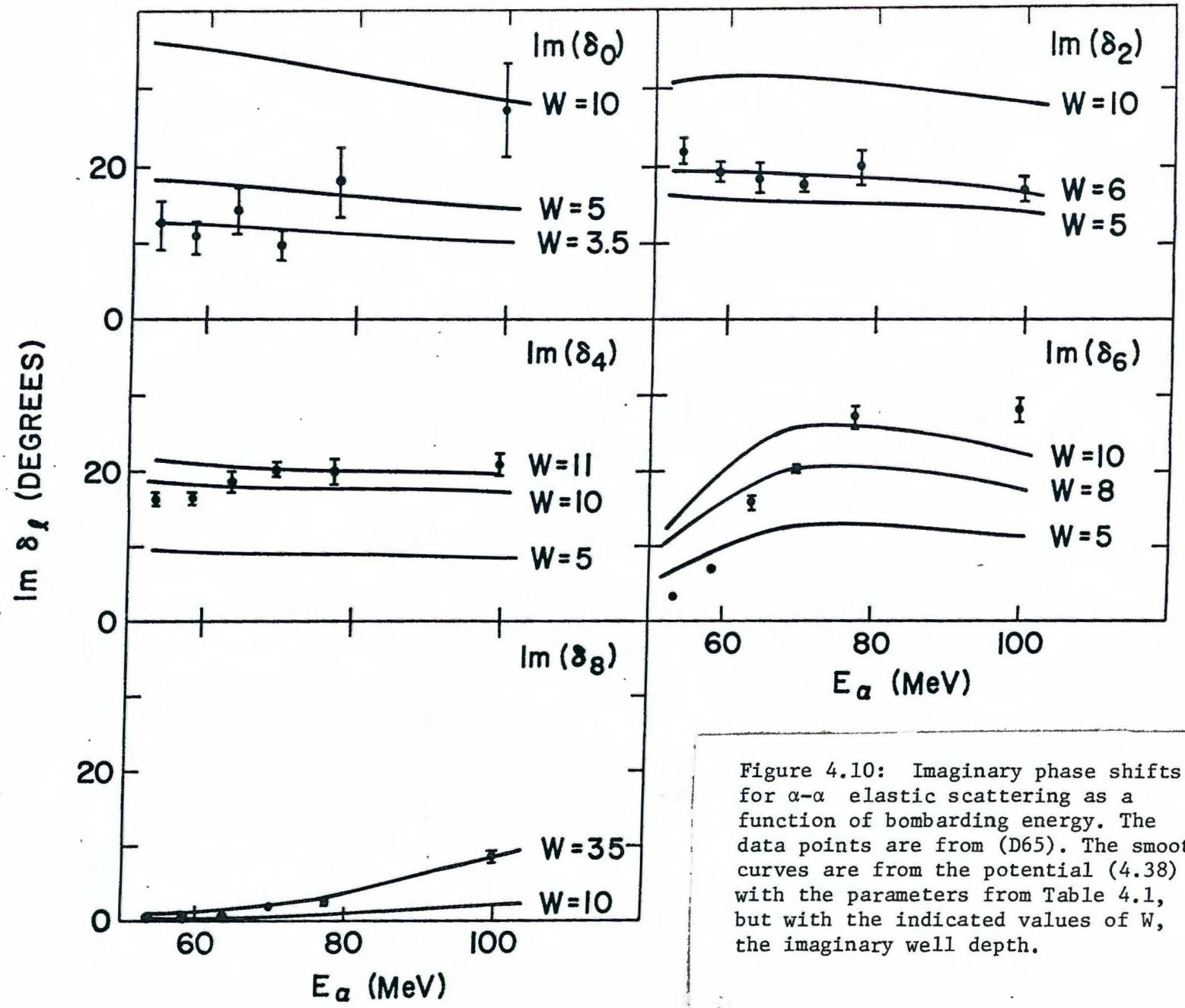

Figure 4.10: Imaginary phase shifts for α-α elastic scattering as a function of bombarding energy. The data points are from (D65). The smooth curves are from the potential (4.38) with the parameters from Table 4.1, but with the indicated values of W, the imaginary well depth.

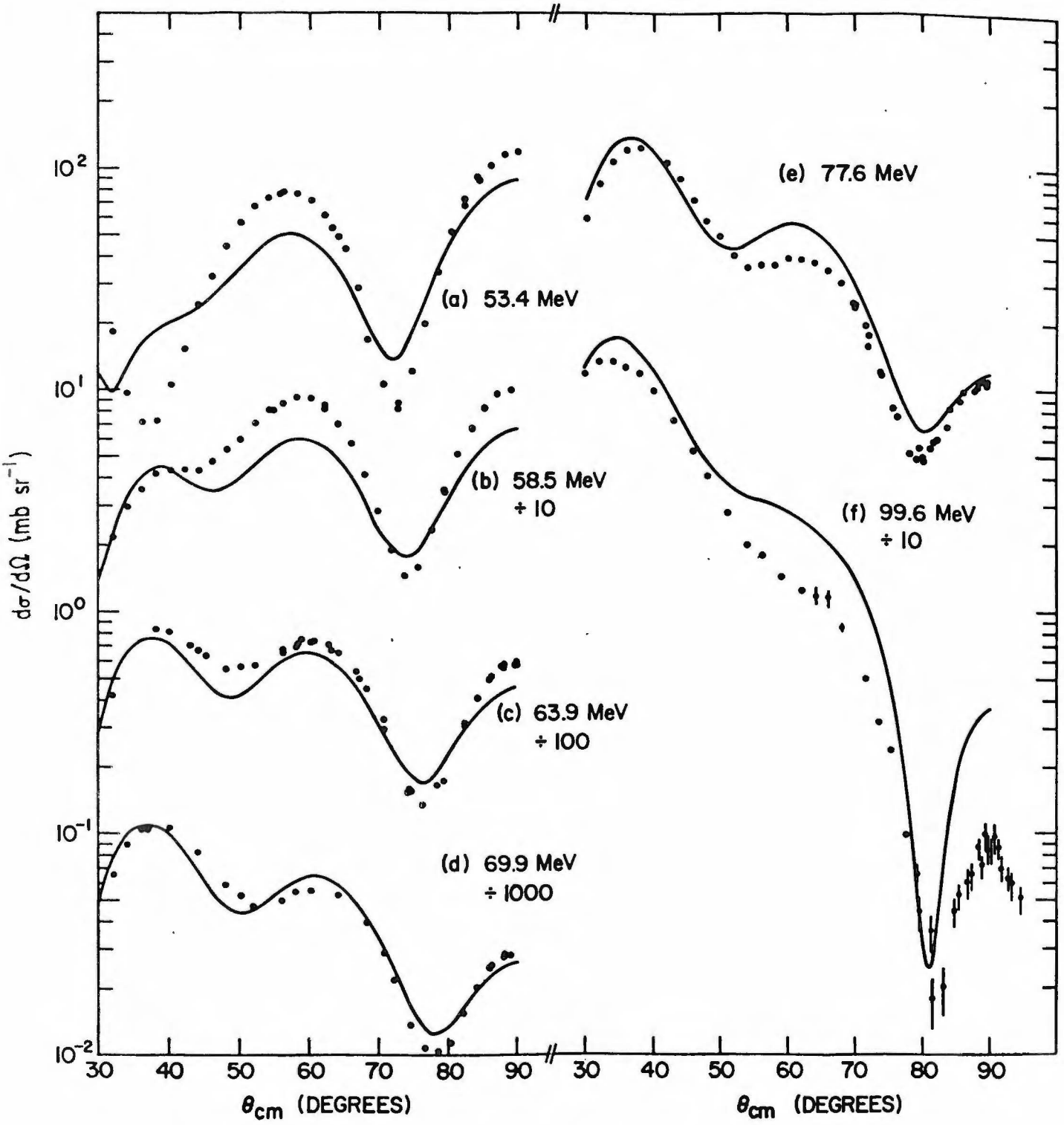

Figure 4.11: Differential cross sections for elastic α-α scattering in the center of mass system. The data points are from (D65). The smooth curves are from the potential (4.38) with the parameters from Table 4.1.

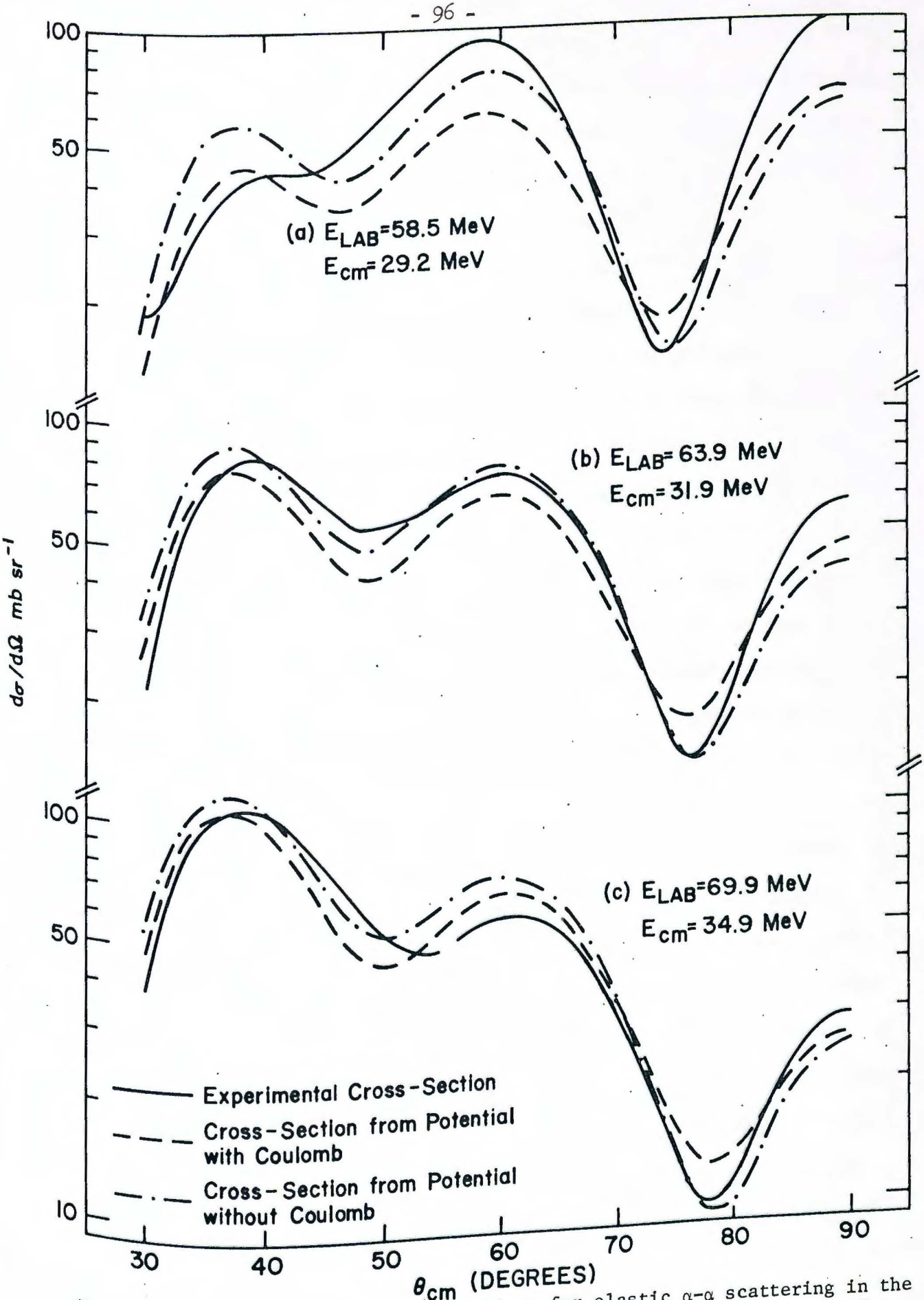

Figure 4.12: Differential cross sections for elastic α-α scattering in the center of mass system. The solid curves are smooth curves through the data of (D68). The broken curves are from the potential (4.38) with the parameters from Table 4.1, both with and without the Coulomb potential.

to find out which off-mass-shell effects are important. For actual fitting of the $(\alpha,2\alpha)$ data, it was felt (and the following discussion will justify that procedure) that interpolating the experimental α-α data from (D65) and using the E_f on-mass-shell approximation was more reliable.

Figure 4.12 shows the data from 58.4, 63.9 and 69.9 MeV again, together with cross sections calculated from the full potential (4.38) and cross sections from the potential (4.38) without the Coulomb potential. It is clear that neglecting Coulomb effects makes an error of about the same size as the discrepancy between the experimental data and the cross sections calculated from the full potential. Therefore, Coulomb effects will be left out completely in the calculations to follow.

When a better α-α potential becomes available, the approximations suggested in Section 4.3.1 for handling Coulomb effects off the mass-shell may be useful. It is worth noting, however, that the present on-mass-shell calculations show that approximating the exact Coulomb amplitude (4.24) with Born Approximation (4.26) makes less than a three percent error in the on-shell cross sections for $\theta_{cm} > 45^{o}$.

In Section 4.31 it was mentioned that there are two cross sections one can define off the mass shell. The first, which will be called $(d\sigma/d\Omega)_I$ is calculated from $\langle \phi_f | V | \psi_i^{(+)} \rangle$. Figure 4.13 shows the off-mass-shell cross section $(d\sigma/d\Omega)_I$ calculated for E_i = 35.1 MeV in the center of mass system (70.3 MeV in the laboratory system). The values of $\Delta E \equiv E_i - E_f$ chosen are 0.0, 1.47, 3.0, 6.0, 9.0 and 12.0 MeV. This figure shows that the cross section decreases rapidly at all angles as ΔE increases. Figure 4.14 shows the same calculations as in Figure 4.13, but with the cross sections all normalized to unity at $\theta_{cm} = 90^{o}$. This figure emphasizes the way in which the angular dependence of $(d\sigma/d\Omega)_I$ depends on ΔE.

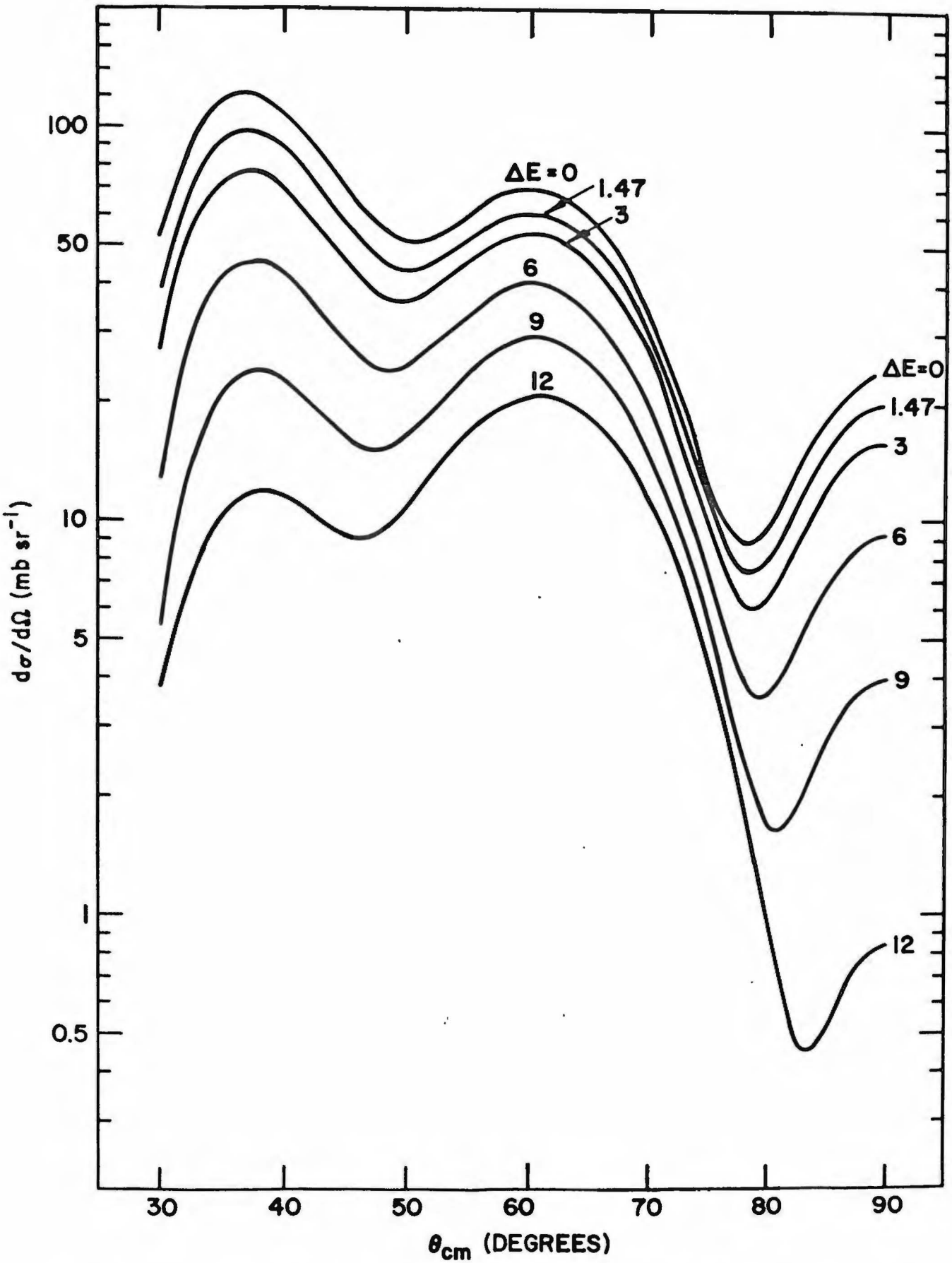

Figure 4.13: Off-mass-shell differential α-α cross sections $(d\sigma/d\Omega)_I$ in the center of mass system. The bombarding energy is 70.3 MeV. $\Delta E = E_i - E_f$ is the distance off the mass-shell. The cross sections are from the potential (4.38) without the Coulomb potential, using the parameters from Table 4.1.

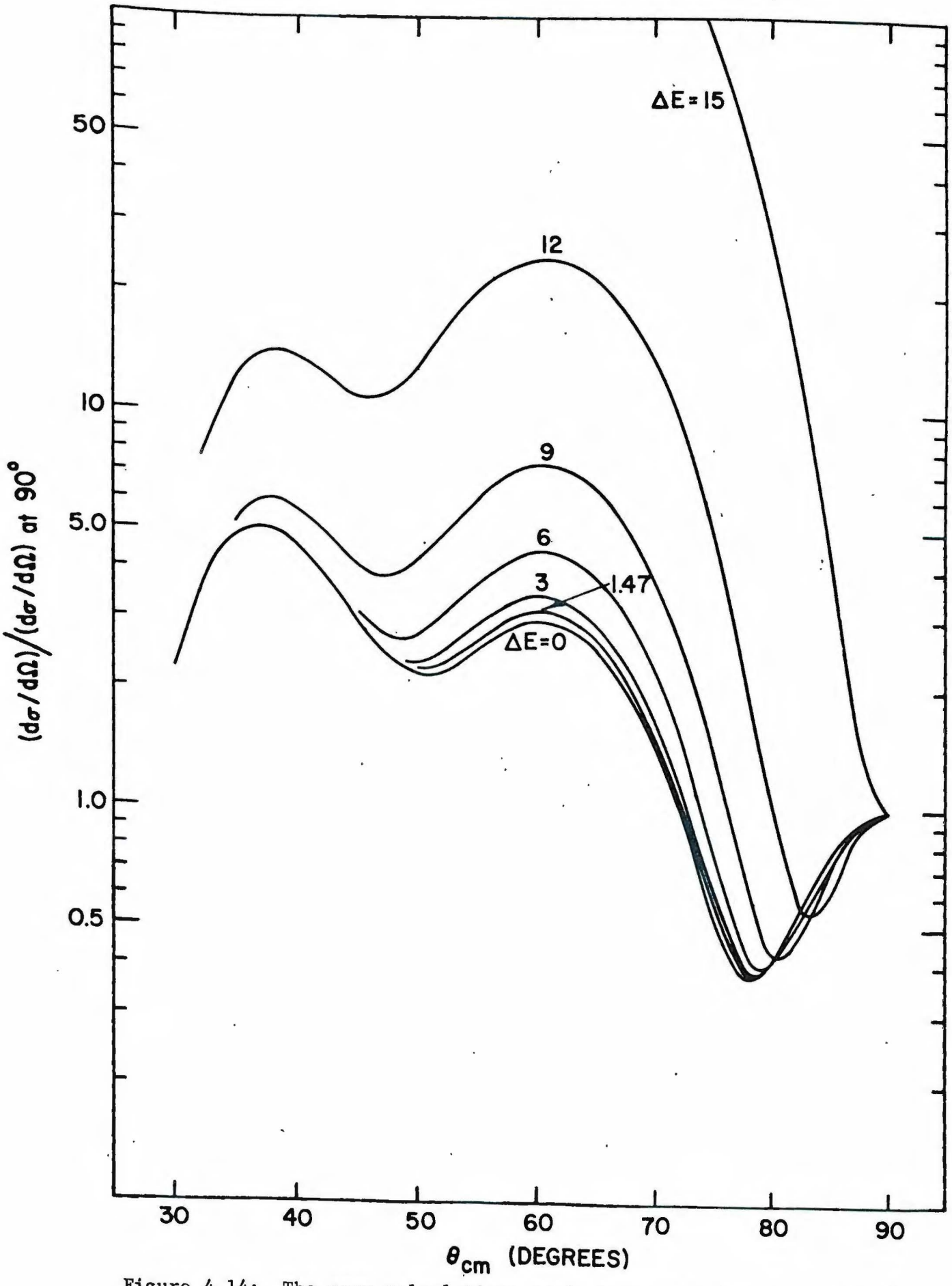

Figure 4.14: The same calculations as in Figure 4.13, but normalized to unity at $\theta_{cm} = 90^{o}$.

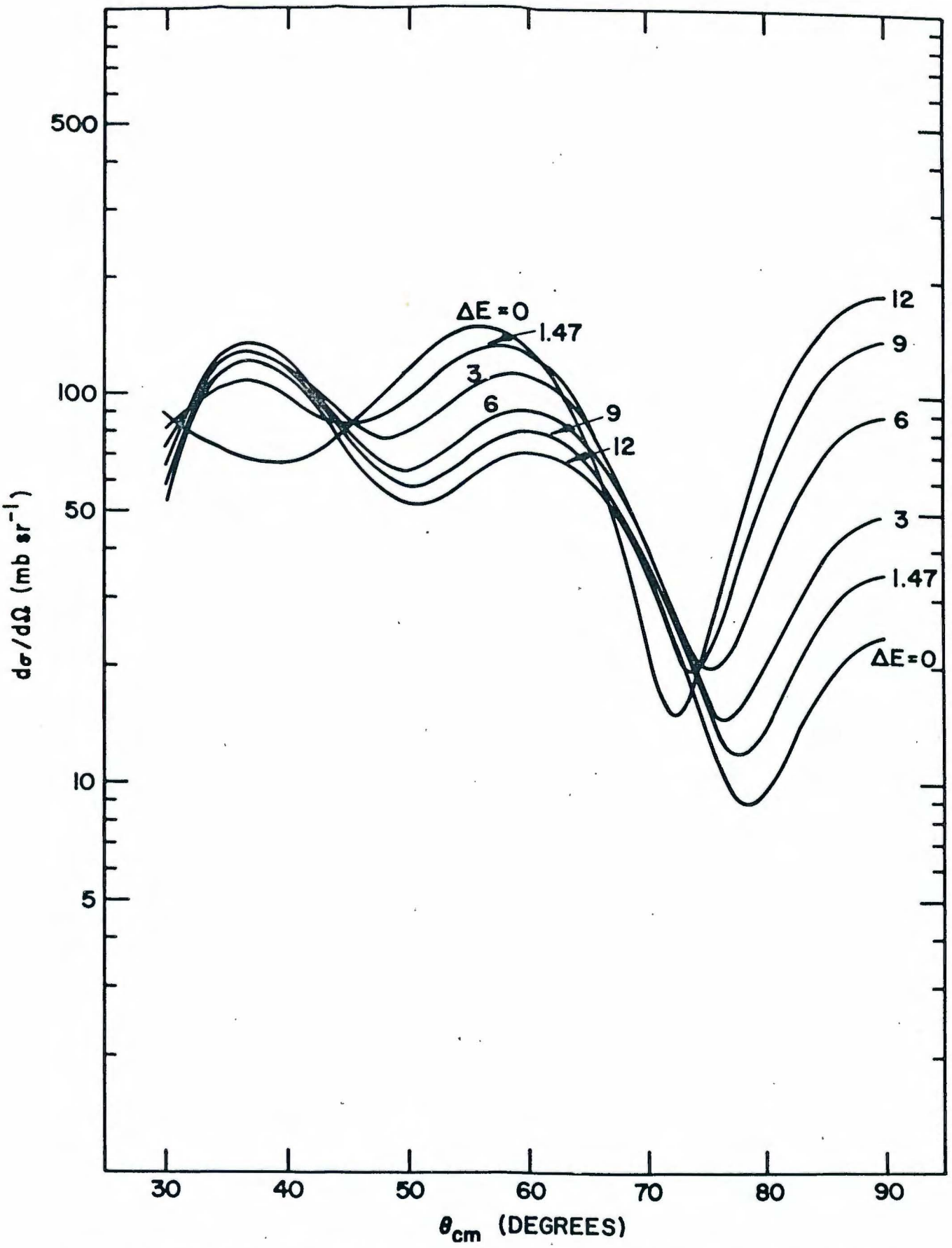

Figure 4.15: Off-mass-shell differential α-α cross sections $(d\sigma/d\Omega)_{II}$ in the center of mass system. The bombarding energy is 70.3 MeV. $\Delta E = E_i - E_f$ is the distance off the mass-shell. The cross sections are from the potential (4.38) without the Coulomb potential, using the parameters from Table 4.1.

The second off-mass-shell cross section one can define which will be called $(d\sigma/d\Omega)_{II}$ is calculated from $\langle \psi_f^{(-)} | V | \phi_i \rangle$. Figure 4.15 shows $(d\sigma/d\Omega)_{II}$ for E_i = 35.1 MeV in the center of mass (70.3 MeV in the lab) at several values of ΔE. As ΔE increases, the cross section $(d\sigma/d\Omega)_{II}$ also increases rapidly at $\theta_{cm} = 90^{\circ}$. Figure 4.16 shows the same calculation as in Figure 4.15 but normalized to unity at $\theta_{cm} = 90^{\circ}$. It will be seen from Figures 4.14 and 4.16 that for small ΔE the shape of the angular distribution is a more rapidly varying function of ΔE in the $(d\sigma/d\Omega)_{II}$ calculations than in the $(d\sigma/d\Omega)_I$ calculations. This may be seen by comparing the curves for ΔE = 0, 1.47 and 3 MeV in the two figures. This is not surprising, since the effect of the potential in the T matrix is at least partially felt through $\psi_i^{(+)}$ or $\psi_f^{(-)}$. In $(d\sigma/d\Omega)_{II}$, $\psi_f^{(-)}$ is changing in energy, whereas $\psi_i^{(+)}$ in $(d\sigma/d\Omega)_I$ is not.

We next consider whether $d\sigma/d\Omega(E_i)$ and $d\sigma/d\Omega(E_f)$, the previously suggested on-mass-shell approximations to the off-mass-shell cross section, are related to $(d\sigma/d\Omega)_I$ and $(d\sigma/d\Omega)_{II}$. One finds that they are indeed closely related. For the calculations of $(d\sigma/d\Omega)_I$ in Figures 4.13 and 4.14 the on-shell approximation $d\sigma/d\Omega(E_i)$ is just the calculation for ΔE = 0. Thus in Figure 4.14 one can see that for ΔE = 1.47 MeV and 3 MeV $(d\sigma/d\Omega)_I$ has almost exactly the same shape as $d\sigma/d\Omega(E_i) = (d\sigma/d\Omega)_I$ for ΔE = 0. This observation should be tempered with remembrance that Figure 4.13 shows that the magnitude of $(d\sigma/d\Omega)_I$ varies rapidly with changing ΔE, even though the shape remains roughly constant for small ΔE.

Figure 4.17 shows a comparison of $(d\sigma/d\Omega)_{II}$ and $d\sigma/d\Omega(E_f)$ for ΔE = 1.47, 3.0 and 6.0 MeV. In each comparison $(d\sigma/d\Omega)_{II}$ and $d\sigma/d\Omega(E_f)$ have been normalized to the same value at $\theta_{cm} = 90^{\circ}$. Again the two methods agree very closely as far as the shape of the angular distributions is concerned, but their absolute

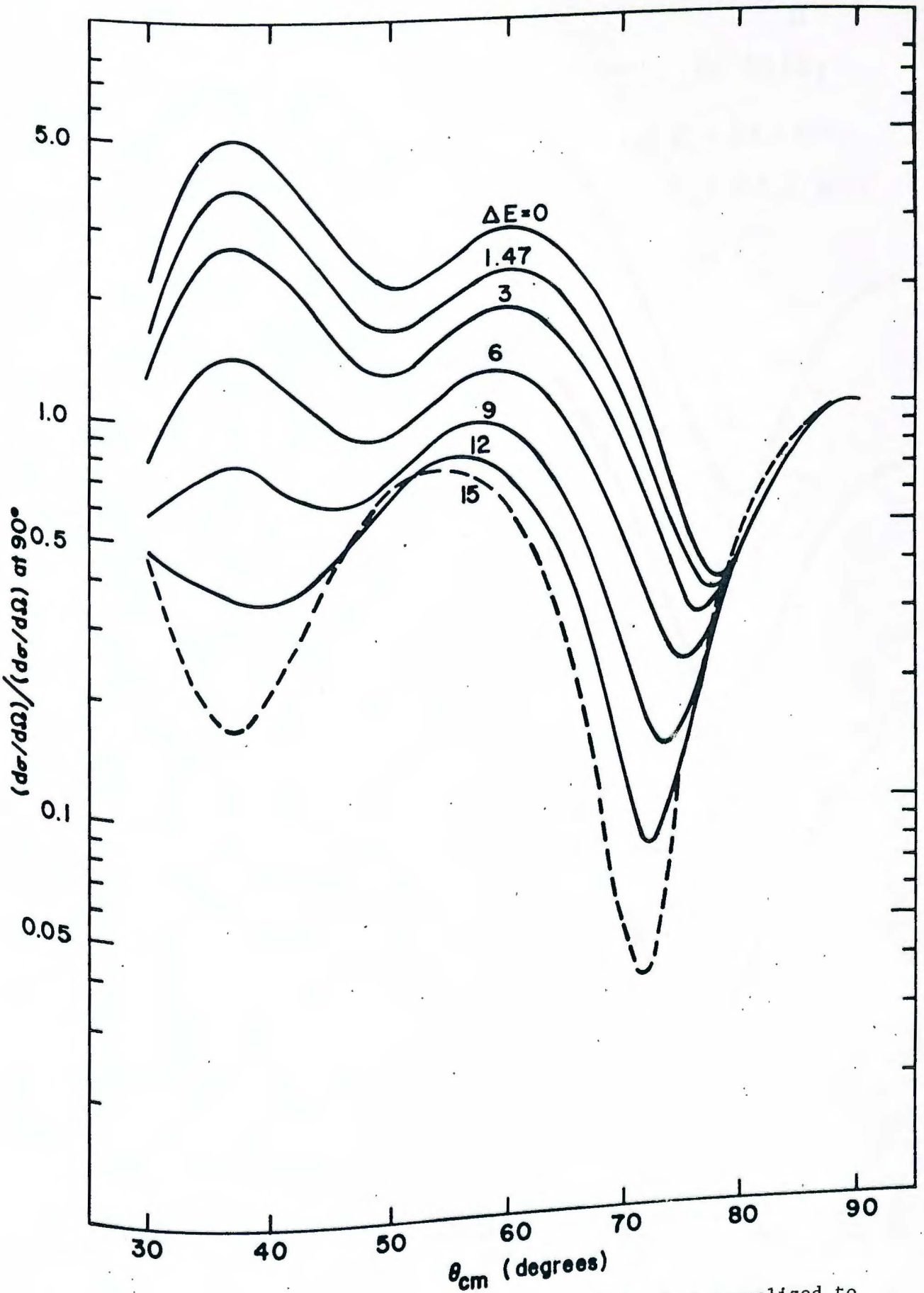

Figure 4.16: The same calculations as in Figure 4.15, but normalized to unity at $\theta_{cm} = 90°$.

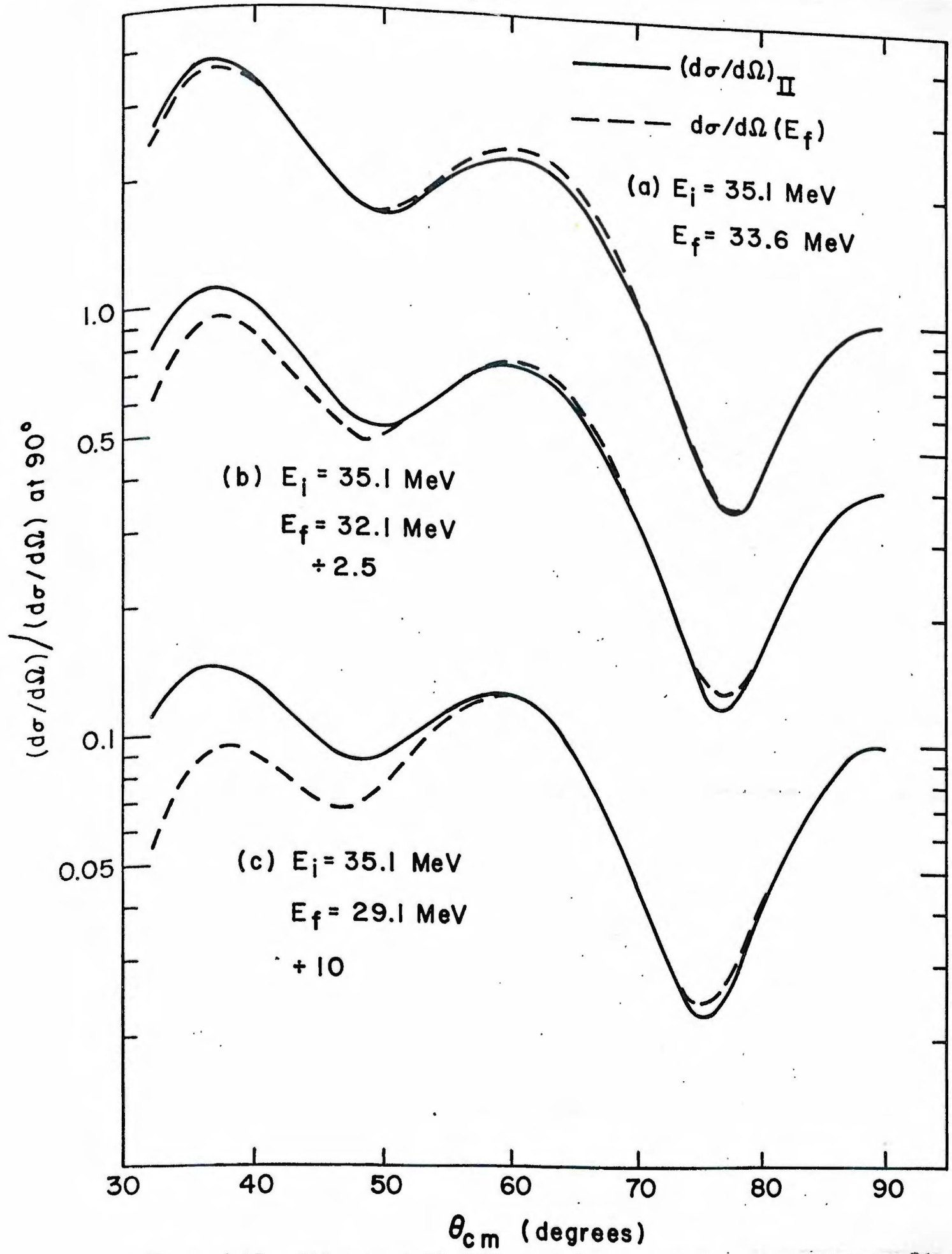

Figure 4.17: Off-mass-shell differential α-α cross sections $(d\sigma/d\Omega)_{II}$ and the on-mass-shell approximation $d\sigma/d\Omega(E_f)$ for $\Delta E \equiv E_i - E_f$ = 1.47, 3, and 6 MeV. The bombarding energy is 70.3 MeV. $(d\sigma/d\Omega)_{II}$ and $d\sigma/d\Omega(E_f)$ are normalized to the same value at $\theta_{cm} = 90^o$.

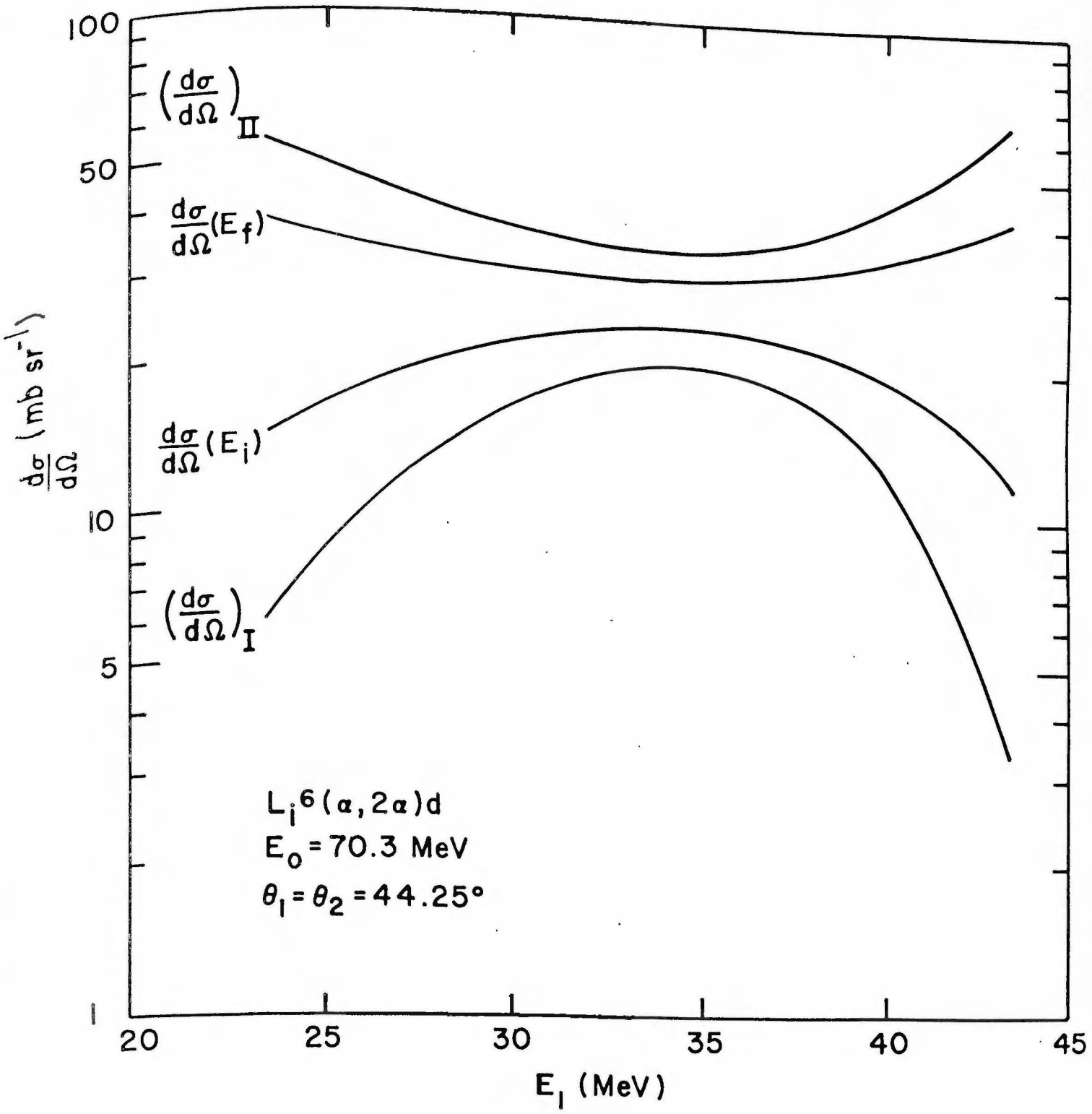

Figure 4.18: The off-mass-shell α-α cross sections $(d\sigma/d\Omega)_I$ and $(d\sigma/d\Omega)_{II}$ and their on-mass-shell approximations $d\sigma/d\Omega(E_i)$ and $d\sigma/d\Omega(E_f)$, displayed as a function of E_1 for the projected energy spectrum of the $Li^6(\alpha,2\alpha)d$ reaction at 70.3 MeV with $\theta_1 = \theta_2 = 44.25°$. These cross sections are from the potential (4.38) without the Coulomb Potential, using the parameters from Table 4.1.

magnitudes are different.

In both the comparison of $d\sigma/d\Omega(E_i)$ with $(d\sigma/d\Omega)_I$ and the comparison of $d\sigma/d\Omega(E_f)$ with $(d\sigma/d\Omega)_{II}$ it was found that the methods are by no means equivalent for predicting the absolute cross section. Figure 4.18 shows $(d\sigma/d\Omega)_I$, $(d\sigma/d\Omega)_{II}$, $d\sigma/d\Omega(E_i)$ and $d\sigma/d\Omega(E_f)$ for the energy spectrum with $\theta_1 = \theta_2 = 44.25^o$ and $E_o = 70.3$ MeV. These cross sections are all calculated from the potential (4.38) without the Coulomb part. The c.m. scattering angle θ_{cm}, is very close to 90^o for all parts of this energy spectrum, but as E_i varies, $\vec{q}$ and hence the distance from the mass-shell changes. In terms of $|\Phi(q)|^2$ to be extracted using these four cross sections, Figure 4.18 shows that analyzing the spectrum using $(d\sigma/d\Omega)_I$ would yield a broader and higher momentum distribution than using $d\sigma/d\Omega(E_i)$. Similarly, using $(d\sigma/d\Omega)_{II}$ would yield a narrower and smaller momentum distribution than $d\sigma/d\Omega(E_f)$. The magnitude of these differences is roughly 20 - 25% in normalization and about 2 MeV/c out of 30 MeV/c in the half width at half maximum of the momentum distribution. These differences are comparable with the experimental uncertainties in the present measurements.

In summary, for the shape of the angular distribution $(d\sigma/d\Omega)_I$ and $d\sigma/d\Omega(E_i)$ are closely equivalent, while $(d\sigma/d\Omega)_{II}$ and $d\sigma/d\Omega(E_f)$ are closely equivalent. The experimental data at $\vec{q} = 0$ shows a strong preference for $d\sigma/d\Omega(E_f)$ or its equivalent $(d\sigma/d\Omega)_{II}$. The uncertainty in absolute magnitude of the experimental data and the rather small range of values of q prevents a test of $(d\sigma/d\Omega)_{II}$ as opposed to $d\sigma/d\Omega(E_f)$. For the purposes of further analysis of the momentum wave function, the on-shell approximation $d\sigma/d\Omega(E_f)$ will be used. The distinction between $(d\sigma/d\Omega)_{II}$ and $d\sigma/d\Omega(E_f)$ might be important for the extraction of momentum wave functions for nuclei where the $(\alpha,2\alpha)$ reaction lies further off the mass-shell. In this respect Li^6

is probably a favorable case.

It should be mentioned that Balashov and Meboniya (B68) have previously formulated the $(d\sigma/d\Omega)_I$ and $(d\sigma/d\Omega)_{II}$ prescriptions for the $(\alpha,2\alpha)$ reaction. After comparing their theory with rather limited data on the $O^{16}(\alpha,2\alpha)C^{12}$, $C^{12}(\alpha,2\alpha)Be^8$, $Be^9(\alpha,2\alpha)He^5$, $Li^7(\alpha,2\alpha)t$ and $Li^6(\alpha,2\alpha)d$ reactions at 25 MeV, they expressed a preference for $(d\sigma/d\Omega)_{II}$. They did not investigate the difference between $(d\sigma/d\Omega)_{II}$ and $d\sigma/d\Omega(E_f)$ but their conclusions appear compatible with the present ones.

CHAPTER 5

THE MOMENTUM DISTRIBUTION FOR α-PARTICLES IN Li^6

The somewhat remarkable success of the Plane Wave Impulse Approximation in analyzing the $\vec{q} = 0$ data encourages us to use P.W.I.A. to extract an experimental momentum distribution for α's in Li^6. The procedure is to divide the measured cross sections by the product of the kinematic factor (1.7) and the on-mass-shell cross section obtained using the E_f approximation:

$$|\Phi(q_b)|^2 = (d\sigma/d\Omega_1 d\Omega_2 dE_1) \times (\text{Kinematic Factor})^{-1} \times (d\sigma/d\Omega)^{-1}_{d-d} \tag{5.1}$$

This results of this procedure are presented in Section 5.1.

It is desirable to compare the experimental momentum distribution with theoretical ones. In Sections 5.2 and 5.3, relative motion wave functions for the α-particle and the deuteron in Li^6 are discussed for the oscillator shell model and the Nuclear Cluster Model. In both cases these wave functions are found to be inadequate in their treatment of the asymptotic properties of the α-d interaction. Therefore, in Section 5.4 a cluster model wave function with the correct asymptotic properties for the α-d interaction is developed. In Section 5.5 this cluster model wave function is compared with the experimental momentum distribution. Because of a gross discrepancy between the predictions of P.W.I.A. and the experimental results, it will be found that the P.W.I.A. must be abandoned. A simple procedure is introduced involving a cutoff in the cluster wave function, and this is found to correct the discrepancy. Then in Section 5.6, both the theoretical and the experimental momentum distributions are compared with the momentum distributions determined in the other experiments on Li^6. This comparison is made in the framework of the P.W.I.A. with a cutoff.

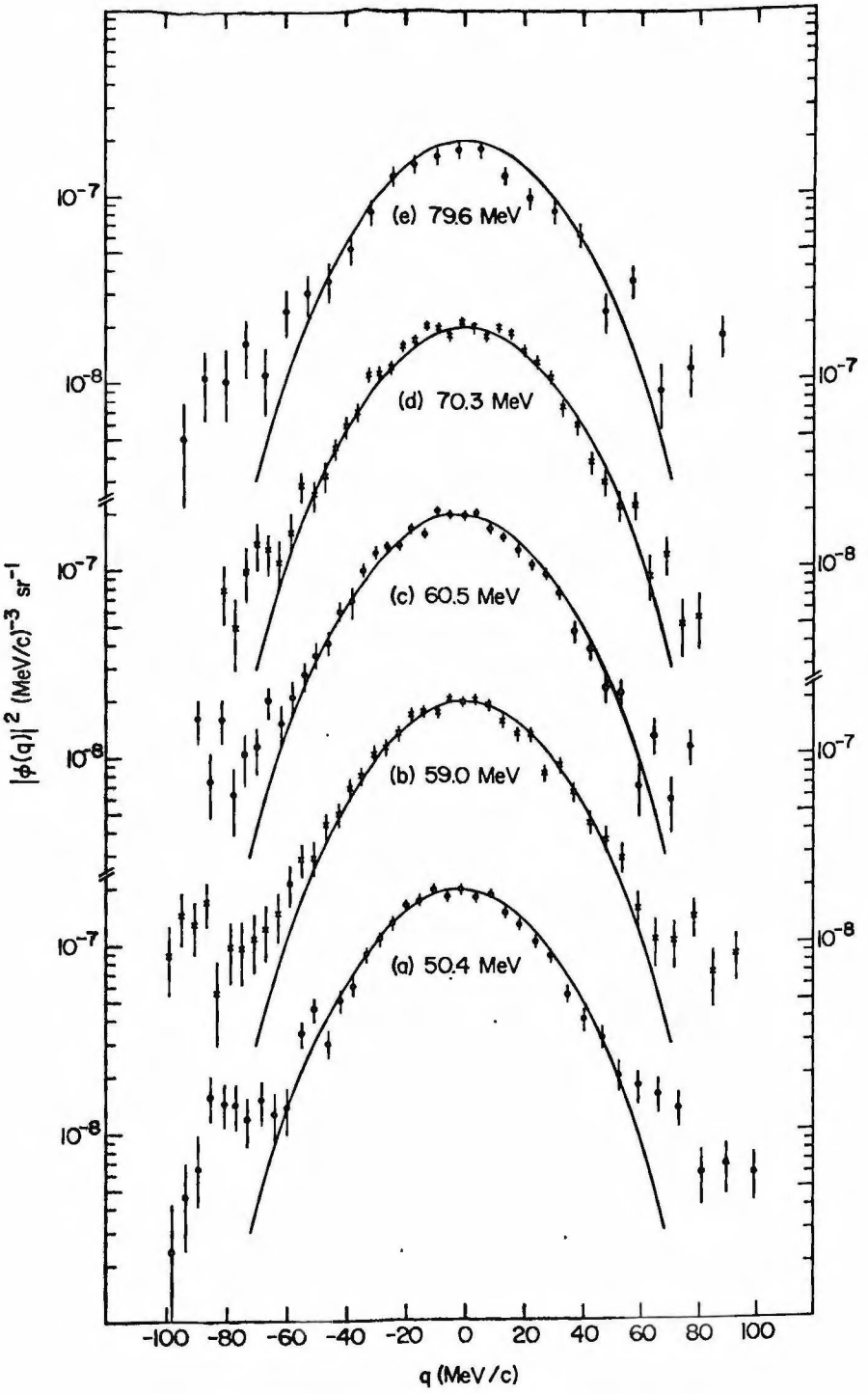

Figures 5.1 (a) - (e): The momentum distributions $|\Phi(q)|^2$ extracted from the $Li^6(\alpha,2\alpha)d$ reaction at 50.4, 59.0, 60.5, 70.3 and 79.6 MeV. These momentum distributions were extracted using $d\sigma/d\Omega(E_f)$.

Section 5.1 The Experimental Momentum Distribution For α's in Li^6

To extract $|\Phi(q)|^2$, the spectra with $\theta_1 = \theta_2 \sim 44^\circ$ were chosen. There are five of these spectra, one for each bombarding energy. Fig. 5.1 shows the momentum distributions $|\Phi(q)|^2$ derived with $d\sigma/d\Omega(E_f)$. The lines show a calculated momentum distribution to be discussed later. The point here is that the line is the same for each set of data, indicating that the shapes of all five momentum distributions are very similar and the values of $|\Phi(\vec{q} = 0)|^2$ are all consistent. Note that the spectra for 60.5 and 50.4 MeV are shifted by approximately 2 MeV/c from the $\vec{q} = 0$ point. This discrepancy is within the experimental error discussed in Section 3.2. It could have been caused by the beam spot being misaligned by 1/32 of an inch, causing an error in the measured angles of $\sim 0.2^\circ$. This will not seriously affect the measurement of the width of the momentum distribution.

These five spectra were also analyzed using $\frac{d\sigma}{d\Omega}(E_i)$. Table 5.1 summarizes some of the parameters of the extracted momentum distributions, using both E_i and E_f. The discrepancy between the value of $|\Phi(\vec{q} = 0)|^2$ for the 50.4 MeV data and the other four spectra when analyzed with E_i is rather substantial. It is clear from Table 5.1 that E_f gives a more consistent picture of $|\Phi(q)|^2$ than E_i. This conclusion agrees with the analysis of off-mass-shell cross sections in Chapter 4. For futher studies of $|\Phi(q)|^2$ in this thesis $d\sigma/d\Omega(E_f)$ will be used.

One could, of course, extract experimental momentum distributions from other data than the $\theta_1 = \theta_2 \sim 44^\circ$ spectra. Each experimental point in each spectrum yields $|\Phi(q)|^2$ for that point. In particular, every spectrum containing $\vec{q} = 0$ could in principle be used to extract a complete $|\Phi(q)|^2$, but it was pointed out in Section 4.2 that many spectra are not quite symmetric about $\vec{q} = 0$, and hence would yield an asymmetric momentum distribution.

TABLE 5.1

	$\|\phi(q)\|^2$ EXTRACTED USING $d\sigma/d\Omega(E_f)$		
E_o	$\|\phi(0)\|^2$ $(MeV/c)^{-3}sr^{-1}$	F.W.H.M.	F.W. 1/10 M.
50.4 MeV	$(1.9\pm0.2)\times10^{-7}$	58 ± 2 MeV/c	113 ± 5 MeV/c
59.0	$(2.1\pm0.2)\times10^{-7}$	58 ± 2	117 ± 5
60.5	$(2.0\pm0.2)\times10^{-7}$	58 ± 2	114 ± 5
70.3	$(2.0\pm0.2)\times10^{-7}$	59 ± 2	112 ± 5
79.6	$(1.8\pm0.3)\times10^{-7}$	57 ± 3	120 ± 10
	$\|\phi(q)\|^2$ EXTRACTED USING $d\sigma/d\Omega(E_i)$		
E_o	$\|\phi(0)\|^2$ $(MeV/c)^{-3}sr^{-1}$	F.W.H.M.	F.W. 1/10 M.
50.4 MeV	$(4.4\pm0.4)\times10^{-7}$	61 ± 2 MeV/c	109 ± 5 MeV/c
59.0	$(2.5\pm0.25)\times10^{-7}$	61 ± 2	120 ± 5
60.5	$(2.6\pm0.25)\times10^{-7}$	62 ± 2	119 ± 5
70.3	$(2.9\pm0.3)\times10^{-7}$	62 ± 2	122 ± 5
79.6	$(2.6\pm0.25)\times10^{-7}$	60 ± 2	129 ± 10

Table 5.1 Parameters of the experimental $|\phi(q)|^2$, extracted from spectra with $\theta_1 = \theta_2 \sim 44°$, using both $d\sigma/d\Omega(E_i)$ and $d\sigma/d\Omega(E_f)$.

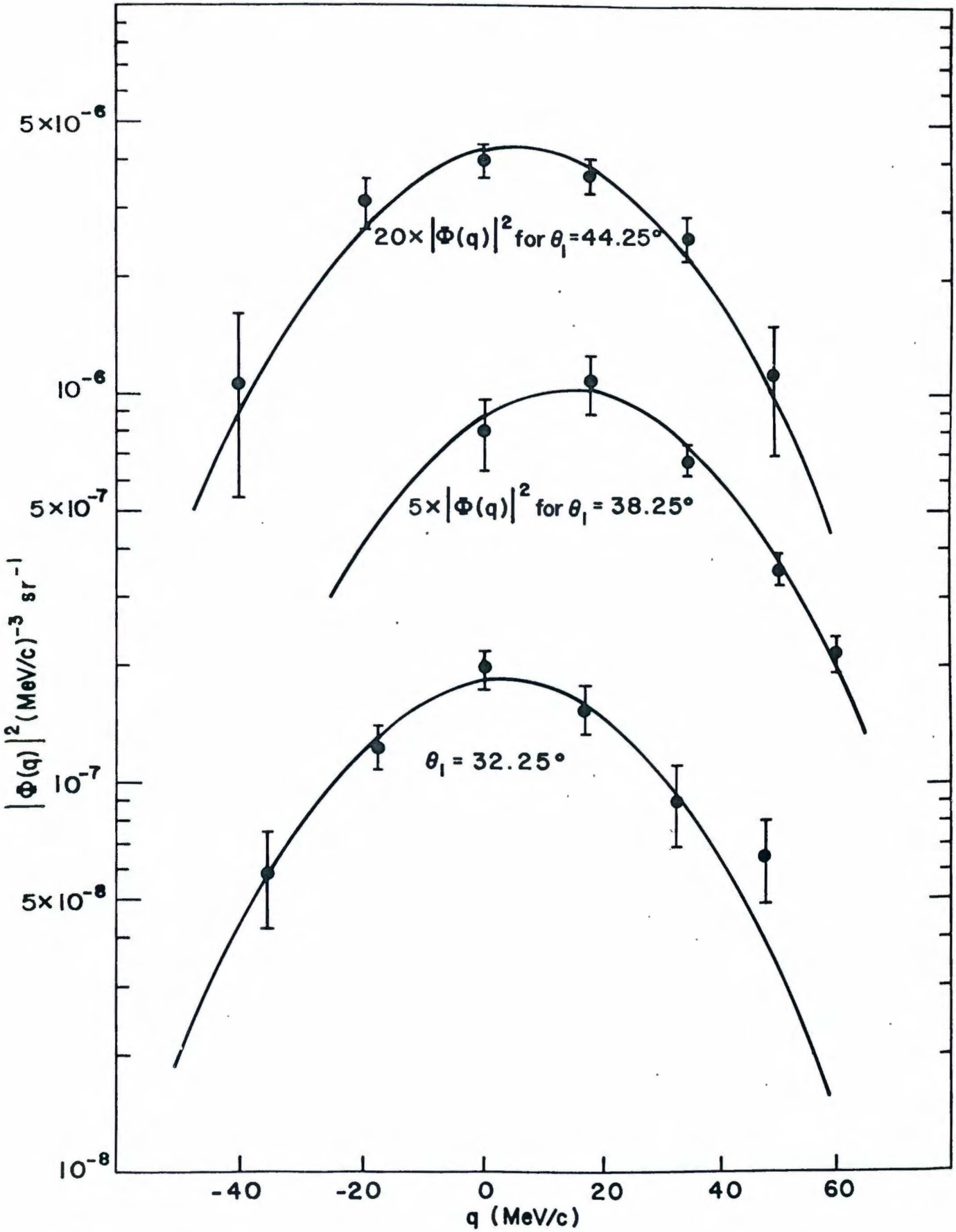

Figure 5.2: Momentum distributions extracted from angular correlation data from the $Li^6(\alpha,2\alpha)d$ reaction at 70.3 MeV. The three angular correlations had θ_1 fixed at 44.25°, 38.25°, and 32.25° respectively. For each angle pair the point of minimum q was used. Positive q corresponds to $\theta_{12} < 88.5°$; negative q corresponds to $\theta_{12} > 88.5°$.

Because these asymmetries cannot exist in the spectra with $\theta_1 = \theta_2$, one avoids the problems caused by these asymmetries by choosing only spectra with $\theta_1 = \theta_2$.

In the data from this experiment there are a number of angular correlations in the 70.3 MeV data which yield essentially independent measurements of $|\Phi(q)|^2$. Although the data does not cover a very large range of $\vec{q}$ it is still useful to extract $|\Phi(q)|^2$ from the data that does exist. There are six spectra with $\theta_1 = 44.25^\circ$, five spectra with $\theta_1 = 38.25^\circ$, and six spectra with $\theta_1 = 35.25^\circ$. For these 17 spectra $|\Phi(q)|^2$ was extracted for the point in each spectrum where $|\vec{q}|$ was a minimum. This data is presented in Fig. 5.2. This analysis was performed using $d\sigma/d\Omega(E_f)$. The curves, which will be discussed more in Section 5.4, are the same curves which were used to fit the momentum distributions from the five $\theta_1 = \theta_2 \sim 44^\circ$ spectra. It has been necessary to displace the curves towards "positive" q by varying amounts to fit the data. The normalizations are all within the range of $|\Phi(o)|^2 = (2.0 \pm 0.2) \times 10^{-7}$ $(MeV/c)^{-3} sr^{-1}$ determined for E_f in the measurement of $|\Phi(q)|^2$ from the five $\theta_1 = \theta_2 \sim 44^\circ$ spectra. Aside from the shifts necessary to fit the data, the momentum distributions extracted in this manner are consistent with that from the five spectra analyzed earlier in this section. The shifts, however, represent a departure from P.W.I.A. and indicate the inadequacy of such a simple model of the reaction mechanism.

It will be noted that the shift in the curves necessary to fit the data in Fig. 5.2 is largest for the $\theta_1 = 38.25^\circ$ spectrum. The angle involved is close to the minimum in the free α-α angular distribution. Whether this is significant is not clear, but at this angle the cross sections are correspondingly smaller and the effects of secondary processes may be correspondingly more serious.

Section 5.2 Shell Model Calculations

5.2.1 Introduction

In this section the wave function for that part of Li^6 which overlaps (α + d) will be calculated, using a shell model description of Li^6. Only one configuration for Li^6, $(1s)^4(1p)^2$, is included, and the filled 1s shell is considered to be an inert, spherically symmetric core, which provides a central field for the two valence particles. Under these conditions, anti-symmetrization of the two valence nucleons with respect to the nucleons in the core can be ignored. The properties of the low-lying levels of Li^6 are, in this model, determined by the p-shell nucleons alone.

Li^6 has been found to be close to the L-S coupling limit (no l·s force). Using L-S coupling notation ($^{2T+1,2S+1}L_J$) the allowed states which can be constructed out of two p-shell nucleons are:

$$^{13}S_1,\ ^{11}P_1,\ ^{13}D_{1,2,3},\ ^{31}S_0,\ ^{33}P_{0,1,2},\ ^{31}D_2\ . \qquad (5.2)$$

These states are all degenerate in the absence of interactions between the two valence nucleons.

The introduction of a residual central interaction between the two p-shell nucleons, splits the levels of different L and T, but since the interaction is diagonal in the L-S representation, J, L, S, and T remain good quantum numbers. The introduction of an l·s force and/or tensor forces will mix some levels with the same J and T leaving J, T and parity as the remaining good quantum numbers. The only states consistent with the experimental assignment of T = 0 and J = 1 for the ground state of Li^6 are $^{13}S_1$, $^{11}P_1$, and $^{13}D_1$.* Thus we may describe the wave function of the ground

---

*The parity of the Li^6 ground state is positive, but this is true of all states of the $(1s)^4\ (1p)^2$ configuration.

state of Li^6 as

$$\psi_{Li^6} = a_1 |{}^{13}S_1\rangle + a_2 |{}^{11}P_1\rangle + a_3 |{}^{13}D_1\rangle \tag{5.3}$$

The coefficients a_i can be determined by perturbation theory, i.e. diagonalization of the interaction matrix for the exchange forces, spin-orbit force and perhaps the tensor force. A large number of people have performed such calculations for Li^6 (I53, E53, R54, T54, A55, K56, M56, F57, S57, P58, B66).

All of these calculations have been very consistent in two respects, namely:

$$|a_1|^2 > 0.95$$
$$|a_1|^2 \gg |a_2|^2 \gg |a_3|^2 \tag{5.4}$$

With respect to the size of a_3, it has been shown by Brennan and his coworkers (A55) and (P58) that the quadrupole moment of Li^6, which is very small ($.80 \pm .08$ e mb) requires that a_3 be very small ($< .03$). Given the size of $|a_1|^2$ it would seem reasonable to consider the ground state of Li^6 to be $^{13}S_1$, i.e. L = 0 as well as T = 0 and J = 1.

5.2.2 Calculations

The overlap of the wave function for two p-shell nucleons of Li^6 with a real deuteron will now be calculated.

The central potential for the p-shell is taken to be an harmonic oscillator well.

$$V(r) = \tfrac{1}{2} K r^2 \tag{5.5}$$

Introducing the following parameters simplifies things:

$$\omega = \sqrt{K/m} \quad ; \quad \nu = \frac{m\omega}{\hbar} = \frac{\sqrt{km}}{\hbar} \tag{5.6}$$

Then

$$V(r) = \frac{m\omega^2}{2} r^2 = \frac{\hbar^2 \nu^2}{2m} r^2 \tag{5.7}$$

With this definition of ν, the eigenfunctions are

$$\psi_{n\ell m}(\vec{r}) = Y_{\ell m}(\hat{r})\, u_{n\ell}(\nu r^2) \tag{5.8}$$

where

$$u_{n\ell}(\nu r^2) = \left[\frac{\nu^{3/2}}{\pi^{1/2}} \frac{(2\ell+2n-1)!!}{(n-1)!} 2^{\ell-n+3}\right]^{1/2} \times (\nu r^2)^{\ell/2} e^{-\frac{\nu r^2}{2}} \sum_{k=0}^{n-1} \frac{(n-1)!}{(n-1-k)!\,k!} \frac{(-2\nu r^2)^k}{(2\ell+2k+1)!!} \tag{5.9}$$

This has the normalization conditions:

$$\int_{\text{all space}} \psi_{n\ell m}(\vec{r})\, d^3r = 1$$

$$\int_0^\infty u_{n\ell}(r)\, r^2 dr = 1 \tag{5.10}$$

The Li^6 wave function is a product of two such 1p wave functions, coupled to J = 1, L = 0, S = 1. Using the transformation brackets of Brody and Moshinsky (B60), this product can be turned into a sum of products of relative and center-of-mass wave functions. If n_1, l_1, m, n_2, ℓ_2, and m_2 are the quantum numbers of the two p-shell wave functions and n, l, m, N, L, and M, those of the relative and center-of-mass wave functions, and λ and μ are the angular momentum and its projection for the total system.

$$|n_1\ell_1 m_1,\ n_2\ell_2 m_2;\ \lambda\mu\rangle = \sum_{n\ell NL} \langle n\ell,\ NL;\ \lambda\,|\,n_1\ell_1, n_2\ell_2;\ \lambda\rangle \times |n\ell m,\ NLM;\ \lambda\mu\rangle \tag{5.11}$$

Where

$$|n_1\ell_1 m_1,\ n_2\ell_2 m_2\ \lambda\mu\rangle = [Y_{\ell_1 m_1}(\hat{r}_1)\, Y_{\ell_2 m_2}(\hat{r}_2)]\, u_{n_1\ell_1}(\nu r_1^2)\, u_{n_2\ell_2}(\nu r_2^2)$$

$$|n\ell m,\ NLM,\ \lambda\mu\rangle = [Y_{\ell m}(\hat{r})\, Y_{LM}(\hat{R})]\, u_{n\ell}\left(\frac{\nu r^2}{2}\right) u_{NL}(2\nu R^2)$$

$$\vec{r} = \vec{r}_1 - \vec{r}_2\ ; \qquad \vec{R} = (\vec{r}_1 + \vec{r}_2)/2$$

$$\vec{\lambda} = \vec{\ell}_1 + \vec{\ell}_2 = \vec{l} + \vec{L}$$

$$\mu = m_1 + m_2 = m + M \tag{5.12}$$

TABLE 5.2

$n_1\ell_1$	$n_2\ell_2$	λ	$n\ell$	NL	ρ	1
1p	1p	0	1s	2S	6	$1/\sqrt{2}$
			1p	1P		0
			2s	1S		$-1/\sqrt{2}$
1p	1p	1	1p	1P	6	1
1p	1p	2	1s	1D	6	$1/\sqrt{2}$
			1p	1P		0
			1d	1S		$-1/\sqrt{2}$

Table 5.2 Moshinsky Transformation Brackets for the product of two 1p-shell oscillator wave function from (B60). Note that the definitions used here for n_1, n_2, n and N are greater by unity than those of (B60), hence ρ is greater by 4.

and μ is the projection of $\vec{\Lambda}$. The transformation bracket $\langle n\ell, NL; \lambda | n, \ell_1 n_2 \ell_2; \lambda \rangle$ is independent of μ, so there are no magnetic quantum numbers included in it. There are additional selection rules based on energy conservation and parity:

$$(2n_1 + \ell_1) + (2n_2 + \ell_2) = (2n + \ell) + (2N + L) \equiv \rho,$$
$$(-1)^{\ell_1 + \ell_2} = (-1)^{\ell + L}. \tag{5.13}$$

The transformation brackets relevant to the Li^6 ground state are given in Table 5.2. Using the convention that the orbital angular momentum quantum number for ℓ and L will be designated by lower and upper case type, respectively, the Li^6 ground state wave function can be written as follows:

$$\psi_{Li^6} = \frac{a_1}{\sqrt{2}} |1s, 2S\rangle - \frac{a_1}{\sqrt{2}} |2s, 1S\rangle + a_2 |1p, 1P\rangle$$
$$+ \frac{a_3}{\sqrt{2}} |1d, 1S\rangle + \frac{a_3}{\sqrt{2}} |1s, 1D\rangle \tag{5.14}$$

As mentioned previously, a_3 has been shown to be very small, because of the small quadrupole moment of Li^6. Thus the last two terms in (5.14) can be ignored. The deuteron contains no $\ell = 1$ components, so the third term in (5.14) can be neglected. Then, with a_1 approximated by unity, one gets

$$\psi_{Li^6} \sim \frac{1}{\sqrt{2}} |1s, 2S\rangle - \frac{1}{\sqrt{2}} |2s, 1S\rangle \tag{5.15}$$

It should be noted that while (5.15) is a very good approximation indeed for the present studies because of the extreme smallness of a_3 and the lack of $\ell = 1$ in the deuteron, it will not be a good approximation for all purposes.

Now that the relative wave function appropriate to Li^6 has been determined, the overlap with a deuteron can be calculated. A Hulthén wave function will be used for the deuteron, with parameters taken from (M58):

$$\psi_d = B\left(e^{-\alpha r} - e^{-\beta r}\right)/r$$
$$\alpha = 0.232 \text{ fm}^{-1}, \quad \beta = 1.202 \text{ fm}^{-1}, \quad B = \left(\frac{2\alpha\beta(\alpha+\beta)}{(\alpha^2-\beta^2)}\right)^{1/2} = .9195 \tag{5.16}$$

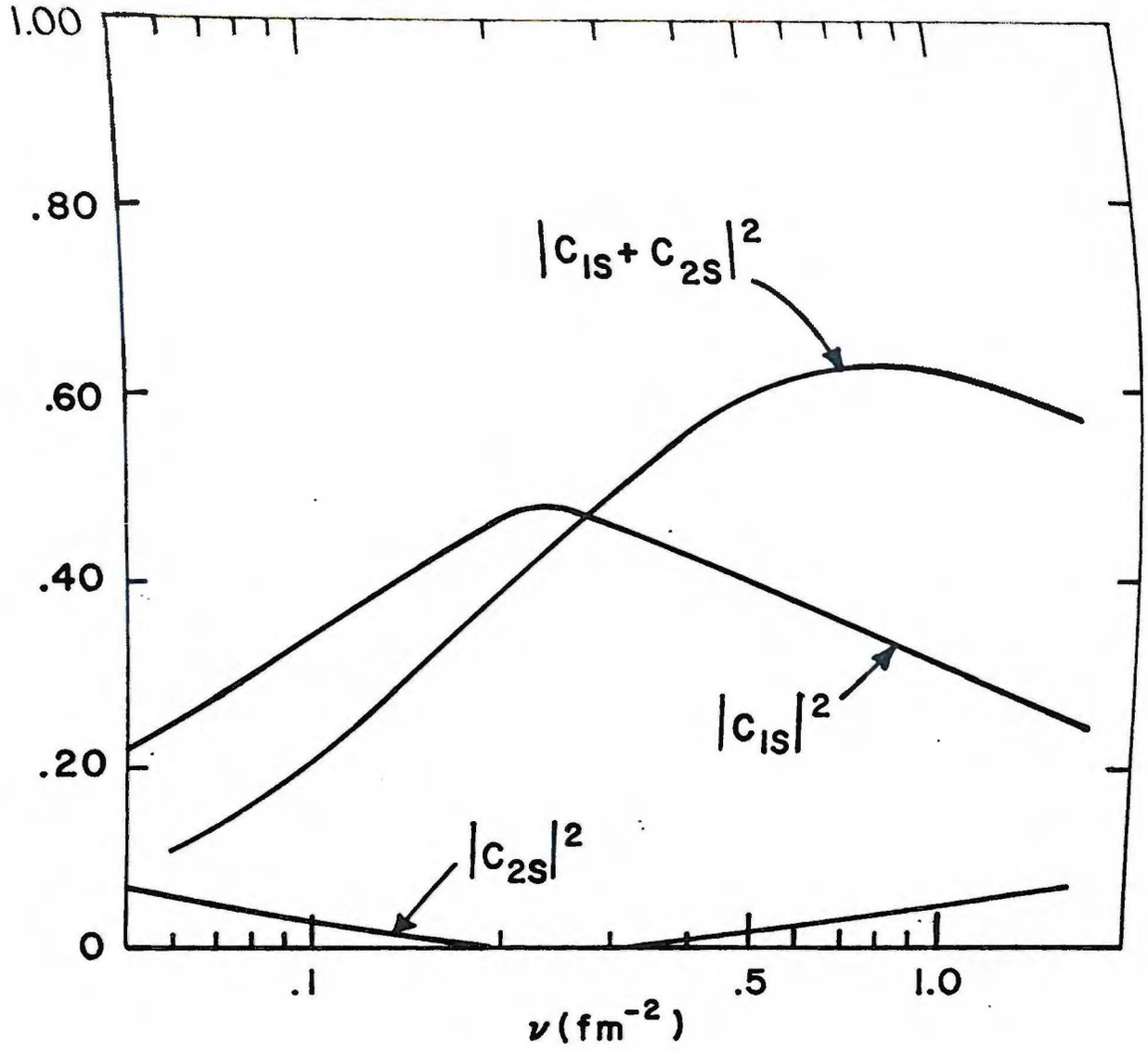

Figure 5.3: $|C_{1S}|^2$, $|C_{2S}|^2$, and $|C_{1S} + C_{2S}|^2$ as a function of ν, the oscillator size parameter. $\sqrt{2}$ C_{1S} is the overlap of a Hulthén wave function with a 1S oscillator wave function. $\sqrt{2}$ C_{2S} is the overlap of a Hulthén wave function with a 2S oscillator wave function.

The 1s and 2s relative wave functions are:

$$u_{1s}\left(\frac{\nu r^2}{2}\right) = \left(\frac{\nu}{2}\right)^{3/4} \frac{2}{\pi^{1/4}}\, e^{-\frac{\nu r^2}{4}}$$

$$u_{2s}\left(\frac{\nu r^2}{2}\right) = \left(\frac{\nu}{2}\right)^{3/4} \frac{6^{1/2}}{\pi^{1/4}}\, e^{-\frac{\nu r^2}{4}} \left[1 - \frac{\nu}{3} r^2\right] \qquad (5.17)$$

The overlap integrals are:

$$C_{1s} = \frac{1}{\sqrt{2}} \int_0^\infty u_{1s}\, \psi_d\, r^2 dr = \left(\frac{\nu}{2}\right)^{3/4} \frac{2^{1/2} B}{\pi^{1/4}} \int_0^\infty (e^{-\alpha r} - e^{-\beta r})\, e^{-\frac{\nu r^2}{4}}\, r\, dr$$

$$C_{2s} = \frac{-1}{\sqrt{2}} \int_0^\infty u_{2s}\, \psi_d\, r^2 dr = \left(\frac{\nu}{2}\right)^{3/4} \frac{3^{1/2} B}{\pi^{1/4}} \int_0^\infty (e^{-\alpha r} - e^{-\beta r})\, e^{-\frac{\nu r^2}{4}} \left[1 - \frac{\nu r^2}{3}\right] r\, dr \qquad (5.18)$$

where ν has been left as a variable. $|C_{1s}|^2$, $|C_{2s}|^2$, and the total overlap $|C_{1s} + C_{2s}|^2$ are displayed as a function of ν in Fig. 5.3. It is seen that the total overlap reaches a maximum of approximately 63% in the vicinity of $\nu = .75$ fm^{-2}, but with a broad range of ν, say .5 fm^{-2} to 1.5 fm^{-2}, giving nearly the same value. The parameter ν is not, of course, a free parameter, since it is usually adjusted to fit the energy level spectrum of Li^6. In (H68) a best fit to the Li^6 spectrum was calculated using the Hamada-Johnson potential for an effective interaction. The value of ν for their "best fit" was = .312 fm^{-2}. This value will be taken as the correct one. Then

$$|C_{1s}|^2 = .44 \;;\; |C_{2s}|^2 = .0025 \;;\; |C_{1s} + C_{2s}|^2 = .51 \qquad (5.19)$$

This choice implies that the center of mass wave function for the component which looks like a deuteron is almost all 2s.

For our purposes it is necessary to have the wave function, not for the center-of-mass motion of the deuteron, but for the relative motion of the deuteron and the center-of-mass of 1s shell nucleons. For convenience, these 1s nucleons will be called an α particle. Thus it is the "α-d" relative wave function which is desired. The α-d separation distance will be called $\mathcal{R} = \frac{3}{2}R$. If we define $A = \frac{8}{9}\nu$, then

$$\psi_{\alpha d} = u_{2s}(2\nu R^2) = u_{2s}\left(\tfrac{8}{9}\nu R^2\right) = u_{2s}(AR^2)$$

$$= \frac{6^{1/2} A^{3/4}}{\pi^{1/4}} e^{-\frac{AR^2}{2}} \left[1 - \tfrac{2}{3} A R^2\right] \qquad (5.20)$$

5.2.3 Deficiencies of the Shell Model Calculations.

There are several deficiencies in the shell model calculations presented in the previous sections. Firstly, although an interaction between the two p-shell nucleons was invoked to produce the splitting of the originally degenerate levels of Li^6, this result was used only to pick out which L-S coupling state made the major contribution to the Li^6 ground state. The residual interaction was completely ignored in the calculation of the overlap integrals, although it clearly must be responsible for the binding of Li^6, given that He^5 and Li^5 are unbound. This type of deficiency is, of course, common to most perturbation theory calculations. Although the binding energies and energy level spacings may be very good, the wave functions can still be poor approximations to reality. Thus, although a fairly realistic wave function was used for the deuteron, the Li^6 ground state wave function was not very realistic. Had a more realistic Li^6 wave function been used, however, the calculations would have been more difficult.

A second deficiency is that only the overlap of a deuteron and the p-shell nucleons has been calculated. There is thus the implicit assumption of the identity of the closed 1s shell and an α-particle. This is clearly only an approximation.

Thirdly, because of the choice of an oscillator well, the wave function (5.20) does not have the right "binding energy" tail $\frac{e^{-\beta R}}{R}$ (neglecting Coulomb effects) where

$$\beta = \sqrt{\frac{2\mu E_B}{\hbar^2}} \qquad (5.21)$$

μ is the α-d reduced mass, and E_B = 1.47 MeV is the binding energy of Li^6 for breakup into an α plus a deuteron.

Section 5.3 The Cluster Model

The possibility of nucleon clustering in nuclei is clearly suggested by the binding energies of light nuclei. He^4 nuclei, or alpha particles, are bound by about 20 MeV. Be^8 is actually slightly unbound with respect to decay into two alpha particles. C^{12} and O^{16} require rather large energies for breakup involving single nucleons, but small energies for breakup into 3 or 4 alphas, respectively.

These obvious suggestions of clustering led many investigators in the 1950's to try quite simple calculations of nuclear properties using cluster wave functions with point α-particles. In many respects, however, these early approaches to clustering failed to explain nuclear properties satisfactorily. The considerable success of the shell model has led to the near abandonment of these early approaches. There is still, however a variety of problems, particularly in very light nuclei, where the success of the shell model has been limited. This has been especially true of Li^6. Therefore, during the past decade, a more realistic "Nuclear Cluster Model" (W58) has been developed. Excellent reviews of the Nuclear Cluster Model are given in (W66), (N65), (R68) and (H69).

The modern "Nuclear Cluster Model" is based on Wheeler's "resonating group" method. An expansion in a complete set of fully antisymmetrized cluster basis state must be capable of describing a nuclear state correctly. Then, for many purposes, it is possible just one or two members of this expansion may describe the relevant nuclear properties adequately. Which members of the expansion are important, often depends on the reaction being studied. The key difference between the modern approach and many of the earlier calculations, is the use of fully antisymmetrized many particle wave function, rather than point clusters.

It has also been found recently, that a high degree of overlap may exist between shell model wave functions and nucleon cluster wave functions. An example of this was seen in Section 5.2.2 where a simple oscillator shell model calculation gave a 51% overlap between the product of two 1p shell oscillator wave functions, and a Hulthén deuteron wave function. A good discussion of such calculations is given in (N65) and also in (R68).

In the description of the nuclear cluster model to follow, we consider only Li^6. The generalization of the formalism should be obvious, however. A good starting point is the oscillator cluster model. Here the cluster expansion is truncated to just one term, α plus deuteron with both clusters in their ground states. With just the α plus deuteron term, the Li^6 wave function is

$$\psi_{Li6} = A\left\{\psi_\alpha(1234)\,\chi_d(56)\,\Psi(\vec{R}_d - \vec{R}_d)\,\chi(1234,56)\right\} \tag{5.22}$$

Where

$$\begin{aligned}
\psi_\alpha &= \exp\left(-\frac{a}{2}\sum_{i=1}^{4}\rho_i^2\right)\\
\chi_d &= \exp\left(-\frac{b}{2}\sum_{j=5}^{6}\rho_j^2\right)\\
\vec{\rho}_i &= \vec{r}_i - \vec{R}_\alpha\,, \qquad \vec{\rho}_j = \vec{r}_j - \vec{R}_d\\
\vec{R}_\alpha &= \frac{1}{4}\sum_{i=1}^{4}\vec{r}_i\,, \qquad \vec{R}_d = \frac{1}{2}\sum_{j=5}^{6}\vec{r}_j
\end{aligned} \tag{5.23}$$

$\psi_\alpha(1234)$ and $\psi_d(56)$ are the internal wave functions of the α and the deuteron in their ground states. A is the antisymmetrization operator, $\Psi(\vec{R}_\alpha - \vec{R}_d)$ is the relative motion function and $\chi(1234,56)$ is a spin-charge function. For future convenience, the following definition is also made:

$$\vec{R} = \vec{R}_\alpha - \vec{R}_d \tag{5.24}$$

The angular part of the relative wave function $\Psi(\vec{R})$ is chosen to be $Y_{oo}(\hat{R})$ since the Li^6 ground state is assumed to be L = 0. It is now necessary

to chose the radial part of $\Psi(\vec{R})$ to be consistent with two oscillator quanta. This is to make the total number of oscillator quanta agree with the $(1s)^4\ (1p)^2$ shell model configuration. Two forms frequently considered are:

$$\Psi_1(R) \propto R^2 e^{-\frac{2}{3}cR^2} \tag{5.25}$$

$$\Psi_2(R) = u_{2s}\left(\tfrac{4}{3}cR^2\right) \propto \left[1 - \tfrac{8}{9}cR^2 e^{-\frac{2cR^2}{3}}\right] \tag{5.26}$$

The second function, Ψ_2, is a 2S oscillator function of the form (5.9) and is identical to the wave function (5.20) derived in the previous section, if $C = \frac{2}{3}\nu$. The first is of the same form as a 1D oscillator function, but it now multiplies $Y_{oo}(R)$. These two forms also have the property, that when a = b = c and the <u>full</u> antisymmetrization operation is carried out, they become identical with each other and with the <u>fully</u> antisymmetrized shell model wave function $|(1s)^4\ (1p)^2\ [42]\ L = 0\rangle$ (K68). For the case of Ψ_1 (5.25) the equivalence to $|(1s)^4\ (1p)^2\ [42]\ L = 0\rangle$ is demonstrated explicitly in (N65) and in Appendix C of (W66). Thus the oscillator cluster model and oscillator shell model yield identical fully antisymmetrized wave functions, when $a = b = c = \nu$, where ν is the oscillator parameter in 5.9. Note that the antisymmetrization here involves exchange between the clusters, whereas the calculations in Section 5.2 did not.

The oscillator cluster model has the advantage here that one need not restrict oneself to a = b = c. The "size parameters" in the exponentials may be treated as variational parameters. In calculations reported recently by Kudeyarov, et al. (K68), the size parameters were adjusted to fit the form factors of elastic Coulomb and elastic M1 electron scattering, and inelastic quadrupole ($1^+ \rightarrow 3^+$) electron scattering. These could all be fit moderately well using Ψ_1 and a value of the parameter X = c/a of approximately 0.3 or 0.4. X is called the "cluster isolation parameter" and a value of $X \ll 1$

indicates that the size of the "clusters" is generally much smaller than their separation. If $X \ll 1$ one might expect the effects of antisymmetrization, i.e. exchange of particles between the clusters, to be small. Indeed the results in (K68) show this. Significantly, their calculations also show that for the relative motion function, $\Psi_1(R)$ (5.25) is preferred to $\Psi_2(R)$ (5.26) for fitting the data mentioned above.

Using an oscillator relative wave function of the form 5.25, Tang, Wildermuth and Pearlstein (T61) have calculated energy level spacings for Li^6 using a Serber force. They find a somewhat larger value of X on the order of 0.7, but it would appear that their calculations are not very sensitive to X.

In general one need not restrict oneself to oscillator wave functions, and extensive variational calculations using multiparameter trial functions have been carried out by several authors: (S63), (T69). The problem of using the variational method, is that the calculations are not very sensitive to the long range behavior of $\Psi(R)$. The only published calculations to date which tried to obtain the correct r.m.s. charge radius for Li^6 are those in (S63), and the value they were seeking to match, 2.73 fm, is now out of date.

Most of the calculations of cluster wave functions mentioned above, therefore, do not give the relative motion function $\Psi(R)$ the correct asymptotic behavior, determined by the 1.47 MeV binding energy of Li^6 for breakup into an α plus a deuteron. It has been emphasized by D.F. Jackson (J67) that in determining spectroscopic factors, it is crucial to have the correct asymptotic tail. This may be doubly important for the $(\alpha,2\alpha)$ reaction, since α-particles are strongly absorbed in nuclear matter and the reaction may largely take place near the nuclear surface.

One solution to this problem, used by M. Jain (J69), was to join an exponential tail on to the cluster wave function of Schmidt et al. (S63),

by matching logarithmic derivatives. The matching radius is uniquely determined by this procedure. This procedure still neglects Coulomb effects, however, and these can have a considerable effect in the region of the nuclear surface.

Section 5.4 Cluster Model Calculations with a Phenomenological Potential

5.4.1 Introduction

In the previous two sections, wave functions for the relative α-d motion in the Li^6 ground state have been discussed for both the shell model and the Nuclear Cluster Model. Because the relative motion wave functions in both cases were oscillator states, the results suffer from a common deficiency, namely incorrect aymptotic behavior. For the $Li^6(\alpha,2\alpha)d$ reaction, which is likely to occur mainly in the nuclear surface, this is a severe deficiency indeed. For this reason, a cluster model calculation was undertaken which could account for several of the asymptotic properties of Li^6.

The basic approach here has been to use a phenomenological α-d potential. The cluster wave function is then obtained for a point α and a point deuteron by numerical integration of the Schrödinger equation. It was felt that full antisymmetrization would have little effect on these asymptotic properties (exchange between the clusters should be unimportant when they are well separated) and so antisymmetrization has been ignored. To partially compensate for the neglect of antisymmetrization, the form of the phenomenological potential was chosen to simulate the repulsive effect known to result from antisymmetrization. By this means the most important effect of antisymmetrization may have been introduced into the calculation.

The determination of the phenomenological potential will now be discussed. There have been several recent studies of the α-d interaction at center of mass energies up to approximately 20 MeV (M67), (D67), (M68), and in particular, phase shifts have been determined for several partial waves. It was required that the phenomenological potential should generate a reasonable fit to the S-wave scattering phase shifts. In addition, it was required

that the potential should have a bound S state at -1.47 MeV and that this bound state should have the correct r.m.s. charge radius, as determined by electron scattering experiments. The method for calculating the r.m.s. radius is discussed in Section 5.4.2.

There are several theoretical problems to the approach outlined above. First of all, since the percentage of α + d clustering in Li^6 is not very well known, it may be quite unrealistic to expect to get the correct r.m.s. charge radius, with only α + d structure included. Secondly, no distortion of the deuteron is allowed. Distortion almost certainly occurs, however, since at separations of less than 1.5 fm. the Coulomb repulsion between the α and the proton (in the deuteron), is greater than the binding energy of the deuteron, or Li^6 for that matter. Yet for all separation distances, the calculations performed below assume the shape of the deuteron is the same as a free deuteron. Thirdly, the computer codes used for calculating phase shifts from a phenomenological potential treat the α and the deuteron as point particles, but the r.m.s. radius calculation in Section 5.4.2 takes into account the finite size of both. Thus there would seem to be a basic inconsistency in approach. It should be pointed out, however, that to the extent that both the r.m.s. charge radius and the phase shifts are asymptotic properties of the α-deuteron interaction, the two approaches are not drastically inconsistent. Likewise, the effects of distortion of the deuteron will be less important at larger separation distances.

5.4.2 Calculation of the r.m.s. Charge Radius of Li^6 with a Cluster Wave Function

The cluster wave function for Li^6 will be written as

$$\Psi(\vec{R}) = \psi(R) Y_{00}(\hat{R}) = \frac{1}{\sqrt{4\pi}} \psi(R) \qquad (5.27)$$

where R is the separation distance between the centers of mass of the α

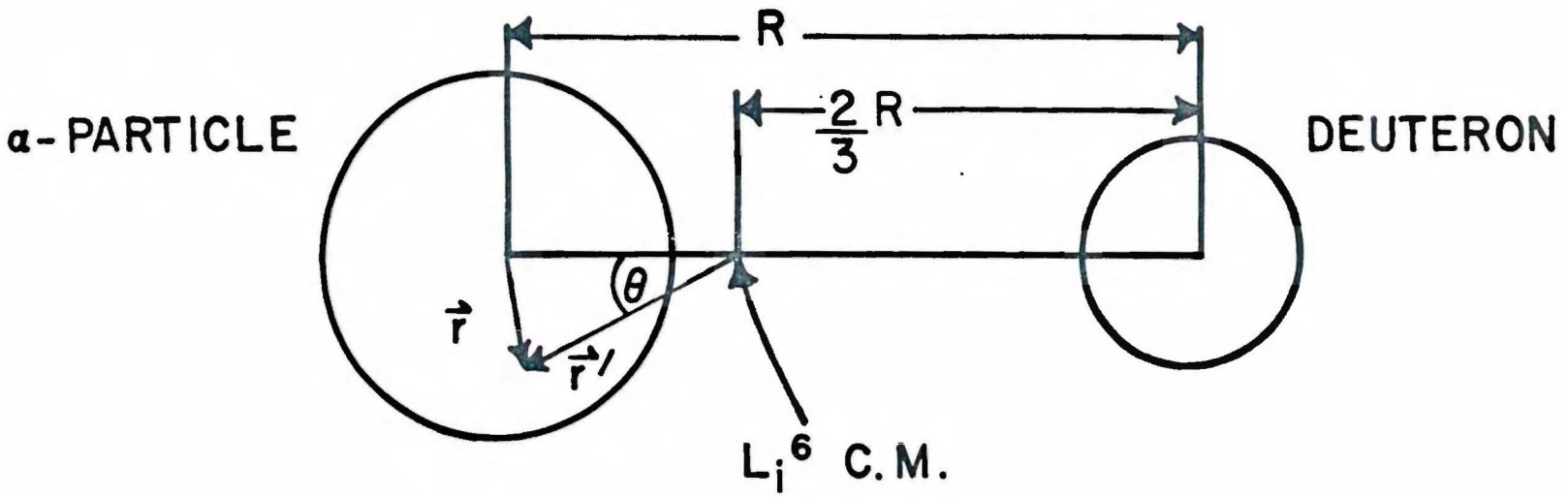

Figure 5.4: Geometry used for folding the finite size of the α-particle and the deuteron into a cluster wave function for Li^6.

and the deuteron. To obtain the overall charge distribution for Li^6, it is necessary to fold the finite size of the α and the deuteron charge distributions into the square of the cluster wave function. Then

$$\rho_{Li6}(r') = \frac{2}{3}\rho_{I}(r') + \frac{1}{3}\rho_{II}(r') \tag{5.28}$$

Where

$$\rho_{I}(r') = \iint \rho_{\alpha}(\vec{r}) \left|\Psi(\vec{R})\right|^2 d\vec{r}\, d\vec{R}\, \delta\left(\vec{r}' - \vec{r} - \frac{\vec{R}}{3}\right) \tag{5.29}$$

ρ_α is the charge distribution of the α particle. See Figure 5.4 for the definitions of $\vec{r}'$, $\vec{r}$ and $\vec{R}$. Eliminating the δ function in (5.27) with the integral over $\vec{r}$ yields

$$\rho_{I}(r') = \int \rho_{\alpha}\left(\vec{r}' - \vec{R}/3\right) \left|\Psi(\vec{R})\right|^2 d\vec{R}$$

$$= \frac{1}{4\pi} \iiint \rho_{\alpha}\left(\sqrt{r'^2 + \frac{R^2}{9} - \frac{2}{3}r'R\cos\theta}\right) \left|\Psi(R)\right|^2 R^2 dR\, d\cos\theta\, d\phi \tag{5.30}$$

Performing the integration over ϕ

$$\rho_{I}(r') = \frac{1}{2}\int_0^\infty \left|\Psi(R)\right|^2 R^2 dR \int_{+1}^{-1} \rho_{\alpha}\left(\sqrt{r'^2 + \frac{R^2}{9} - \frac{2}{3}r'R\cos\theta}\right) d\cos\theta \tag{5.31}$$

Similarly

$$\rho_{II}(r') = \iint \rho_{d}(r') \left|\Psi(\vec{R})\right|^2 d\vec{r}\, d\vec{R}\, \delta\left(\vec{r}' - \vec{r} - 2\vec{R}/3\right) \tag{5.32}$$

$$= \int \rho_{d}\left(\vec{r}' - 2\vec{R}/3\right) \left|\Psi(\vec{R})\right|^2 d\vec{R} \tag{5.33}$$

$$= \frac{1}{4\pi} \iiint \rho_{d}\left(\sqrt{r'^2 + 4R^2/9 - \frac{4r'R}{3}\cos\theta}\right) \left|\Psi(R)\right|^2 R^2 dR\, d\cos\theta\, d\phi \tag{5.34}$$

$$= \frac{1}{2}\int_0^\infty \left|\Psi(R)\right|^2 R^2 dR \int_{+1}^{-1} \rho_{d}\left(\sqrt{r'^2 + 4R^2/9 - \frac{4r'R}{3}\cos\theta}\right) d\cos\theta \tag{5.35}$$

The double integrals (5.31) and (5.35) were performed numerically on an IBM 360/44 computer using Simpson's Rule. 201 points were used in the radial integrals; 31 points were used in the angular integrals. It is believed that the error in the calculation of r.m.s. charge radii for Li^6, using ρ_{Li6} in (5.28) and the above numerical integrations is less than 2%, based on calculations which could also be performed analytically.

For ρ_α, the charge distribution in the α, the following "Fermi Three Parameter" form was used (L67)

$$\rho_\alpha = \rho_o \left(1 + \frac{wr^2}{c^2}\right) \Big/ \left(1 + \exp\left(\frac{r-c}{z}\right)\right) \tag{5.36}$$

Where

$$c = 1.01 \text{ fm.} \qquad z = .327 \text{ fm.} \qquad w = .445, \tag{5.37}$$

and by numerical integration it is determined that

$$\rho_o = 1.3406 \tag{5.38}$$

The charge distribution of the deuteron has not been so conveniently parameterized. To obtain a charge distribution for the deuteron, and incidentally test the double integral program mentioned above, the charge distribution of the proton was folded into a relative wave function for the deuteron. The deuteron wave function used was Moravcik's best 4 parameter fit to the Gartenhaus S-state wave function (M58):

$$\psi_d(r) = 0.9195 \left(1 - e^{-2.5r}\right)\left(1 - e^{-1.59r}\right)\left(e^{-0.232r} - e^{-1.90r}\right)/r \tag{5.39}$$

The proton charge distribution was taken as

$$\rho_p = \frac{1}{\pi^{3/2} a_p^3} e^{-r^2/a_p^2} \tag{5.40}$$

where $\langle r^2 \rangle_p^{1/2} = \left(\frac{3a_p^2}{2}\right)^{1/2} = 0.72$ fm.; and $a_p = 0.588$ fm. Then in a manner analogous to the calculation of ρ_{Li^6} one finds:

$$\rho_d(r') = \frac{1}{2} \int_0^\infty |\psi_d(R)|^2 R^2 dR \int_{+1}^{-1} \rho_p\left(\sqrt{r'^2 + \frac{R^2}{4} - Rr'\cos\theta}\right) d\cos\theta \tag{5.41}$$

The numerical integrals were performed with 401 points in the radial integral and 121 points in the angular integral. The r.m.s. radius of the resultant charge distribution was 2.17 fm. The experimental value is (2.17 ± .05) fm. (L67).

5.4.3 Numerical Results

Before calculating r.m.s. radii of the wave functions in a variety of potentials, some studies of the scattering phase shifts for various potentials were made. This helped to narrow the region of search, an important consideration, since the r.m.s. radius computer code described in Section 5.4.2 was quite slow (nearly ten minutes per case).

Only the S-wave phase shift was considered here, as an extension of the assumption that the Li^6 ground state is all L = 0. Any coupling between the L = 0, J = 1 and the L = 2, J = 1 partial waves was ignored. This is equivalent to ignoring those parts of the nuclear interaction that mix L - S coupling states and treating the Li^6 ground state as all L = 0.

Two basic types of potentials were studied: those without a repulsive core, and those with a repulsive core. The basic shape of both types of potentials was taken to be of the "Woods-Saxon" form. To this was added a Coulomb potential for a uniformly charged sphere of the same radius R as the "Woods-Saxon" part. Finally a repulsive core could be added. Thus

$$V = V_{w.s.} + V_{Coulomb} + V_{core} \tag{5.42}$$

$$V_{w.s.}(r) = -V_o \times \left(1 + \exp\left(\frac{r-R}{a}\right)\right)^{-1} \tag{5.43}$$

$$V_{Coulomb}(r) = 2e^2\left(\frac{3R^2 - r^2}{2R^3}\right) \quad \text{for} \quad r \leq R$$

$$= \frac{2e^2}{r} \quad \text{for} \quad r \geq R \tag{5.44}$$

For all of the calculations, a, the "diffuseness" was fixed:

$$a = 0.7 \text{ fm.} \tag{5.45}$$

For the potentials without a repulsive core, it was found that no potentials with a 1S bound state at -1.472 MeV could fit the α-d S-wave scattering phase shifts continuously to a deuteron laboratory energy

greater than about 4 MeV. Of the coreless potentials with a 2S bound state at -1.472 MeV a good fit to the S-wave scattering phase shifts up to a deuteron laboratory energy of about 27 MeV was found with R = 2.2 fm. (note that V_o = 62 MeV is uniquely determined).

Two types of repulsive cores were considered, "soft" cores and "hard" cores. The soft cores were of the form G/r^n, with both G and n being variables. This form was suggested by the radial form of $\psi_1(R)$ in (5.25). The comment was made in Section 5.3 that (5.25) has the same analytic form as a 1D oscillator wave function. Hence the potential for (5.25) would be of the form of an oscillator plus a G/r^2 core, the core having the same form as the centrifugal barrier for the 1D state. Specifically:

$$\frac{G}{r^2} = \frac{\hbar^2}{2m} \times \frac{2(2+1)}{r^2} = \frac{3\hbar^2}{mr^2} \qquad (5.46)$$

Calculations of phase shifts for potentials with a G/r^2 core, even with G taken as a variable, were unable to fit the s-wave phase shifts above 5 MeV deuteron laboratory energy. By generalizing the form to G/r^n it was possible to obtain fits to the phase shifts, up to 27 MeV deuteron energy, for $n \geq 4$. This generally involved a good deal of parameter juggling, since V_o, R, n, and G were all variables, and the only constraint was that the binding energy equal 1.472 MeV.

The "hard core" potentials had $V_c = \infty$ for r smaller than some radius R_c. For potentials with R between 1.5 and 3.5 fm. it was possible to find values of R_c which gave reasonable fits to the s-wave phase shifts up to 27 MeV, with V_o adjusted to give the right 1.472 MeV binding energy.

Since the "soft core" potentials G/r^n with $n \geq 4$ are really rather "hard" and to reduce the number of parameters, this form was abandoned in favor of the "hard core" approach, which has only 3 parameters. The only "no core" potential which could fit the phase shifts above 5 MeV deuteron

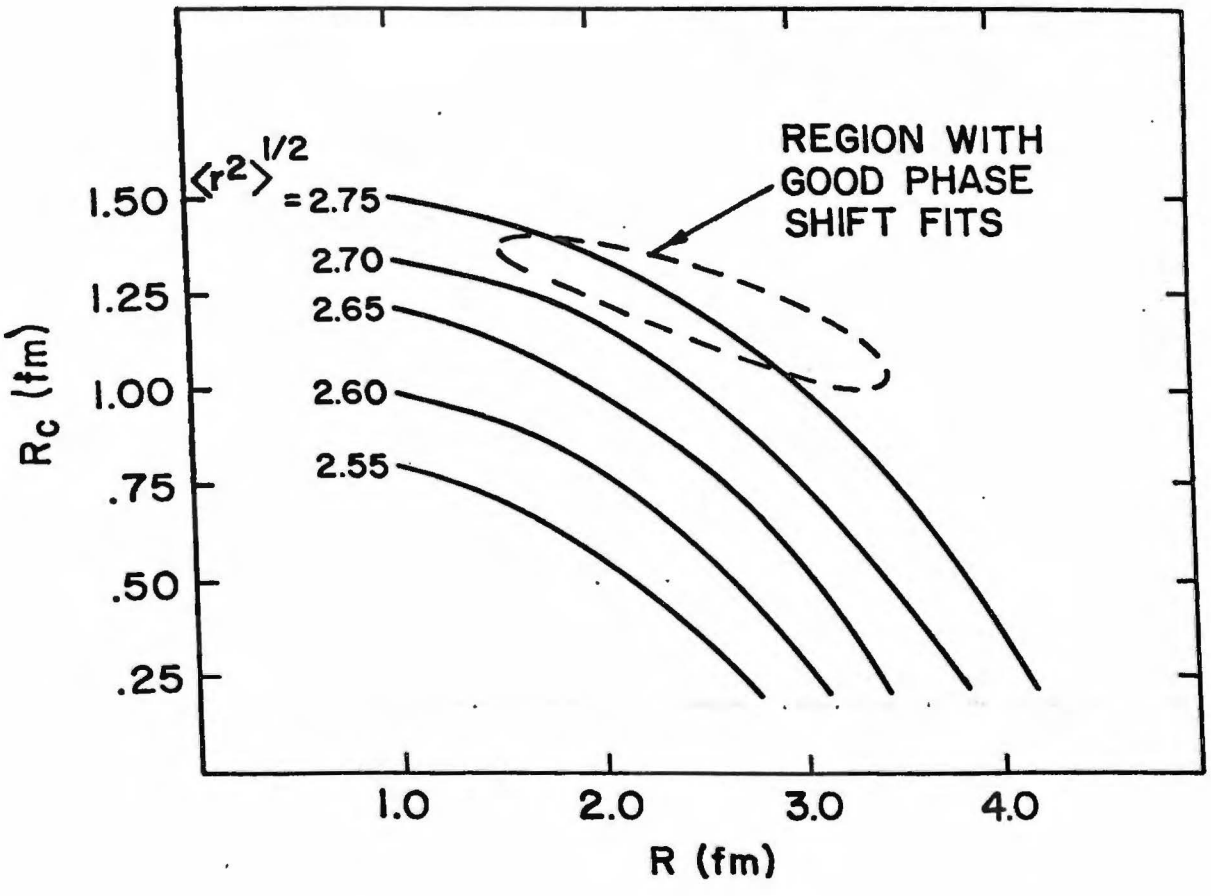

Figure 5.5: R vs. R_c contours of constant r.m.s. charge radius for Li^6. R_c is the hard core radius and R is the Woods-Saxon well radius of a phenomenological α-d potential with a bound 1S state at -1.47 MeV. The diffuseness is fixed at a = 0.7. The region where good fits to the α-d S-wave phase shift are found is indicated.

energy was that with a 2S state at -1.472 MeV. This is a theoretically unsatisfying type of potential. The level structure of Li^6 has only one bound state, and it is unsatisfying to have this state be a 2S, that is a two node state, with a fictitious 1S or 1 node state lying at some lower energy. However, if one imagines the insertion of a repulsive core with the same radius as the node in the 2S bound state, then one gets a 1S state of identical asymptotic properties except for a slight change in normalization. A relatively small part of the 2S wave function exists inside the node, hence the overall character of the state is little changed by the insertion of the core. A hard core approach was therefore decided on.

Bound state cluster wave functions with 1.472 MeV binding energy were calculated for several values of R and R_c, the Woods-Saxon and core radii. Then, using the methods of Section 5.4.2, r.m.s. charge radii were obtained. The results of these calculations are shown in Figure 5.5. Contours of constant $\langle r^2 \rangle^{1/2}$ (r.m.s. radius) are plotted against R and R_c. Also shown is the region where reasonable fits to the S-wave α-d scattering phase shifts could be obtained. The most recent value of the r.m.s. charge radius for Li^6 is 2.61 ± 0. fm. (Y69). If an error of ± 0.05 fm. is assumed for the calculated r.m.s. radius, due to the limitations of the numerical integration then a choice of R = 2.0 fm. and R_c = 1.25 fm. is indicated. This point actually gives $\langle r^2_{charge} \rangle^{1/2}_{Li^6}$ = 2.72 fm. Figure 5.5 shows the usefulness of using the information of phase shifts. Given a wide variety of potentials which yield $\langle r^2 \rangle^{1/2}$ = 2.72 fm. the additional information on phase shifts indicates a clear preference for the potential chosen above.

As a check on the assumptions which went into the choice of a potential with a hard core, r.m.s. charge radii were calculated for some of the other types of potentials. For the "no core" potentials, the one with a 1S state

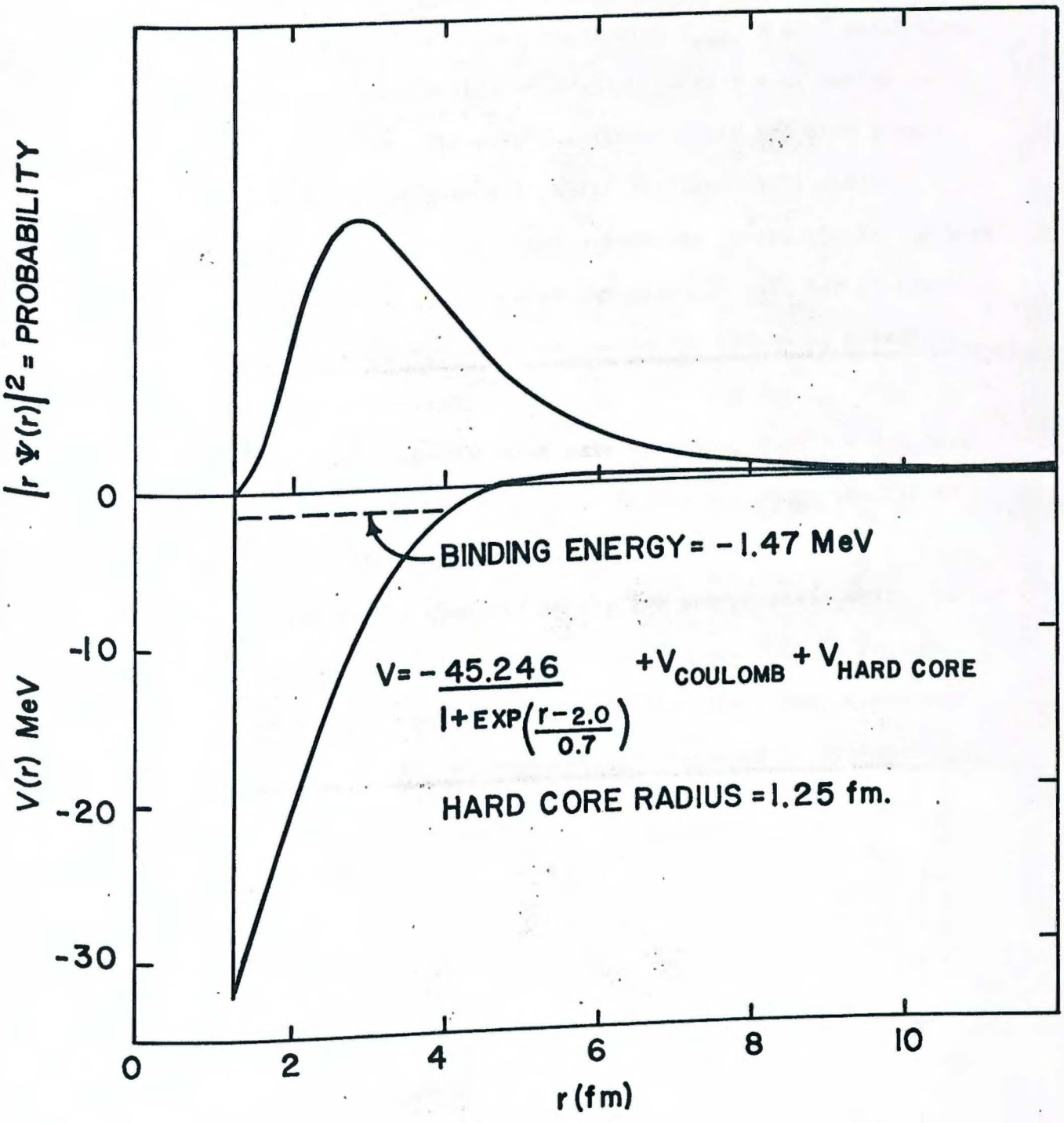

Figure 5.6: The probability distribution and the potential for the phenomenological α-d cluster wave function for Li^6.

at -1.472 MeV which also gave a "best fit" to the S-wave phase shifts has $\langle r^2 \rangle^{1/2}$ = 2.81 fm. The potential with a 2S state at -1.472 and a "best fit" has $\langle r^2 \rangle$ = 2.77 fm. Several potentials with $V_{core} = G/r^6$ which gave "best fits" for various fixed values of R all yielded r.m.s. charge radii between 2.75 fm. and 2.80 fm. The very best phase shift fit with a hard core potential (center of the good fit region in Figure 5.5) yields $\langle r^2 \rangle^{1/2}$ = 2.75 fm. Note that all of these potentials except the 1S "no core" potential yield good fits to the phase shifts up to 27 MeV. All of these also yield r.m.s. radii in a narrow range, hence the choice of potential seems to be relatively uncritical.

Figure 5.6 shows the final choice of wave function, with R = 2.0 fm., R_c = 1.25 fm., V_o = 45.246 MeV, a = 0.7 fm. Figure 5.7 shows the fit to the S-wave phase shifts with this potential.

It should be noted that a good fit to the low energy phase shifts is more important than a good fit to the high energy ones. This is because the higher energy scattering probes smaller interaction radii, where exchange effects, ignored in this calculation, are expected to be important.

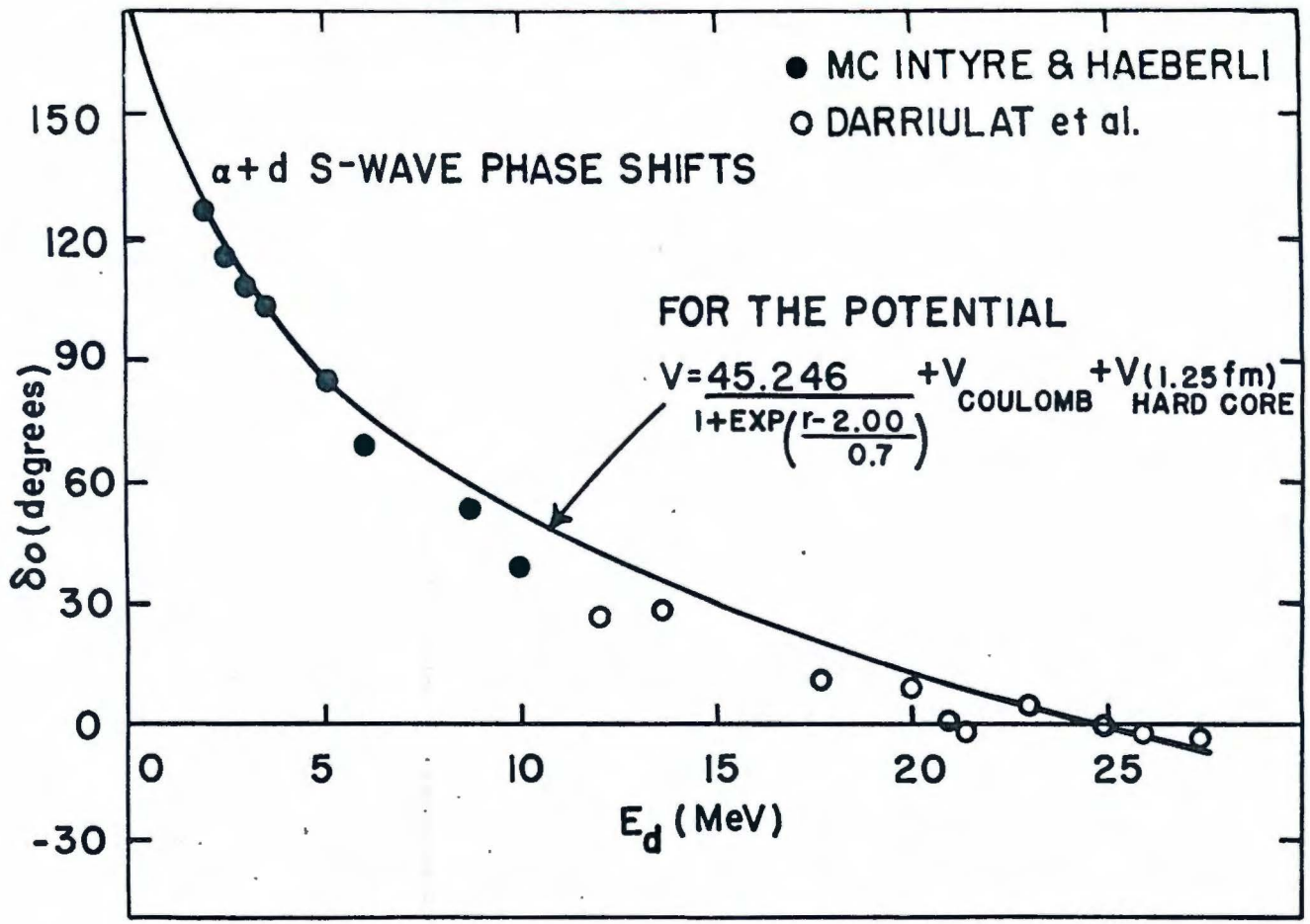

Figure 5.7: The S-wave phase shifts for α-d scattering from the phenomenological potential for the α-d cluster wave function. The data of (M67) and (D67) is also shown.

Section 5.5 Comparison of Theory and Experiment

In this section the "experimental" momentum distribution presented in Section 5.1 will be compared with the cluster wave function derived in Section 5.4.3. If the wave function in Figure 5.6 is Fourier transformed and squared one finds $|\Phi(\vec{q} = 0)|^2 = 1.21 \times 10^{-6}$ $(MeV/c)^{-3}sr^{-1}$ and a width at half maximum of 38.4 MeV/c. This compares with experimental values of $|\Phi(\vec{q} = 0)|^2 \sim 2.0 \times 10^{-7}$ $(MeV/c)^{-3}sr^{-1}$ and a width of 29 ± 2 MeV/c. Clearly the two do not agree. Calculations for the other wave functions discussed in Section 5.4.3 which fit α-d scattering and yield a reasonable r.m.s. charge radius for Li^6 do not yield theoretical wave function parameters appreciably different from those quoted. The reduction in the measured value of $|\Phi(\vec{q} = 0)|^2$ due to finite resolution effects is thought to be only about 5%. In Section 5.2.2 it was shown that a simple shell model leads to a reduced clustering probability of only about 50%. This reduction is not nearly enough to account for the observed reduction in $|\Phi(\vec{q} = 0)|^2$. Thus theory and experiment appear to be in serious disagreement.

As was seen in Section 4.2, effects were seen to be present in the data which could be attributed to distortion effects in the reaction mechanism. It is also known that α-particles are generally strongly absorbed in nuclear matter. Thus a calculation of the effects of a very simple model of the absorption process was attempted. The model is this: when the separation of the α and the deuteron in Li^6 is smaller than some given amount, the incident α interacts not only with the α in Li^6, but with the deuteron as well. This process will lead to other processes, such as $\alpha + He^3 + n + d$ or $\alpha + \alpha + n + p$ breakup and also to $\alpha + \alpha + d$ events far away from $\vec{q} = 0$. It is assumed that all interactions inside this separation radius do not lead to events inside the quasi-free peak. This will be called the "sharp

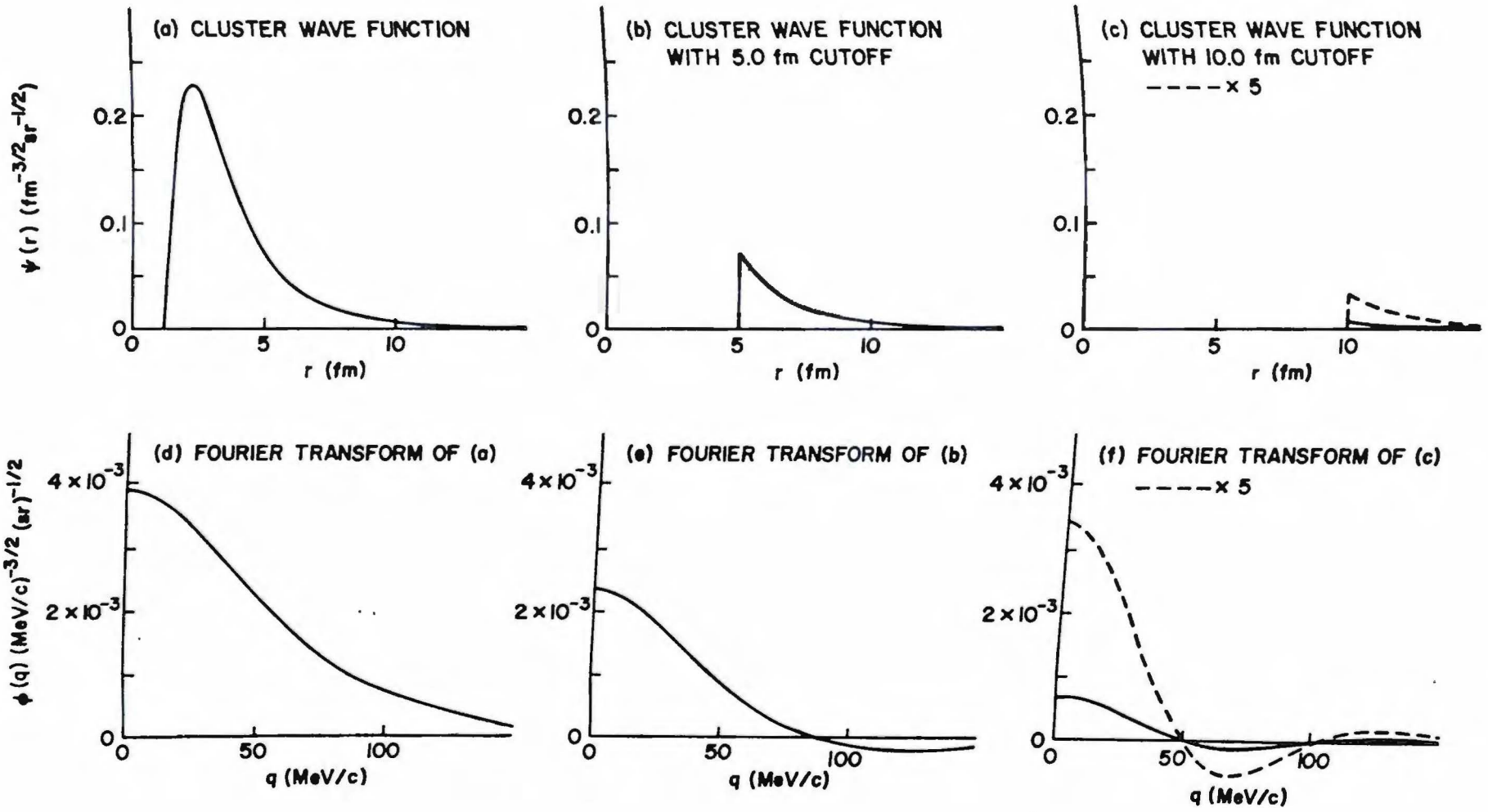

Figure 5.8: The cluster wave function $\psi(r)$ and its Fourier transform $\phi(q)$ for cutoff radii of 0, 5 and 10 fm.

cutoff" model, in that none of the α-d cluster wave function inside a given α-d separation distance participates in the quasi-free scattering process. This distance will be called the "cutoff radius". The observed momentum distribution is then the Fourier transform of only that part of the wave function that lies outside the cutoff radius. Although the sharp cutoff method may seem to be a drastic procedure, it is a fairly frequently used device in nuclear reaction calculations. It has been used previously for knockout reactions by several authors, including Green and Brown (G60) and Sakamoto (S65). The cutoff procedure is also equivalent to the well known Butler model for stripping and pickup reactions, where the matrix element for the interaction is calculated using plane waves and integrating over all space outside a sphere of radius R.

The introduction of a cutoff radius in the cluster wave function has two desirable effects. First of all, removing the center of the spatial wave function removes high momentum components from the momentum wave function, reducing the width. Secondly, the effective number of α's in Li^6 for the quasi-free scattering process is reduced, which in turn reduces $|\phi(q = 0)|^2$. Figure 5.8 shows the spatial wave functions and their Fourier transforms for cutoff radii of 0, 5 and 10 fm. The two effects mentioned above are quite clear.

Figure 5.9 shows the dependence of $|\phi(0)|^2$ and the width at half maximum of $|\phi(q)|^2$ as a function of cutoff radius for the cluster wave function calculated in Section 5.4.3. When the width is 30 MeV/c at a cutoff radius of 5 fm. $|\phi(0)|^2 = 4.36 \times 10^{-7}$ $(MeV/c)^{-3} sr^{-1}$. If the 51% clustering calculated in Section 5.2.2 or the experimental deuteron reduced width of .5 is assumed then $|\phi(0)|^2 \sim 2.0 \times 10^{-7}$ $(MeV/c)^{-3} sr^{-1}$ which is just about the experimental value observed in this $Li^6(\alpha,2\alpha)d$ reaction. If one assumes

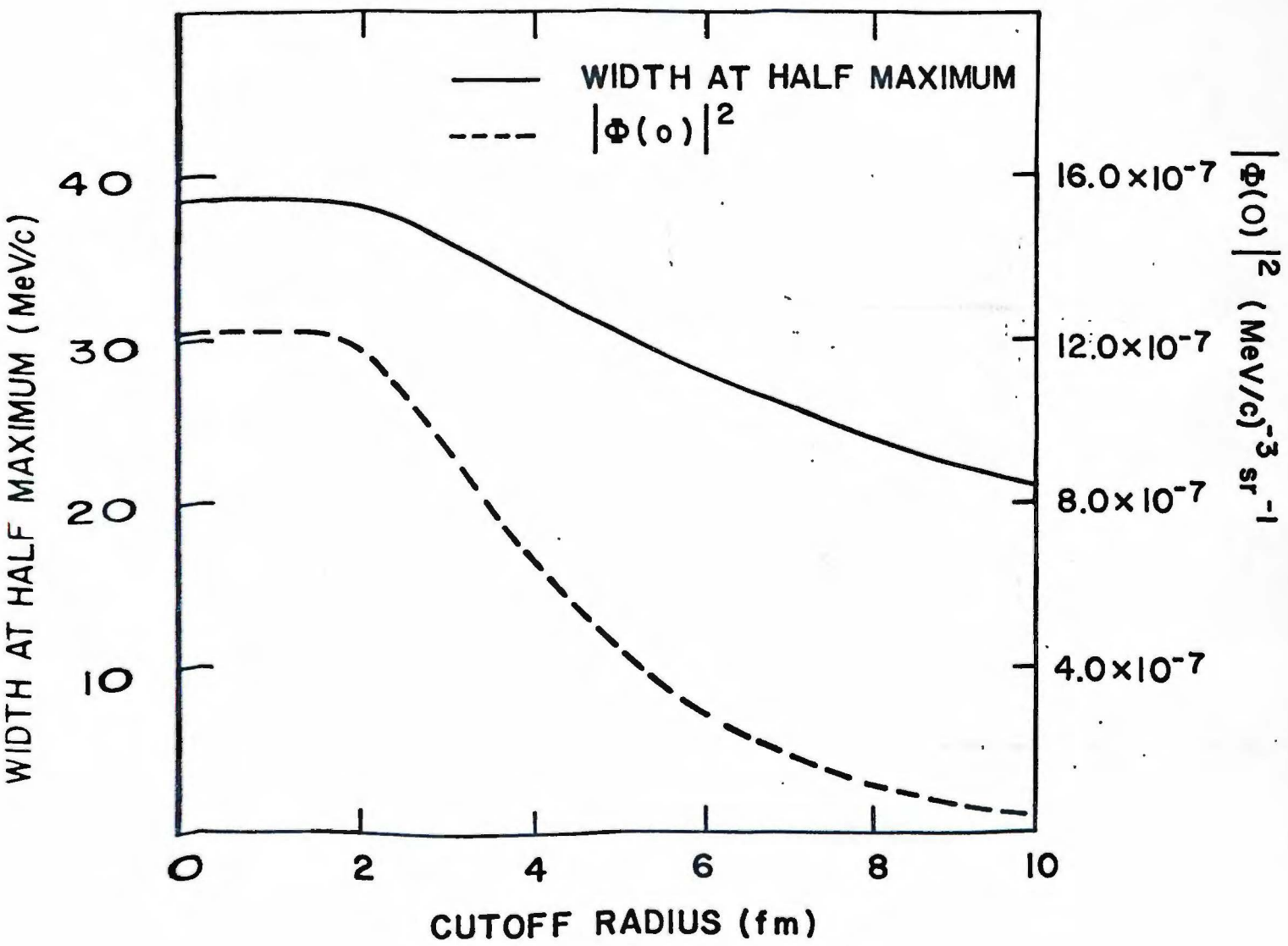

Figure 5.9: $|\Phi(0)|^2$ and the half width at half maximum of $|\Phi(q)|^2$ as a function of cutoff radius. $\Phi(q)$ is the Fourier transform of $\psi(r)$, the phenomenological α-d cluster wave function.

100% clustering, a larger cutoff radius is needed to fit $|\Phi(0)|^2$. Then the predicted width is 26 MeV/c, somewhat too small. Due to the large uncertainty in the absolute cross sections, however, $|\Phi(0)|^2$ also has a large uncertainty. This in fact makes any width between 24 MeV/c and 28 MeV/c compatible with 100% clustering. Thus qualitatively the discrepancies between the theoretical and experimental momentum distributions for α's in Li^6 can be accounted for by this simple model of the absorption.

The theoretical momentum distributions in Figures 5.1 and 5.2 are the square of the Fourier transform of the cluster wave function from Section 5.4.3 with a 5 fm. cutoff. Considering the overall fit to the momentum distribution this wave function seems to do best, in the sharp cutoff approach. For the 50.4 MeV and the 60.5 MeV data, the theoretical wave function has been shifted 2 MeV/c to the left to compensate for the discrepancies noted in Section 5.1. It is clear in Figure 5.1 that the theoretical curve gives a good fit up to 60 MeV/c, but thereafter falls off too fast.

Figure 5.10 shows all of the data for 70.3 MeV, together with the cross sections predicted with P.W.I.A. The momentum distribution used here is the "experimental" momentum distribution but differs only slightly from the distribution from the wave function with a 5 fm. cutoff. Beyond 50 MeV/c it is somewhat larger to compensate for the slightly too fast fall off of the theoretical distribution at large q. The spectra in Figure 5.10 are arranged with θ_1 as the abscissa and θ_{12} as the ordinate. This means that all the spectra with $\vec{q} = 0$ are in the row with $\theta_{12} \sim 88^o$.

Following the row with $\theta_{12} \sim 88^o$ across, the quality of the fits is generally good but the "shifts" of the experimental peaks relative to theory (which showed up in the shift in angle of the effective free cross sections

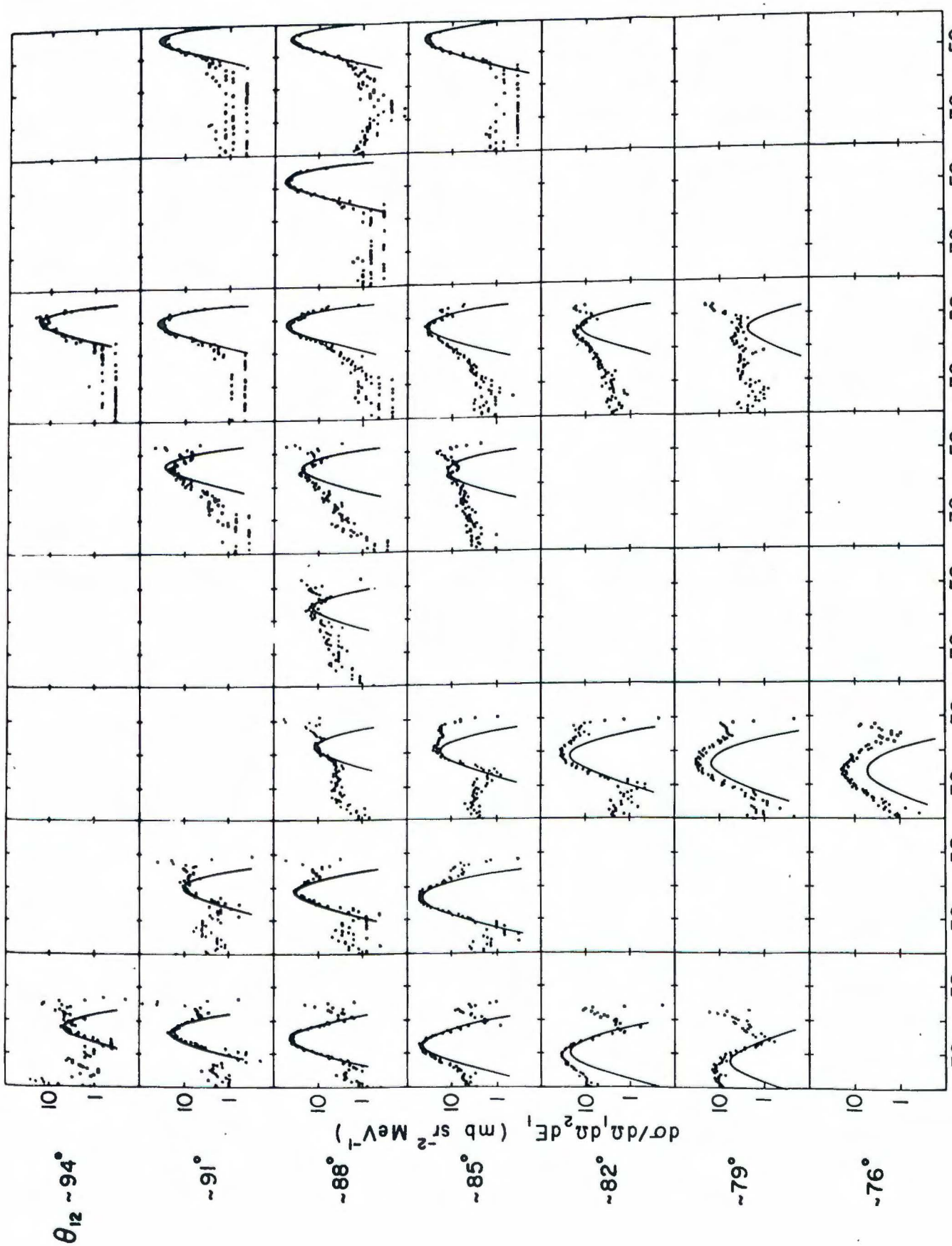

Figure 5.10: 28 projected energy spectra for the $Li^6(\alpha,2\alpha)d$ reaction at 70.3 MeV. The spectra arranged in rows and columns according to θ_{12} and θ_1. The solid curves are calculated from P.W.I.A. with a cutoff in the α-d cluster wave function.

in Section 4.2) are apparent. For $\theta_1 = 38.25^\circ$ the theory falls progressively more and more below the experiment as θ_{12} gets smaller than $\sim 88^\circ$. This phenomenon was seen before in Section 5.1 as a shift in the momentum distribution to positive q.

In the vicinity of $\theta_1 = 32.25^\circ$ an interesting phenomenon seems to be occurring. On the low energy side of the peak the experimental cross sections are significantly larger than the theory without a similar phenomenon on the high energy side of the peak. For $\theta_1 = 44.25^\circ$ and $\theta_{12} < 88^\circ$ the same thing also seems to be happening. This has the same appearance as an effect seen recently in the $H^2(\alpha,\alpha p)n$ reaction which seems to be attributable to multiple scattering effects (Bo69). If this is in fact the result of multiple scattering, it may represent a much more serious deviation of the experiment from P.W.I.A. than the other "shift" phenomena. The "shifts" can quite possibly be accounted for by a distorted wave impulse approximation calculation, but explicit calculations of higher order diagrams would be much more difficult.

As a general conclusion, however, it seems that P.W.I.A. can account for much of the observed data and in the vicinity of $\vec{q} = 0$ ($\theta_{12} \sim 88^\circ$) provides a good quantitative description of the reaction mechanism. It should be remembered that large absorption effects are apparent in the wave function extracted from the $\theta_1 = \theta_2 \sim 44^\circ$ spectra and given the crude model used for absorption, minor deviations from P.W.I.A. with scattering angle are not unexpected.

Section 5.6 Other Measurements of the Li^6 Wave Function

5.6.1 Studies with the $Li^6(p,pd)He^4$ and $Li^6(\alpha,\alpha d)He^4$ Reactions

The $Li^6(p,pd)He^4$ reaction has been studied at 30, 55 and 155 MeV. Devins, Scott and Forster studied this reaction at 30 MeV (De65). With $\theta_p = \theta_d$ they obtained an angular correlation by integrating the cross section over E_p for each angle pair. Fitting this angular correlation with the Fourier transform of a Yukawa wave function yields a half width at half maximum between 21 and 32 MeV/c and N_{eff}, the effective number of clusters, between .04 and .12.

Hendrie et al. studied $Li^6(p,pd)He^4$ at 55 MeV (H66). Analysis of this data for one spectrum with $\theta_p = 60^o$ and $\theta_d = 46^o$, and for an angular correlation with $\theta_p = 60^o$, $E_d = 23$ MeV yields a half width at half maximum of 32 ± 2 MeV/c and $N_{eff} = .15 \pm .075$.

Ruhla et al. have studied the $Li^6(p,pd)He^4$ reaction at 155 MeV (R63). With $\theta_p = \theta_d$ and $E_p = 100$ MeV they measured an angular correlation. This had a half width at half maximum of 34 ± 4 MeV/c and $N_{eff} = .31 \pm .16$.

The $Li^6(\alpha,\alpha d)He^4$ reaction has been studied by Bahr et al. with 24 MeV α's (Ba69). Throughout the experiment θ_d was held fixed at 45^o. From coplanar and non-coplanar angular correlations about $\theta_\alpha = 23^o$, and an energy spectrum for $\theta_\alpha = 23^o$ they obtained a half width at half maximum of 24 ± 3 MeV/c with $N_{eff} = .035$ to .065.

5.6.2 Studies with the $Li^6(\pi^+,2p)He^4$ and $Li^6(\pi^-,2n)He^4$ Reactions

The $Li^6(\pi^+,2p)He^4$ and $Li^6(\pi^-,2n)He^4$ reactions can also be analyzed in terms of a peripheral mechanism, similar to Figure 2.9c. The difference is that the $\pi^+ + d \rightarrow 2p$ or $\pi^- + d \rightarrow 2n$ process replaces the upper vertex. Then by detecting the two neutrons or two protons the momentum distribution of the deuteron can be deduced.

The $Li^6(\pi^+,2p)He^4$ reaction has been studied by two groups. Charpak et al. studied this reaction with 80 MeV pions (C67). They find their data to be consistent with a peripheral mechanism, but a large amount of experimental resolution has been folded into their theoretical fits to the data and no width is quoted. They find $N_{eff} \sim 0.4$. Burman and Nordberg have studied the $Li^6(\pi^+,2p)He^4$ reaction with 31 MeV pions (Bu68). Again no width is available from their data, although they do find positive results for invariance under Trieman-Yang rotation, which supports the peripheral mechanism for that type of reaction.

The $Li^6(\pi^-,2n)He^4$ reaction has been studied by Davies, Muirhead, and Woulds using pions at rest (D66). For their momentum distribution a width of 32 ± 3 MeV/c is indicated, along with a clustering probability of 37% ± 10%.

5.6.3 Studies Using the $Li^6(p,p\alpha)d$ and $Li^6(\alpha,2\alpha)d$ Reactions

M. Jain of the University of Maryland has studied the $Li^6(p,p\alpha)d$ reaction using 57 MeV protons from the ORIC cyclotron (J69). His data for the Li^6 wave function using this reaction consists of an energy spectrum for $\theta_p = 105^o$, $\theta_\alpha = 30^o$, and an angular correlation moving θ_α about the above angle with E_p held fixed at 28 MeV. His data give a width of 34 ± 4 MeV/c and he quotes $N_{eff} = 0.16$. No error is given for N_{eff}, but based on his estimate of ± 25% error in the absolute cross section, and the uncertainties in the analysis, the error in N_{eff} will be taken to be 50%.

Ruhla et al. have studied the $Li^6(p, p\alpha)d$ reaction at 155 MeV (R63). Their data is an angular correlation with $\theta_p = \theta_\alpha$ and E_p fixed at 120 MeV. Their angular correlation has a width of 30 ± 5 MeV/c and $N_{eff} = .20 \pm .10$.

The $Li^6(\alpha,2\alpha)d$ reaction has very recently been studied at 55 MeV by Pizzi et al. (P69). Their data consists of an equal angle angular correlation, and an energy spectrum for $\theta_1 = \theta_2 = 44.3^o$. Their analysis, received since

the present analysis was completed, also favors the use of $d\sigma/d\Omega(E_f)$. Using E_i for Li^6 they find a width of 20 MeV/c and N_{eff} = .015 to .105; using E_f they find a width of 29 MeV/c and N_{eff} = .04 to .11. Although no error is quoted for the width, a study of their data would suggest 29 ± 4 MeV/c for their E_f analysis. These results are in agreement with the present analysis.

M. Jain has studied the $Li^6(\alpha,2\alpha)d$ reaction at 62 MeV using the ORIC cyclotron (J69). His data for the Li^6 wave function consists of an energy spectrum with $\theta_1 = \theta_2 = 44.2^o$ and a 5 point equal angle angular correlation. Using E_i he found a width of 31 ± 3 MeV/c and N_{eff} ~ 0.15; using E_f he found a width of 29 ± 3 MeV/c and although none is quoted, N_{eff} ~ .10 ± .05 would seem to be appropriate. These results are in agreement with the present analysis.

For the data in this thesis, studying the $Li^6(\alpha,2\alpha)d$ reaction at 50 to 80 MeV, a width of 29 ± 2 and N_{eff} of .08 ± .04 were found using E_f. For E_i the results were a width of 31 ± 2 and N_{eff} = .15 ± .10.

5.6.4 Studies Using the $C^{12}(Li^6,d)O^{16}$ and $O^{16}(Li^6,d)Ne^{20}$ Reactions

The $C^{12}(Li^6,d)O^{16}$ and $O^{16}(Li^6,d)Ne^{20}$ reactions at 25.8 MeV have recently been studied by Davydov and Pavlichenkov (D69). They analyzed the angular distributions of rotational levels of O^{16} and Ne^{20} excited in this reaction, using the following assumptions: (1) Li^6 has an α + d cluster structure; (2) The cross section of the reaction is proportional to the probability of finding an α-particle with angular momentum L in the volume of the target nucleus. L is the spin of the rotational state of the final nucleus; (3) The probabilities of α-particle capture are the same for all the levels of the rotational band; (4) Relative motion of nuclei in both channels is described by plane waves.

With these assumptions they show that the cross section can be factorized with $|\Phi(\hbar K)|^2$ as a factor, where $K = k_d - \frac{1}{3} k_{Li^6}$. For a given

TABLE 5.3

	Reaction	Energy	Width	N_{eff}	Reference
1	$Li^6(p,pd)He^4$	30 MeV	21-32 MeV/c	.04-.12	De65
2	"	55 MeV	32±2	.15±.075	H66
3	"	155 MeV	34±4	.31±.155	R63
4	$Li^6(\alpha,\alpha d)He^4$	24 MeV	24±3	.035-.065	B69
5	$Li^6(\pi^-,2n)He^4$	at rest	32±3	.37±.10	D66
6	$Li^6(p,p\alpha)d$	57 MeV	34±4	.16±.08	J69
7	"	155 MeV	30±5	.20±.10	R63
8*	$Li^6(\alpha,2\alpha)d$	55 MeV	29±4	.04-.11	P69
9*	"	62 MeV	29±3	.10±.06	J69
10*	"	50-80 MeV	29±2	.08±.04	This work

*Results for E_f analysis only.

Information on the Width-at-Half-Maximum and the Effective Clustering Probabilities (N_{eff}) for the Ground State Momentum Distribution for Li^6 as Determined with Various Reactions.

rotational band they then extract $|\Phi(\hbar K)|^2$ from the data. Unfortunately, the minimum value of $\hbar K$ they observe is 25 MeV/c, and no definitive statements can be made about N_{eff} or the width of the momentum distribution observed in this reaction. It appears, however, that these reactions are ones in which a detailed knowledge of the α-d relative motion wave function is essential, and which could, in principle, provide further information on cluster structure and the cutoff model.

5.6.5 Discussion

In Sections 5.6.1, 5.6.2, and 5.6.3 ten different measurements of the $Li^6(\alpha + d)$ wave function using five different reactions have been discussed. The results are summarized in Table 5.3, with only the results for E_f presented for the $Li^6(\alpha,2\alpha)d$ reaction. Many of the measurements appear to be inconsistent, particularly the $Li^6(\alpha,\alpha d)He^4$ reaction and the $Li^6(\pi^-,2n)He^4$ reaction. In most of the more recent measurements the authors make a point of indicating which other measurements are consistent with theirs and which are not.

In Section 5.4, it was pointed out that in the sharp cutoff model both N_{eff} and the width at half maximum decreased with increasing cutoff radius. This was used to show that the measurements for this thesis were consistent with the cluster wave function calculated in Section 5.2.3, in the "sharp cutoff" model for absorption. In Table 5.3 this pattern tends to be repeated in the data. The measurements with small values for N_{eff} tend to have smaller widths. This is shown in Fig. 5.11 where the data of Table 5.3 is displayed with N_{eff} plotted against the width at half maximum. The solid curve is for the wave function calculated in Section 5.2.3 with various cutoff radii. The dashed curve is for the same wave function, but with only a 50% clustering probability for Li^6, i.e. with N_{eff} reduced by ½.

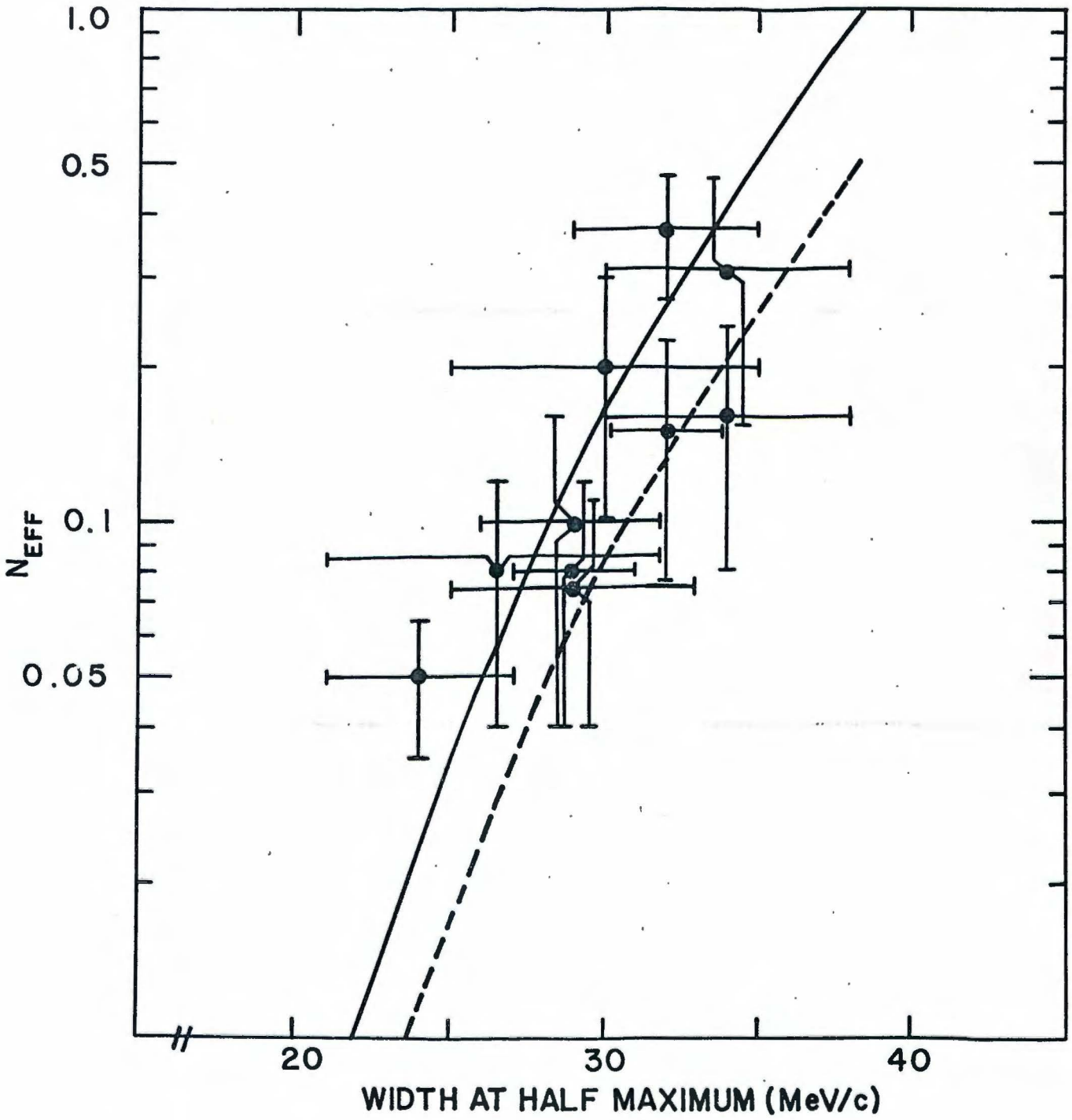

Figure 5.11: N_{eff} the effective number of clusters vs. the half width at half maximum for the momentum distribution from ten different experiments on Li^6. The data is taken from Table 5.3. The solid curve is for the phenomenological α-d wave function with a cutoff. The dashed curve is the same as the solid but multiplied by 0.5.

The curve reproduces the general trend of the data in a very gratifying way. It is unfortunate that the uncertainties in the measurements are generally so large. It is possible that improved accuracy in the various experiments might enable one to determine not only the absolute magnitude of N_{eff}, but also the detailed shape of the N_{eff} vs. half width at half maximum curve. This would then be a complete determination of the α-d relative wave function. However, improved accuracy might only reveal the inadequacy of the cutoff model. What is clear, however, is that all the existing measurements can be explained by our wave function with one adjustable parameter, the cutoff radius.

CHAPTER 6

SUMMARY AND CONCLUSIONS

Section 6.1 Off-Mass-Shell α-α Scattering

In Chapter 4, the Plane Wave Impulse Approximation was used to extract off-mass-shell cross sections from the $Li^6(\alpha,2\alpha)d$ reaction. The primary off-mass-shell data was taken from those points in the experimental spectra where $\vec{q}$, the momentum in the target nucleus of the knocked out α-particle, was zero. These off-mass-shell cross sections were found to be in excellent agreement with free α-α scattering as a function of both scattering angle and bombarding energy, if the free cross section was evaluated at E_f, the center-of-mass energy in the final state of the off-mass-shell α-α collision. These off-mass-shell data were sufficiently accurate to display a clear preference for free cross sections at this final state center-of-mass energy as opposed to the initial state center-of-mass energy. This result was published in Physical Review Letters (Pu69) and it has recently been confirmed by Pizzi, et al. (P69).

Off-mass-shell α-α cross sections were also extracted from points in the experimental spectra where $|\vec{q}|$ = 30 MeV/c. This data was also in general agreement with free α-α scattering cross sections, but it was necessary to introduce an ad hoc shift in α-α scattering angle. The necessity for this shift must be taken as an indication of the failure of P.W.I.A. to account for the fine details of the reaction mechanism. Presumably the "shift" is the result of distortion of the incoming and outgoing waves or similar effects. It should be pointed out, however, that these deviations of the data at $|\vec{q}|$ = 30 MeV/c from P.W.I.A. are in fact very small. Significantly the "shift"

in α-α scattering angle appeared to decrease as the bombarding energy increased.

. Off-mass-shell cross sections were calculated using a phenomenological α-α potential, taken largely from (D65). It was found, however, that the on-mass-shell cross sections calculated for this potential were in worse agreement with the measured free α-α cross sections than were the experimental $\vec{q} = 0$ off-mass-shell cross sections. Hence these off-mass-shell calculations were taken as model calculations only.

There are two off-mass-shell T matrices one can define: $\langle \phi_f | V | \psi_i^{(+)} \rangle$ and $\langle \psi_f^{(-)} | V | \phi_i \rangle$. These produce different off-mass-shell cross sections. It was found that near the mass-shell $\langle \phi_f | V | \psi_i^{(+)} \rangle$ yields a cross section which varies with angle in much the same way as $d\sigma/d\Omega(E_i)$ where E_i is the initial state energy. Similarly near the mass-shell $\langle \psi_f^{(-)} | V | \phi_i \rangle$ yields a cross section which behaves with angle like $d\sigma/d\Omega(E_f)$, where E_f is the final state energy. In both cases, however, the magnitudes of the on- and off-mass-shell cross sections were different. For the $Li^6(\alpha,2\alpha)d$ reaction at $\vec{q} = 0$ (which is rather near the mass-shell) the agreement of the off-mass-shell cross section with $d\sigma/d\Omega(E_f)$ indicates that $\langle \psi_f^{(-)} | V | \phi_i \rangle$ is the preferred off-mass-shell T matrix. This is in agreement with the results of Balashov and Meboniya (B68), who reached the same conclusion from rather more limited data at lower energies.

These model calculations of off-mass-shell cross sections indicate that the use of $d\sigma/d\Omega(E_f)$ as an approximation to the true off-mass-shell cross section is well justified theoretically, for points near the mass-shell. In this respect Li^6 would appear to be a particularly favorable case because of its small binding energy against α + d breakup. For this experiment the difference in magnitude of the on and off-shell cross sections (in the

model calculation) would appear to be smaller than the experimental uncertainties.

Section 6.2 The Momentum Distribution for α's in Li^6.

In Chapter 5 an experimental momentum distribution for α's in Li^6 was extracted from the $Li^6(\alpha,2\alpha)d$ data assuming the validity of the P.W.I.A., and using $d\sigma/d\Omega(E_f)$. The five spectra with $\theta_1 = \theta_2 \sim 44^o$ were chosen, to eliminate any asymmetries in the momentum distribution which might result from the known small departures of the reaction mechanism from P.W.I.A. The extracted momentum distributions were all highly consistent.

A fairly realistic wave function for the α-d relative motion in Li^6 was desired. A survey was made of the traditional calculations of an α-d relative wave function in the oscillator shell model and in the fully antisymmetrized oscillator nuclear cluster model. These were found to be inadequate in their treatment of the asymptotic behavior of the cluster wave function, as so a cluster wave function was calculated which accounted more completely for the asymptotic behavior.

Specifically, the calculation involved a phenomenologic α-d potential. This potential was required to have a bound S state at -1.47 MeV, and to reproduce the S-wave shifts determined from recent α-d scattering experiments. The wave function for the bound state at -1.47 MeV was then required to produce the correct r.m.s. charge radius for Li^6, when the finite charge distributions of the α and the deuteron were folded in. Throughout these calculations antisymmetrization was ignored.

It was found that there were two types of potentials which generated the correct S-wave α-d scattering phase shifts. The first has a 2S state at -1.47 MeV and a spurious 1S state at some deeper binding energy. The second type of potential has a 1S state at -1.47 MeV but also has a repulsive core. The presence of the spurious state in the first type of potential is due to the lack of antisymmetrization in the calculation. The repulsive

core in the second type of potential simulated the main effect of antisymmetrization, namely repulsion at small radii, and there is no spurious state. The second type of potential was therefore chosen as the better form, given the lack of antisymmetrization. The absence of a spurious state indicates that the lack of antisymmetrization has been at least partially compensated for. For computational simplicity, the repulsive core was taken to be a hard core, and the rest of the potential had the "Woods-Saxon" form. The Coulomb potential was also included. With this the form of the potential, the parameters were searched to satisfy the above criteria on the potential and the bound state wave function, and a satisfactory solution was found. The wave function obtained is felt to be very reliable for reaction calculations involving the long range $\alpha + d$ structure of Li^6.

This cluster wave function was Fourier transformed and squared to produce a theoretical momentum distribution for α's in Li^6. When the experimental momentum distribution from the $Li^6(\alpha,2\alpha)d$ reaction was compared with this theoretical one, the two were found to be in serious disagreement, both in width and in magnitude. It was found, however, that the introduction of a cutoff radius of about 5 fm. in the cluster wave function produced good agreement in both width and magnitude. In addition, by making the cutoff radius an adjustable parameter, the theoretical momentum distribution was found to be consistent with momentum distributions for Li^6 from a large variety of reactions, over a wide range of energies. Although the use of a cutoff radius is an ad hoc procedure, it is a well known technique and has been used successfully in other types of reaction calculations for many years.

The necessity of introducing a cutoff into the cluster wave function, indicates that the $Li^6(\alpha,2\alpha)d$ knockout reaction tends to be localized to the nuclear surface. In a sense this is a severe failure of the P.W.I.A.

The remarkable overall consistency of P.W.I.A. with a cutoff indicates, however, that the reactions taking place (other than quasi-free knockout), do not generally contribute to the $\alpha + \alpha + d$ final state in the same region of phase space as quasi-free knockout, and that the impulse approximation is a good description of those knockout events that do occur.

Section 6.3 Conclusions

There are several conclusions that can be drawn from the data analysis and the calculations in this thesis. The first major conclusion is that the off-mass-shell α-α cross section extracted from the $Li^6(\alpha,2\alpha)d$ reaction at $\vec{q} = 0$ appears to be in very good agreement both as a function of angle and energy with free α-α scattering at the final state energy. This agreement implies that $d^3\sigma/d\Omega_1 d\Omega_2 dE_1$ does indeed factorize, and strongly supports the P.W.I.A. or peripheral model. It also implies that the preferred off-mass-shell T matrix is $\langle \psi_f^{(-)} | V | \phi_i \rangle$ rather than $\langle \phi_f | V | \psi_i^{(+)} \rangle$.

The second major conclusion is that the measured α-particle momentum distribution and the one calculated from the theoretical cluster wave function do not agree. It is necessary to introduce an ad hoc cutoff into the cluster wave function to produce agreement. This implies that strong absorption effects are present, and that the reaction seems to be localized in the nuclear surface region. The necessity for a cutoff justifies the effort that went into guaranteeing that the cluster wave function had the correct asymptotic properties, while the short range behaviour, which requires a detailed treatment of the antisymmetrization, was treated approximately. It also indicated that this reaction is not sensitive to the details of the Li^6 wave function at short distances, so that other reactions must be found for studying them.

The third major conclusion is that a cutoff works surprisingly well. With the cutoff radius as an adjustable parameter, the measurements of the cluster wave function for Li^6 from this and a variety of other reactions are consistent with the cluster wave function calculated here. This may mean that the use of this very simple model may have a rather general usefulness for extracting spectroscopic information from medium-energy reactions, until more complex models are formulated.

APPENDIX I

THREE BODY KINEMATICS

A1.1 General Considerations

In this appendix the following conventions will be used:

$\vec{P} = (\vec{p}, iE)$ is a four momentum

$\vec{p}$ is a momentum

$E = T + m$ is a total energy

T is a kinetic energy

m is a mass.

Note that these conventions may differ from those used in the body of this thesis. They are consistent with the notation of the 3-body kinematics program QUASTA.

Figure A1 shows the initial and final states in the laboratory system. Particle o with mass m_o and momentum $\vec{p}_o$ is incident on a stationary target of mass m_T. In the final state there are 3 particles with masses m_1, m_2, m_3 and momenta $\vec{p}_1$, $\vec{p}_2$, and $\vec{p}_3$.

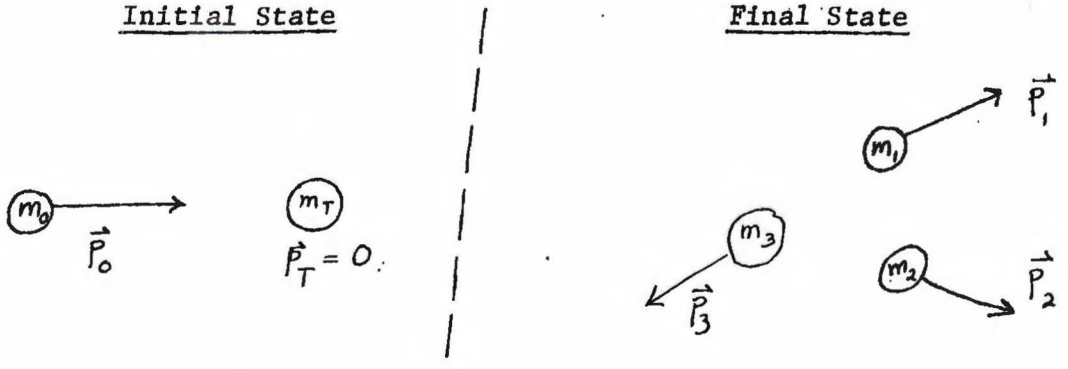

Figure A1: The initial and final states of the reaction, as seen in the laboratory.

The coordinate system will be a spherical polar system with the polar axis defined by $\vec{p}_o$, i.e. the incident beam direction. The components of a momentum are then $\vec{p}_i = (p_i, \theta_i, \varphi_i)$. For the angle θ_{ij} between two momenta $\vec{p}_i$ and $\vec{p}_j$ the following relationship holds:

$$\cos\theta_{ij} = \cos\theta_i \cos\theta_j + \sin\theta_i \sin\theta_j \cos(\varphi_i - \varphi_j) \tag{A1.1}$$

The basic quantities of interest are T_2 and $\vec{p}_3$, given $\vec{p}_o$, $\vec{p}_1$, θ_2, φ_2, and Q. Q is the "energy loss" or "Q value" of the reaction, defined by:

$$Q = m_o + m_T - m_1 - m_2 - m_3 \tag{A1.2}$$

The starting point of the calculation is four momentum conservation:

$$\mathbb{P}_3 = \mathbb{P}_T + \mathbb{P}_o - \mathbb{P}_1 - \mathbb{P}_2 \tag{A1.3}$$

Squaring both sides of (A1.3):

$$\begin{aligned} \mathbb{P}_3^2 &= \mathbb{P}_T^2 + \mathbb{P}_o^2 + \mathbb{P}_1^2 + \mathbb{P}_2^2 \\ &+ 2\mathbb{P}_T\cdot\mathbb{P}_o - 2\mathbb{P}_T\cdot\mathbb{P}_1 - 2\mathbb{P}_T\cdot\mathbb{P}_2 - 2\mathbb{P}_o\cdot\mathbb{P}_1 - 2\mathbb{P}_o\cdot\mathbb{P}_2 + 2\mathbb{P}_1\cdot\mathbb{P}_2 \end{aligned} \tag{A1.4}$$

Now $\mathbb{P}_i^2 = -m_i^2$ hence in the laboratory one finds

$$\begin{aligned} m_3^2 &= m_T^2 + m_o^2 + m_1^2 + m_2^2 \\ &+ 2m_T E_o - 2m_T E_1 - 2m_T E_2 - 2E_o E_1 - 2E_o E_2 + 2E_1 E_2 \\ &+ 2p_o p_1 \cos\theta_1 + 2p_o p_2 \cos\theta_2 - 2p_1 p_2 \cos\theta_{12} \end{aligned} \tag{A1.5}$$

Using (A1.2) and rearranging (A1.5) yields

$$\begin{aligned} 0 &= 2Qm_3 + Q^2 \\ &+ 2T_o(m_3 - m_o + Q) - 2T_1(m_3 + m_1 + Q) \\ &- 2T_o(m_3 + m_2 + Q) - 2T_oT_1 - 2T_oT_2 + 2T_1T_2 \\ &+ 2p_op_1\cos\theta_1 + 2p_op_2\cos\theta_2 - 2p_1p_2\cos\theta_{12} \end{aligned} \tag{A1.6}$$

Rearranging (A1.5) and dividing by 2 yields

$$\begin{aligned}&\left[Qm_3 + Q^2/2 + T_0(m_3 - m_0 + Q) - T_1(m_3 + m_1 + Q + T_0)\right.\\&\qquad\left. + p_0 p_1 \cos\theta_1\right]\\&- T_2\left[m_3 + m_2 + Q + T_0 - T_1\right]\\&+ p_2\left[p_0\cos\theta_2 - p_1\cos\theta_{12}\right] = 0\end{aligned} \tag{A1.7}$$

This will be written as

$$\alpha - \beta T_2 + \gamma p_2 = 0 \tag{A1.8}$$

There are two ways of solving (A1.8). The first method is to substitute $(T_2^2 + 2T_2 m_2)^{1/2}$ for p_2 in (A1.8) and squaring:

$$\gamma p_2 = \beta T_2 - \alpha \tag{A1.9}$$

$$\gamma\left(T_2^2 + 2T_2 m_2\right) = \beta^2 T_2^2 + \alpha^2 - 2\alpha\beta T_2 \tag{A1.10}$$

$$T_2^2\left(\gamma^2 - \beta^2\right) + T_2\left(2\gamma^2 m_2 + 2\alpha\beta\right) - \alpha^2 = 0 \tag{A1.11}$$

(A1.11) can be solved by the quadratic formula, but if there are two disadvantages. Firstly, this method usually requires double precision on the computer for reasonable accuracy in obtaining, p_2 and T_2. Secondly, the sign of p_2 is ambiguous, i.e. solution may be possible with particle two traveling either direction along the (θ_2, φ_2) line.

The second method for solving (A1.8) involves substituting $(p_2^2 + m_2^2)^{1/2} - m_2$ for T_2, and then squaring:

$$\alpha + \gamma p_2 = \beta T_2 \tag{A1.12}$$

$$\alpha + \gamma p_2 + \beta m_2 = \beta\left(p_2^2 + m_2^2\right)^{1/2} \tag{A1.13}$$

$$\alpha^2 + 2\alpha\beta m_2 + \beta^2 m_2^2 + 2(\alpha+\beta m_2)\gamma p_2 + (\gamma^2-\beta^2) p_2^2 = \beta^2 m_2^2 \tag{A1.14}$$

$$p_2^2(\gamma^2-\beta^2) + 2(\alpha+\beta m_2)\gamma p_2 + [\alpha^2 + 2\alpha\beta m_2] = 0 \tag{A1.15}$$

This will be called

$$A p_2^2 + B p_2 + C = 0 \tag{A1.16}$$

Hence

$$p_2 = \frac{-B \pm \sqrt{B^2 - 4AC}}{2A} \tag{A1.17}$$

The remaining kinematic variables follow from conservation of momentum

$$\vec{p}_3 = \vec{p}_0 - \vec{p}_1 - \vec{p}_2 \tag{A1.18}$$

$$p_3^2 = p_0^2 + p_1^2 + p_2^2 - 2p_0p_1\cos\theta_1 - 2p_0p_2\cos\theta_2 + 2p_1p_2\cos\theta_{12} \tag{A1.19}$$

T_2 and T_3 can of course be calculated from p_2 and p_3. θ_3 and ϕ_3 can be found conservation of the various components of momentum, i.e.

$$p_3\cos\theta_3 = (p_0 - p_1\cos\theta_1 - p_2\cos\theta_2) \tag{A1.20}$$

$$p_3\sin\phi_3\sin\theta_3 = -p_1\sin\phi_1\sin\theta_1 - p_2\sin\phi_2\sin\theta_2 \tag{A1.21}$$

$$p_3\cos\phi_3\sin\theta_3 = -p_1\cos\phi_1\sin\theta_1 - p_2\cos\phi_2\sin\theta_2 \tag{A1.22}$$

An additional kinematic quantity of interest is the center of mass energy of pairs of existing particles. This is found by considering the Lorentz invariant scalar product of the sum of the four momenta of two particles A and B.

$$(\mathcal{P}_A + \mathcal{P}_B)^2_{Lab} = (\mathcal{P}_A' + \mathcal{P}_B')^2_{Cm} = (0, i\,(E_{ABCM}))^2 \tag{A1.23}$$

$$-m_A^2 - m_B^2 - 2E_AE_B + 2\vec{p}_A\cdot\vec{p}_B = -E^2_{ABCM} \tag{A1.24}$$

Then

$$E_{ABCM} = \left[m_A^2 + m_B^2 + 2(T_A + m_A)(T_B + m_B) - 2P_A P_B \cos\theta_{AB}\right]^{1/2} \quad \text{(A1.25)}$$

$$T_{ABCM} = E_{ABCM} - m_A - m_B \quad \text{(A1.26)}$$

It should be noted that there are two possible solutions to (A1.17), which makes the kinematics double valued, i.e. there can be two values of T_2 for a given value of T_1. The solution to (A1.17) with the minus sign for the radical corresponds to the larger value of T_2.

A1.2 Kinematic Variables for Off-Mass-Shell Cross Sections in Knockout Reactions

For the off-mass-shell cross section there are three kinematic variables: T_i, the initial state c.m. energy; T_f, the final state c.m. energy; θ_{cm} the c.m. scattering angles. The off-mass-shell collision is presumed to involve particles 1 and 2 with particle 3 being a spectator. The target contains two particles, particle 3 and particle S (for struck). The impulse approximation requires that

$$\mathcal{P}_S = -\mathcal{P}_3 \tag{A1.27}$$

It is also assumed that particle 0 becomes particle 1 and particle S becomes particle 2.

T_f has already been derived. It is just T_{12cm} from (A1.25) and (A1.26). Specifically:

$$T_f = \left[m_1^2 + m_2^2 + 2(T_1+m_1)(T_2+m_2) - 2p_1p_2\cos\theta_{12}\right]^{1/2} - m_1 - m_2 \tag{A1.28}$$

To calculate T_i it is necessary to first determine what $\mathcal{P}_S$ is. There are two conservation laws assumed for the reaction. One for the three body reaction, and one for the two body off-mass-shell scattering:

$$\mathcal{P}_0 + \mathcal{P}_T = \mathcal{P}_1 + \mathcal{P}_2 + \mathcal{P}_3 \tag{A1.29}$$

$$\mathcal{P}_0 + \mathcal{P}_S = \mathcal{P}_1 + \mathcal{P}_2 \tag{A1.30}$$

These two conservation laws require

$$\mathcal{P}_S = \mathcal{P}_T - \mathcal{P}_3 \tag{A1.31}$$

Thus in the laboratory system

$$(\mathcal{P}_S)_{LAB} = \left[-\vec{P}_3,\ i(m_T - E_3)\right]_{LAB} = \left[\vec{P}_S,\ iE_S\right] \tag{A1.32}$$

Now because of (A1.30)

$$E_{0scm} = E_{12cm} \tag{A1.33}$$

And E_{12cm} is already known. Thus T_{0Scm} the center-of-mass kinetic energy in the initial state can be calculated easily:

$$T_i = T_{oscm} = E_{oscm} - m_o - m_s = E_{12cm} - m_o - m_s \tag{A1.34}$$

m_o is of course already known. m_s, the invariant mass of the off-mass-shell particle is determined as follows:

$$-m_s^2 = \mathbb{P}_s^2 = P_3^2 - E_s^2 \tag{A1.35}$$

$$= P_3^2 - (m_T - E_3)^2 \tag{A1.36}$$

So

$$m_s = \left[(m_T - m_3 - T_3)^2 - P_3^2\right]^{1/2} \tag{A1.37}$$

Note that

$$m_s \neq m_2 \tag{A1.38}$$

i.e., the struck particle is off the mass-shell.

The remaining quantity of interest is θ_{cm}. This is the angle between the vectors $\vec{p}_o$ and $\vec{p}_1$ in the center-of-mass system for the two body collision. One starts with the dot product of $\mathbb{P}_o$ and $\mathbb{P}_1$

$$(\mathbb{P}_o \cdot \mathbb{P}_1)_{LAB} = (\mathbb{P}_o \cdot \mathbb{P}_1)_{CM} = \mathbb{P}_{0CM} \cdot \mathbb{P}_{1CM} \tag{A1.39}$$

$$-E_o E_1 + P_o P_1 \cos\theta_1 = -E_{OCM} E_{1CM} + P_{OCM} P_{1CM} \cos\theta_{1CM} \tag{A1.40}$$

Therefore:

$$\cos\theta_{1CM} = \frac{P_o P_1 \cos\theta_1 - E_o E_1 + E_{OCM} E_{1CM}}{P_{1CM} P_{OCM}}$$

$$= \frac{P_1 P_1 \cos\theta_1 - E_o E_1 + E_{OCM} E_{1CM}}{(E_{OCM}^2 - m_o^2)^{1/2} (E_{1CM}^2 - m_1^2)^{1/2}} \tag{A1.41}$$

So E_{0cm} and E_{1cm} are needed. But

$$[(\vec{P}_1 + \vec{P}_2)\cdot\vec{P}_0]_{LAB} = [(\vec{P}_{1CM} + \vec{P}_{2CM})\cdot\vec{P}_{0CM}] \tag{A1.42}$$

$$\vec{P}_1\cdot\vec{P}_0 + P_2\cdot P_0 - E_0(E_1+E_2) = (0, i E_{12CM})\cdot(\vec{P}_{0CM}, i E_{0CM})$$

$$= E_{12CM}\cdot E_{0CM} \tag{A1.43}$$

Hence

$$E_{0CM} = \frac{E_0(E_1+E_2) - P_0(P_1\cos\theta_1 + P_2\cos\theta_2)}{E_{12CM}} \tag{A1.44}$$

Similarly from $(\vec{P}_1 + \vec{P}_2)\cdot\vec{P}_1$ one obtains

$$E_{1CM} = \frac{m_1^2 + E_1E_2 - P_1P_2\cos\theta_{12}}{E_{12CM}} \tag{A1.45}$$

Hence $\cos\theta_{1cm}$ in (A1.37) can be calculated, using (A1.44) and (A1.45).

APPENDIX 2

MOMRATH

The following is a more complete description of the program discussed in Section 2.1.4. MOMRATH is a computer program that will calculate the effects of finite resolution in a three body breakup reaction. The principal quantity generated by MOMRATH is the "resolution function" W(x) for a given kinematic variable x. This resolution function W(x) depends on the geometry and kinematics of the reaction, the sizes of the detectors, and the E_1 energy bin width but not on any assumptions made about the reaction mechanism. The resolution function W(x) is a measure of the ability of the experimental system to resolve the kinematic quantity x. The discussion to follow will be specialized to the calculation of $W(p_3)$ where p_3 is the magnitude of the momentum of the residual nucleus. The generalization for other kinematic variables is obvious.

For a given reaction, at a specified bombarding energy, p_3 has a unique value for every point in the five dimensional volume $\Delta\Omega_1\Delta\Omega_2\Delta E_1$ defined by the solid angles of the detectors and the width of the E_1 energy bin. $W(p_3)dp_3$ is defined as the probability of finding p_3 in the range dp_3 for events occurring in the volume $\Delta\Omega_1\Delta\Omega_2\Delta E_1$, assuming that each volume element is equally probable. The normalization of $W(p_3)$ is

$$\int W(p_3)\, dp_3 = 1. \qquad \text{(A2.1)}$$

Operationally, MOMRATH generates $W(p_3)$ by calculating p_3 for a large number of points in $\Delta\Omega_1\Delta\Omega_2\ \Delta E_1$ and making a distribution of values obtained.

MOMRATH selects this large number of points in a systematic manner. A grid of points is selected for each counter and a series of points is selected for the E_1 energy interval. Figure A.2 shows how such an array of points might look

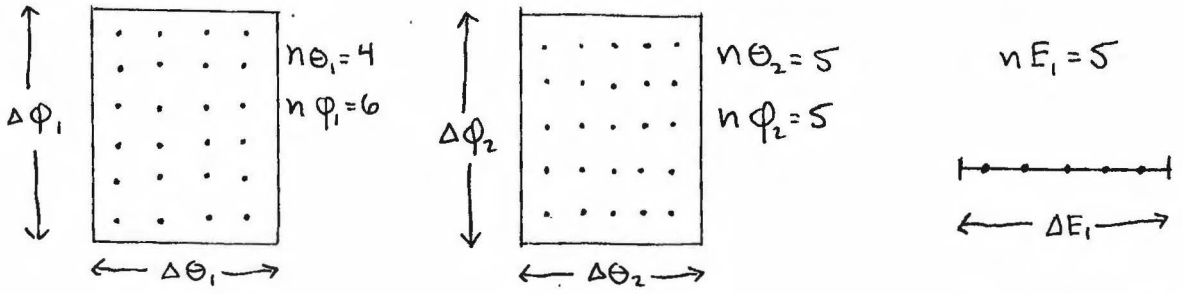

Counter One Counter Two E_1 Energy Bin

Figure A2 Grid Points on the Counters and E_1 Energy Bin

The number of grid points $n\theta_1$, $n\phi_1$, $n\theta_2$, $n\phi_2$ and nE_1 for each of the five variables θ_1, ϕ_1, θ_2, ϕ_2, and E_1 is assigned according to the sensitivity of p_3 to changes in the five variables. This sensitivity is determined in the early stages of the program by varying the five variables one at a time. MOMRATH then calculates p_3 for every possible combination of a grid point from counter one, a grid point from counter two, and a grid point from the E_1 energy bin. This means typically p_3 is evaluated for about 3000 different combinations. The values of p_3 are stored and displayed in a histogram which is $W(p_3)$.

When $W(p_3)$ has been calculated it can be used within certain limitations to evaluate the amount to which the measured cross section will be smeared by the finite resolution of the system for p_3. This is done as follows. The cross section is assumed to be a function of p_3 only. For quasi-free scattering in the Plane Wave Impulse Approximation (1.7) this means that the kinematic factor and $(d\sigma/d\Omega)$ are assumed to be constant over the volume $\Delta\Omega_1 \Delta\Omega_2 \Delta E_1$. Then

$$\frac{d^3\sigma}{d\Omega_1 d\Omega_2 dE_1} = C \left| \overline{\Phi}(p_3) \right|^2 \qquad \text{(A2.2)}$$

The measured cross section which will be called σ_M is an average of $d^3\sigma/d\Omega_1 d\Omega_2 dE_1$ over $\Delta\Omega_1\Delta\Omega_2\Delta E_1$

$$\sigma_M = \int_{\Delta\Omega_1} d\Omega_1 \int_{\Delta\Omega_2} d\Omega_2 \int_{\Delta E_1} dE_1 \left(d^3\sigma/d\Omega_1 d\Omega_2 dE_1\right) \tag{A2.3}$$

$$= C \int_{\Delta\Omega_1} d\Omega_1 \int_{\Delta\Omega_2} d\Omega_2 \int_{\Delta E_1} dE_1 \left| \Phi(p_3) \right|^2 \tag{A2.4}$$

Since the cross section is a function of p_3 only, σ_M can be evaluated directly from $W(p_3)$, i.e.:

$$\sigma_M = \int W(p_3) \left| \Phi(p_3) \right|^2 dp_3 \tag{A2.5}$$

If MOMRATH is given a momentum distribution $|\Phi(p_3)|^2$ it will calculate σ_M from (A2.5) after evaluating $W(p_3)$.

If $d^3\sigma/d\Omega_1 d\Omega_2 dE_1$ were not expected to depend on only p_3 within the volume $\Delta\Omega_1\Delta\Omega_2\Delta E_1$, a more elaborate program would have to be devised.

APPENDIX 3

LITHIUM TARGET PREPARATION

Self-supporting Li targets were made by evaporating a thin film of Li metal onto a glass plate and then removing the Lithium from the glass. Before the evaporation the glass plate was dipped into a saturated solution of Hexadecylamine in Hexane, and then allowed to dry thoroughly. The plates were then brushed with laboratory wipes to remove most of the deposit, so that a thin fairly uniform layer was left. This layer of Hexadecylamine served as a releasing agent, and the best thickness for the layer on the plates was determined by experience.

A boat made of stainless steel was used for the evaporation (Lithium reacts with Tantalum or Tungsten). The evaporation was done over a period of several minutes in a vacuum of 10^{-6} or 10^{-7} torr.

After the Lithium was evaporated onto the plates the evaporator bell-jar was filled with Helium to minimize oxidation of the Li deposit. From this point on, speed was essential. The plates were quickly placed in Hexane and removed from the evaporator. Working under Hexane, the Li film was peeled off the glass with a clean sharp razor blade. The ease with which this could be done depended on the thickness of the Hexadecylamine deposit. Too thin a deposit would cause the target to curl badly while being peeled off the glass. Too thick a deposit would allow the Lithium to float off the glass plate and then to the surface of the Hexane where it oxidized.

Still working under Hexane, the Li foil was mounted in a target frame and then transferred quickly to a vacuum container and pumped down to a good vacuum. The layer of Hexane on the Lithium protected it from oxidation during the transfer and pump-down. With a cold trap and a vacuum of one

micron the targets could be kept for a day or more without deterioration. To transfer the target to and from the scattering chamber, the chamber was filled with Argon. Very little deterioration was found to occur in this process.

The work in Hexane was done under a hood to remove noxious vapors. It also was necessary to work with bare hands because gloves were found to significantly slow down the process. The Hexane was kept clean and water free because Lithium oxidizes violently in contact with water. The resultant reaction has been known to ignite the Hexane, which is highly flammable.

With the above procedure it is easy to make self-supporting Lithium targets as thin as 600 $\mu gm/cm^2$, and probably as thin as 300 $\mu gm/cm^2$.

REFERENCES

A55 R. Adkins and J.G. Brennan, Phys. Rev. 99. 706 (1955).

B60 T.A. Brody and M. Moshinsky, "Table of Transformation Brackets" Monografias del Institudo de Fisica, Mexico (1960).

B66 F.C. Barker, Nucl. Phys. 83, 418 (1966).

B68 V.V. Balashov and D.V. Meboniya, Nucl. Phys. A107, 369 (1968).

B69 A.D. Bacher et al.,Bull. Am. Phys. Soc. 14, 534 (1969).

Ba69 K. Bähr et al., Phys. Rev. 178, 1706 (1969).

Be66 T. Berggren and H. Tyren, Ann. Rev. Nuc. Science 16, 153 (1966).

Bo69 D.I. Bonbright, private communication.

Bu68 R.L. Burman and M.E. Nordberg, Jr., Phys. Rev. Lett. 21, 229 (1968).

C59 A.M. Cormack et al., Phys. Rev. 115, 599 (1959).

C60 H.E. Conzett et al., Phys. Rev. 117, 1075 (1960).

C67 G. Charpak et al., "International Nuclear Physics Conference" p. 465, ed. R.L. Becker, Academic Press, New York (1967).

D65 P. Darriulat, Thesis, Univ. of Paris (1966).
P. Darriulat et al., Phys. Rev. 137, B315 (1965).

D66 H. Davies et al., Nucl. Phys. 78, 663 (1966).

D67 P. Darriulat et al., Nucl. Phys. A94, 653 (1967).

D69 V.V. Davydov and I.M. Pavlichenkov, Phys. Lett. 29B, 551 (1969).

De65 D.W. Devins et al., Rev. Mod. Phys. 37, 396 (1965).

Do69 V.K. Dolinov, Sov. J. Nucl. Phys. 8, 15 (1969).

E53 J.P. Elliott, Proc. Roy. Soc. (London) A218, 706 (1953).

F54 G.M. Frye, Phys. Rev. 93, 1086 (1954).

F57 J.B. French and A. Fujii, Phys. Rev. 105, 652 (1967).

F62 E. Ferrari and F. Selleri, Nuovo Cimento Supp. 24, 453 (1962).

G55 A. Galonsky and M.T. McEllistrem, Phys. Rev. 98, 590 (1955).

G60 A.M. Green and G.E. Brown, Nucl. Phys. 18, 1 (1960).

H66 D.L. Hendrie et al., UCRL #16580, 146 (1966) unpublished.

H68 E.C. Halbert et al., Preprint.

H69 H.D. Holmgren, U. of Md. Tech. Report 998 (1969).

I53 D.R. Inglis, Revs. Mod. Phys. 25, 390 (1953).

J63 A.N. James and H.G. Pugh, Nucl. Phys. 42, 441 (1963).

J66 G. Jacob and Th.A.J. Maris, Revs. Mod. Phys. 38, 121 (1966).

J67 D.F. Jackson, Nuovo Cimento 41B, 49 (1967).

J69 M. Jain, Thesis, Univ. of Md. (1969).

K56 D. Kurath, Phys. Rev. 101, 216 (1956).

K59 Th. Kanellopoulos and K. Wildermuth, Nucl. Phys. 14, 349 (1959).

K68 Yu.A. Kudeyarov et al., Sov. J. Nucl. Phys. 6, 876 (1968).

L56 J.G. Likely and F.P. Brady, Phys. Rev. 104, 118 (1956).

L67 H.H. Landolt, "Zahlenwerte und Funktionen aus Naturwissenschaften und Technik" New Series, Group I, Vol. 2, Nuclear Radii, Springer Verlag, Berlin (1967).

M56 S. Meshkov and C.W. Ufford, Phys. Rev. 101, 734 (1956).

M58 M.J. Moravçsik, Nucl. Phys. 7, 113 (1958).

M61 M.A. Melkanoff et al., "A FORTRAN Program for Elastic Scattering Analyses with the Nuclear Optical Model", Univ. of Calif. Press, Los Angeles (1961).

M67 L.C. McIntyre and W. Haeberli, Nucl. Phys. A91, 382 (1967).

M68 G.S. Mani and A. Tarrats, Nucl. Phys. A107, 624 (1968).

Ma68 S. Matsuki, J. Phys. Soc. Japan 24, 1203 (1968).

N65 V.G. Neudachin and Yu.F. Smirnov, Atomic Energy Rev. 3 (1965).

P56 J.K. Perring and T.H.R. Skyrme, Proc. Phys. Soc. 69, 600 (1956).

P58 W.T. Pinkston and J.G. Brennan, Phys. Rev. 109, 499 (1958).

P69 J.R. Pizzi et al., preprint.

Pu69 H.G. Pugh et al., Phys. Rev. Lett. 22, 408 (1969).

R54 T. Regge, Nuovo Cimento 11, 285 (1954).

R63 C. Ruhla et al., Phys. Lett. 6, 282 (1963).

R66 R.E. Rand et al., Phys. Rev. 144, 859 (1966).

R67 L.S. Rodberg and R.M. Thaler, "Introduction to the Quantum Theory of Scattering", Academic Press, New York (1967).

R68 I. Rotter, Fortschritte der Physik 16, 195 (1968).

S57 J.M. Soper, Phil. Mag. 2, 1219 (1957).

S63 E.W. Schmidt et al., Phys. Lett. 7, 263 (1963).

S65 Y. Sakamoto, Nucl. Phys. 66, 531 (1965).

S66 I.S. Shapiro, Proc. Int. School Physics, "Enrico Fermi", Varenna, XXXVIII, 210, Academic Press, New York (1966).

T54 G.E. Tauber and T. Wu, Phys. Rev. 93, 295 (1954).

T61 Y.C. Tang et al., Phys Rev. 123, 548 (1961).

T69 D.R. Thompson and Y.C. Tang, preprint.

W54 H.E. Walchli, ORNL 1775 (1954).

W58 K. Wildermuth and Th. Kanellopoulos, Nucl. Phys. 7, 150 (1969).

W64 L. Wharton et al., Phys. Rev. 133, B270 (1964).

W66 K. Wildermuth and W. McClure, "Springer Tracts in Modern Physics," Vol. 41, Springer Verlag, Berlin (1966).

W69 J.W. Watson and H.G. Pugh, private communication.

Y69 M.R. Yearian, private communication.